# Flat versus normal subduction zones : a comparison based on 3-D regional travel-time tomography and petrological modeling of Central Chile and Western Argentina (29°-35°S)

Marianne Marot

UNIVERSITÉ DE NICE-SOPHIA ANTIPOLIS – UFR SCIENCES
École Doctorale de Sciences Fondamentales et Appliquées

# THÈSE

pour obtenir le titre de

## Docteur en Sciences

**de l'Université de Nice-Sophia Antipolis**

Spécialité : Sciences de la Terre et de l'Univers – Sismologie et Géodynamique

Présentée et soutenue par

**Marianne MAROT**

# Zones de subduction horizontale versus normale: Une comparaison basée sur la tomographie sismique en 3-D et de la modélisation pétrologique de la lithosphère continentale du Chili Central et de l'Ouest de l'Argentine (29°S-35°S)

*Flat versus normal subduction zones: A comparison based on 3-D regional travel-time tomography and petrological modeling of Central Chile and Western Argentina (29°-35°S)*

Thèse dirigée par **Guust NOLET** et **Tony MONFRET**
Préparée au laboratoire GéoAzur, Sophia-Antipolis
Financée dans le cadre du projet European Research Council

Soutenue le 27 Juin 2013 à 14h, devant le Jury :

| | | |
|---|---|---|
| RITSEMA Jeroen | Professeur | Rapporteur |
| TASSARA Andres | Maître de Conférence | Rapporteur |
| DORBATH Catherine | Directeur de Recherche | Examinatrice |
| GERBAULT Muriel | Chargé de Recherche | Examinatrice |
| BELLIER Olivier | Professeur | Examinateur |
| NOLET Guust | Professeur | Directeur de Thèse |
| MONFRET Tony | Chargé de Recherche | Co-directeur de Thèse |

# Acknowledgements

First of all, I am grateful to all the members of my jury, for accepting the heavy task of reading and judging this thesis research: *Jeroen Ritsema*, *Andres Tassara*, *Catherine Dorbath*, *Olivier Bellier* and *Muriel Gerbault*. *Muriel*,a special thank you for your vivid enthusiasm, curiosity and moral support. Your constant questioning was stimulating and your contribution brought colors to my thesis (literally).

I cannot thank enough my thesis supervisors, *Tony Monfret* and *Guust Nolet*, for their constant encouragement, moral support, patience, guidance, faith in me, and for giving me freedom in my choices. With you, everything sounded possible (even starting up a museum business), and I am extremely thankful for the opportunity I was given me to participate in a volcano geophysics course in Hawaii: it was unique.

I thank *Giorgio Ranalli*, who accompanied and guided me since my undergrad, and became a very special friend over the years. G., your first-year Earth Science course (which resembled more a gastronomy course - milk and camembert to describe plate tectonics), your personal empirical equations about human behaviors and your Italian proverbs, always brightened up my days. I am glad I met you.

I thank all the *GéoAzur* team of I.T., administration and communication for their availability and effectiveness in solving my (many) problems, and for their joyfulness: *Lionel*, *Julien*, *Caroline*, and the fabulous ladies: *Jenny*, *Corinne*, *Véronique*, *Reine*, *Valérie*, *Fabienne* and *Magalie*.

I thank all my *family* for helping me achieve my dreams, believing in me, and for being present to all my achievements: my *Marraine*, *Tonton*, *Mamet*; and particularly my beloved *Dad*, who has always kept an eye on me. Thank you to my darling *Yannick*, who represents my harbor during storms, and much more. I also thank my adored little siblings, *Pierre-Shams*, *Noor-Hélia* and *Jules-Amir*, for all the fun and silly distractions we've had together (more to come!), and for the strong bond that we form when times get really tough : Never give up.

Finally, I thank all my friends and colleagues, whom I've met during this PhD or long ago, for making me giggle and learn, and whom I have a huge respect for: *Benoît*, *Flore*, *Swann*, *Maurin*, *Nils*, *Yaser*, *Clément*, *Alain*, *Imane*, *Juan Carlos*, *Cécile*, *Clarita*, *Quentin*, *Nestor*, *Yvegenia*, *Alice*, *Inna*, *Michel*, *Vivien*, *Alison*, *Sarah*, *Zanete*, and *Jenna*. I mostly owe a particular strong acknowledgement to my officemates, *Benoît*, *Flore* and *Swann*: true friends who have made these four years memorable and fun, and without whom I wouldn't have made it this far, both in my professional and personal achievements; Guys, thanks for enduring my everyday ups-and-downs, for our endless scientific and personal debates, and for your total craziness and silliness in not taking life too seriously. You were my breath of fresh air and you will be so missed!

Take care, all, for now. We shall meet again!

# Abstract

Beneath central Chile and western Argentina, the oceanic Nazca slab drastically changes geometry from horizontal to dipping at an angle of 30°, and correlates with the subduction of the Juan Fernandez seamount ridge. The aim of our study is to assess, using a thermo-petrological-seismological approach, the differences of the overriding lithosphere between these two regions, in order to better understand the deep structure of the continental lithosphere above the flat slab, and the links between the deformations at the surface and at depth. We show the most complete regional 3-D seismic tomography images of this region, whereby, in comparison to previous studies, we use (1) a much larger seismic dataset compiled from several short-term seismic catalogs, (2) a much denser seismic station network which enables us to resolve better the subduction zone from the trench to the backarc and into the upper ~ 30 km of the slab, and (3) a starting 1-D background model calculated for this region specifically and refined over the years. We assess and discuss our tomography results with supporting existing models of seismic attenuation results for this region, and predicted rock types which we calculated using Hacker and Abers (2004) mineral and rock database, and by estimating the pressure and temperature conditions at depth from thermo-mechanical modeling. We show significant seismic differences between the flat and normal subduction zones. As expected, the flat slab region is impacted by colder temperatures imposed by the slab geometry, and is characterized by faster seismic velocities and more intense seismic activity, both within the slab and in the overriding plate, compared to the normal slab region. We show evidence that the flat slab dehydrates within the mantle wedge, but also along the subducting ridge prior to re-subducting. The forearc crust above the flat slab is described by unusual seismic properties, correlated to the slab geometry at depth, and/or, to the aftershock effects of the 1997 Mw 7.1 Punitaqui earthquake which occurred two years before the recording of our events. The continental crust above the flat slab has very heterogeneous seismic properties which correlate with important deformation structures and geological terranes at the surface. We confirm previous studies that have shown that the thick lower crust of the present day Andean arc is non-eclogitized and maybe representing the felsic Chilenia terrane, whereas to the east, the Cuyania terrane in the backarc is more mafic and contains an eclogitized lower crust. We also suspect that well identified major crustal faults or shear zones extend towards the plate interface and/or channelize slab-derived fluids through the continental crust.

**Key words**: Central Chile, flat subduction, seismic tomography, rock composition, thermo-mechanical modeling, eclogite crust, dehydration/hydration

# **Résumé** (in French)

Sous le Chili central et l'ouest de l'Argentine (29°-35°S), la plaque océanique Nazca, en subduction sous la plaque continentale Amérique du Sud, change radicalement de géométrie : inclinée à 30°, puis horizontale, engendrée par la subduction de la chaine de volcans de Juan Fernandez. Le but de mon étude est d'évaluer la variation de nature et de propriétés physiques de la lithosphère chevauchante entre ces deux régions, afin de mieux comprendre (1) sa structure profonde et (2) les liens entre les déformations observées en surface et en profondeur. Pour répondre à cette thématique, j'utilise une approche originale couplant la sismologie, la thermomécanique et la pétrologie. Je montre ainsi des images 3-D de tomographie sismique les plus complètes de cette région, par rapport aux études précédentes, qui intègrent (1) de nombreuses données sismiques provenant de plusieurs catalogues, (2) un réseau de stations sismiques plus dense, permettant de mieux imager la zone de subduction de la fosse à l'arrière-arc, ainsi que les 30 premiers km du *slab*; et (3) un modèle de vitesse 1-D calculé en particulier pour cette région et affiné au fur et à mesure de la croissance du nombre de données. J'évalue les différences sur les résultats de tomographie pour la zone de subduction plate et inclinée (en 2-D), en prenant en compte (i) un modèle préexistants, régional, d'atténuation sismique, et (ii) les propriétés sismiques prédites pour des roches à des conditions de pression et température estimées par nos modèles thermomécaniques, utilisant la base de données Hacker et Abers (2004). Je montre des différences sismiques importantes entre ces deux zones. Comme prévu, la région à subduction plate connait des températures amoindris imposées par la géométrie du *slab* et l'absence d'asthenosphere. Elle se caractérise par des vitesses sismiques plus rapides et une sismicité plus intense dans la plaque océanique, mais également dans la plaque continentale chevauchante. J'apporte la preuve que le *flat slab* se déshydrate dans deux régions distinctes : (1) le coin mantellique, et (2) le long de la ride subduite avant qu'elle ne re-plonge plus profondément dans le manteau. La croûte continentale au-dessus du *flat slab* possède des propriétés sismiques très hétérogènes en relation avec les structures de déformations profondes et les domaines géologiques spécifiques. La croûte chevauchante d'avant-arc, au-dessus du *flat slab*, est décrite par des propriétés sismiques inhabituelles, liées à la géométrie particulière du *slab* en profondeur, et/ou liées aux effets du séisme de 1997 de Punitaqui (Mw 7.1). Mes résultats, confirmant les études antérieures, montrant que le bloc Cuyania, situé plus à l'est, dans la zone d'arrière-arc, est plus mafique et contient une croûte inférieure éclogitisée; quant à, la croûte continentale inférieure, sous l'arc Andin, est épaisse et non-éclogitisée, décrivant surement le bloc felsique de Chilenia. Je suppose également que les failles ou zones de cisaillement principales de la croûte chevauchante, identifiées en surface et approximativement en profondeur, atteignent la zone interplaque, canalisant ainsi les fluides en provenance du *flat slab*.

**Mots-clés** : Chili Central, subduction plate, tomographie sismique, composition de roches, modélisation thermo-mécanique, croûte éclogitisée, déshydratation/hydratation

# **Résumé Étendu** (in French)

Ce travail de thèse se focalise sur la région de subduction du Chili central et l'ouest de l'Argentine. Dans cette région, la plaque océanique Nazca est jeune (35 Ma) et entre en subduction sous l'Amérique du Sud. A environ 100 km de profondeur, la plaque en subduction (*slab*) devient horizontale avec une très forte activité sismique. La géométrie du *slab* à ces profondeurs est très bien corrélée avec la géométrie des monts sous-marins en subduction de Juan Fernandez (JFR), mais aussi avec l'absence de volcanisme à la surface. La plaque chevauchante, actuellement en compression, est composée d'une série de terrains accrétés de diverses origines, compositions et d'âges. Dans cette thèse, je propose l'hypothèse générale que la multitude de phénomènes inexpliqués observés à la surface est liée à la géométrie du *slab* en profondeur.

L'objectif de ce travail est de caractériser les conséquences de la subduction plate sur la plaque chevauchante, en termes des variations de vitesse d'ondes sismiques et de sa structure compositionnelle. Et, puisqu'il n'y a pas de consensus général sur la formation de cette subduction plate, nous testons les hypothèses d'une croûte océanique sur-épaissis, d'une éclogitisation retardée et en conséquence, de fluides conservés dans le *slab*. Nous abordons les principales questions: Est-ce que la déshydratation du *slab* plat se produit dans ces conditions de pression et de température particulière? Si oui, à quel point est-ce que le *slab* plat est hydraté, à quelle profondeur la déshydratation se produit, où sont les fluides transportés, et où sont-ils stockés? Le magmatisme est-il toujours active sous l'arc, qui est aujourd'hui inactif? Sont les terrains accrétés et les zones de sutures des attributs importants de cette zone de subduction et de sa dynamique? Est-ce qu'ils possèdent leurs propres entités du manteau sous-jacent?

Pour ce faire, j'ai comparé les variations du champs des ondes sismiques P et S et des compositions de roches que nous prédisons pour les régions où la subduction est plate (30°-33°S) et « normale » (pendage de 30°, > 33.5°S). Le champ de vitesses des ondes sismiques de première arrivée (P et S) a été calculé au moyen de la méthode de tomographie sismique à l'échelle régionale, sur la base d'une vaste base de données de séismes locaux enregistrés par les campagnes sismiques dans la région à différents intervalles de temps. Puis, nous avons couplé nos résultats de tomographie sismique avec des modèles 2D de thermomécaniques instantanés calculées pour deux coupes verticale le long du *slab* plat et normal, afin de prédire les types de roches en profondeur dans des conditions de température et de pression élevée.

Notre base de données est un ensemble de sources passives, locales, enregistrées au cours de quatre campagnes sismiques de courte durée, complétée par le réseau permanent Chilien, et d'un modèle initial, régional, de vitesse spécifique à la région. Pour assurer la stabilité et la fiabilité de nos résultats de tomographie sismique, nous avons sélectionné uniquement les événements de la plus haute qualité avec les critères de sélection suivants pour les P et S, respectivement: (a) une erreur maximale de pointé manuelle de ± 0.25 s et ± 0.4 s, (b ) un indice de qualité maximum à 2 et 3 (0 étant excellent, 4 étant éliminé), (c) une incertitude d'hypocentre maximum de 5 km dans toutes les directions, (d) une valeur maximale de la RMS ($\sqrt{\Sigma Ri^2/N}$, où Ri est le temps résiduelle à la $i^{ème}$ station) de < 0.6 s, et (e) au moins 8 et 4 observations d'arrivées aux stations. Ainsi, nous conservons un total de 3 603 événements pour le processus d'inversion, y compris 52 011 et 51 631 arrivées d'ondes P et S, respectivement. Tous les événements sont relocalisés préalablement, en utilisant HYPOINVERSE (Klein, 2000), au sein d'un modèle de vitesses 1D qui décrit au mieux la région, construit à partir de sources actives et passives, et avec le programme VELEST (Kissling et al., 1994) pour des profondeurs de plus de 20 km. Ce modèle de vitesse représente un modèle de 17 couches avec un ratio moyen de Vp/Vs égal à 1.76. En comparaison avec le modèle moyen global IASEP-91, qui est utilisé

pour de nombreuses études précédentes, notament celle de Wagner et al. (2005), notre modèle fournit généralement des vitesses plus rapides et une discontinuitée du Moho continental plus profond.

L'algorithme de tomographie sismique que nous utilisons est TLR3 (Latorre et al., 2004; Monteiller et al., 2005). Il est divisé en deux étapes principales: (1) la résolution du problème directe, qui s'attaque au tracés des rayons en 3D par la résolution des différences finies de l'équation Eikonal (Podvin et Lecomte, 1991) à travers d'un modèle de vitesse quadrillé finement, suivi de (2) la résolution du problème inverse, par laquelle les temps de trajets synthétiques et les temps de trajets résiduels sont calculés et inversés à travers un modèle quadrillée plus grossier en utilisant l'algorithme de LSQR (Paige et Sanders, 1982). Ces deux étapes, combinées avec une réévaluation systématique des hypocentres, sont répétées de manière itérative jusqu'à ce que le temps résiduel minimal soit atteint. Lors de la première itération, les modèles de vitesses initiaux des ondes P et S sont utilisées et, pour chaque autre itération, les résultats de l'itération précédente sont utilisés comme les nouveaux modèles initiaux de l'itération suivante. Le nombre d'itérations nécessaires pour obtenir la stabilité de la solution dépend de la quantité et de la qualité des données. Le choix du nombre d'itération à laquelle la solution finale du modèle est pris est une décision semi-subjective, cependant, le modèle ne varie pas beaucoup entre deux solutions voisines. L'erreur acceptable du modèle final est donnée par la valeur de RMS finale, qui représente la racine carré normalisé des résidus en temps des trajets d'ondes ($= \sqrt{\Sigma Ri^2/N}$, où Ri est le temps résiduel à la $i^{ème}$ station), dès que la RMS tombe en dessous d'un certain seuil (~ 0.2 s). Une fois un modèle final est obtenu, nous évaluons statistiquement la dimension du maillage de la grille d'inversion et de la résolution du modèle final avec les tests de résolution de *Checkerboard* et de *Spike*. L'algorithme TLR3 a été choisi pour sa relative simplicité, sa rapidité de calcul et sa précision suffisante.

Les limites de notre modèle sont définies entre les longitudes 73.5°W et 64.5°W, les latitudes 28.5°S et 37.5°S, et entre les profondeurs 0 à 215 km, ce qui représente un volume total de 960 x 840 x 220 $km^3$. Ce volume est discrétisé en un système de grille régulière avec un maillage de 40 x 40 x 10 $km^3$. Les trajectoires des rayons synthétiques sont calculées selon un modèle plus fin, de taille 2 x 2 x 2 $km^3$, et les temps de trajectoires des rais sont calculées dans le modèle plus grossier, pour une l'efficacité informatique. Les valeurs des paramètres de pré-conditionnement du model, le *damping* et le *Cp/Cs*, ont été ajustés séparément en fixant un paramètre à la fois et en permettant à l'autre de varier, afin d'obtenir les valeurs qui minimisent la valeur de la RMS finale. Les paramètres qui ont conduit à de meilleurs résultats étaient une valeur de *damping* de 0.7 et une valeur de *Cp/Cs* de 0.5.

Afin de lier la géologie superficielle avec les mécanismes de déformation à l'échelle lithosphérique, nous avons comparé les propriétés sismiques de roches à des conditions de pression et température (P-T) appropriées avec nos vitesses sismiques calculés. Pour ce faire, nous avons estimé numériquement le champ de P-T pour deux sections verticales (2-D) le long des zones de subduction plate (31.5°S) et normale (33.5°S), en modélisant le comportement thermomécanique des lithosphères. Le code de différences finis "Parovoz" (Poliakov et Podladchikov, 1992) a été utilisé, et est basé sur la méthode FLAC (Fast Lagrangian Analysis of Continuum ; Cundall et Board, 1988). La version du code utilisée ici est la même que celle utilisée dans Gerbault et al. (2009). Les équations du mouvement et de transfert de chaleur sont explicitement résolues dans un système de petit incrément en temps, et permettent de prendre en compte des rhéologies élasto-visco-plastiques.

Le domaine modélisé est divisée en unités rhéologiques de différents paramètres thermomécaniques (décrivant le comportement élastique, rupture de Mohr-Coulomb, et le fluage visqueux en loi de puissance) qui décrivent les différentes parties de la lithosphère continentale et océanique. Le temps de calcul est choisi pour couvrir ~ 4 Ma, au cours duquel nous supposons que la configuration initiale trouve un équilibre thermomécanique transitoire qui n'évolue plus beaucoup, ne considérant que les principaux processus qui sont importants à cette échelle de temps (diffusion thermique, équilibre isostatique).

Les géométries des modèles de départ sont établis en fonction de la répartition des hypocentres de notre catalogue en profondeur, et complétées par la réflexion sismique et de données à grand angle, pour les profondeurs inférieures à 10 km (Flueh et al., 1998). Les âges thermiques de la lithosphère océanique et continentale sont fixés à 35 Ma et 200 Ma, respectivement, et calculés comme dans Burov et Diament (1996). L'épaisseur de la lithosphère continentale (LAB) est déterminée par l'isotherme 1350°C, qui est fixée à 100 et 150 km de profondeurs dans la région à subduction plate et normale, respectivement (à proximité des valeurs déterminées par Tassara et al. 2006). De plus, le réchauffement radiogénique ($8 \times 10^{-10}$ W/kg, avec une décroissance exponentielle fixée à 10 km) est imposé dans la croûte continentale, qui a une épaisseur de référence de 35 km. La vitesse de convergence des plaques est appliquée à 7.5 cm/an sur la base des prévisions à long terme par Somoza et Ghidella (2005) et d'O'Neill (2005).

Pour une coupe en 2-D représentative de la subduction normale (33.5°S) et plate (31.5°S), et pour chaque cellule du modèle et aussi à des endroits spécifiques de ces régions, nous avons analysé les types de roches correspondant au mieux à nos vitesses sismiques calculées pour le manteau continental, la base de la croûte continentale et la partie supérieure du *slab* pour laquelle nous avons de la résolution. Nous avons fondé notre analyse sur les propriétés isotropes, mesurées expérimentalement, des compositions rocheuses mafiques et ultramafiques représentatives des zones de subduction en général (Hacker et al., 2003). La base de données rocheuses de Hacker et Abers (2004) fournit une liste de plusieurs compositions de roches pour lequel nous avons testés, dont 25 roches type-MORB, 19 péridotites hydratées (10 harzburgites, 9 lherzolites) et 21 péridotites non-hydratées (10 lherzolites, 7 harzburgites, 1 dunite, wherlite, olivine clinopyroxénite et pyrolite). Nous avons pris en compte une incertitude en Vp et Vs de ± 0.1 km/s, en température de ± 100°C, et en pression de ± 0.5 GPa. Nous n'avons pas comparé les ratios Vp/Vs, puisque de petites variations en Vp ou Vs, ou les deux, au sein de la contrainte d'incertitude, induit des différences importantes dans les rapports Vp/Vs. Par conséquent, nous ne reconnaissons que les vitesses absolues.

Nous n'avons pas utilisé des bases de données de roches plus complètes, comme par exemple Perple_X (Connolly, 2005) et Theriak (Capitano et Petrakakis, 2010), puisque ces méthodes nécessitent généralement que la composition détaillée de la roche et des minéraux soit connus (obtenu à partir de l'échantillonnage sur le terrain et d'analyses de laboratoire), ce qui n'est pas notre cas ici. En outre, les incertitudes liées à nos données tomographiques et thermomécaniques sont trop importantes pour justifier le recours de méthodes plus complexes et plus précises, qui de plus, sont les mieux appliqués aux domaines de la croûte terrestre que du domaine du manteau. En revanche, la base de données de Hacker et Abers (2004) a été très bien développé pour les domaines du manteau, ce qui est notre principal intérêt dans cette étude.

Nous avons également analysé les compositions de roches et de minéraux utilisés par Wagner et al. (2005) pour expliquer leur champ de vitesse des ondes sismiques pour le manteau continental au-dessus du slab *plat* pour cette région, et nous les avons comparés à ceux de Hacker et Abers (2004).

Le but de cet exercice n'est pas de trouver une composition spécifique de roche qui décrit au mieux le champ de vitesse des ondes sismiques à une certaine profondeur, mais plutôt d'observer si des tendances se manifestent, comme par exemple des faciès de roche récurrents (e.g. éclogites vs schistes bleus) ou dans le cas des roches du manteau, hydraté vs non-hydraté, péridotites à grenat vs péridotites de plagioclase. Nous avons cartographié la distribution et la moyenne des pourcentages en volume (% vol) d'eau et d'autres minéraux des roches pour chaque cellule. Cependant, il est important de considérer le nombre de solutions obtenues pour chaque cellule, car elle quantifie statistiquement la fiabilité de nos résultats.

Nos résultats montrent qu'il y a des changements importants entre les propriétés sismiques affectant la lithosphère continentale du Chili central et de l'ouest Argentine par-dessus la zone de subduction plate et la normale. La croûte de l'avant arc, au-dessus de la subduction plate, présente des

propriétés de vitesses sismiques anormales (rapports Vp/Vs très faibles) que nous ne parvenons pas à expliquer, cependant, ils semblent liés avec la géométrie du *slab* en profondeur, et/ou, la région de répliques de Punitaqui (1997, Mw 7.1) qui présente des tendances sismiques similaires, et/ou, à la déformation de la croûte. La croûte de l'arc Andin se caractérise par d'importantes réductions sismiques et d'un rapport Vp/Vs plus fort le long des zones de dommages structurels importants (*fold-and-thrust belts*), et aussi près de sa racine crustale, que nous décrivons comme étant non-éclogitisée, peut-être même felsique et contenant des fluides. Il semble exister une corrélation positive entre les zones de rapports Vp/Vs relativement élévés et les extensions estimées de zones de cisaillement crustales. Nous suggérons que ces grandes zones de cisaillements recoupent le manteau continental, atteignant l'interface de la subduction et de fournir des chenaux pour qu les fluides dérivés du *slab* atteingnent la croûte continentale, où les rapports Vp/Vs sont tout aussi élevé. Nous imageons le terrain de Cuyania, dans la région du backarc, comme une anomalie de vitesse sismique rapide avec une croûte inférieure éclogitisée en dessous de 50 km de profondeur, soutenant de nombreuses interprétations précédentes. Le coin mantellique continental présente des niveaux similaires d'hydratation au-dessus de la zone à subduction plate et normale, sur une gamme de profondeur limitée entre 50 et 60 km de profondeur. Nous suggérons que le coin mantellique continental au-dessus du *slab* normale (30°) est étonnamment sec, bien que chaud, et qu'il reflète les conditions transitoires de la zone plus «normal» de la subduction plus au sud. Le manteau continental au-dessus du slab plat est exprimé par des vitesses sismiques rapides, attribué à une géothermie inférieure. Cela explique bien le style de déformation plus intense à la surface, et l'arrêt du volcanisme d'arc dans la région à subduction plate. Nous montrons la preuve que la chaine du mont sous-marin de Juan Fernandez en subduction relâche des fluides dans le manteau continental avoisinant en bordure du *slab* plat, avant qu'il ne re-subduct (68.5°W/31.5°S). Nous interprétons cela en raison de processus d'éclogitisation déclenchée par la température supérieure du manteau à cet emplacement. Dans toute la région, l'eclogite pourraient se produire dans la croûte océanique à partir de 50 km de profondeur, en contradiction avec la flottabilité du *slab* plat apparent et de nombreuses autres observations. D'autres explications sont que le maillage de notre modèle ne résout pas la croûte océanique, ce qui suggère qu'elle serait plus mince que 10 km d'épaisseur (de l'ordre de notre modèle de résolution verticale), soit que la crôute oceanique est entièrement éclogitisée, tel que proposé par une étude précédente.

# Table of Contents

# Introduction

The Andean Cordillera is a continuous mountain range running along the western margin of South America. It is the fruit of 200 Myr of oceanic-continent subduction. Though, the Andean orogeny is considered an ideal model for mountain building at a convergent boundary, its high elevation and geometry cannot be entirely explained by subduction processes only (e.g. Swift and Carr, 1974; Ramos, 1999; 2009; Ramos and Aleman, 2000; Cembrano et al., 2007; Contardo and Cembrano, 2007; Gerbault et al., 2009).

Its strong segmentation of systematic along-strike variations in topography, morphology, tectonics, basin distribution, volcanism, subduction geometry, deep lithospheric structure and geologic history are not entirely understood yet. However, nowadays, the segmentation appears correlated with areas of subducting oceanic features (ridges, faults, plateaus) and variations in the degree of plate coupling, slab age and slab shape (Figure 0.1) (e.g. Cembrano et al., 2007; Ramos, 2009).

It is noticed that the Andean segmentation is well correlated with the current variations in the slab geometry. The slab alternates in along-strike slab dip angle between 0° and 35°, with at least two well defined, ongoing, flat slab (0° inclination) occurrences: (i) the Peruvian (5°-15°S), (ii) the Pampean (27°-33°S), and the two highly debated (iii) Bucaramanga and (iv) Ecuadorian (< 5°N) flat slabs (Gutscher et al., 2000a; Ramos et al., 2002; Espurt et al., 2008). Globally, there are an estimated 4 or 5 known and accepted cases of flat subductions occurring on Earth today, two of which are located along the South American convergent margin (Gutscher et al., 2000; Gutscher, 2002; Heuret et al., 2007; Skinner and Clayton, 2013). On the other hand, the Andean segmentation is a long-standing geological feature (100 Myr) that cannot be exclusively explained by the current medium-standing (of the order of 1 and 10 Myr) flat slab configurations (Tassara et al., 2006; Espurt et al., 2008). This suggests that the composition of the South American geological heritage must play an additional role in controlling the deformation of the Andes.

The central Chilean "Pampean" flat slab is located between 27°S and 33°S, and relates to the relatively young (30-35 Ma) and rapidly subducting Nazca plate beneath the thick continental South American lithosphere. Here, the flat slab underplates the overriding lithosphere at about 100-120 km depth and for 200-250 km inland, before resuming its descent into the mantle, at 68°W (Cahill and Isacks, 1992).

This flat slab is the best documented on Earth today because (i) the geology of the region exhibits a higher structural evolution and exposure level than other flat subductions, due to the region's dry climate, (ii) it is ongoing since a relatively long time (15-18 Ma, Kay and Abbruzzi, 1996; Ramos et al., 2002), (iii) it is characterized by high seismic activity that stimulated numerous explorations of the flat slab and its consequences, and (iv) the drastic tectonic changes that occur between the flat and normal subduction regions, over a very short distance, make central Chile and western Argentina the ideal place to study the causes and effects of flat subduction.

Currently, the driving forces behind this flat subduction are argued, since the buoyancy effects of the ridge's overthickened crust, measured offshore, are demonstrated insufficient to result in such a large and well developed flat slab segment (Martinod et al., 2005). Yet, there exists an outstanding correlation between the geometry and inferred subduction path of the Juan Fernandez volcanic seamount ridge and the shape and extent of the flat slab.

The paradox is that there are a number of ridges and fractures, and even much younger oceanic lithospheres which are currently subducting beneath South America and which are not related to observed variations in the slab geometry (e.g. the Iquique and Carnegie ridges beneath northern Chile and Ecuador, respectively). In central Chile, some authors have suggested that the subducted portion of the Juan Fernandez ridge may be thicker and broader at depth, producing the necessary buoyancy

forces to create the observed flat slab geometry (Yáñez et al., 2002; Cembrano et al., 2007; Gans et al., 2011). It was shown that the overriding plate plays an additional major role in the flattening of the slab, for instance, by including slab suction forces due to its fast westward motion and thick cratonic lithosphere to the east (van Hunen et al., 2001; 2004; Manea et al., 2012). Whereas the process of slab flattening and its impacts on the shallow continental crust are relatively well studied, little is understood about the deformations induced at deeper levels of the continental lithosphere or the causes that maintain flat subduction for such long eastward distances. In this work, I test the hypothesis that the Juan Fernandez ridge is overthickened at depth and whether evidence exists which suggests the ridge is the main inducer of the flat subduction.

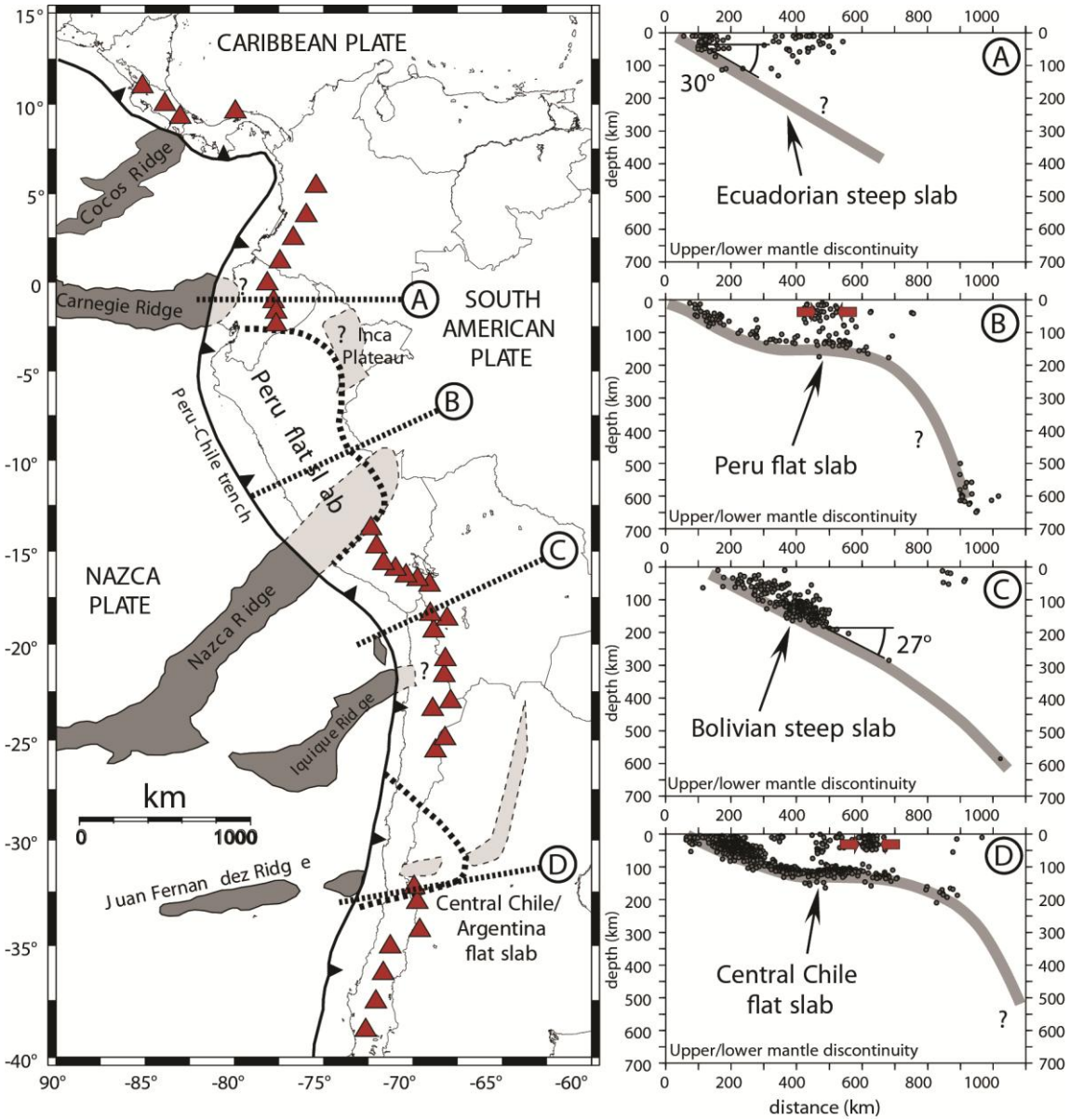


**Fig. 0.1 :** *Modern morpho-tectonic segmentation of the Andean mountain belt, showing the areas of flat subduction, their associated subducting oceanic features and gaps in the volcanic arc. Cross-section A-D show the shape of the slab at depth, based on the USGS earthquake catalog. Active volcanoes are indicated by red triangles. From Espurt et al. (2008)*

The most important and evident effect of the Pampean flat subduction, explaining the intense deformations observed at the surface of the overriding plate, is a general cooling of the subduction system due to underplating and absence of an asthenosphere wedge. In central Chile and Peru, the geotherm is as low as those found for old cratonic lithospheres (Lenardic et al., 2000; Muñoz et al., 2005). These low values can be associated to the absence of arc volcanism and to the more brittle and seismogenic behavior of the continental crust. Several independent studies proposed that the continental mantle is also cooler than in usual normal-dipping circumstances (Wagner et al., 2005; 2006; 2008), making it more rigid and impermeable, and acting as an indenter on the subducting plate (Tassara et al., 2005; Gerbault et al., 2009; Marot et al., 2013).

A reduced geotherm also tends to reduce greatly chemical reaction rates. Within normal-dipping slabs, the subducting crust is subject to a series of dehydration reactions due to progressive metamorphism, which densify the slab and increases the slab pull force that drives subduction. In such cases, the initial basalt/gabbro oceanic crust deforms into heavier eclogites, expelling fluids. The first transformation begins happening at ~ 50 km depth, and at 80-90 km depth, anhydrous eclogites are expected to occur (e.g. Kirby et al., 1996; Hacker et al., 2003). Therefore, to create and maintain this flat subduction episode, we expect this fluid-releasing eclogitization to have become totally, or partially, inhibited along the flat slab segment, causing retention of fluids inside the slab, reducing its bulk density, and maintaining it buoyant. Furthermore, if the oceanic crust is unusually thick, as a regional study by Gans et al. (2011) suggested using local receiver functions suggested, the effects of this retarded eclogitization on the buoyancy of the slab will be accentuated. These authors also indicated the possibility of a much shallower slab surface, and that the seismogenic zone of the slab is hence located inside the oceanic mantle. Therefore, in addition to testing whether an overthickened crust exists along the flat slab segment, this study also examines the possible location of the slab surface and the entrapment of fluids inside it.

The purpose of this thesis is to illuminate, in three-dimension, the physical properties of the continental lithosphere above the flat and normal slabs of central Chile and western Argentina, in order (i) to complement and argument the region's long list of individual local-scale studies, (ii) to better understand the links between the surface and deeper deformations, (iii) to correlate seismogenic zones with variations in petro-physical properties, (iv) map the locations of (if any) fluids, and (v) to explain the current buoyancy of the flat slab and resulting continental mantle rheology.

By imaging the normal (33.5°S) and flat (31.5°S) slabs, which are positioned at only ~ 100 km along-strike distance from each other, we are able to compare two different slab configurations, whereas other conditions remain identical (slab age, plate kinematics, main portions of continental crust composition…), making the slab geometry the only main variable to consider. Although not the most sensitive tool for detecting fluids, we chose to perform P- and S-wave traveltime residual seismic tomography, using a compilation of local, short-spanned, earthquake recordings. The asset of this method, for our purpose, is the gain in computation time due to the relatively short ray trajectories. And given our good seismic station coverage, we are able to detect with good precision the fine-scale (40 x 40 x 10 km) structures of the overriding lithosphere and parts of the upper slab where the seismicity is dense. However, imaging of the slab mantle and backarc region has its limitations, due to the heterogeneity in the distribution of slab events (e.g. normal slab earthquakes below ~ 125-150 km depth, in our study area, are rare). In addition, we had access to unpublished seismic attenuation models for this region, calculated by Perrine Deshayes during her PhD theses (2008), and based on a portion of the seismic dataset which we used in this study. Her results have helped us interpret and justify certain of our seismic velocity variations.

We further complemented our study with an analysis of the rock and mineral compositions of the continental lower crust and its mantle, and upper portion of the slab. For this, we used published databases of rock and mineral physical properties that enabled the calculation of their predicted

seismic behaviors at varying pressure and temperature (P-T) conditions in the Earth, for isotropic mafic and ultramafic compositions common to subduction zones. We used a synthetic thermo-mechanical model to estimate the P-T conditions for the flat and normal slab configurations, using *a priori* self-consistent information. Although these estimations have limitations and uncertainties of their own, in addition to those for our final velocity model, we managed to pick out the main trends that describe the regions analyzed, adding coherency to past studies and our results.

Previous tomography experiments for this region have used only one dataset at a time, and employed global velocity models as their initial background model for their inversion, causing extreme variability in their values. As an upgrade, our study incorporates four independent regional earthquake datasets (OVA99, CHARSME, CHARGE and CHASE), recorded with different instruments, sensitive to different frequency bands, enabling us to image the physical state of the region at a larger time-scale and with a larger accuracy and constraint on our results. We also complemented our data with the permanent Chilean station network, and used a regional 1-D velocity model specifically calibrated for this region. We relocated all four event catalogues within this model, in order to obtain one coherent dataset. For instance, the events recorded during the CHARGE campaign (Alvarado et al., 2004) were previously located in the slower global velocity model *IASEP-91*, resulting in depth differences of about -20 km prior to their relocation in our velocity model. Most seismic and gravity investigations performed in this region are based on these event locations (e.g. Wagner et al., 2005; Gilbert et al., 2006; Gans et al., 2011; Tassara and Echaurren, 2012). The final velocity model is very dependent of the initial model, and having a background model that already approximates reasonably well the average lateral and vertical velocity variations of the region provides us with an additional improvement towards recovering a final velocity model that we believe is closer to reality than previous studies. And finally, we cover a larger area than Wagner et al. (2005)'s tomography study, since we added more stations to the north (OVA99), filled in their gaps with more data to increase the resolution of the upper plate's crust from the coastline to the backarc region of Sierra Pie de Palo, and we included denser slab seismicity in order to interpret parts of it.

Chapter 1 introduces the reader to the region's dynamic, tectonic, geologic context and the correlations with the flat slab geometry. Included, is a brief overview of the historical geological events that have impacted the region prior to ridge subduction, such as the different accretionary events, periods of major deformation episodes, the onset of flat subduction and how it is recorded at the surface, as well as a summary of the major megathrust events and previous seismic studies for this region.

Chapter 2 describes the basics of the methods used of first wave arrival travel-time residual seismic tomography, and geodynamical and petrological numerical modeling. At the end of this chapter, I included one published article in Earth and Planetary Science Letters (Marot et al., 2012) describing the reactivation of a pre-existing (outer rise) fault cross-cutting nearly half of the normal slab lithosphere at intermediate-depth; and, one submitted article in Journal of Geophysical Research, currently expecting minor revisions, which details for the first time the central Chilean Double Seismic Zone, in terms of its seismicity, focal mechanisms, and stress tensor, as well as our interpretation of qualifying it as a rare "type III" category.

It is followed by Chapter 3, a synthesis of our results and of my interpretations, written in (long-version) article format for future submission. It is followed by a recapitulative summary of the methods and main outcomes of this thesis project. Our results provide support to previous interpretations while others not, and they explain unanswered questions while raising new ones. And finally, I name a few future research perspectives to further the understanding of the region's flat subduction.

# **Introduction** (in French)

La Cordillière des Andes est une chaîne de montagnes bordant en continu l'Ouest de l'Amérique du Sud. Cette chaîne orogénique résulte de 200 Ma d'un système en convergence lié à la subduction océanique de la plaque Farallon, puis de la plaque Nazca, sous la plaque continentale chevauchante de l'Amérique du Sud. Bien que, l'orogenèse Andine soit considérée comme un cas idéal de formation des grands orogènes dans un contexte de convergence, son altitude particulièrement élevée et sa géométrie ne peuvent pas s'expliquer uniquement par des processus de subduction (ex. Swift et Carr, 1974; Ramos, 1999; 2009; Ramos et Aleman, 2000; Cembrano et al., 2007;. Contardo et Cembrano, 2007; Gerbault et al., 2009).

Les variations topographiques et morphologiques de la plaque chevauchante de l'Amérique du Sud, ainsi que la distribution particulière des bassins sédimentaires, du volcanisme, et sa structure lithosphérique profonde, sont issues d'une histoire géologique complexe. Ses différentes variations sont systématiques et mal comprises. Cependant, cette segmentation régionale de la plaque chevauchante semble être corrélé aux zones d'anomalies bathymétriques de la plaque subduite (rides, failles, plateaux), le couplage des plaques en interaction, et l'âge du *slab* (plaque plongeante) (Figure 0.1) (ex. Cembrano et al., 2007; Ramos, 2009). Ces segments correspondent à des régions où l'inclinaison du *slab* varie entre 0° et 35°. On observe la présence de *slab* plat: (i) le *slab* plat péruvien (5°-15°S), (ii) le *slab* plat de Pampia (29°-33°S), ainsi que deux autres régions encore débattues (iii) proche de Bucaramanga en Colombie et (iv) dans la région équatorienne (< 5°N) (Gutscher et al., 2000a; Ramos et al., 2002; Espurt et al., 2008). Au niveau mondial, on estime qu'il existe 4 à 5 cas avérés et acceptés de subduction plate en cours, dont deux se situe en Amerique du Sud (Gutscher et al., 2000; Gutscher, 2002; Heuret et al., 2007). D'autre part, la segmentation des Andes résulte d'une longue histoire géologique (100 Ma) qui ne peut pas être expliquée uniquement par des configurations particulières de *slab* à moyen terme (de l'ordre de 1 et 10 Ma) (Tassara et al., 2006; Espurt et al., 2008). Ceci suggère que la nature lithosphérique de l'Amérique du Sud doit jouer un rôle important dans le contrôle de la déformation de la plaque chevauchante.

Notre région d'étude se situe géographiquement dans le Chili central et l'ouest de l'Argentine. Cette zone se caractérise par l'apparition en profondeur d'un *slab* plat de la plaque Nazca entre 29°S et 33°S. Ce *slab* plat est corrélé à une subduction rapide de la plaque Nazca « jeune » (30-35 Ma) et de son massif sous-marin (ride) de Juan Fernandez, sous la lithosphère continentale épaisse sud-américaine. Le *slab* sous-plaque cette lithosphère à environ 100-120 km de profondeur sur une distance de plus de 200-250 km vers l'intérieur des terres, avant de reprendre sa descente dans le manteau, à 68°W (Cahill et Isacks, 1992).

Ce *slab* plat est actuellement le mieux documenté sur Terre, car la région d'étude possède de nombreuses particularités intéressantes à aborder: (i) les terrains géologiques de la plaque chevauchante affleurent sous un climat aride, propice aux études géologiques et donc aux interprétations géologiques de surface; (ii) ce *slab* présente un caractère plat depuis un temps relativement long (15-18 Ma) (Kay et Abbruzzi, 1996; Ramos et al., 2002); (iii) ce *slab* est marqué par une forte activité sismique qui suscite de nombreuses études sismologiques; et (iv) des changements tectoniques radicaux surviennent sur une très courte distance entre le *slab* plat et normal (inclinaison plus forte). Ces caractéristiques font que la région du Chili central et d'ouest de l'Argentine sont des zones idéales pour étudier les causes et les effets d'une subduction plate.

Actuellement, les forces motrices contrôlant cette subduction plate sont encore débattues et très méconnues. Un certain nombre de rides, de fractures, et de jeunes lithosphères océaniques actuellement en subduction le long de la marge active de l'Amérique du Sud, n'induisent pas de fortes

variations géométriques du *slab* (ex. les rides d'Iquique et de Carnegie au nord du Chili et sous l'Écuateur, respectivement), énonçant un paradoxe intéressant à approfondir.

Dans la région centrale du Chili, Martinod et al. (2005) montrent par des modèles analogiques que les effets « de flottabilité » de la croûte sur-épaissie le long de la ride en mer sont insuffisants pour aboutir à un tel segment de *slab* plat. Pourtant, la bonne corrélation entre le prolongement intérieur de la ride en subduction et l'étendue du *slab* plat suggèrent une relation étroite.

De plus, certains auteurs suggèrent que la croute de la ride de Juan Fernandez est peut être plus épaisse et plus large que prévues en profondeur, produisant alors les forces de flottabilité nécessaires pour créer la géométrie du *slab* observé à 100-120 km de profondeur (Yáñez et al., 2002; Cembrano et al., 2007; Gans et al., 2011).

Van Hünen et al. (2001; 2004) et Manea et al. (2012) montrent que la plaque chevauchante joue également un rôle majeur dans la formation d'un *slab* de faible inclinaison, grâce à des forces d'aspiration du *slab* dues au déplacement rapide vers l'ouest de la lithosphère continentale, caractérisée par un craton.

Bien que le(s) processus(s) de *slab* plat et leurs impacts sur la croûte continentale à faible profondeur soient relativement bien étudiés, les déformations induites en profondeur dans la lithosphère continentale, ou les causes qui maintiennent la subduction plate, sont encore très peu connues.

L'effet le plus important et marquant de la subduction plate du Chili, qui pourrait bien expliquer les déformations observées au niveau de la plaque chevauchante, est un refroidissement général du système de subduction lié au sous-plaquage et à l'absence d'un coin asthénosphérique. Dans le Chili Central et au Pérou, par exemple, le géotherme est aussi faible que celui constaté dans des cratons anciens (Lenardic et al., 2000; Muñoz et al., 2005). Ces anomalies de faibles valeurs peuvent être associées à l'absence de volcanisme d'arc et au comportement plus fragile et sismogénique de la croûte continentale. Plusieurs études indépendantes proposent alors que le manteau continental est anormalement plus froid (Wagner et al., 2005; 2006; 2008), le rendant plus rigide et imperméable, jouant le rôle d'un indenteur sur la plaque en subduction (Gerbault et al., 2009; Marot et al., 2013).

Une diminution du géotherme tend également à ralentir considérablement les taux de réactions chimiques dans la plaque en subduction. Dans le cas d'un *slab* normal, la croûte subduite est soumise à une série de réactions de déshydratation liées au métamorphisme progressif des roches de la plaque océanique. Le métamorphisme en faciès éclogitique des basaltes et gabbros précédemment métamorphisés s'initie dans des conditions de pression et température (P-T) constatées à des profondeurs proches de 50 km. Puis, entre 80 et 90 km de profondeur, l'éclogite anhydre apparait (ex. Kirby et al., 1996;. Hacker et al., 2003). Dans le cas d'un *slab* plat, la réaction d'eclogitization, libérant les fluides contenus dans la plaque subduite, doit être totalement ou partiellement inhibée le long de ce segment, induisant la rétention des fluides à l'intérieur du *slab*, et provoquant ainsi son maintien vers la surface et sa faible inclinaison. En outre, une étude régionale, utilisant des fonctions récepteur locales, effectuée par Gans et al. (2011), suggère que la limite supérieure du *slab* plat se situe plusieurs dizaines de kilomètres au-dessus de la zone sismogénique de ce *slab*, et que la largeur et l'épaisseur de la croûte de Juan Fernandez sont supérieures le long du segment *slab* plat, induisant une force de flottabilité plus accentuée. Dans cette étude, nous testons l'hypothèse que la croûte oceanique soit sur-épaissit et pas totalement éclogitisée en profondeur.

L'objectif de cette thèse est d'identifier, en trois dimensions, les propriétés physiques de la lithosphère continentale au-dessus des *slabs* plats et normaux du Chili central et de l'ouest de l'Argentine, afin de : (i) argumenter les études précédentes de la région; (ii) mieux comprendre les liens entre les déformations profondes et celles de surface; (iii) mettre en corrélation les zones sismogènes avec les variations des propriétés pétrophysiques; (iv) cartographier les emplacements des

fluides; et (v) expliquer la dynamique actuelle du *slab* plat et ses conséquences sur la rhéologie du manteau continental.

En imageant les *slabs* normal et plat, espacés de seulement une centaine de kilomètres l'un de l'autre, nous pouvons comparer deux configurations différentes de *slab*s, tandis que les autres conditions restent quasi-identiques (âge du *slab*, cinématique des plaques, compositions principales de la croûte continentale...). Ainsi, seule la configuration géométrique de la plaque subduite est alors considérée. Cette thèse aborde des thématiques de modélisation variées et complémentaires.

Nous avons choisi d'effectuer, dans un premier temps, une imagerie sismique des ondes P et S, en utilisant une compilation d'enregistrements temporels de séismes locaux. L'atout de cette méthode dans notre étude, est un gain considérable en temps de calcul dû aux trajectoires relativement courtes des rayons. Compte tenu de la bonne couverture des stations sismiques, nous sommes en mesure de détecter avec une bonne précision, et à une échelle fine (40 x 40 x 10 km), les structures de la lithosphère chevauchante et des parties du *slab* où la sismicité est dense. Cependant, l'imagerie du *slab* mantellique et de la région arrière-arc de la plaque chevauchante, a ses limites, liée aux hétérogénéités dans la répartition des événements sismiques du *slab* (par exemple, les tremblements de terre du *slab* normal en dessous de ~ 125-150 km de profondeur, dans notre zone d'étude, sont rares). De plus, nous avons eu accès à des modèles d'atténuations sismiques inédits pour cette région, calculés par Perrine Deshayes au cours de sa thèse (2008), se basant sur une partie des données sismiques que nous avons utilisé dans cette étude. Ses résultats nous ont permis d'interpréter et de justifier certaines variations de vitesse des ondes sismiques, que nous avons observées.

Nous complétons notre étude, dans un second temps, par un modèle pétrologique permettant d'obtenir la composition des roches et minéraux de la croûte inférieure et du manteau lithosphérique de la plaque chevauchante, ainsi que la partie supérieure de la plaque subduite. Pour ce faire, nous avons utilisé des bases de données préexistantes dans la littérature donnant les propriétés physiques de roches et minéraux mafiques (isotrope) et ultramafiques, communes dans les zones de subduction. Cela a permis le calcul de leurs comportements sismiques prévus à différentes conditions P-T dans les profondeurs de la Terre interne. Nous avons utilisé un modèle thermomécanique synthétique pour estimer les conditions P-T des *slabs* plat et normal, en implémentant des conditions initiales préexistantes dans la littérature. Malgré certaines limites et incertitudes dans notre modèle pétrologique, nous avons réussi à repérer les principales tendances qui décrivent les régions analysées, cohérentes avec les résultats des études passées.

Les études précédentes de tomographie sismique effectuées dans la région ont utilisé un seul jeu de données, et des modèles de vitesse mondiaux comme modèles de référence pour leur inversion, provoquant ainsi d'extrêmes variabilités dans leurs valeurs. Notre étude comporte quatre ensembles indépendants de séismes régionaux, enregistrés avec différents instruments sensibles à différentes bandes de fréquence, ce qui permet d'imager plus finement l'état physique de la région à une échelle temporelle plus grande. Nous avons également complété nos données avec des enregistrements du réseau sismique chilien, et utilisé un modèle de vitesse 1-D régional spécifiquement calibré pour cette région. Nous avons relocalisé les quatre catalogues d'événements au sein de ce modèle, afin d'obtenir un jeu de données cohérent. Par exemple, les événements enregistrés au cours de la campagne de CHARGE (Alvarado et al., 2004) étaient localisés dans le modèle de vitesse global plus lent, *IASEP-91*, ce qui entraîne des différences de profondeur d'environ -20 km avant leur relocalisation dans notre modèle de vitesse. La plupart des études sismiques et gravimétriques effectuées dans cette région sont basées sur ces localisations (ex. Wagner et al., 2005; Gilbert et al., 2006; Gans et al., 2011; Tassara et Echaurren, 2012). Le modèle de vitesse finale étant fortement dépendant du modèle initial, il est important de considérer un modèle de référence le plus proche de la réalité, en approximant au mieux les variations de vitesse latérale et verticale moyenne. En utilisant un modèle initial calculé localement, nous considérons que notre modèle final offre une amélioration supplémentaire et une

meilleure cohérence des résultats par rapport aux modèles préexistants dans la région. De plus, notre modèle apporte des informations supplémentaires par rapport à celui de Wagner et al. (2005), car : - nous couvrons une zone géographique plus grande, grâce à l'ajout des données enregistrées par les stations situées dans la région nord (OVA99), - nous avons couvert les lacunes par de nouvelles données, dans le but d'augmenter la résolution de la croûte de la plaque chevauchante de la côte à l'arrière-arc de Sierra Pie de Palo, - et nous avons intégré les données sismiques du *slab* afin d'interpréter les parties de celui-ci.

Le manuscrit s'organise autour de trois chapitres, suivi d'une conclusion générale. Le chapitre 1 présente le contexte géodynamique et géologique de la région, ainsi qu'une présentation générale de la plaque en subduction et ses particularités. Ce chapitre propose ainsi un bref aperçu des événements historiques géologiques qui ont affecté la région avant la subduction de la ride, tels que les différents événements d'accrétion, les grandes phases de déformations, et l'initiation de la subduction plate et son enregistrement en surface par des déformations. Ce chapitre apporte également un résumé bibliographique des principaux événements sismiques de type *mega-thrusts* qui se sont produit dans la région d'étude.

Le chapitre 2 décrit la méthodologie utilisée pour la modélisation tomographique par résidus des premières arrivées d'ondes P et S, et pour la modélisation numérique thermomécanique et pétrographique. A la fin de ce chapitre, j'ai inclus un article publié dans *Earth and Planetary Science Letters* (Marot et al., 2012) décrivant la réactivation d'une faille préexistante affectant près de la moitié de la lithosphère du *slab* normal à des profondeurs intermédiaires, ainsi qu'un deuxième article publié dans le *Journal of Geophysical Research* (Marot et al., 2013), qui décrit en détail pour la première fois la Double Zone Sismique du Chili central, en termes de sismicité, mécanismes au foyers et tenseur des contraintes, ainsi que notre qualification de catégorie rare "de type III".

Le chapitre 3 est une synthèse de nos résultats et de mes interprétations, écrite sous la forme d'un article pour une soumission prochaine. Cette synthèse est suivie par un résumé récapitulatif des méthodes employées et des principaux résultats obtenus lors de ma thèse.

La conclusion générale apporte des réponses aux questions soulevées précédemment, mais en annonce de nouvelles grâce à nos résultats originaux. Et enfin, je terminerai en perspectives par des nouveaux axes de recherche futurs pour mieux comprendre ces subductions anormalement plates.

Chapter One

# 1 An Introduction to the Geology & Tectonics of the South American & Central Chilean Subduction Margin

## 1.1 Origins of the South American Continent

Today, the entire N-S length (~ 9000 km, from Columbia to the Chilean triple junction with Antarctica and South America at 46°S) of the Andes is described as segmented, with each segment having different geological signatures, reflecting the complex deformation style of the Andean uplift. And, since this Andean segmentation was explained partly by its inherited structure and composition, I now introduce the general constitution of South America and its historical deformations.

The Gondwana supercontinent was formed ~ 570-510 Ma (Cattermole, 2000) by the agglomeration of different continental blocks of Achaean-Proterozoic age, including pieces of Antarctica, Australia, India, Africa, the Guianan-Brazilian shield, and South America, and it was once located near the South Pole (Fig. 1.1). The South American block was then made up of the Amazonia, Rio de la Plata and Sao Francisco cratons (Fig. 1.2A and B). The distinctive feature of the South American crust is its variations in crustal composition that arose from the accretion of several consecutive exotic terranes over the past 600 Ma, which have strongly influenced the structure and tectonic evolution of its crust, including that of central Chile (Ramos et al., 1986; Ramos, 1988b; Alvarado et al., 2005; Alvarado et al., 2011).

The early tectonic Andean development started in the Paleozoic, when terrane amalgamation was the main process until the Mesozoic. Nevertheless, there is a general consensus that the current Andean formation occurred mainly during the Mesozoic (140 Ma) until nowadays, as a result of eastward subduction and the spreading of the Atlantic Ocean (Ramos et al., 1988a; Ramos, 1999). Arc volcanism, associated to subduction processes that affected the western Gondwana margin, began ~ 200 Ma, and backarc basin formation only began in Late Jurassic (~ 150 Ma). Backarc deformation and closure started during the Late Jurassic, impacting first both extremes of the subduction front and propagated towards the center, with the youngest deformation is recorded at the center (Ramos et al. 1986). One exception is at 25°S where no deformation is observed (Ramos and Aleman, 2000). The dominant features of the modern Andean mountain belt are the Altiplano-Puna plateau, the Santa Barbara, the Sierra Pampeanas and Sub-Andean thrust systems (Fig 1.2C), describing past and present subduction processes with changing structural and geological characters.

## 1.2 The Tectonic and Geological Terranes of Central Chile

The Rio de la Plata craton, and other foundation blocks that makeup the crust of Brazil, Uruguay and eastern Argentina, were amalgamated against the Gondwana super-continent by 560-530 Ma, when the western margin was already convergent by then (Ramos, 1998b). In central Chile, this was followed by three consecutive major collisions against the Rio de la Plata craton: i) the Pampia terrane at ~ 530-515 Ma, ii) the Cuyania terrane ~ 460 Ma, and iii) the Chilenia at ~ 420-315 Ma (Kay et al., 1996b; Ramos, 2004). Major suture zones separate the different amalgamated terranes and are represented by series of ophiolotic belts of varying ages (Ramos et al., 2002; Ramos, 2009). The ancient magmatic arc that was produced above a west-dipping slab before the collision of the Pampia terrane is observed in the Sierras de Cordoba, in central Argentina (Ramos et al., 2002).

### *1.2.1 Pampia*

The Pampia terrane is located in the backarc region of the central Chilean Andes and includes the eastern Sierra Pampeanas. It is located east of the Famatina plutonic arc which developed on the continental crust at ~ 490-460 Ma while subduction continued along the (1700 km long) western margin of Pampia after its accretion (Dahlquist et al., 2008). It is interpreted as a micro-continent of Precambrian age (1.0 - 1.9 Ga, Schwartz and Gromet, 2004), with felsic quartz-rich composition.

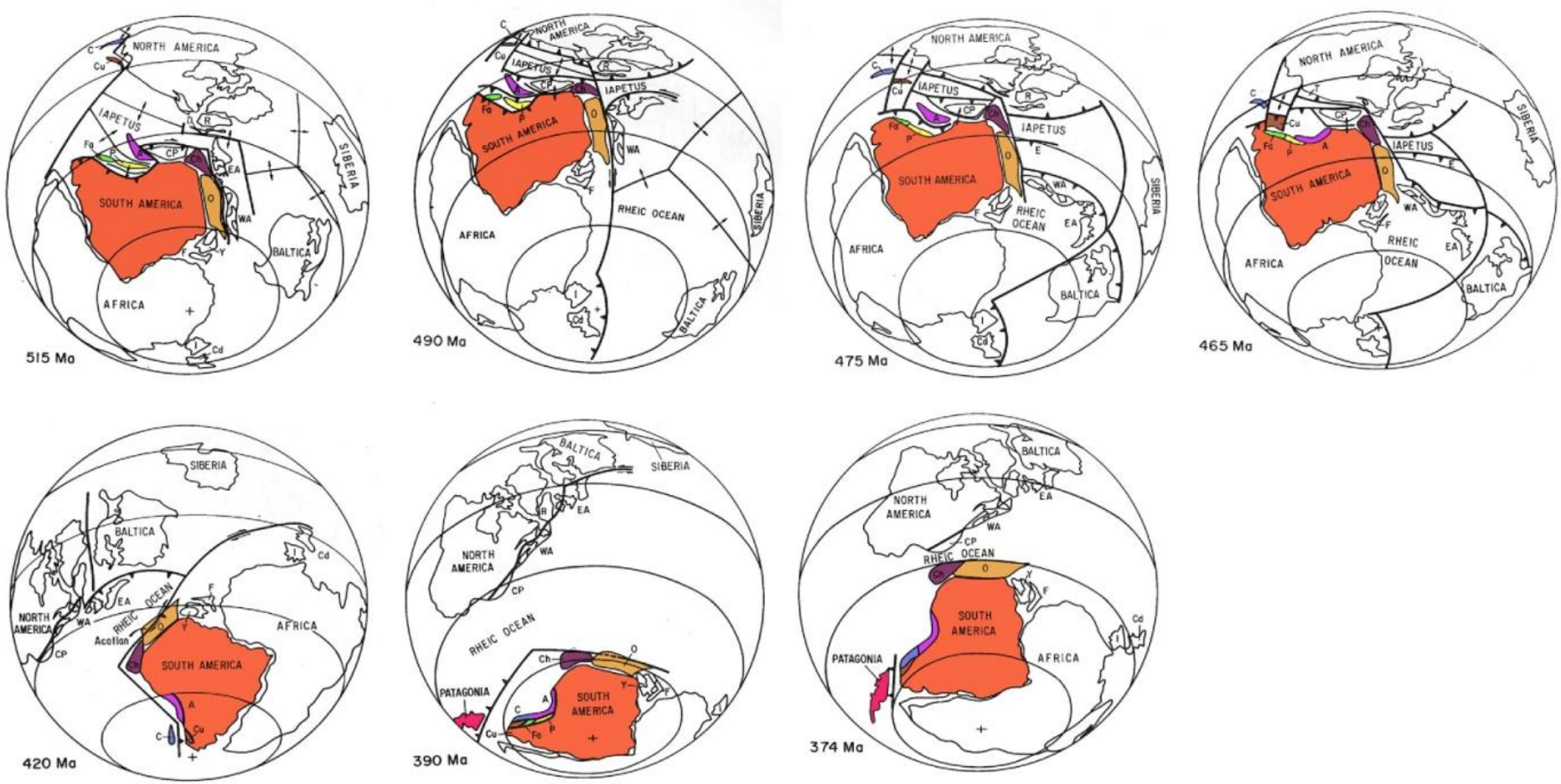


**Fig. 1.1**: *Global tectonic and geological reconstruction of the South American continent since Mid- to Late Cambrian. Geological terranes: A: Arequipa-Antofalla; Fa: JPGatina; P; Puna; C: Chilenia; Cu: Cuyania-Precordillera; O: Oxaquia; Ch: Chortis. From Keppie and Ramos (1999).*

Pampia's exact origin is debated, and was proposed to represent a detached fragment of the Rio de la Plata craton.

### *1.2.2 Cuyania*

Recent studies have interpreted the Cuyania terrane as a composite terrane comprised of two sub-terranes, Pie de Palo and Precordillera, which were assembled prior to their collision with the western Gondwana. The Cuyania rocks document a calcareous platform (the Precordillera) deposited along a continental shelf and slope, with a continent to the west and an ocean basin to the east (Pie de Palo) (Ramos et al., 1986). The deformed Precordillera limestones have been sampled in the sub-surface until ~ 37°S, evidencing a much broader extent than the outcrops indicate (over 1000 km in N-S extent) (Ramos et al., 1986; Ramos, 2004). The northern extent of the Precordillera is difficultly traced north of 29°S (Ramos et al., 1986).

Basement rocks exposed in the uplifted region of Pie de Palo document an ophiolite sequence with chemical signature of an oceanic arc or backarc, as proposed for the paleo-environment of this terrane (Abbruzzi et al., 1993; Kay et al., 1996). Isotope dating (U-Pb) of basement rocks in xenoliths found in Cerro Ullum and Pie de Palo report Grenville ages (1.1-1.2 Ga) (Ramos et al., 1986). Thermo-barometry of Pie de Palo basement rocks describe a 45 km thick Cuyania crust as it was overridden by the Gondwana proto-margin (Ramos, 2004). The rocks bear a unique non-radiogenic Pb signature that mimics that of the Ouachita region basement rocks, in modern Texas (at the latitude of El Llano), and anciently located in southern super-continent Laurentia (Ramos et al., 1986). For these reasons, it is proposed that Cuyania originated, and was detached, from the Ouachita embayment as the Iapetus Ocean closed between Cuyania and Pampia (Fig. 1.1) (Ramos et al., 1986).

### *1.2.3 Chilenia*

The suspected ocean basin on the west margin of the Cuyania terrane is evidence for the allochthonous origin of the next accretion event: the Chilenia terrane (Ramos et al., 1986). The ample Upper Paleozoic to Neogene magmatism, and the sedimentation and deformation events of the Andes orogeny in this region, have destroyed most of the evidence for the existence of Chilenia, and thus little is known about its nature. The question is, whether Chilenia was a block that drifted away from Cuyania and was later re-attached, or whether it is a far-travelled exotic terrane derived from Laurentia, like Cuyania (Ramos et al., 1986).

The oldest rocks in the Frontal Cordillera indicate that Chilenia is possibly a micro-continent, cross-sected by ultramafic batholiths. Although these rocks of only 0.5-0.4 Ga indicate a probable younger metamorphic event related to its collision (Ramos et al., 1986), there is however indirect evidence for Precambrian Chilenia basement rocks. This evidence is based on reported chemical signatures of old continental crust (interpreted as recycled Chilenia basement rocks) in young intrusive rocks found in the Frontal Cordillera and in sediments and meta-sediments of the Coastal Cordillera forearc rocks at 32°S (Ramos et al., 1986). As for Cuyania, this signature ends south of 37°S (Ramos et al., 1986).

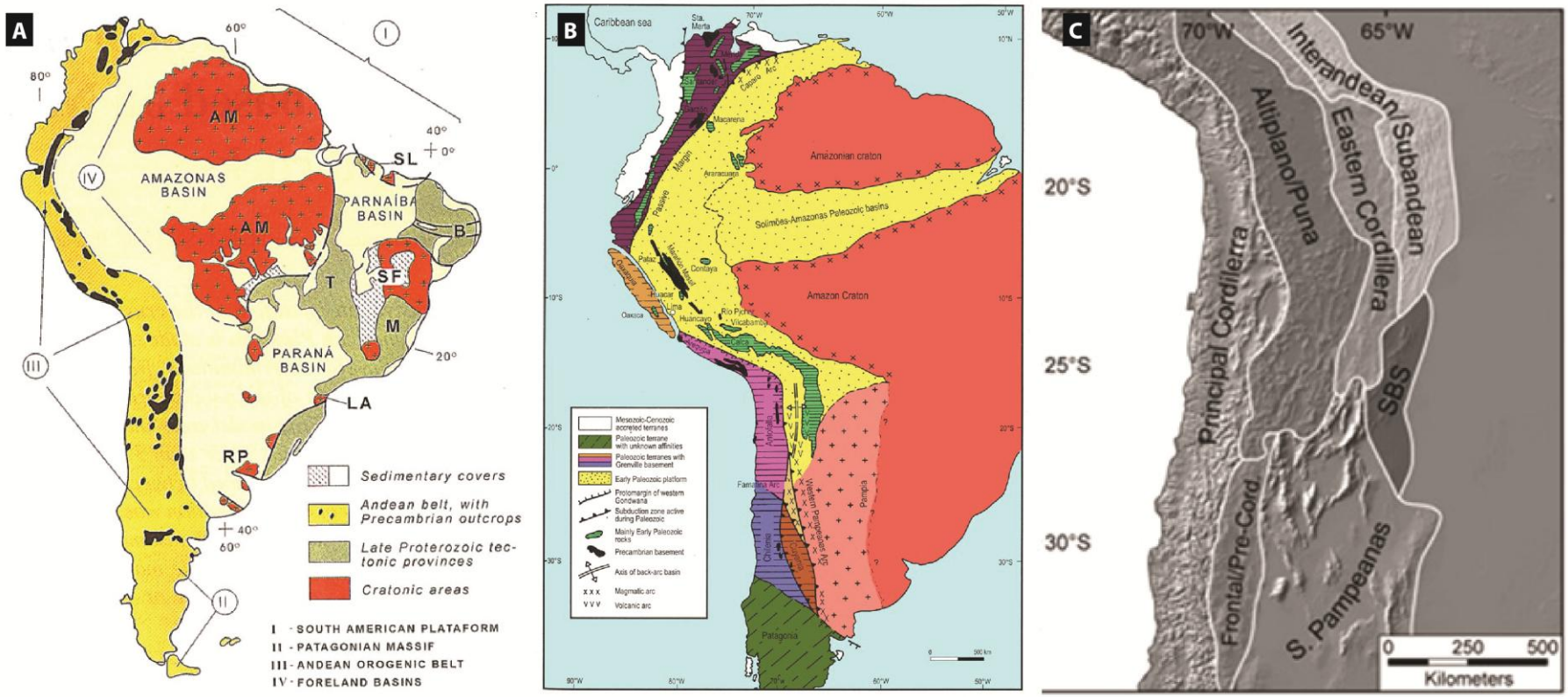


**Fig. 1.2**: *(A) Cratonic provinces of South America: AM: Amazonian; SF: Sao Francisco; RP: Rio de la Plata; SL: Sao Luis fragment; LA: Luis Alves fragment. From Cordani and Sato (1999). (B) Terrane map of South America according to Ramos and Aleman (2000). This map does not include the Coastal Cordillera terranes (Mejillonia, Pichidangui, Chañaral, Chiloe terranes), (C) Major geological provinces of the Andes and topography from Shuttle Radar Topography Mission (SRTM). Image from http://www.geo.uni-potsdam.de/Leibnizzentrum/research/andes_southern_central/AndesSouthernCentral.html and modified from Jordan et al. (1987)*

### *1.2.4 The Coastal Block*

Although paleomagnetic studies reveal important lateral displacements during the Late Triassic-Early Jurassic, the coastal block (forearc crust) is not interpreted as an exotic terrane (Ramos et al. 1986). Between 28°S and 36°S, the coastal block describes an old accretionary wedge (or forearc basin) probably formed during the Gondwana Orogeny (Ramos et al. 1986), and over-printed by large intrusions.

## 1.3 The Suture Zones of Central Chile

The suture zones that separate the different accreted terranes are often described by narrow ophiolotic belts representing fragments of obducted oceanic crust. The characteristics of these terrane boundaries have been obscured by younger overlapping sediments and the Andean deformation (Ramos et al., 1986).

U-Pb dating and thermo-barometry place the boundary between the Laurentia-derived Cuyania rocks and the Gondwana-derived Pampia rocks along the Valley Fertíl lineament (Fig. 1.3) (Ramos et al. 1986). Where this limit can be observed, it is abrupt (< 10 km wide) and bears mafic to ultramafic oceanic rock characteristics (Ramos et al., 1986). Today, the Valley Fertíl boundary is a major reverse fault.

A belt of Grenville ophiolotic rocks, pre-dating the Cuyania-Gondwana collision event, lie between the Precordillera and Pie de Palo rocks (thin line within Cuyania in Fig. 1.3). In addition to seismic reflection data, which detect an east-dipping discontinuity at ~ 25 km at this locality (Cominguez and Ramos, 1991), this ophiolotic belt is interpreted as an old inherited suture zone between the Precordillera and western Sierra Pampeanas basement rocks, supporting the theory that Cuyania is a composite terrane (Ramos et al. 1986).

And, the boundary between Chilenia and Cuyania is located beneath the Iglesias, Calingasta, Barreal and Uspalatta valleys, and corresponds to ocean crust fragments obducted during the Ordovician (Ramos, 2004). At depth, Ramos et al. (1986) infer its trace to be located beneath the Frontal Cordillera. The seismic and petrological results obtained through this PhD work suggest a possible scenario for the distribution of such sutures and terranes at depth.

## 1.4 The Central Chilean Deformations

Subsequent to the terrane accretion history of Central Chile, are many episodes of variable stress and deformation regimes that have resulted in the reactivation of old suture zones as major faults, and created rock anisotropy fracturing. These later controlled the tectonic style of deformation in the region (Ramos, 2009). While the exact timing of collisions and location of the boundaries between the terranes are still argued, old suture zones have had an important influence on the Cenozoic uplift of the Sierra Pampeanas (Ramos et al., 2002).

Three dominant and successive episodes of extension took place in Late Paleozoic (~ 250 Ma), Late Triassic-Early Jurassic (~ 200 Ma) and Early Cretaceous (~ 150 Ma) (Ramos et al., 2002). The first and second episodes are related to oblique subduction that resulted in pull-apart rifting (Ramos et al., 2002), and the third episode to the spreading of the South Atlantic Ocean. These have resulted in intraplate felsic magmatism/volcanism, normal and strike-slip faulting along suture zones, and the formation of half-grabens and sedimentary basins (e.g. the Cuyo basin at ~ 240 Ma, one of the oldest synrift systems in the region) (Ramos et al., 1986).

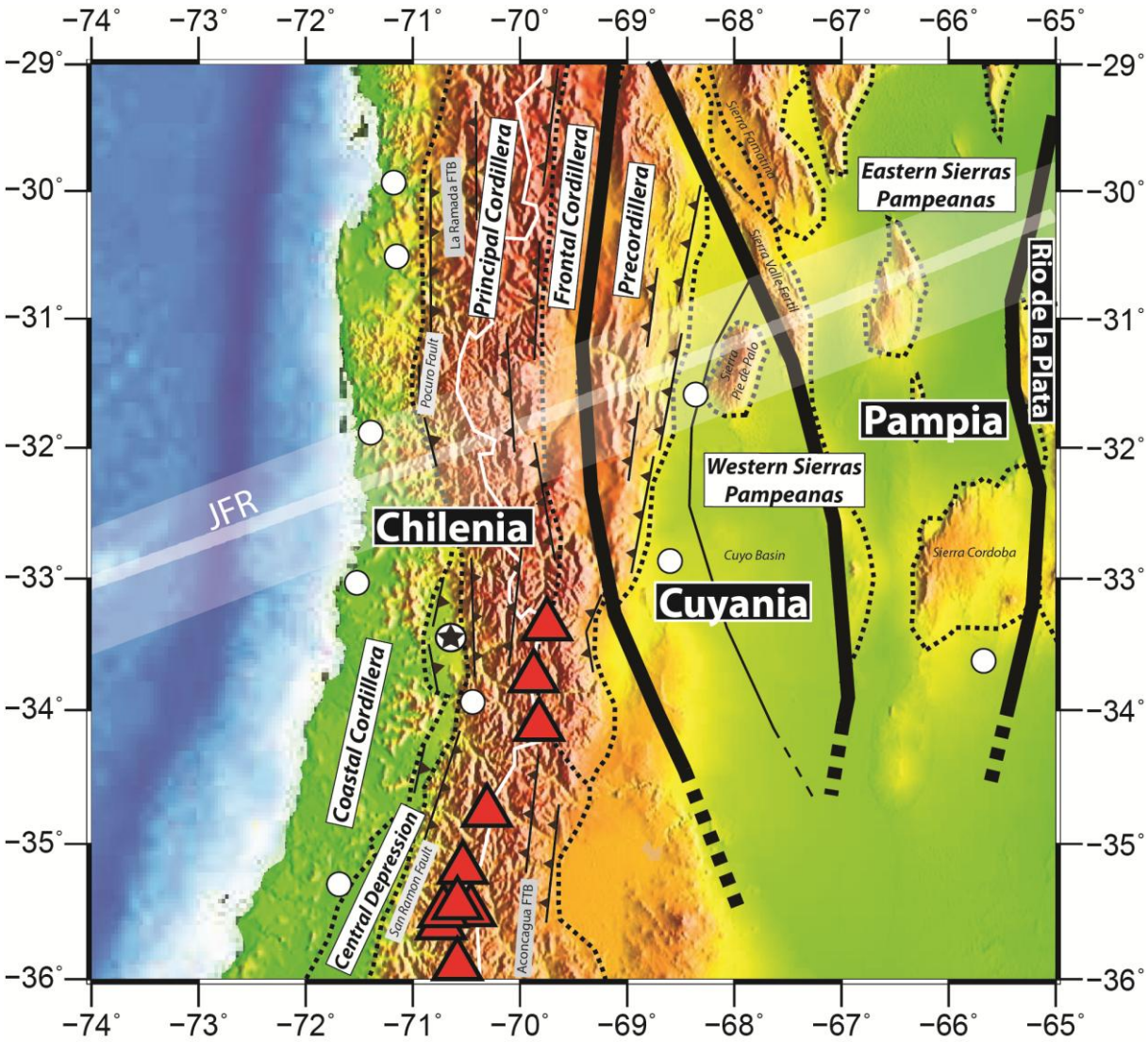


**Fig. 1.3**: *Geological and tectonic settings of the central Chilean subduction zone, showing the different accreted terranes (black boxes) and their outcrops (dotted lines) separated by zones of suture (thick and thin black lines). Tectonic provinces (white boxes) and the locations of the main thrust faults (line-triangle) are shown. Active volcanoes are shown by red triangles. The main cities are located with white circles, including the Chilean capital Santiago with a star. And the inferred inland prolongation of the Juan Fernandez ridge is shown by the while line, with an expected width of ~ 100 km, based on Kopp et al. (2004) and slab seismicity.*

Whereas the earliest periods of compression are related to terrane accretion (Ramos, 2010), the combination of the South Atlantic Ocean rifting and the subduction along the western margin of South America since ~ 130 Ma, have created compression, consequent uplifting, reactivation of old fault structures, and the beginning of the first magmatic arc. The breakup of the oceanic Farallon Plate at ~ 25 Ma, into the smaller Cocos and Nazca Plates, resulted in changes in convergence orientation between the South America and Nazca Plates, from oblique to the present-day normal convergence. This generated a change from extensional to compression regime between 20-16 Ma (Kay and Mpodozis, 2002). The Juan Fernandez ridge began subducting in the flat slab region at ~ 15 Ma (Kay and Mpodozis, 2002), contributing further to the compressional and crustal shortening of this period.

Today, it is noticed that central Chile is divided into five morpho-tectono-structural-geological provinces that have arisen since 25 Ma, and was shortly sequenced by additional compression due to

the progressive Pampean slab flattening and the consequent eastward migrations of the volcanic and orogenic belts (Ramos et al., 2002). These provinces are the Coastal, Principal and Frontal Cordilleras, the Precordillera and the Sierra Pampeanas (Fig. 1.3 and 1.8).

The Andes are a double-vergent orogen bounded by thrust faults that accommodate the uplift deformation of the Principal and Frontal Cordilleras (Allmendiger et al., 1997; Farias et al., 2010). Within the Principal Cordillera is the thin-skinned La Ramada (< 33°S) and Aconcagua (> 33°S) deformation thrust belts (Fig. 1.3), which are classical examples of Andean back thrusts, located along the western (La Ramada) and middle (Aconcagua) Andean front (Cristallini and Ramos, 2000). At the western boundary of the Andean front belt, at the limit with the Coastal Cordillera, is the east-dipping San Ramon and Pocuro thrust faults (forming one more-or-less continuous fault segment) (Farias et al., 2010). The main Andes (Principal and Frontal Cordilleras) above the flat subduction segment (~ 27°-32.5°S), the orogeny is narrower (100-150 km wide) (Gerbault et al., 2009) and composed of thin-skinned tectonics in association with the highest peaks in the region (max. 6700 m, Aconcagua), whereas the northern and southern regions are composed of thick-skinned tectonics. And the Precordillera and Sierra Pampeanas form the uplifted region of the backarc, above the flat slab segment (more details in Section 1.6).

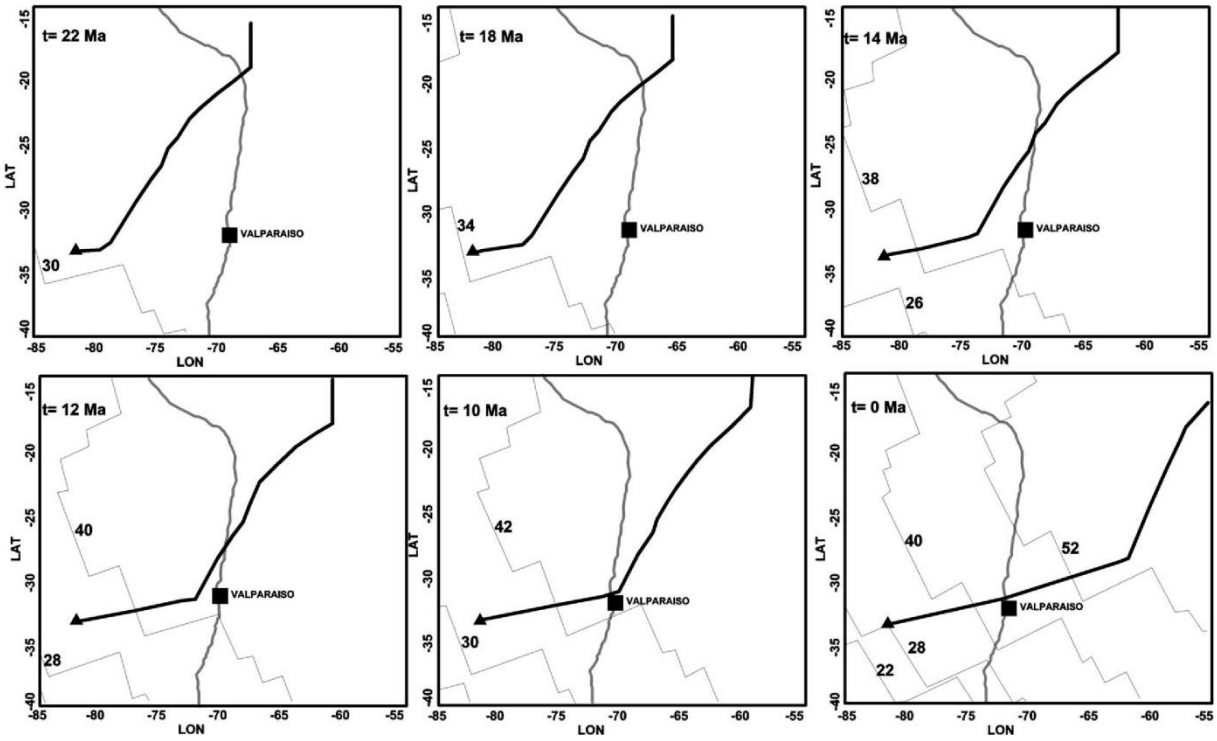


**Fig. 1.4**: *Predicted path and southward migration of the Juan Fernandez ridge since the Miocene. The continental margin (grey line) moves westward through time, while the hotspot location (black triangle) remains stationary. Seafloor ages are from magnetic anomaly lineations. From Yañez et al. (2002)*

## 1.5 The Beginning of the Pampean Flat Subduction

Between ~ 27 to 21 Ma, the Nazca Plate subducted similarly to the modern subduction configuration south of 35°S, with a dip angle of 35° (Kay and Abbruzzi, 1996; Kay and Mpodozis, 2002). Volcanism then appears equivalent to the Southern Volcanic Zone today (> 35°S), and continuous throughout the Principal Cordillera, with backarc volcanism occurring in the Frontal Cordillera (Kay and Gordillo, 1994). Lava chemistries indicate that continental thickness was then ~ 40-45 km.

Marine and land magnetic anomalies indicate that the ridge was intercepting the Chilean trench at 20°S around 22 Ma, and migrated rapidly southward to its present location (33°S) where it has been relatively stationary since 11 Ma (Fig. 1.4) (Yáñez et al., 2001; Ramos et al., 2002).

Slab flattening in the region (27°-32.5°S) began around ~ 15-18 Ma (Fig. 1.5B). It is supposed that the slab geometry was then alike that observed today at 33°S, i.e. ~ 20-30° dip angle (Fig. 1.5A), based on lava chemistry (Kay and Mpodozis, 2002). It resulted in compression and faulting in the Principal Cordillera, as well as sedimentary basin formation and eastward migration of the volcanic arc (Kay and Abbruzzi, 1996; Kay and Mpodozis, 2002; Ramos et al., 2002). As slab shallowing progressed, arc magmatism in the Principal Cordillera significantly diminished ~ 10 Ma, and migrated east into the Precordillera, then later in the Pampia regions, forming a long chain of intrusive rocks (Kay et al., 2005).

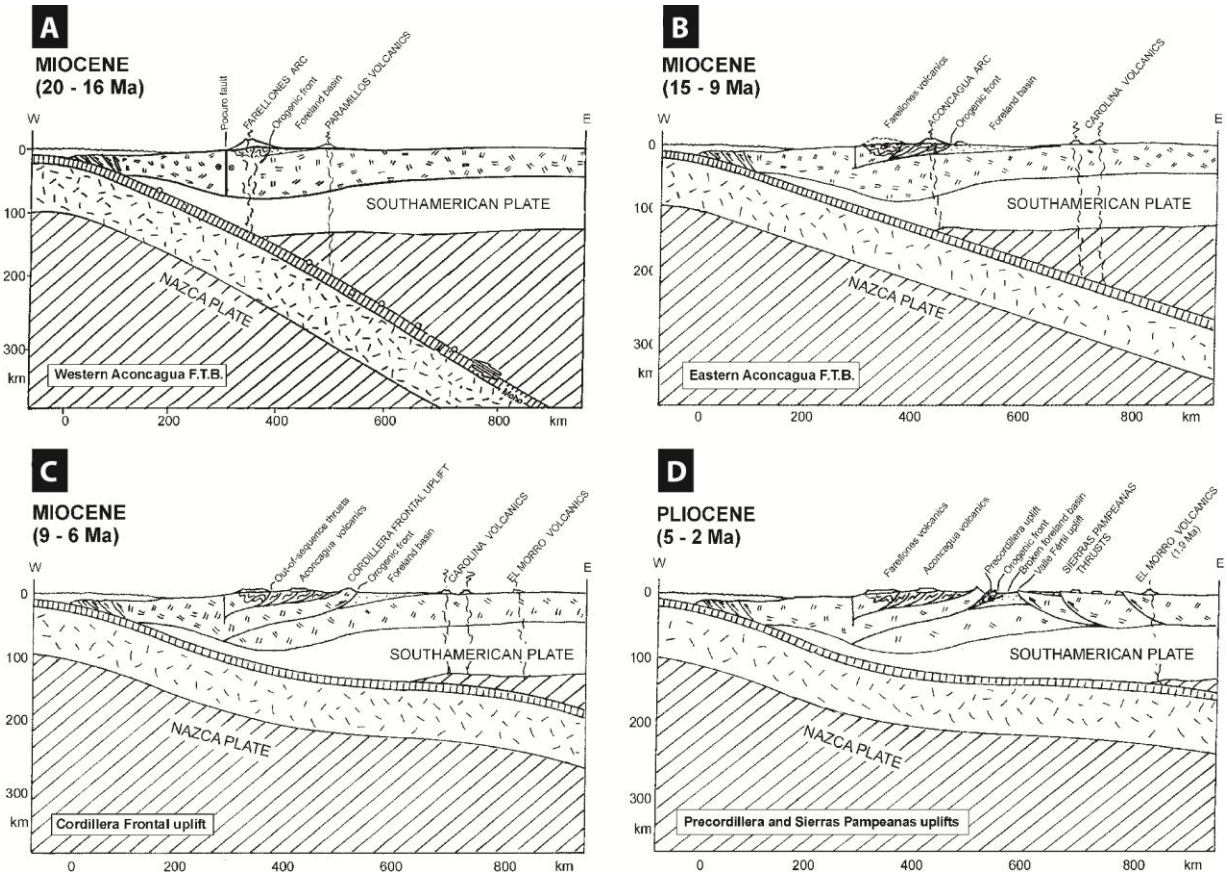


**Fig. 1.5**: *Reconstitution of the tectonic and magmatic evolution during the process of slab flattening in central Chile. From Ramos et al. (2002)*

Volcanic activity ceased entirely at 6 Ma in the Principal Cordillera and Precordillera. The last traces of volcanism reported for the region are documented in the Pampia region at the Pocho field ~ 4.5 Ma and near San Luis ~ 1.9 Ma, representing ~ 800 km inland from the trench. Given that the lavas from the Principal Cordillera indicate that its current crustal thickness of 70 km was acquired since ~ 6 Ma (Kay and Abbruzzi, 1996) and that the timing and location of the Pocho and San Luis volcanic rocks occur near today's eastern Andean front, it was postulated that today's slab configuration has been acquired since at least 7-6 Ma (Kay et al. 1991; 2005).

The deep crusts of the forearc and Principal Cordillera as well as part of their mantle are believed to have been removed and ejected eastward during slab flattening, based on an absence of Paleozoic and Mesozoic crust (Kay and Kay, 1993; Kay and Abbruzzi, 1996) and on crustal signatures for deep and old crust present in the Pocho lavas (Kay and Gordillo, 1994). Smalley et al. (1993) even postulated that the entire continental mantle was expelled eastward.

## 1.6 Backarc Tectonics and Seismicity

### *1.6.1 Deformation and Seismicity*

The continental crust of the Precordillera and western Sierra Pampeanas, in the backarc region, located above the inferred Juan Fernandez ridge subduction, is seismically very active and hosting large (Mw > 7, historic and modern) earthquakes (Fig. 1.6A) (for details, see Alvarado et al., 2005; 2007; 2009), with ongoing vertical uplift of the Sierra Pie de Palo (31°-31.5°S) (Fig. 1.6B). In contrast, above the normally-dipping slab (> 33°S), the seismicity is dominantly concentrated in the Andean crust beneath the active volcanoes (Fig. 1.6A) (Pardo et al., 2002; Alvarado et al., 2005) and the backarc region of Mendoza (33°S) undergoes higher shortening rates but, instead, very little vertical deformation with few large earthquakes (Alvarado et al., 2005).

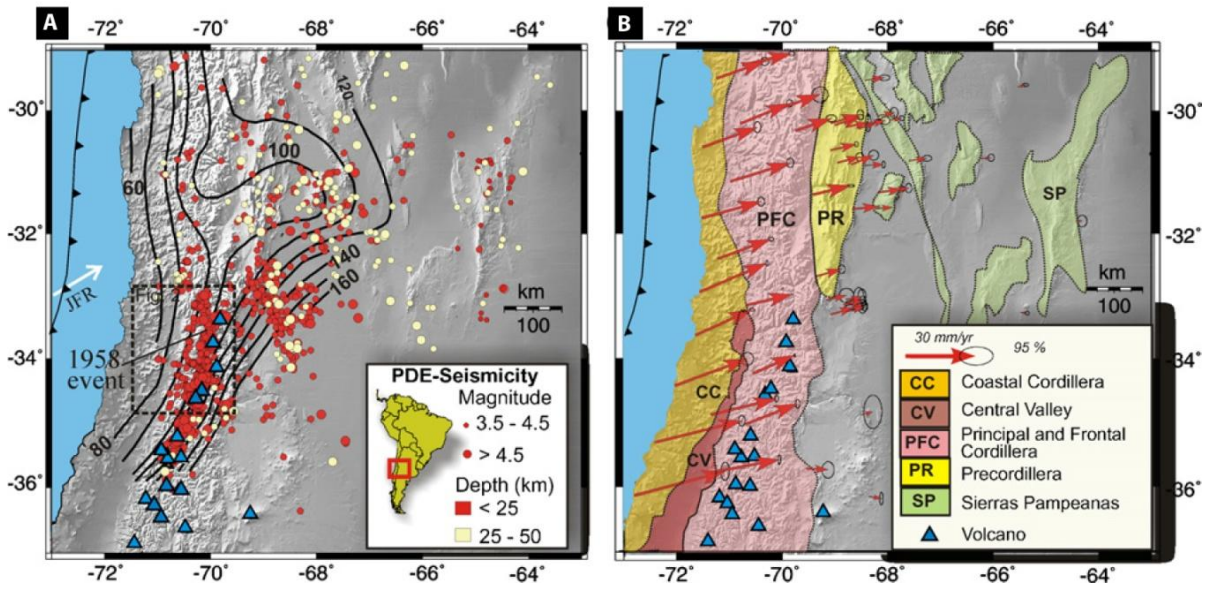


**Fig. 1.6**: *Backarc seismicity and GPS displacements of central Chile. (A) Intraplate crustal seismicity recorded by the Chilean and Argentinean seismic catalog over the past 20 years. Slab shape contours from Anderson et al. (2007), blue triangles are the active volcanoes. The 1958 Las Melosas epicenter and affected region is located within the dotted box. (B) Main geological and tectonic provinces from Ramos et al. (2002) and GPS velocity vectors with their uncertainty-ellipses from Brooks et al. (2003). From Alvarado et al. (2009)*

The Precordillera and Sierra Pampeanas crusts are described as thick and brittle (Miranda, 2001). At mid-crustal depths of Sierra Pie de Palo, three seismic interfaces at 20, 30 and 50 km depths are interpreted as detachment or decollement faults (Fig. 1.8) (Smalley and Isacks, 1990; Regnier et al., 1992; Calkins et al., 2006; Perarnau et al., 2010; Gans et al., 2011). This region is dominated by deep compressional hypocenters (> 20 km depth) (Fig. 1.6A and Fig. 1.8), with alignment along sutures zones. In comparison, the eastern Sierra Pampeanas is less seismically productive, with smaller magnitude earthquakes (Mw < ~ 4) (Fig. 1.6A).

### *1.6.2 Deformation and Stress Tensor*

Above the flat slab and southern transition zones, the calculated stress tensor orientations for the backarc regions (San Juan, Sierra Pie de Palo, Mendoza) and for the slab above 70 km depth are nearly identical, showing dominant horizontal compression parallel to plate convergence (Fig. 1.7) (78°, DeMets et al., 1990). Details and references are given in Table 1.1, below. The GPS velocity field indicates that the plate boundary between the converging Nazca and South America Plates is fully locked (the backarc is creeping at 4.5 mm/yr), and impacting the region as far as 800 km inland from the trench (Alvarado et al., 2009), at which point the slab resumes its subduction and the crust's elastic loading is restored (upper graph in Fig. 1.8) (Brooks et al., 2003). Below 70 km depth, the slab indicates horizontal and slabdip tension (Pardo et al., 2002; Anderson et al., 2007; Marot et al., 2013).

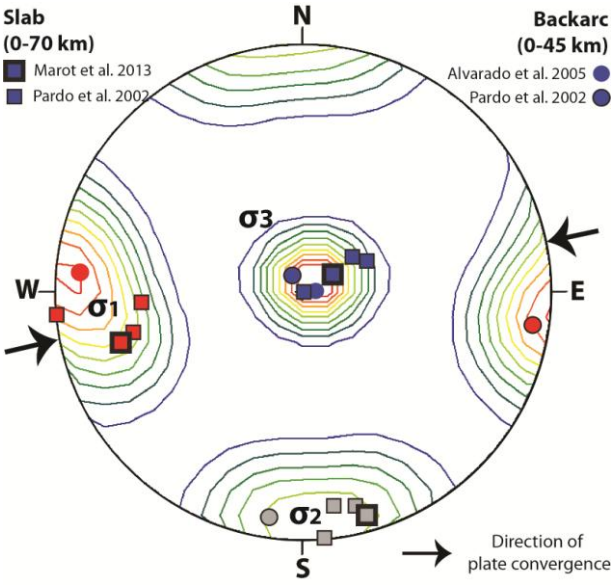


**Fig. 1.7**: *Stress tensors for the slab and backarc region (from Table 1.1) plotted onto a lower-hemisphere projection and showing the orientations of the principal stress orientations (σ1 (red), σ2 (grey), σ3 (blue)). We show here that the slab above 70 km is subject to identical stresses as those impacting the backarc region of the continental crust.*

**Table 1.1***: Stress tensors for the backarc region and slab, from different regional studies between 31°S and 33°S, plotted in Fig. 1.7. The * indicates that this reference is included in Section 2.2.8 of Chapter 2.*

| **Region** (depth, km) | **Reference** | **σ1** Strike/Dip (°) | **σ 2** Strike/Dip (°) | **σ 3** Strike/Dip (°) |
|---|---|---|---|---|
| **Slab** (0-70) | Pardo et al. (2002) | 257.1/20.2 | 166.3/7.0 | 54.5/62.3 |
| **Slab** (50-70) | Marot et al. (2013)* | 255.0/15.0 | 164.0/4.0 | 58.0/74.0 |
| **Slab** (70-110) | Marot et al. (2013)* | 159.0/77.0 | 354.0/13.0 | 263.0/3.0 |
| **Slab** (100-200) | Pardo et al. (2002) | 81.8/82.6 | 320.8/2.7 | 230.5/4.6 |
| **Backarc** (0-45) | Pardo et al. (2002) | 97.7/4.0 | 188.3/5.0 | 329.1/81.2 |
| **Backarc** (0-45) | Alvarado et al. (2005) | 275.0/6.0 | - | 90.0/84.0 |

### *1.6.3 Crustal Thickness*

A total crustal shortening of 150-170 km has occurred since the Oligocene over the flat slab region and along the thrust belt (Gerbault et al., 2009; Allmendinger and González, 2010). This thickening was essentially attributed to thrusting above a decollement in the Precordillera, along thin-skinned thrust faults, and to a lesser extent to thick-skinned block faulting in the Sierra Pampeanas.

The continental Moho signal above the flat slab is complex and discontinuous (Gans et al., 2011). The CHARGE seismic catalog has been the focus of many efforts to better constrain the region's crustal properties, including head-wave refraction analyses (Fromm et al., 2004), seismic moment tensor inversion of moderate crustal earthquakes (Alvarado et al., 2005), teleseismic receiver functions (Gilbert et al., 2006), and forward modeling of long-period (10-100 s) seismic waveform inversion (Alvarado et al., 2007). Taking also into account other seismic and gravity studies, and comparing with the global average crust thickness of ~ 40 km (Christensen and Mooney, 1995), a deep Moho of ~ 70 km characterizes the Andean Cordillera above the flat slab, with an equally unusually thick crust of 55-60 km (and 70 km for Heit et al. 2008) beneath the Precordillera and western Sierra Pampeanas (Regnier et al., 1994; Fromm et al., 2004; Beck et al., 2005; Gilbert et al., 2006; Alvarado et al., 2007; Heit et al., 2008). The Moho lies at approximately ~ 35 km beneath the eastern Sierra Pampeanas (Fig. 1.8) (Gilbert et al., 2006).

### *1.6.4 Lower Crust Composition and Gravimetric Data*

Whereby the Andean cordillera appears in isostatic equilibrium (Miranda, 2001), east of 69.5°W, the low elevations of the Precordillera (~ 2000 m) and western Sierra Pampeanas (~ 1000 m) are considerably lower than what can be expected for their crustal thicknesses and from isostasy, indicating gravitationally uncompensated, or exceptionally dense crusts. In fact, the low elevations can only be fitted with the observed crustal thicknesses by accounting for some excess density in the crust or upper mantle (Miranda, 2001; Alvarado et al., 2009).

Modeling lateral density variations in the underlying mantle is vindicated as insufficient to accommodate isostatic imbalance (Miranda, 2001). Several authors have also proposed a key role of the flat slab in compensating isostatically the thick crust at slab depths, however, it is difficult to conciliate it with the expected lower slab density thought to account for the flat subduction (Yáñez et al., 2001).

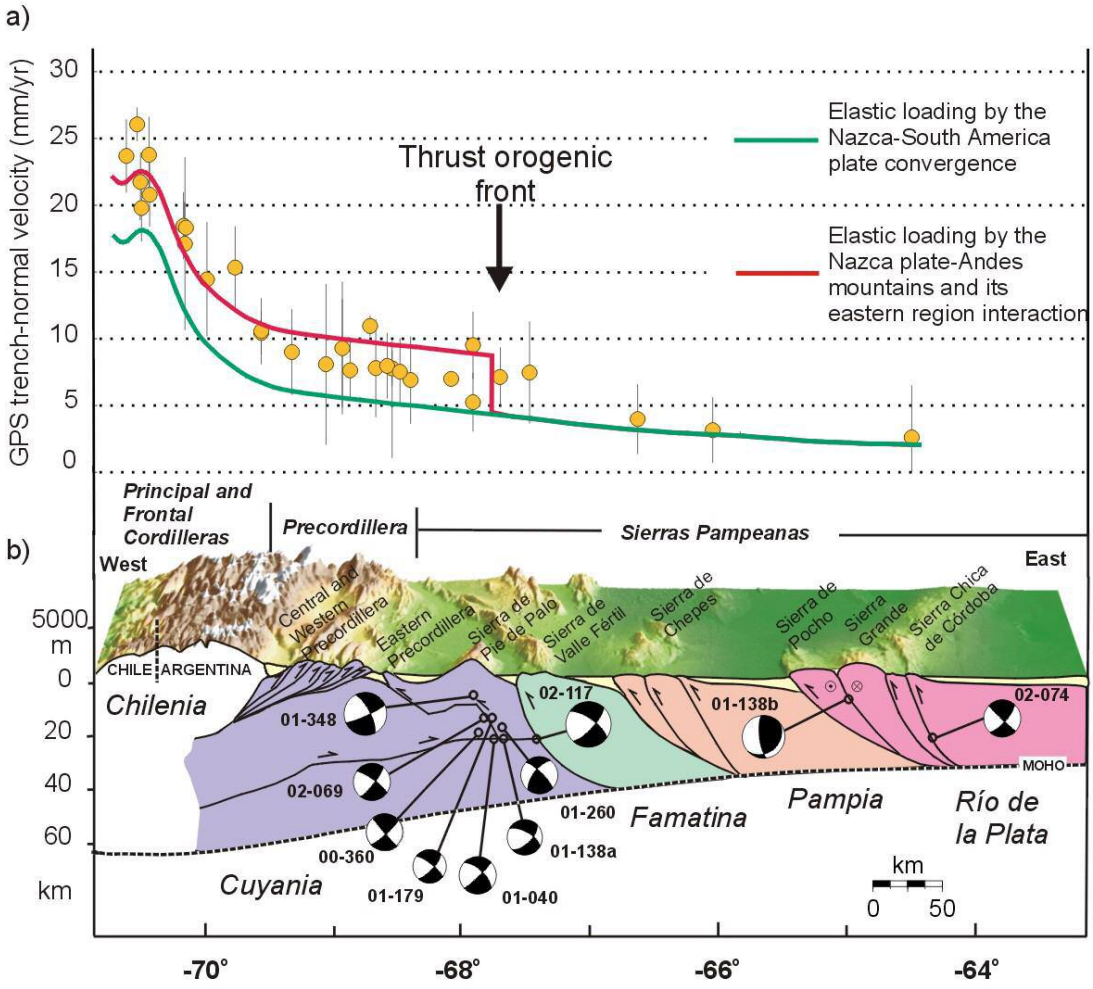


**Fig. 1.8**: *Earthquake focal mechanisms and average crustal thickness at 31°S. Upper panel shows the GPS velocities (yellow circles) from Brooks et al. (2003), and lower panel indicates a geological interpretation from Ramos et al. (2002) of the backarc setting, superimposed with backarc seismicity evidencing the western Sierra Pampeanas as being more seismically active the eastern Sierra Pampeanas. From Alvarado et al. (2009)*

Seismic receiver function analyses show a progressive increase in the seismic velocities in the lower 15-20 km of the backarc crust (Gilbert et al., 2006; Calkins et al., 2006). Gravity data indicate the presence of high density rocks near the sub-surface and within the lower crust beneath San Juan, Bermejo, Mendoza, the Precordillera and parts of the Frontal Cordillera (Christensen and Mooney, 1995; Miranda, 2001; Tassara et al., 2006). In addition, there is a lack of Moho signal here, that becomes clearer, more singular and greater in amplitude further east (Gilbert et al., 2006; Heit et al., 2008). Combining these observations, many workers have proposed a multilayered lower crust comprised of eclogites in its deepest parts (e.g. Gilbert et al., 2006; Alvarado et al., 2007; Corona, 2007).

For eclogitization to occur at these depths, the lower crust must be more mafic than an andesite in composition (Tassara et al., 2006), since felsic rocks are unable to produce high density eclogites or the observed high density anomalies. Alvarado et al. (2009) speculated that the partially eclogitized lower crust above the flat slab may also be found to the south (and possibly north), where the slab dips normally, to explain the backarc earthquakes that are also observed in these adjacent provinces (Fig.

1.6A). An additional effect for these high crustal densities is the cooler temperature characteristic of the region.

## 1.7 Thermal Heat Flux

The total thermal flux of a lithosphere can be decomposed into a crust and mantle thermal component (Muñoz, 2005). Mantle heat flow patterns are demonstrated as spatially uniform, whereas crustal heat flow tends to vary more, in correlation with different radiogenic heat productions relative to varying ages and compositions, as well as fractures and fluid circulations.

Heat flow from the continental mantle is low (12-14 $mW/m^2$) and homogeneous in shield and cratonic areas, ageing between 0.4 and 2.7 Ga, such as the Grenville Province of the Canadian Shield and the Appalachians (Lenardic et al., 2000). The lithospheric mantle beneath regions of low heat flow along the Andes is found with similar low values (Muñoz, 2005). The expected radiogenic heat generation for old terranes of Grenvillian age is also low, compared to global averages (Muñoz, 2005).

The surface thermal heat flux in Central Chile is low (30-45 $mW/m^2$) and characteristic of the San Juan (32°S) and Mendoza (33°S) regions as well as between 28°S and 29°S (20-25 $mW/m^2$) (Uyeda et al., 1978). It increases progressively towards the south (Muñoz, 2005). Areas exhibiting low surface heat flow along the Andes, are found in correlation with flat slab segments, e.g. in central Peru (~ 30 $mW/m^2$), and have been attributed to the absence of asthenosphere mantle wedge (Muñoz, 2005).

In eastern North America (Texas), from where the Cuyania terrane is believed to have derived, similar characteristic low heat flow values (< 40 $mW/m^2$) have been found and linked to low radiogenic heat generation or to dissipation of heat due to important groundwater circulation (Muñoz, 2005).

Magnetotelluric imaging of the Southern Volcanic Zone of Chile (Brasse and Soyer, 2001) indicates higher temperatures and fluid content than to the north, but mostly in the vicinity to the volcanic arc and its associated faults. Slightly higher surface heat flux is measured west of the active volcanic arc (Muñoz, 2005).

## 1.8 Erosive versus Accretionary Continental Margin

The Chilean continental margin, between 20°S and 33°S, is tectonically erosive, described by a sediment-poor trench and a narrower and steep continental slope, compared to the southern segment, between 33°S and 45°S, where the continental margin is accretive and the trench is sediment-filled (Fig. 1.9) (von Huene et al., 1997). The trench-sediment thickness in the central Chilean region is about ten times thicker to the south of the trench-ridge intersection (32.5°-33°S) than to the north (~1 km versus ~ 0.1 km, respectively) (Marquardt et al., 2004; Lamb, 2006; Contreras-Reyes et al., 2010). Along the present-day accretionary margin (> 33°S), there may have been alternating episodes of accretion and erosion over the long-term, whereas the erosive margin < 33°S seems to have been particularly intense and a permanent dominant feature during the whole Andean cycle (since the Jurassic) (Marquardt et al., 2004).

Erosive margins are linked with subduction basal erosion, which ablates continental material and results in continental basement rocks being located close to the slab surface and to the trench (Fig. 1.10). They develop preferentially in regions of high convergence rates (> 6 cm/a) and little sediment accumulation in the trench (< 1 km) (Clift and Vannucchi, 2004). Conversely, accretionary margins gather material (forearc accretionary prism) derived from the subducting and overriding plates, either by i) scrapping the top of the oceanic plate at the trench axis, or, ii) underplating the base of the

forearc. It is favored in slow convergent margins (< 7.6 cm/a) with sediments over 1 km thick in the trench (Clift and Vannucchi, 2004).

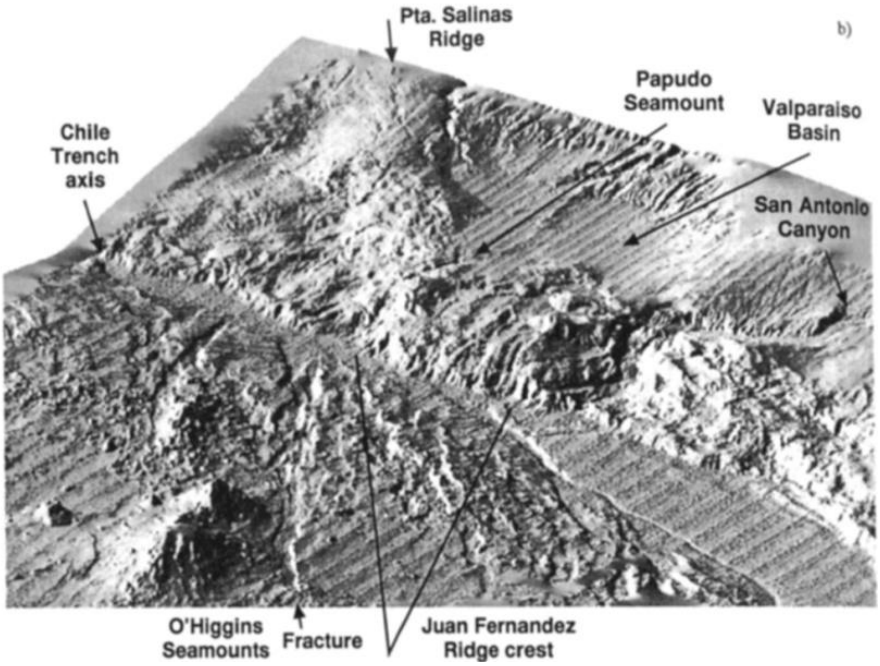


**Fig. 1.9**: *Ocean bathymetry along the subduction margin where the Juan Fernandez ridge enters the trench, showing the sediment-filled and sediment-poor trench to the south and north of the ridge, respectively. From von Huene et al. (1997)*

Trench-sediments have an important effect on the subduction process at plate interface depths (Gerya and Meilick, 2011). The thermal flux along the subduction channel is associated to the thermal structure of the subducting plate and to the basal shear heating at the interface (Lamb, 2006). Though it is approximately similar throughout the Chilean margin (only ~ 100°C variation), the shear stresses (connoted to the degree of plate coupling, Gerya and Meilick 2011) are however significantly different between these two regions (Fig. 1.11) (Lamb, 2006). This suggests that the temperature at the megathrust interface zone is not the dominant factor differentiating these two regions, but instead, the rheology of the plate interface, as Lamb (2006) pointed out its important role in affecting both the crust and mantle portions. Therefore, the sediment-starved trench, to the north of 33°S, deprives the plate interface (i.e. subduction channel) from lubrication, normally indulged by subducted sediments, resulting in reduced pore fluid pressure and increased frictional sliding (Fig. 1.10 and Fig. 1.11) (Lamb, 2006; Gerya and Meilick, 2011). Extensive underplating and basal erosion of the margin may also result in sediment "convection", whereby fluid-rich sediments are entrained into the subduction zone, however, accumulate and ascend towards the updip limit of the seismogenic zone, restricting further sediments subduction (Lamb, 2006). It is suggested that the highly landward-inclined extensional faults found in the region north of 33°S are the coastal expressions of such a process (Fig. 1.11), and that the resulting higher degree of coupling explains the Andean elevations above 4000 m in this region (Lamb, 2006). In opposition, the sediment-filled trench characterizing the southern Chilean subduction margin is proposed to have a smoother interface topography and a well lubricated subduction channel, as sediment and water are entrained deep down along the subduction interface.

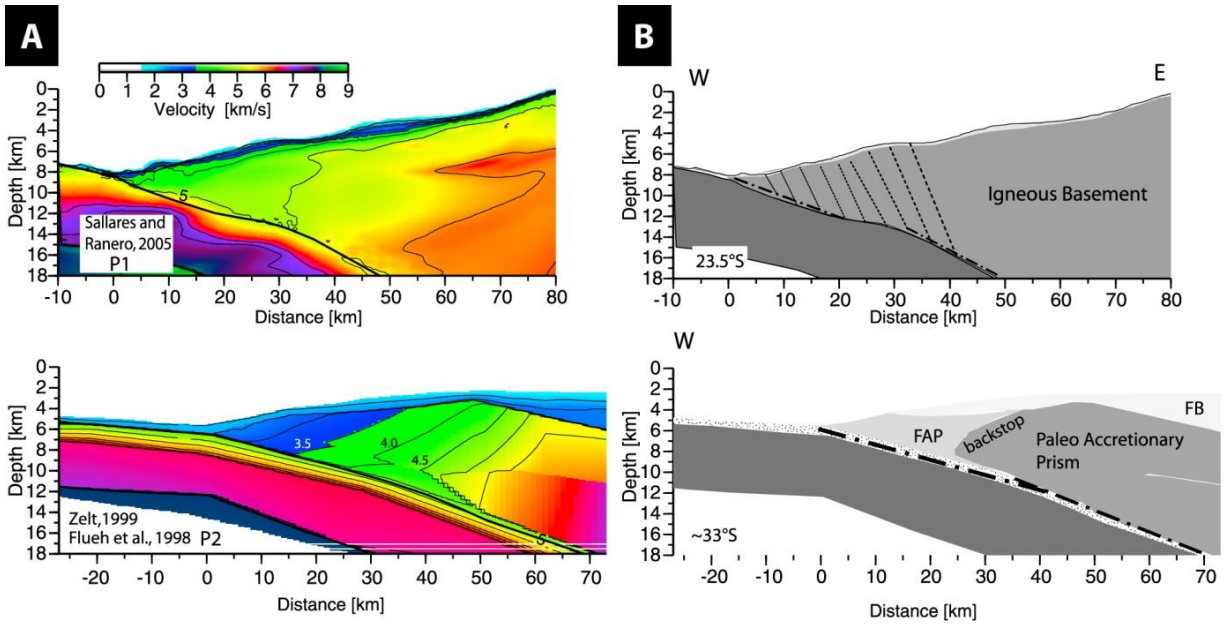


**Fig. 1.10**: *E-W vertical profiles of the subduction margin in northern Chile at 23.5°S and southern Chile at 33°S, based on seismic refraction and multi-channel reflection data. (A) Velocity-depth models with their (B) geological interpretation. The northern erosive continental margin (23.5°S) is comprised dominantly of metamorphic igneous lithologies that have undergone a hydro-fracturing process (Sallares and Ranero, 2005). From Contreras-Reyes and Osses (2010)*

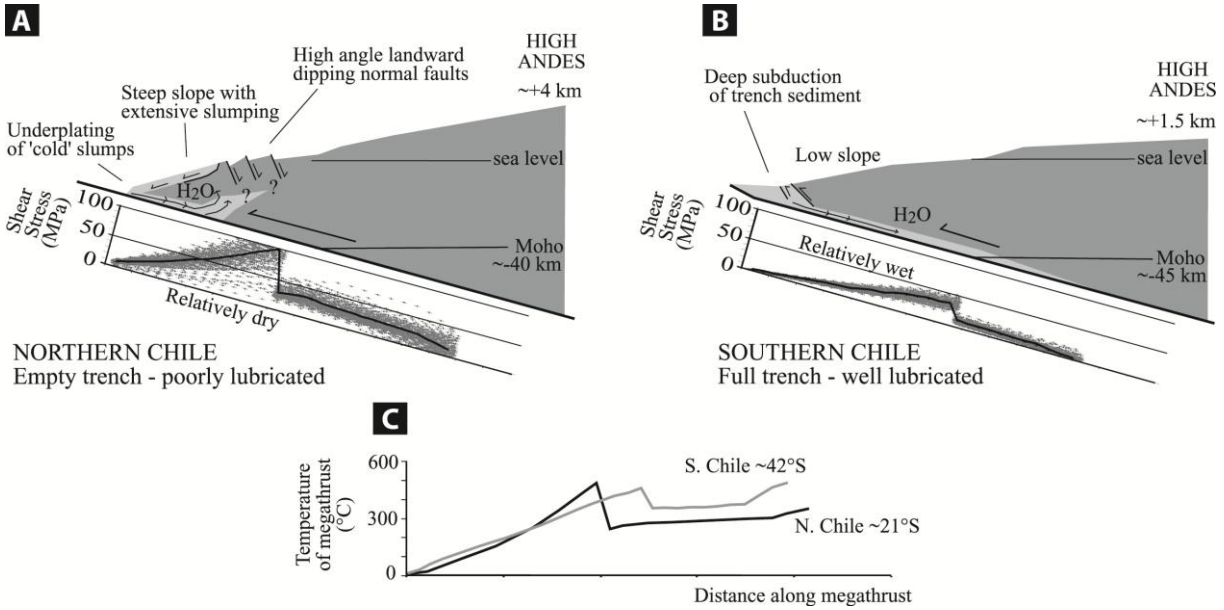


**Fig. 1.11**: *Illustrations of the principal effects of shear stress and (C) temperature along an (A) erosive margin at ~ 21°S and an (B) accretive margin at 42°S, of the Chilean subduction margin. From Lamb (2006)*

## 1.9 Plate Coupling and the Seismic Cycle

Several major historical earthquakes have ruptured the subduction margin of the Chilean subduction zone. The convergence rate between the Nazca and South American plates are categorized as one of the highest on the planet. The two largest earthquakes to have affected the region are the 1960 Mw 9.5 Valdivia earthquake (Campos et al., 2002) and the very recent 2010 Mw 8.8 Maule earthquake (Delouis et al., 2010). The other major events that have occurred in the region are annotated in Fig. 1.12.

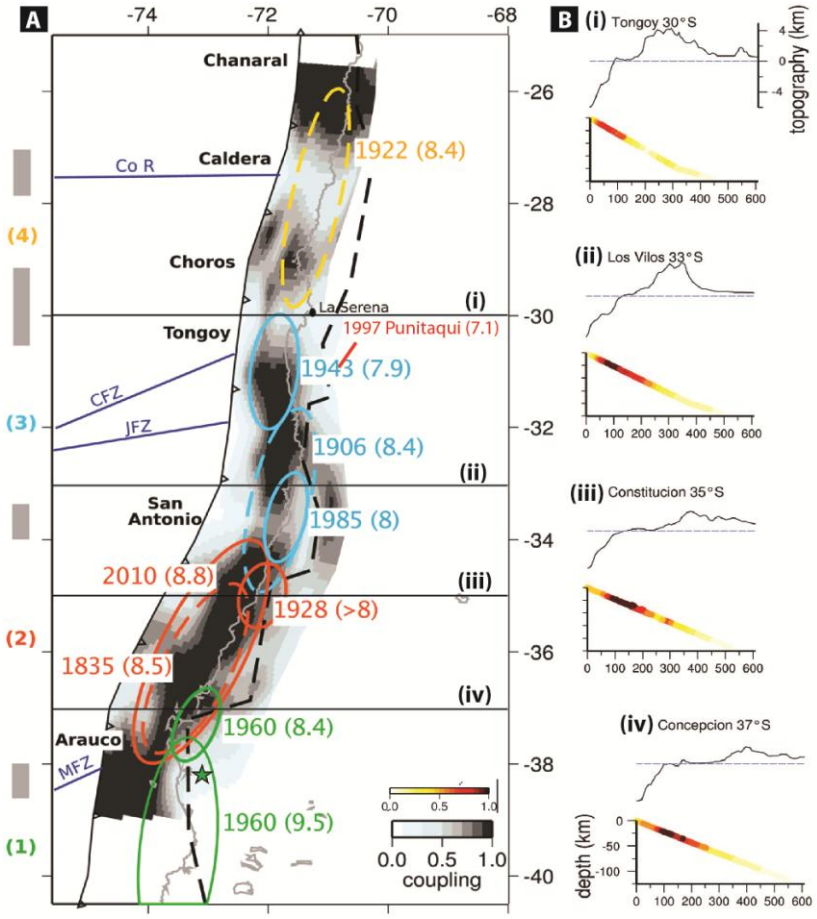


**Fig. 1.12**: *Historical earthquakes and degree of plate coupling along the central Chilean margin based on GPS data. (A) Coupling distribution and rupture zones of major instrumental or historical earthquakes. Rupture segments areas are color coded: (1) Valdivia, (2) Maule (red), (3) Metropolitan (blue), and (4) Atacama (yellow). Grey boxes on the left are the intersegment zones of major rupture areas. Dashed black line is the intersection between the subducting slab interface and the continental Moho (Tassara et al., 2006). Green star denotes the CMT epicenter location of the 1960 Mw 9.5 Valdivia earthquake and the red line indicates the epicenter of the 1997 Punitaqui earthquake. Annotated are particularly coastal features and major oceanic features (dark blue line): Co R: Copiapo Ridge, CFZ: Challenger Fracture Zone, JFR: Juan Fernandez Ridge, and MFZ: Mocha Fracture Zone. (B) Vertical profiles (i-iv in (A)) showing topography and the plate interface best fitting coupling coefficient along 30°S, 33°S, 35°S and 37°S. From Métois et al. (2012)*

The recurrent earthquake rupture patterns indicate that the subduction zone (between 19°S and 40°S) is segmented into four areas of high amounts of coupling (> 70%), where major events repeatedly occur (1-4 in Fig. 1.12) (Beck et al., 1998; Métois et al., 2012). These are separated by narrow zones of low plate coupling (< 60%) associated with subducting oceanic features, such as ridges or fractures (Contreras-Reyes and Carrizo, 2011). Subduction of such asperities contribute to the interface locking effect (Clouard et al., 2007; Contreras-Reyes et al., 2010). It was noticed that coastal bays or peninsulas are spatially correlated with either the termination, or nucleation, of these major mega-thrust fault zones (for further details, see Métois et al., 2012).

The inter-seismic deformation pattern along the Chilean subduction zone is well explained by simple elastic and plate coupling models (Métois et al., 2012). The downdip extent of the seismogenic zone corresponds to 50-60 km depth (Pardo et al., 2002; Comte et al., 2002) and ~ 200°C (Clouard et al., 2007), with GPS data suggesting that aseismic slip (creep) occurs below this depth at 6.5 cm/yr (Klotz et al., 2001).

The segments between 19°-24°S (northern Chile) and 34°-38°S (Maule) were identified as seismic gaps that had not ruptured since 1877 and 1835, respectively. The Maule segment ruptured in 2010 by an earthquake of magnitude 8.8 (Delouis et al., 2010). The co-seismic rupture slip (12-15 m; Lay et al., 2010) distribution corresponds well with the inter-seismic coupled pattern which was terminated to the north at 33.5°S by the San Antonio "decoupled zone", close to the Juan Fernandez ridge, and to the south at ~ 38°S near the Arauco peninsula (Métois et al., 2012). Between 25°S and 30°S, the Atacama segment last ruptured in 1922 by an Ms 8.4 earthquake (Fig. 1.12).

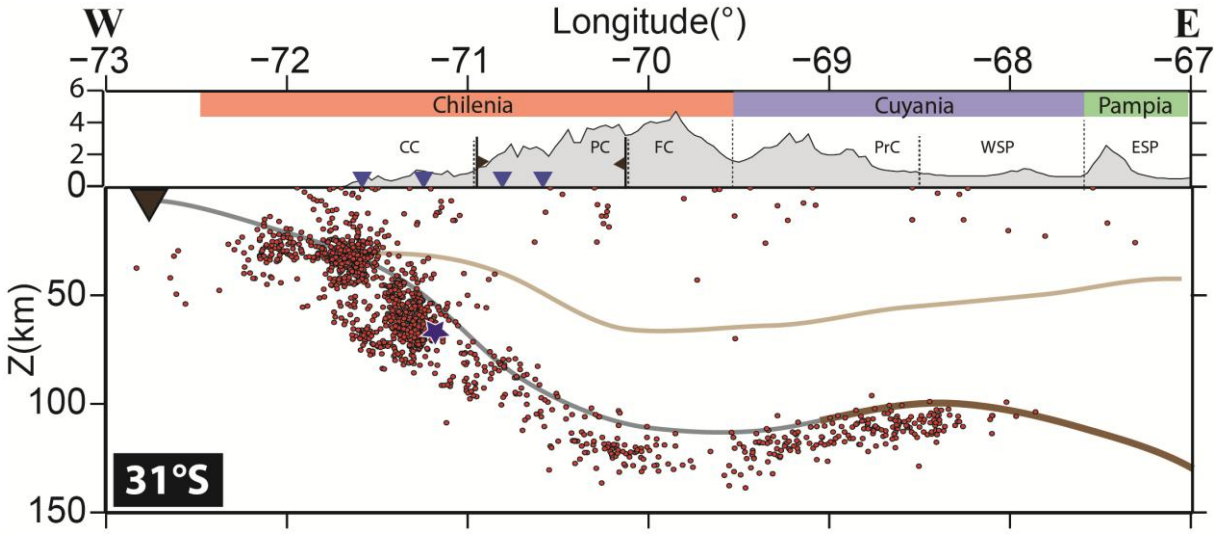


**Fig. 1.13**: *Local seismicity at 31°S from our compiled seismic catalog (see Chapter 2) showing the very dense microseismicity in the aftershock region of the 1997 Punitaqui earthquake (blue star). The majority of the events defining this zone are from the 1999-2000 OVA99 catalog.*

The segment between 30°S and 34°S (the Metropolitan area, Fig. 1.12) is very active. The Ms 8.4 Valparaiso earthquake is believed to have entirely ruptured it in 1906. It was later partially broken in 1943, 1971 and 1985 (Métois et al., 2012). The interplate seismicity of this region suddenly rose in early July 1997, when several shallow thrust events of Mw > 6 occurred within only three weeks (Gardi et al., 2006) and propagated ~ 40 km southward towards the future location of the 15 October 1997 Mw 7.1 Punitaqui intraslab earthquake (Fig. 1.12). It triggered abundant plate interface

seismicity (Mw > 6) for almost a decade later (Gardi et al., 2006), and seismicity only began to stabilize in mid-1998. The seismic database used for our study, recorded many aftershocks between November 1999 and March 2006 (Fig. 1.13), and indicate a region of anomalous seismic properties, described in more detail in Chapter 3. Furthermore, there has been a remarkable seismic paucity in the slab > 70 km depth in this region, over the past 15 years (Gardi et al., 2006). Today, this region lies in an inter-seismic cycle (Clouard et al., 2007). The Punitaqui earthquake occurred at the downdip end of the coupled zone (70 km depth) (Lemoine et al., 2002; Métois et al., 2012) and nearly 60 years after the Mw 7.9 1943 earthquake that last ruptured the updip zone. Stress transfer models favor a triggering mechanism by aseismic slip which, in turn, explains well the foreshock cascade pattern and the rupture plane orientations (Gardi et al., 2006). Such events may occur at any time during the seismic cycle, once the stresses produced by aseismic slip near the edge of the seismogenic zone reached their threshold (Gardi et al., 2006).

## 1.10 Modern-day Tectonics of the Subducting Slab

The age of the Nazca Plate along the continental margin ranges from 0 Ma at the Triple Junction with the Antarctic and South American Plates at 46.5°S, to 48 Ma at 20°S (Tassara et al., 2006). In Central Chile, the age of the Nazca Plate at the trench is around 35 Ma (Müller et al., 1997; Tebbens and Cande, 1997). Almost half of its crustal thickness is anomalously thick (Tassara et al. 2006; Tassara and Echaurren, 2012) compared to the globally average of 7 ± 1 km (White et al. 1992; Bown and White, 1994), and these regions are correlated mostly with plume-related ocean ridges or plateaus, such as the ridges of Juan Fernandez and Iquique, or the Nazca Ridge (Fig. 1.14). The Nazca Ridge has a continuous crustal root of up to 35 km thick (Fig. 1.14B), twice the thickness of the Iquique and Juan Fernandez ridges (~ 15 km thick, using gravity data, Tassara et al. (2006); and 8 km for the Juan Fernandez ridge using seismic data, Kopp et al., (2004)), and its load is additionally compensated by reduced mantle densities due to lithospheric hydration (Fig. 1.18B) (Kopp et al., 2004; Tassara et al., 2006).

The crustal thickness of the Juan Fernandez ridge appears discontinuous (Fig. 1.14B), and does not thicken toward the trench, as is the case for the Nazca Ridge (Tassara et al., 2006). Near the trench and to the north of the Juan Fernandez ridge, reduced mantle densities of < 100 km width are observed and attributed to lithosphere hydration (Fig. 1.18) (Kopp et al., 2004).

Along all the fracture zones (e.g. Challenger, Valdivia-Mocha, Mejillones, Nazca Fracture Zones), the oceanic crust is thin (< 6 km) (Fig. 1.14). The Challenger Fracture Zone spans from 35°S, transects the Juan Fernandez Ridge, and subducts beneath the South American continent at 30°S. It formed as an eastward-propagating rift center during the Farallon Plate reconfiguration at 25 Ma, during which the individualization of the Nazca and Cocos Plates occurred, to support the associated change in pole of rotation (Yáñez et al., 2002). This fracture zone divides the older and faster northern portion of the Nazca Plate created at the East-Pacific Rise, from the younger and slower southern portion formed at the Antarctic-Nazca Rise (Cande and Haxby, 1991). Seismic imaging along it (Kopp et al., 2004) suggests that it is hydrated down to mantle depths, with a possible 15% serpentinization

.

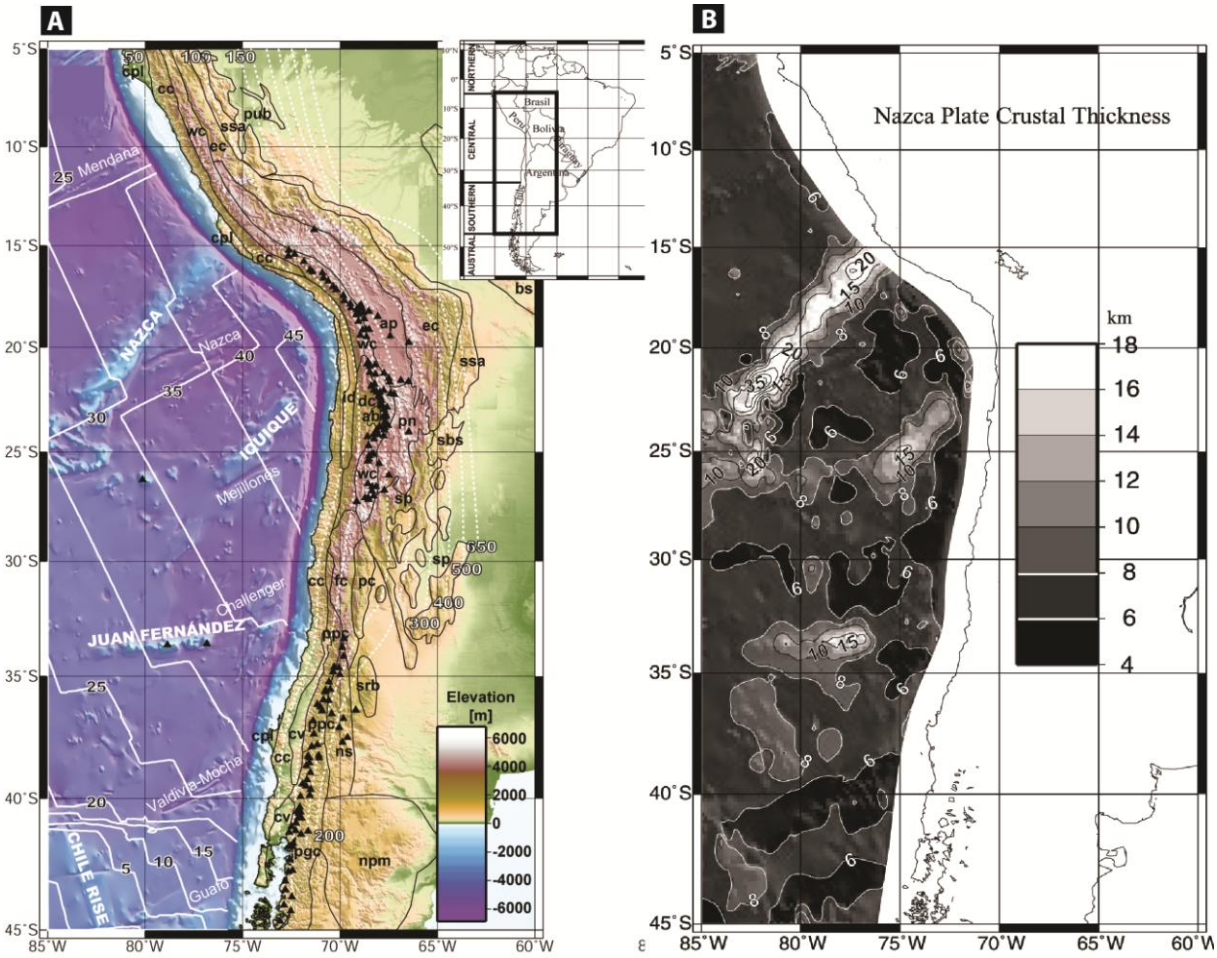


**Fig. 1.14**: *(A) Geological, tectonic and bathymetric setting of the Peru-Chilean subduction zone. The inset shows the four main regions of the Andean segmentation. Nazca plate age (Ma) is from magnetic anomalies determined by Müller et al. (1997); the main aseismic features are in capital letters and in miniscule letters are the main fracture zones. Onshore, the white dotted lines with numbers describe the subducted slab shape from the GMT software package (Wessel and Smith, 1998); black triangles are the locations of active volcanoes, geological-tectonic boundaries are outlined in solid lines and annotations are described in Tassara et al. (2006). (B) Oceanic crustal thickness. From Tassara et al. (2006)*

The Chile Rise oceanic spreading center is perceived with an over-thickened crust (> 8 km) in Tassara et al. (2006) models (Fig. 1.14) due to their method of calculation (oceanic Moho depth minus the satellite-derived bathymetry). However, the higher topography and seismic tomography of Russo et al. (2010) reflect the presence of light and hot mantle material along the ridge axis (Fig. 1.15A), typical of these types of tectonic settings. The Chile Rise subducts beneath the South American continent, forming a Triple Junction between the Nazca, South America and Antarctica Plates (Barazangi and Isacks, 1976). Its subduction started at the southern tip of Patagonia (55°S), at 14-15 Ma, and progressively migrated northward to 48°S by 10 Myr. It is currently located at 46°S (Cande et al., 1987; Scalabrino et al., 2009). At the onset of ridge subduction, a shift in the arc lava chemistry occurred, followed by intense effusive volcanism forming large continental flood basalt plateaus that ceased very recently, at 4 Ma. These events were associated to upwelling hot asthenosphere through the slab window or gap (Fig. 1.15B) (Murdie and Russo, 1999; Scalabrino et al., 2009; Russo et al., 2010) which formed due to the difference in convergence rates between the Antarctic and Nazca Plates

(2 cm/a versus 7 cm/a, respectively). The subduction of the spreading ridge is associated with strong continental marginal erosion (Bourgois et al., 1996), backarc plateau basalts, volcanism unusually close to the trench, and uplift and plutonism on the continental margin (Cande et al., 1987; Scalabrino et al., 2009). It is also correlated with unusual isotopic lavas chemistries, seismicity, gravity observations, and upper mantle flow.

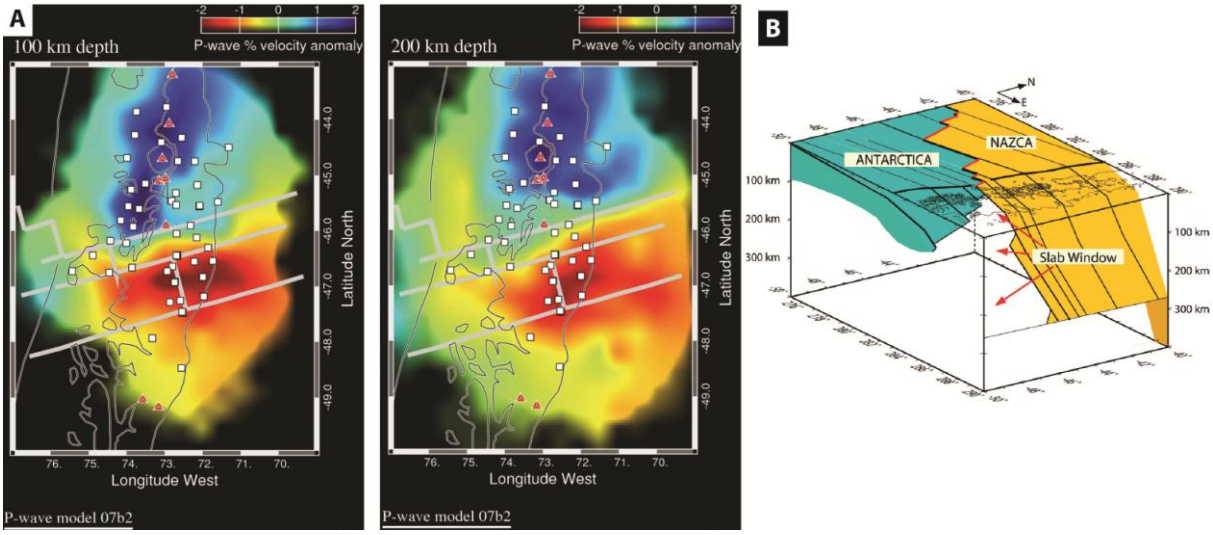


**Fig. 1.15**: *Teleseismic P-wave tomography of the subducted Chile Rise, relative to the global model IASEP-91 (Kennett and Engdahl, 1991). (A) Plan view at velocity perturbation at 100 and 200 km depth. The subducted Nazca slab is noticed as the linear NNE-trending fast anomaly. The slab window is perceived as the slow velocity anomaly. Plate structure is shown by the heavy grey lines. Stations of the CRSP seismic network are indicated by white squares. Active arc volcanoes are the red triangles. Thin white lines are the Chilean trench, coastline and the Chile-Argentina political border. (B) Separation of the trailing edge of the Nazca Plate and the leading edge of the Antarctic Plate, forming a slab window, once ambient mantle temperatures are high enough to prevent lithosphere formation. From Russo et al. (2010)*

## 1.11 Pampean Flat Slab Mechanisms

The first images of the Nazca slab underneath South America were acquired by locating the Wadati-Benioff zone using global catalogs (Fig. 1.16) (Barazangi and Isacks, 1976; Engdahl et al., 1998; Gutscher, 2002). Today, only about 4 or 4 flat subductions are recognized worldwide (Heuret et al., 2007; Skinner and Clayton, 2013) and many mechanisms have been suggested for their onset: 1) subduction of buoyant lithosphere due to young age, subduction of overthickened oceanic crust and hydrated underlying mantle, 2) rapid plate convergence (van Hunen et al., 2004, Martinod et al., 2010), and, 3) suction forces (Perez-Gussinyé et al., 2008; Manea et al., 2012) which are caused by "increases in the non-hydrostatic pressure forces related to subduction driven flow within the asthenosphere", cited from Manea et al. (2012). The Pampean flat slab could meet all three criteria.

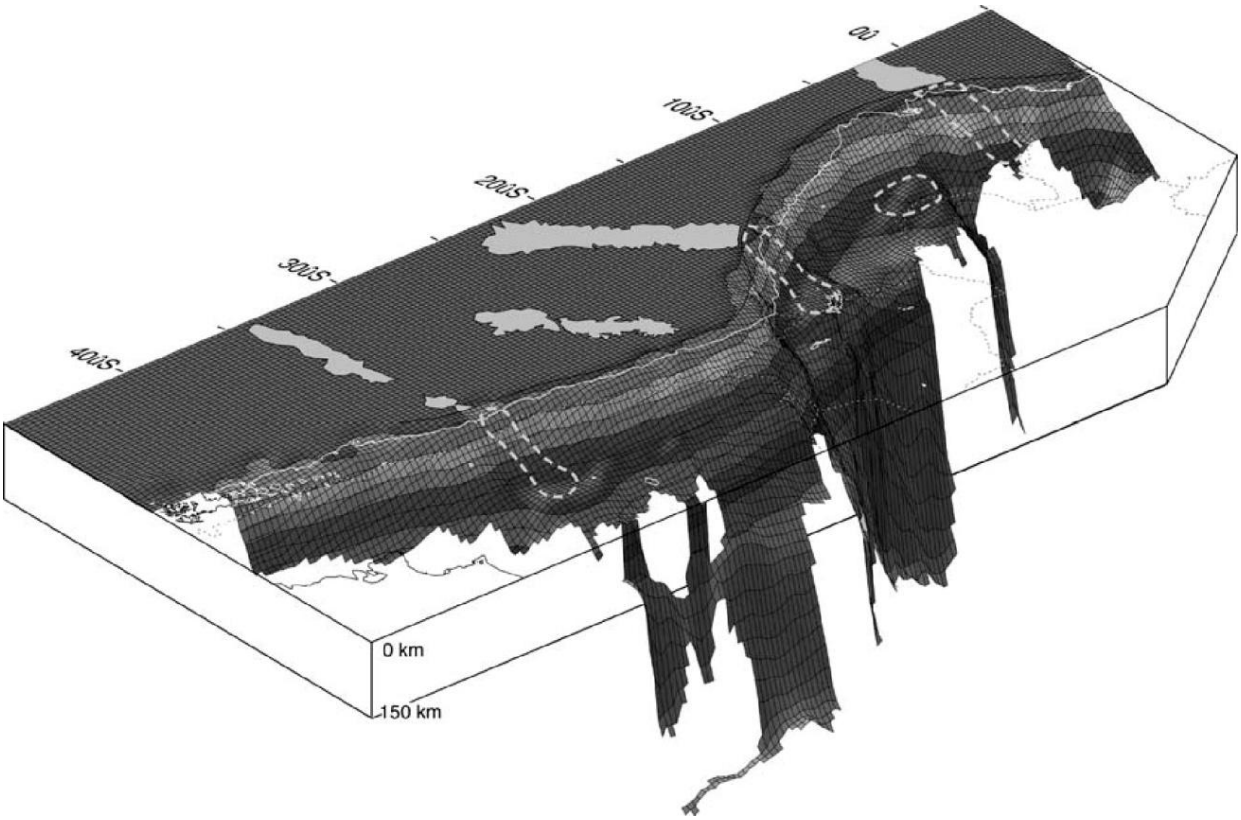


**Fig. 1.16**: *Three-dimensional view of the subducting Nazca Plate as determined by gridded hypocenter distribution (Engdahl et al., 1998). Also shown are the locations of oceanic ridges and plateaus (grey shaded areas) and their inferred subduction path (dashed grey lines). From Gutscher (2002)*

A slab of 35 Ma without overthickened crust is expected to have reached the limits of its thermal buoyancy (Afonso et al., 2007). In that case, the entire subducting Nazca slab to the south of ~ 35°S (age < 35 Ma) would tend to subduct horizontally; which is not the case, indicating that the slab age is probably not the leading factor generating its flat subductions.

It is noticed that the Iquique ridge of northern Chile has a more continuous crustal root (Fig. 1.14) than the Juan Fernandez ridge; however, paradoxically it subducts steeply (35°) (Fig. 0.1 and Fig. 1.16). Flexural modeling of the free air anomaly and seismic reflection data along the Juan Fernandez ridge, agree with a 100 km wide ridge (Yáñez et al., 2002; Kopp et al., 2004), which is also the width of the dense and strong seismic activity that aligns along its inland prolongation, compared to the adjacent areas (Anderson et al., 2007).

Whereas most authors support the continuation of the Juan Fernandez ridge underneath the South American plate, others contest flat subduction completely, notably Muñoz (2005). Magnetic and bathymetry studies, offshore the coast of Chile, confirm the existence of at least two subducted seamounts (O'Higgins and Papudo) which are part of the Juan Fernandez mountain chain, presently located beneath the continental slope (von Huene et al., 1997; Yáñez et al., 2001; 2002). Martinod et al. (2005; 2010) conducted 3-D analogue experiments of subducting oceanic plateaus and seamounts, and interpreted the offshore dimension and orientation of the Juan Fernandez ridge insufficient to initiate flat subduction alone. Van Hunen et al. (2002) showed that an 18 km thick oceanic plateau provides sufficient buoyancy forces to withhold flat subduction; whereas Gutscher et al. (2000) modeled isostatically that an oceanic plateau of only 12 km thick over a 50 Myr old slab, can sustain

neutral buoyancy. Therefore, considering only crustal overthickening effects, we would expect the Juan Fernandez ridge crust to be between 10 and 20 km thick at depth.

Gans et al. (2011) used local receiver functions to outline crustal thicknesses of over 13 km for most of the flat slab segment (70%), and not just along its ridge prolongation were seismicity is most intense. However, offshore seismic reflection data by Kopp et al. (2004) do not indicate an over-thickened crust offshore, but a moderately thick (8-10 km) seamount ridge (Fig. 1.17). They propose that the slab's extra buoyancy is instead attributed to lithospheric hydration, which reduces rock density. Geochemical studies indicate that the Juan Fernandez is composed of hotspot-derived material (Pilger and Handschumacher, 1981; Stuessy et al., 1984; Montelli et al., 2004). Perhaps its unusual chemical or thermal structure provides additional buoyancy along the ridge; however this aspect is very uncertain. The Pampean flat slab's seismicity and the directions of tensional axes determined from their focal mechanisms (Anderson et al., 2007), agree with slab flattening caused by subduction of buoyant material along the inland prolongation of the Juan Fernandez ridge (Yáñez et al., 2002).

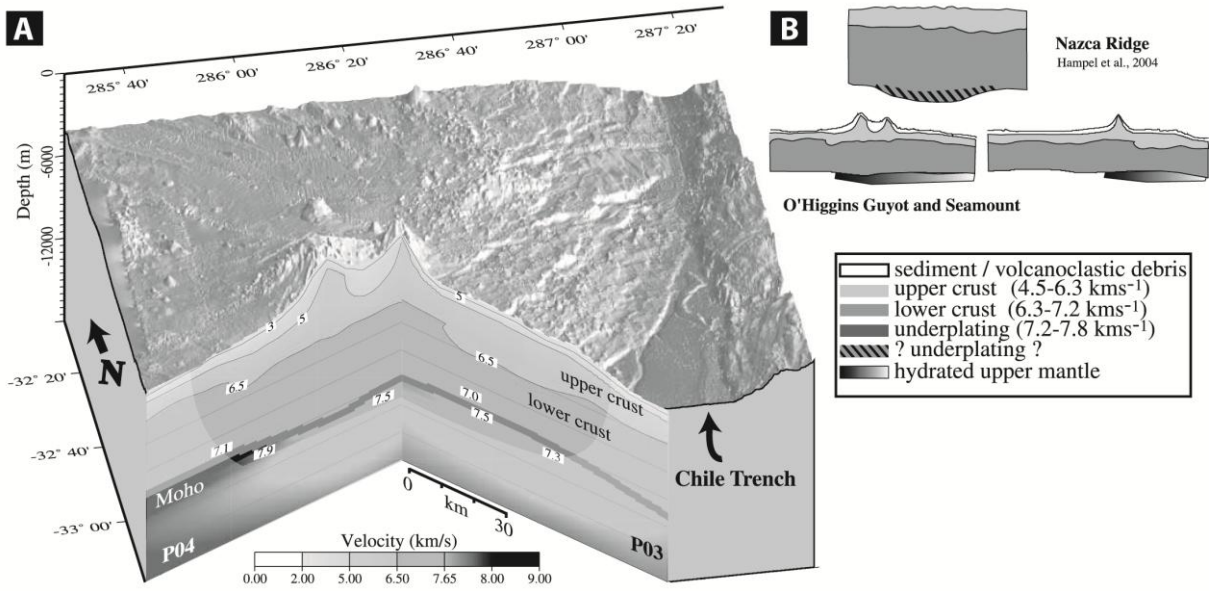


**Fig. 1.17**: *Velocity structure and crustal thickness of the Juan Fernandez ridge. (A) 3-D seismic velocity distribution representation of the O'Higgins Seamount Group, the main part of the Juan Fernandez ridge oceanward to the trench. Reduced crustal and upper mantle seismic velocities can only be observed along intense fracturing of the crust, suggested to be associated to plate hydration rather than to hotspot-related magma underplating. (B) Comparison between velocity structure and thickness of the Nazca and Juan Fernandez ridges, showing reduced upper mantle velocities and no crustal root, as is nearly always the case for other hotspot related seamounts. From Kopp et al. (2004)*

To maintain flat subduction for such distances, it is important that the basaltic crust remains meta-stable in the eclogite stability field (Gans et al., 2011). The central Chilean flat slab is expected to experience a delay of ~ 8-10 Ma in the basalt/gabbro-eclogite transformation, due to i) the region's reduced heat flow (due to plate coupling), ii) a young slab age, and iii) a high subduction rate. These factors act to inhibit the chemical reactions in the flat slab portion and allow inland progression of the flat slab for long periods of time (Sacks, 1983; van Hunen et al., 2002; Gans et al., 2011). A basalt/gabbro crust is ~ 400 kg/m$^3$ less dense than mantle, and an overthickened crust will

substantially increase the buoyancy force of the slab. Once eclogite is fully formed (~ 200 kg/m$^3$ denser than mantle) it will induce sufficient negative buoyancy forces (i.e. slab pull) to provoke subduction. For a ~ 50 Ma oceanic crust, such as the Pampean flat slab, a sufficient amount of (buoyant) basaltic oceanic crust must be present for the slab to support flat subduction (Gans et al., 2011).

.

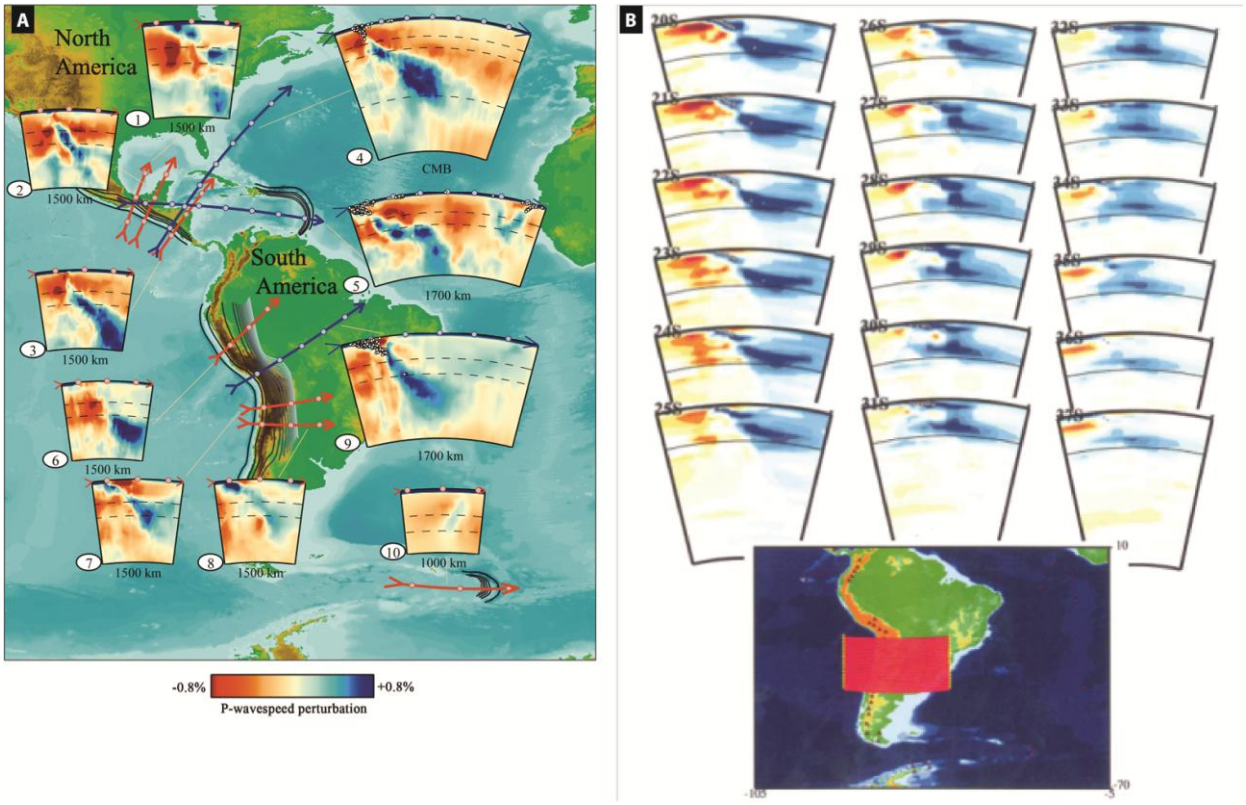


**Fig. 1.18**: *Teleseismic P-wave tomography images along the South American subduction zone, based on the ak135 Earth model (Kennett et al., 1995). From (A) Li et al. (2008), and (B) M. Obayashi, personal communication.*

The interface of the flat slab portion is associated with a weak and complex P- and S-wave signal, based on local receiver functions (Gans et al., 2011). This was explained by low impedance contrasts, in opposition to the northern part of the flat slab (~ 31°S), which exhibits simple and smooth signals (Gans et al., 2011). This low impedance contrast can be explained either by 1) the low geotherm effect, 2) large-scale offsets of faults at its surface, or 3) an eclogitized oceanic crust, contradicting the hypothesis of a delayed eclogitization

However, this interface detected by Gans et al. (2011) is located about 10-20 km above the flat slab seismicity, placing the flat slab earthquakes within the slab mantle, and may not represent the slab's surface after all. Nevertheless, if it is correct, it would indicate that the oceanic crust is coupled ("stuck") to the base of the overriding plate and deforming aseismically, as remarked by the authors.

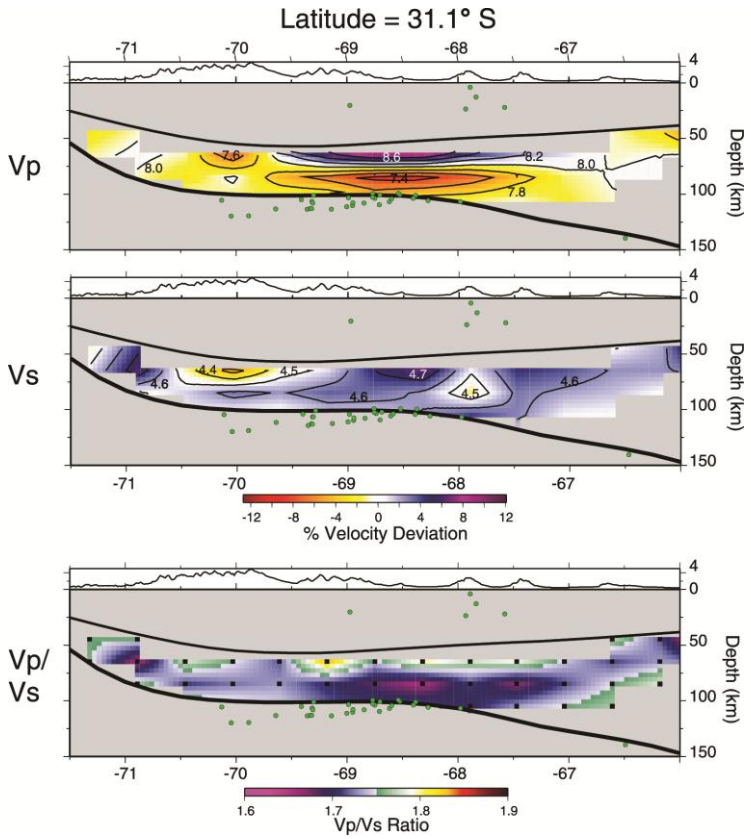


**Fig. 1.19**: *Seismic tomography of the continental mantle above the flat slab from CHARGE seismicity (green dots), showing absolute values (contour lines) and perturbations relative to the global IASEP-91 model (Kennett et al., 1995), and Vp/Vs. The Moho is by Fromm et al. (2004), slab interface is from Cahill and Isacks (1992). Black dots are the grid node locations. From Wagner et al. (2005)*

## 1.12 The Nazca Slab in the Deep Mantle

Teleseismic imaging of the deeper parts of the Nazca slab is poorly resolved. Some tomographic studies indicate that the slab, perceived as a fast velocity anomaly (in blue), crosses the 660 km discontinuity zone (Fig. 1.18A and Fig. 1.21C) (Li et al., 2008; Pesicek et al., 2012), while others indicate that it stagnates at this depth (Fig. 1.19B) (Fukao et al., 2009; M. Obayashi, personal communication). The abrupt cessation of the slab seismicity south of the Challenger-Juan Fernandez-Maipo Fracture zone (~30°S) (Fig. 1.16) (Barazangi and Isacks, 1976; Yáñez et al., 2002) is supported by seismic tomography studies as slab break-off occurring around 200-300 km depth (Fig. 1.18 and Fig. 1.21C) (Engdahl et al., 1995; Li et al., 2008; Fukao et al., 2009; Pesicek et al., 2012; M. Obayashi personal communication). Below the Pampean flat slab, there seems to be a piece of slab stagnating at ~ 660 km depth (Fig. 1.18 and Fig. 1.21B4).

In northern and southern Chile, local- and regional-scale studies observe the subducting oceanic crust as a low seismic velocity zone with high Vp/Vs ratios, extending down to 50-80 km depth along the plate interface (Schurr et al., 2006; Dorbath et al., 2008; Haberland et al., 2009), in agreement with the location of the Wadati-Beniof zone. In the overriding plate, the lower forearc crust is also regularly perceived with relatively low Vp/Vs ratios (Husen et al., 2000; Haberland et al., 2009).

In central Chile, the continental mantle above the flat slab segment is described by Wagner et al. (2005; 2006; 2008) with fast S-waves and reduced P-waves, resulting in very low Vp/Vs ratios (Fig. 1.19), not supportive of mantle hydration. However, the continental mantle further east, above the re-

subducting slab, is observed by Bianchi et al. (2013) as a slow P-wave anomaly (Fig. 1.21A and Appendix B4) exhibiting high mantle conductivity values relative to the adjacent mantle above the flat slab (Fig. 1.22A and B) (Orozco et al., 2013), this time suggesting mantle hydration. The asthenosphere to the east of the re-subducting slab is also highly conductive down to 600 km (Fig. 1.22A and C) (Booker et al., 2004; Orozco et al., 2013), a sign for the presence of fluids or occurrence of partial melt.

Seismic anisotropy in the continental mantle above the flat slab in the forearc region (30°S) and south of 33°S, show alignments of fast SK(K)S polarizations parallel to the trench axis (Fig. 1.20A, light blue lines) and interpreted as flow deflected southward by retrograde slab motion flow. These then rotate progressively eastward above the eastern edge of the flat slab (Fig. 1.20, light blue lines (A) and black lines (B)) and was interpreted as mantle flow entrained eastward with the subducting flat slab (Anderson et al., 2004; MacDougall et al., 2012).

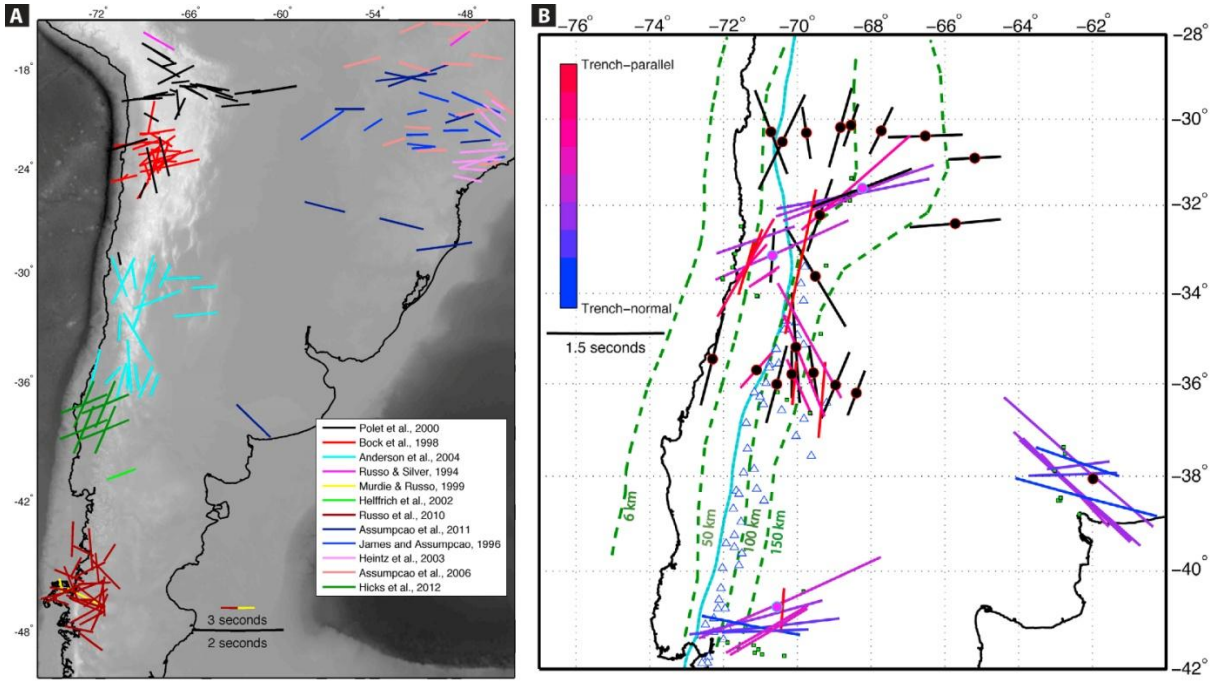


**Fig. 1.20**: *Seismic anisotropy measurements along the Chilean subduction margin, of (A) *KS shear wave splitting. Line azimuths are drawn with respect to North and represent the direction of fast polarization; length represents splitting time. (B) SK(K)S shear wave splitting. Color scale based on orientation relative to trench axis. The plotted locations are at half distance between where their ray-paths intersect the upper mantle at 410 km (green squares) and the station. Black vectors show station averages from Anderson et al. (2004). Black circles are the CHARGE stations; pink circles are permanent stations. Slab contours are from Syracuse and Abers (2006); and the light turquoise line defines the intersection between the forearc and the backarc. From MacDougall et al. (2012)*

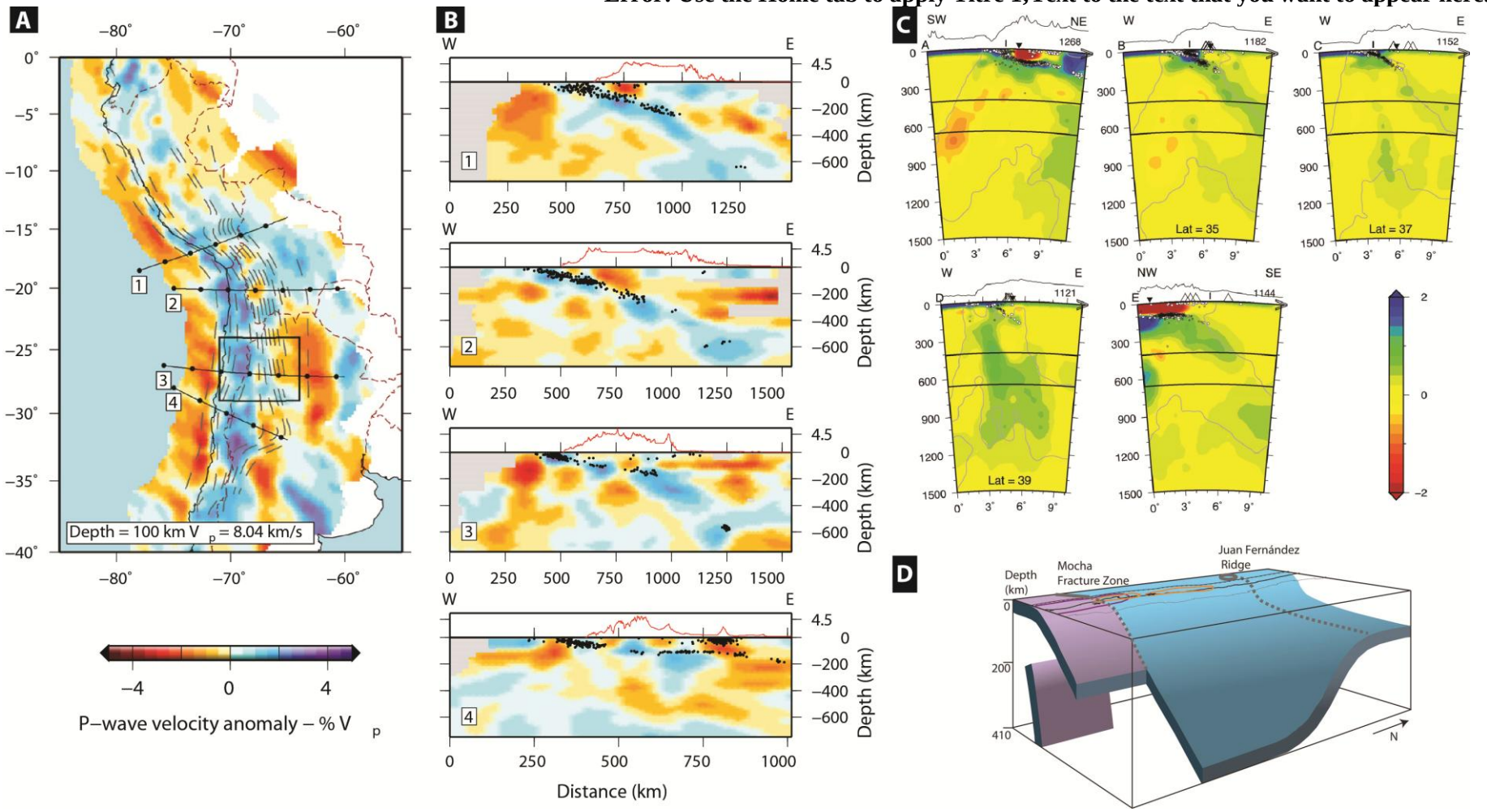


**Fig. 1.21**: *Teleseismic P-wave tomography images of northern, southern and central Chile: (A) from Bianchi et al. (2013), based on the ISC earthquake catalog (black circles). Horizontal cross-section at 100 km depth. The locations of the vertical profiles in (B) are shown, with markers (black dots) every 250 km in horizontal distance; and (C) from Pesicek et al. (2012), based on the global ak135 model (Kennett et al., 1995), based on relocated earthquake EHB locations (white circles) from local deployments (inverted black triangles); active volcanoes (empty triangles). The top left images is parallel to the Juan Fernandez ridge axis; the others represent the normal subduction in the Maule region. The bottom left image shows slab tearing and detachment at 200 km depth at 39°S, and the bottom right image shows slab bending at the transition from moderate to flat slab subduction to the north. (D) 3-D diagram illustrating the slab geometry. From Pesicek et al. (2012)*

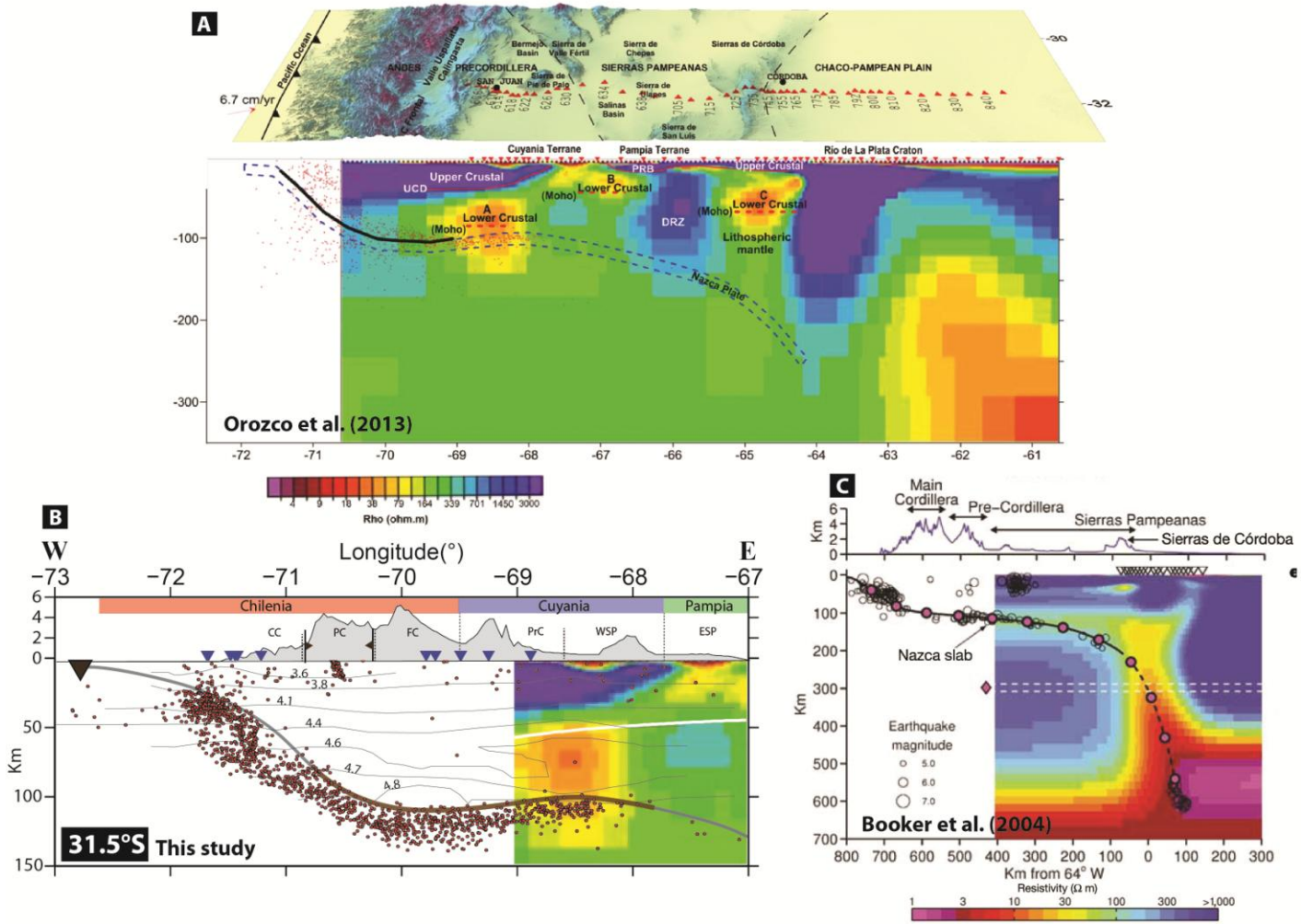


**Fig. 1.22**: Magnetotelluric profiles of the central Chilean flat subduction zone. (A) From Orozco et al. (2013). Topographic map, superimposed with the profile site of the experiment and terrane boundaries. UCD: upper crust discontinuity, A, B and C are conductors corresponding to the lower crust; DRZ: deep resistive zones (> 1000 Ω m). Earthquake hypocenters are from the CHARGE catalog. (B) Superposition of parts of A on our region. Contour lines represent the absolute Vs obtained in our, showing the strong correlation between the reduced Vs and the conductive zone. More detail in Chapter 3. (C)From Booker et al. (2004), showing the high mantle conductivity adjacent to re-subducting slab. Purple circles represent the 1 Myr isochrones since subduction. Inverted triangles are the position of the array

Chapter Two

# 2 Seismic Tomography, Thermo-Mechanical & Petrological Modeling: Approximating the Physical Properties of the Subduction Zone

## 2.1 Regional Travel-Time Seismic Tomography of First Wave Arrivals: Imaging the Internal Seismic Structure of the Central Chilean Subduction Region (29°-35°S)

### *2.1.1 Introduction to Seismic Tomography*

Tomography is a technique used in several science disciplines, such as medicine, biology and geophysics. Its etymology originates from the Greek expressions *tomos*, meaning segment, and *graphy*, meaning drawing. The basic principle of tomography is to deduce an object's internal physical properties which are not directly observable.

In seismic tomography, earthquake data contained on a seismogram (direct, reflected, refracted, surface and body waves) are used to recover the three-dimensional (3-D) seismic wave velocity distribution throughout the Earth. And, since seismic velocities are sensitive to properties of the medium (density, elasticity …), indirect information about the physical properties can be made, including the chemical and thermal compositions, texture, structure, interfaces, etc. With proper seismic ray coverage, a 3-D image of the Earth can be used for better understanding the links between the deep and shallow processes which influence the past and present dynamics of our planet (and extraterrestrial bodies), as well as predicting long-term trends.

The signal used in seismic tomography is either passive (natural) or active (controlled). Depending on the purpose of the study, it can be used (i) at various spatial scales (teleseismic, regional, local), (ii) for different datasets (waveform, refraction/reflection, first arrivals, white noise…), and (iii) with different algorithm techniques (double-difference, finite/infinite frequency…). It is typically solved as an inverse problem by minimizing the differences between observed and synthetic parameters as seismic wave travel times in our case.

Earthquakes can emanate seismic energies over a broad frequency spectrum. As these travel through the Earth, they become increasingly attenuated and lose their higher-frequency content. Therefore, the greater the distance travelled by the seismic wave, the poorer it becomes in high-frequencies. And because the seismic wavelength is more sensitive to structures of the same size or smaller, local and regional tomography studies have to use higher-frequency signals to solve for finer structures, opposed to teleseismic tomography.

However, tomographic problems are susceptible because of the errors in the data and the uneven geometrical distribution of sources and receivers, which result in many parts of the medium being sampled only by a few rays.

Finite-frequency tomography is popularly used for its capacity to integrate a greater volume of information contained in the seismogram, incorporating several wave arrivals, and proving to be, a posteriori, a more accurate estimate of the Earth than first wave arrival seismic tomography.

The pioneer and still principle use of seismic tomography is to invert for travel-time residuals to recover small velocity perturbations along the ray trajectory linking the source to the receiver. The time residuals are mostly due to lateral heterogeneities, which the reference 1-D velocity model does not account for. We therefore calculate travel-time residuals for each set of datum and perform 3-D inversion to recover velocity perturbations relative to the reference model. In our study, this is done, by using the inversion code TLR3 (Latorre et al., 2004; Monteiller et al., 2005) to invert for P- and S-wave travel-times residuals.

### *2.1.2 The Tomography Inverse Problem*

In general problems, the observable data ***d*** are a function of the physical properties of the model ***m***:

$$\boldsymbol{d} = A\boldsymbol{m} \quad (1)$$

e.g.

$$\begin{bmatrix} d_1 \\ d_2 \\ . \\ . \\ . \\ d_n \end{bmatrix} = \begin{bmatrix} A_{11} & \cdots & A_{1p} \\ \vdots & \ddots & \vdots \\ A_{n1} & \cdots & A_{np} \end{bmatrix} . \begin{bmatrix} m_1 \\ m_2 \\ . \\ . \\ m_p \end{bmatrix} \quad (2)$$

where $A$ is a $n \times p$ matrix, of physical property terms. When the model parameters are known and the resulting data are calculated, then it is a *forward problem*. Conversely, if one wishes to determine the unknown model parameters from measured data, then it is an *inverse problem*.

#### *2.1.2.1 The forward problem: Determining ray trajectories*

Solving the forward problem is the first step, where one must determine the travel-time of a seismic wave from a point source a to a receiver b. However, it might be computationally costly and complicated when used in a heterogeneous 3-D medium, and one must take into account its limitations that include the occurrence of areas of shadow and the requirement for a smooth medium as initial starting model.

Rays are traced by solving the Eikonal equation which is a basic mathematical model that describes the travel-time propagation of a wave front through a velocity field.

$$(\nabla\tau)^2 = n^2(x, y, z)$$

where $\tau(x, y, z)$ is the travel-time (eikonal) from the source to the point $x$, $y$, and $z$; and $n$ is the slowness (see next section) at that point. It is recognized as a fast and efficient way of computing travel-times (Podvin and Lecomte, 1991).

#### *2.1.2.2 The Inverse Problem and its Linearization*

The principal argument of travel-time tomography is that residual times contain important information on the velocity perturbation characterizing a medium. Most strategies used to linearize such problems are based on the Taylor series expansion (Roecker, 1982; Lay and Wallace, 1995) and on only small perturbations δm around a reference a priori model m0. Following equation (1), one can write:

$$\boldsymbol{m} = \boldsymbol{m}_0 + \delta\boldsymbol{m} \quad (3)$$

Therefore,

$$\boldsymbol{d} = A(\boldsymbol{m_0} + \delta\boldsymbol{m}) = A\boldsymbol{m_0} + \nabla A\delta\boldsymbol{m} + \cdots \quad (4)$$

where the derivative matrix $G$

$$\nabla A = \left[\frac{\partial A}{\partial m_1}, \frac{\partial A}{\partial m_2}, \ldots, \frac{\partial A}{\partial m_p}\right]^T = G$$

Assuming small variations $\delta \boldsymbol{m}$, equation (4) is then expressed by, at first order:

$$\delta \boldsymbol{d} = G\delta \boldsymbol{m} \text{ (5)}$$

where $A\boldsymbol{m_0} = \boldsymbol{d_{calc}}$ and $\delta \boldsymbol{d}$ is the difference between the observed data $\boldsymbol{d}$ and the expected $\boldsymbol{d_{calc}}$ calculated for a source *a* and a receiver *b* within a reference model $\boldsymbol{m_0}$. Therefore, assuming the velocity field *V* described in $\boldsymbol{m}$ is based on the travel-time integral, equation (5) becomes equivalent to:

$$\delta T_{a,b} = -\int_a^b \frac{1}{V_0}\frac{\delta V}{V_0} dL \text{ (6)}$$

where $\delta \boldsymbol{d} = \delta T_{a,b}$ and is the travel-time residual $T_{obs} - T_{calc}$ between source *a* and receiver *b*, induced by a velocity perturbation $\delta V$ relative to a reference velocity model $V_0$. And *dL* is a fractional length of the ray-path joining the source *a* and the receiver *b*. Considering the slowness $S = \frac{1}{V}$, equation (6) is written:

$$\delta T_{a,b} = \int_a^b \delta S dL \text{ (7)}$$

This equation is linear and is commonly used in tomography of first arrival time residuals. To adapt this problem numerically, the predicted travel-times $T_{calc}$ are computed as a line integral along the total ray-length *L* for each ray trajectory between source *a* and receiver *b* (Fig. 2.1.1).

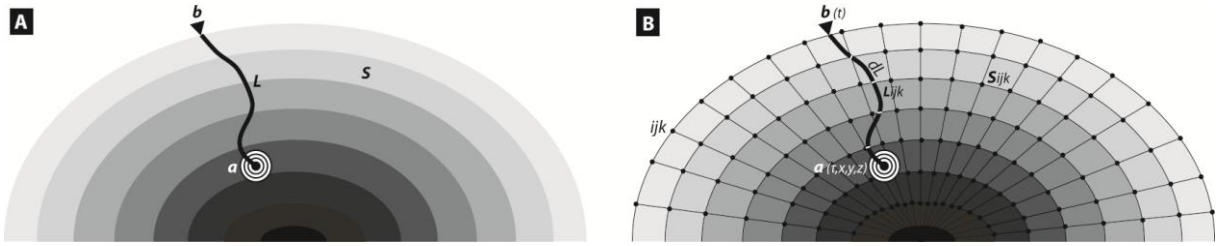


**Fig. 2.1.1**: *(A) Schematic of the tomography problem, and how it is tackled numerically (B). a is the source, b the receiver, L the ray-length path, S the slowness field ($\frac{1}{V}$) sub-divided into nodes ijk, and dL is the fractional ray-length.*

In seismic experiments, the dataset and consequent ray trajectories can be large, resulting in a great number of equations. Hence, travel-time equation (8) is transcribed to matrix and vector formats using basic linear algebra:

$$\Delta T_{(n)} = L_{(n\times p)}\Delta S_{(p)} \text{ (8)}$$

where *n* is the number of rays, *p* is the number of nodes the rays transect, $\Delta T$ is the vector of travel-time residuals (with as many rows as there are rays), *L* is the matrix of ray distances (with a row for

each ray and a column for every node), $\Delta S$ is the vector of slowness residual (with as many columns as there are cells).

Although, $T_{obs}$ is accurately determined from the experiment, $L_{calc}$ is just an approximation funded on assumed $S_{calc}$from ray modeling, and this leaves too many unknowns to clarify. This can be partly remedied by assuming that $L_{calc}$ is close enough to reality, and thus, $L_{calc} = L_{real}$.

### *2.1.3 Model Regularization*

In reality, the inversion problem is often 'mixed-determined' (both under- and over-determined) due to uneven source and receiver distributions in the model (at least for passive seismic experiments), contributing to cells/nodes being crossed several times by rays and others not at all. Even the highest quality and largest possible dataset will result in uneven sampling of the volume. In under-determined problems, as are most seismic tomography problems, there is not enough information to resolve all the unknowns. To overcome this limitation, it is possible to add a priori information on the model solution, however, may be unsatisfactory. Therefore, the problem (equation 8) needs to be regularized in the L2-norm (also called Eucledian norm) by minimizing the penalty function $P(\Delta S)$ using least-square methods:

$$P(\Delta S) = \|L\Delta S - \Delta T\|^2 + \lambda^2\|\Delta S\|^2 \quad (9)$$

where $\lambda^2$ is the damping parameter. The statistical distribution of real data being usually skewed, it is crucial to select only high quality data with few or no outliers, so that outlying residuals are restricted and influence less on the model solution.

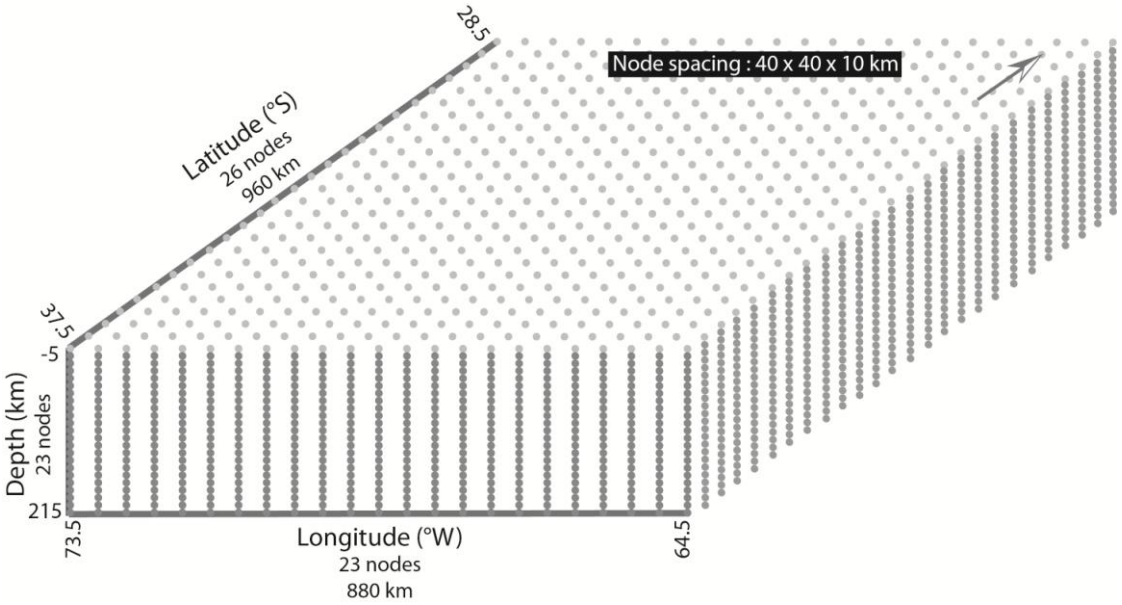


**Fig. 2.1.2:** *Our gridded model domain used in our inversion algorithm TLR3.*

#### *2.1.3.1 Damped Least Squares Solution*

The aim is to find a solution that minimizes the linear combination (9) whereby the latter terms are multiplied by a damped/smoothed least-square factor, which ease convergence towards a "reasonable" least-square solution. They act as an adjuster to the influence in magnitudes on different parts of the model, particularly when two adjacent cells have radically difference ray sampling qualities. However, this also has the effect of under-estimating the actual slowness values. Since a large and sparse linear system of equations needs to be inverted at each iteration step, the regularization scheme needs to be implemented to the problem before inversion, which consists in pre-conditioning the model parameters. Equation (8) becomes:

$$\Delta TP = L \times \Delta S' KWP \quad (10)$$

where $\Delta S = \Delta S' KW$ (Woodward et al. 2008). P is a row-weighting diagonal matrix, which permits the significance of different segments of the data to vary; KW is a preconditioning term describing the shape of this update, with K being the smoothing parameters implemented as a 3-D convolution with specific wavelengths (x, y, z), and W is a column-weighting diagonal matrix acting via the damping function as an adjuster to the influence in magnitudes on different parts of the model, particularly when two adjacent cells have radically difference ray sampling qualities.

The best damping values is the one that produces the smoothes the slowness model with the best data fit. Finding the appropriate damping factor for a data set is a pre-requisite to obtain high quality and highly reliable tomographic images (Kissling and Haslinger, 2001). However, there is no straightforward method to define it and is normally evaluated by trial and error.

One way of estimating the best $\Delta S$ which minimizes equation (9) and takes into account equation (10), is to apply an iterative scheme, whereby $S_{real}$ ($\Delta S = S_{real} - S_{calc}$) of the previous iteration is used as the new reference model $S_{calc}$ for the next iteration. During the tomography inversion, $S_{calc}$ of the first iteration is best to be taken as the reference or initial model to obtain faster solution convergence in the estimation of $S_{real}$ within acceptable error range. This continues until little, or no, variations are observed between $S_{calc}$ and $S_{real}$, which is the most accurate estimation possible of $S_{real}$.

### *2.1.4 TLR3 Algorithm*

The *TLR3* algorithm was developed by Montellier and co-authors (Monteiller et al., 2005) and used by Latorre et al. (2004) to perform local imaging of the Corinth Golf in Greece using passive seismicity. It stands for "Tomography, Localization, Relocalisation", and is in its third version. Besides the inversion algorithm and its programs written in Fortran 77, the package also includes the possibility to independently convert various data formats to input format style for the code, and construct 1-D into 3-D cellular models.

It is split into two principle steps: (1) solving the forward problem, which tackles the 3-D ray-tracing by ray theory using finite-difference resolution of the Eikonal equation (Podvin and Lecomte, 1991) through a fine gridded velocity model; followed by (2) solving the inverse problem, whereby synthetic travel-times and travel-time residuals inversion are computed through a coarser gridded model using the *LSQR* algorithm (Paige and Sanders, 1982). These two steps, combined with a systematic hypocenter re-evaluation, are repeated iteratively until the minimum residual time is reached. At the first iteration, starting (reference) P- and S-wave velocity models are used and for each iteration and for both P- and S-waves self-consistently, the results of the previous iteration are used as the new reference models of the next iteration. The number of iterations necessary to achieve solution

stability depends on the quantity and quality of the data. The choice of iteration number at which the final model solution is picked is a semi-subjective decision, however, does not vary much between two neighboring solutions. The acceptable final error is given by the final RMS, a normalized root mean square of residual times (= $\sqrt{\Sigma R_i^2/N}$ where *Ri* is the time residual at the ith station), as soon as it falls below a certain threshold.

Once a final model is obtained, we evaluate statistically the final model's significance using the checkerboard and spike resolution tests. The TLR3 algorithm was chosen for its relative simplicity, computational rapidity and sufficient accuracy.

In this study, the data d are the observed arrival times $T_{obs}$ for P- and S-waves at each receiver which depend on the velocity field the rays travel through, and the source location. $T_{obs}$ is the sum of (i) the time Tp taken for a ray to travel from its source to receiver, (ii) the origin time T0, (iii) station-time errors es (due to station elevation, station-clock errors,…) and (iv) time picking errors em:

$$T_{obs} = T_0 + T_p + e_s + e_m \quad (11)$$

Usually, because the data errors $e_s$ and $e_m$ are difficult to estimate and supposed uncorrelated, they are not taken into account in the inversion. However, they introduce "noise" to $T_{obs}$.

### *2.1.5 Model Boundaries and Discretization*

The inversion process is segmented into a set of iterations, for which hypocenters and the velocity field are jointly updated to adapt better the fit between the calculated data and the observables. This results in progressive hypocenter migration during the inversion process. Therefore, the boundaries of the volume inverted for must be constructed large enough to accommodate the source displacements (in our case, we limited horizontal and vertical displacements to 500 m and 700 m, respectively) without exiting the numerical domain and producing numerical errors and instabilities. Our model domain is adapted to be 0.5° larger in latitude and longitude, and 15 km deeper, relative to the source and station domain, representing a total volume of 960 x 880 x 220 $km^3$ (Fig. 2.1.2). Spherical coordinates are converted to Cartesian coordinates in this study.

The travel-time of seismic waves is a continuous function of distance. Therefore, they are made suitable for numerical evaluations and implementations on digital computers by discretizing the domain and transforming the governing equations. The common approach is to divide the domain into a gridded model with constant model parameters in each cell or node. The finer the grid, the higher the spatial resolution and the more accurate travel-time approximation can be. However, the numerical calculation and memory storage might be very costly. This can be done (without loss in precision for travel-time) by computing (1) ray paths in a very fine and regular gridded model (Fig. 2.1.3A), necessary for calculating accurately and in a numerically stable fashion, the ray trajectories and (2) travel-times in a coarse enough gridded model (Fig. 2.1.2 and Fig. 2.1.3A), because computation of the arrival times are relatively independent of the discretization through which the rays are traced, even though a second-order dependency subsists due to the ray trajectory determination. Hence, the forward model parametrization for ray trajectory calculation is different from that used to compute travel-time residuals. Also, smoothness and continuity of the spatial velocity (slowness) derivatives $\nabla S$ are important (Kissling and Haslinger, 2001). Velocity (slowness) derivatives are interpolated tri-linearly between each node of the model. Node spacing depends on the "illumination qualities" of the data, portrayed by the ray density coverage, shown in

.

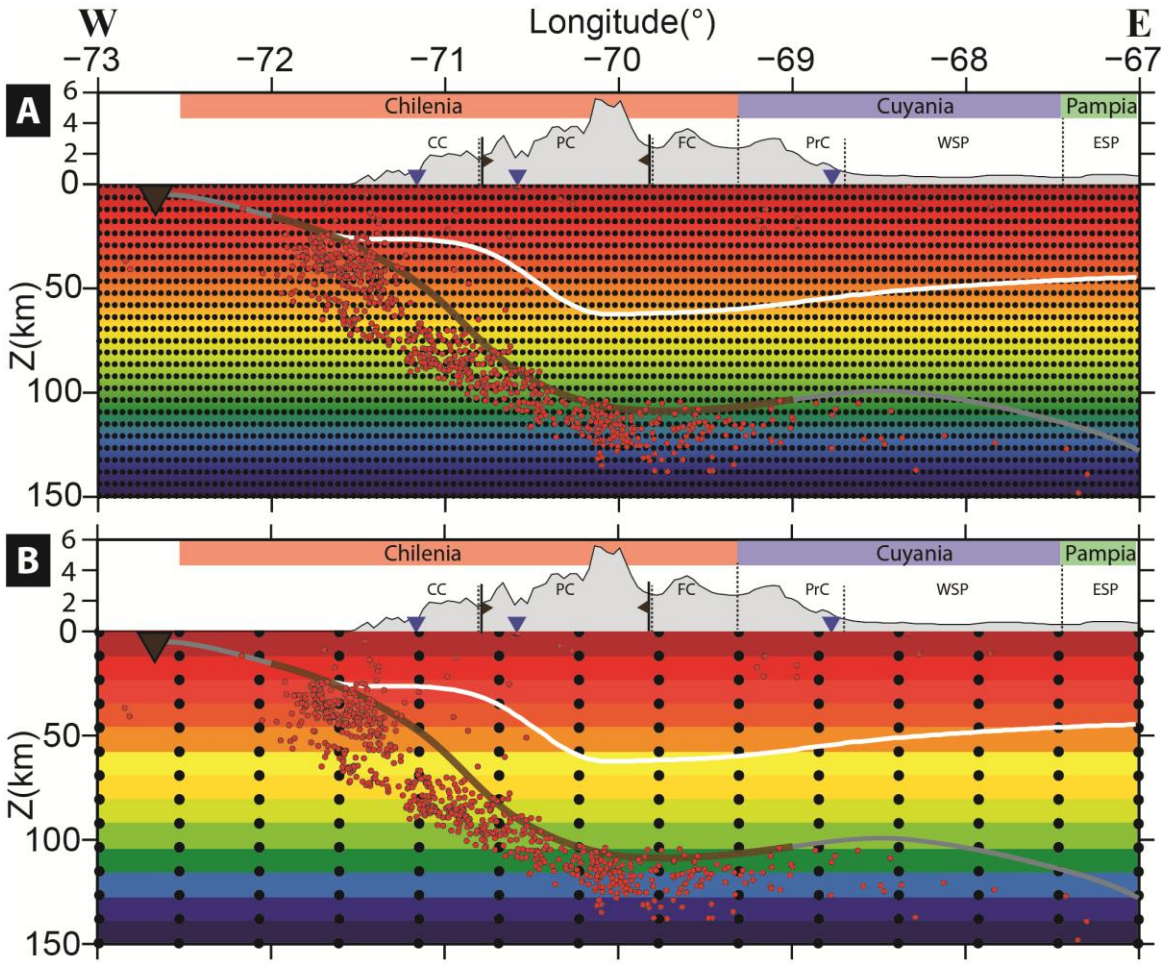


**Fig. 2.1.3:** *Schematic of the (A) fine grid model used to calculate ray trajectories, and (B) coarser grid model used to compute the expected travel-times along the pre-defined ray trajectories.*

### *2.1.6 Our 1-D Reference Model*

An average 1-D reference model is imposed at the start of the inversion process, and the final 3-D velocity model is in fact dependent on it, so it is primordial to determine it with a best data fit. Our best average reference model is comprised of 17 velocity layers and an average Vp/Vs value of 1.76 (Fig. 2.1.4). It was constructed on the basic assumption that density and wave velocities increase with depth, and is represented by a simple layer arrangement of constant thicknesses and velocities which increase with depth. It was determined using the *VELEST* algorithm, developed by Kissling et al. (1994), with only chosen most reliable hypocenters and arrival times, and was complemented with mine blast travel-times (Barrientos et al., 2004) to improve model accuracy for the first 15 km of depth. Comparing it with the global 1-D reference model IASEP-91, which is regularly used by other studies in this region, we note that our model is faster, probably due to regional effects of the low geotherm (see Chapter 3).

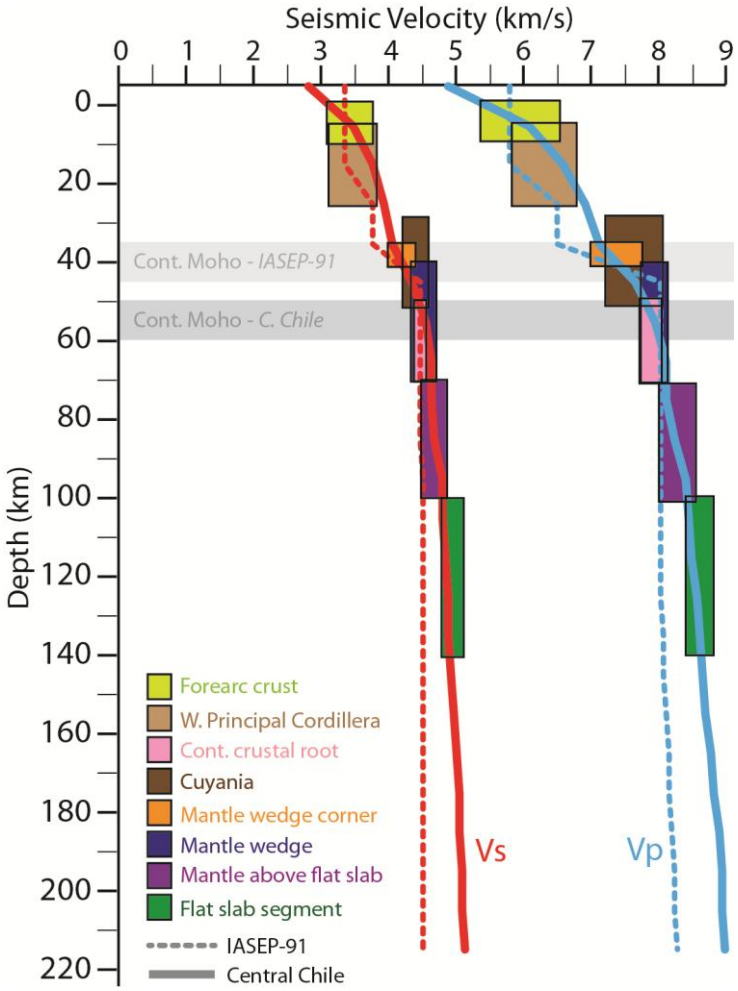


**Fig. 2.1.4:** *1-D velocity models determined for the region of Central Chile (solid lines) and for the global Earth model IASEP-91 (dotted line). We also show that the range of seismic velocities, obtained by our 3-D inversion, for most regions.*

### *2.1.7 Our Seismic Catalog*

In the terms of a collaboration between the French laboratory GéoAzur (Valbonne) and the Geophysical Department of the University of Chile (Santiago), three temporary seismic networks (OVA99, CHARSME and CHASE) were installed in Central Chile and Western Argentina from November 1999 to March 2006, and in the meantime, the American seismic project CHARGE (Anderson et al., 2004; Wagner et al., 2005) was emplaced from Dec. 2000 to Nov. 2002 (Fig. 2.1.5). Because the CHARGE database was initially located in the IASEP-91 velocity model (Fig. 2.1.4), depth discrepancies of -20 km relative to the rest of the data, existed (Fig. 2.1.6A). In order to make compatible all datasets, we consistently relocated all sources in our 1-D velocity model (Fig. 2.1.6B), with the earthquake location program *HYPOINVERSE* (Klein, 2000) of the earthquake analysis package *SEISAN*.

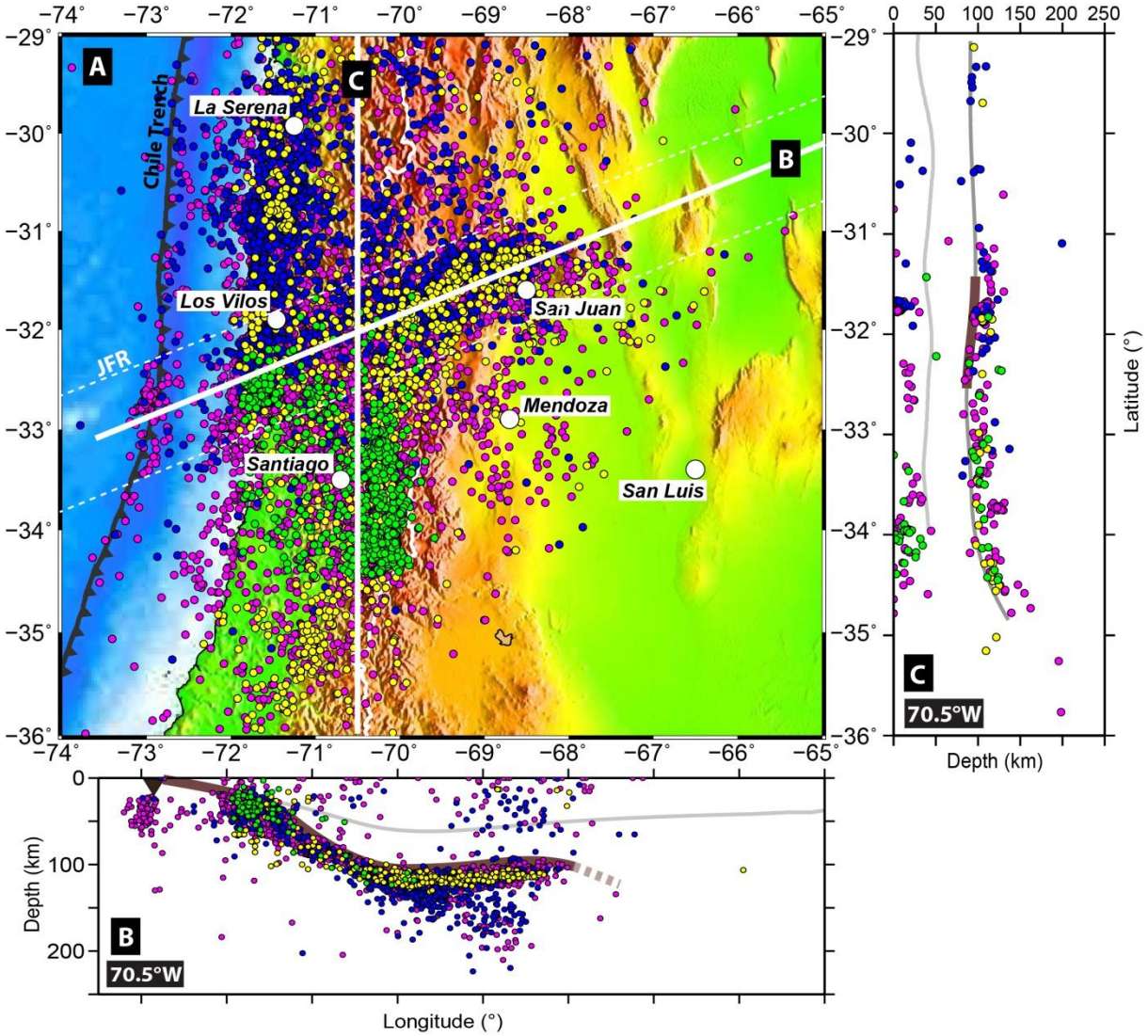


**Fig. 2.1.5:** *(A) Earthquake distribution in plan view of our seismic catalog, compiled from the temporary networks of OVA99, CHARSME, CHARGE and CHASE (blue, pink, yellow and green circles, respectively), and of the permanent Chilean database. The seismic station distribution is shown in Fig. 3.2. The subducting Juan Fernandez ridge (JFR) track (Yáñez et al., 2002) is shown with a supposed width of ~ 100 km based on offshore measurements by Kopp et al. (2004) (dotted box limits). Solid lines show the location of the E-W and N-S vertical profiles parallel to (B) the subducting ridge track and (C) to the slab strike. The continental Moho (light grey line) is determined from gravity data by Tassara et al. (2005) and the slab surface (dark grey line) is inferred from the earthquake distribution. Where the JFR is expected at depth is shown in the thick dark brown line.*

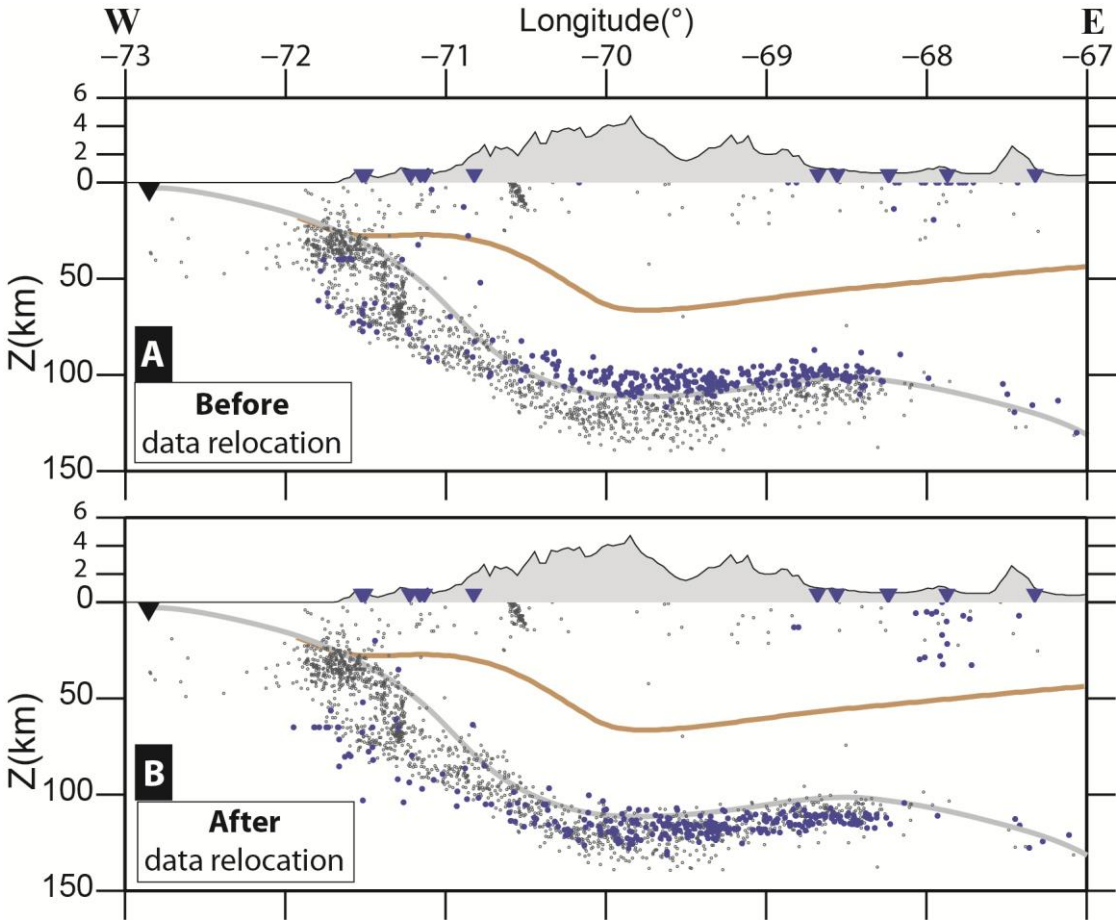


**Fig. 2.1.6:** *Earthquake distribution for the CHARGE database (blue circles), relative to the rest of the earthquake database, (A) before and (B) after relocation in our 1-D velocity model calculated for the region. A resulting depth difference of +20 km is observed, in agreement that our 1-D model is faster. Seismic station distribution and trench position are shown by the inverted blue and black triangles, respectively. Included are the continental Moho (brown line) and oceanic slab interface (grey line).*

### *2.1.8 Our Quality Selection Criteria for our Tomography Inversion*

In order to limit outliers and render a faster convergence and stability of solution, we selected only the highest quality events with the following selection criteria (Fig. 2.1.7): (a) maximum picking error of ± 0.25 s and ± 0.4 s, (b) maximum pick quality index 2 and 3 (0 being excellent, 4 being discarded), (c) maximum hypocenter uncertainty of 5 km in all directions, (d) maximum RMS misfit ($\sqrt{\Sigma R_i^2}/N$ where *Ri* is the time residual at the i$^{th}$ station) < 0.6 s, and (e) minimum 8 and 4 station observations, for P- and S-waves, respectively. We retain a total of 3 603 events for the inversion process, including 52,011 and 51,631 P- and S-wave arrival times, respectively.

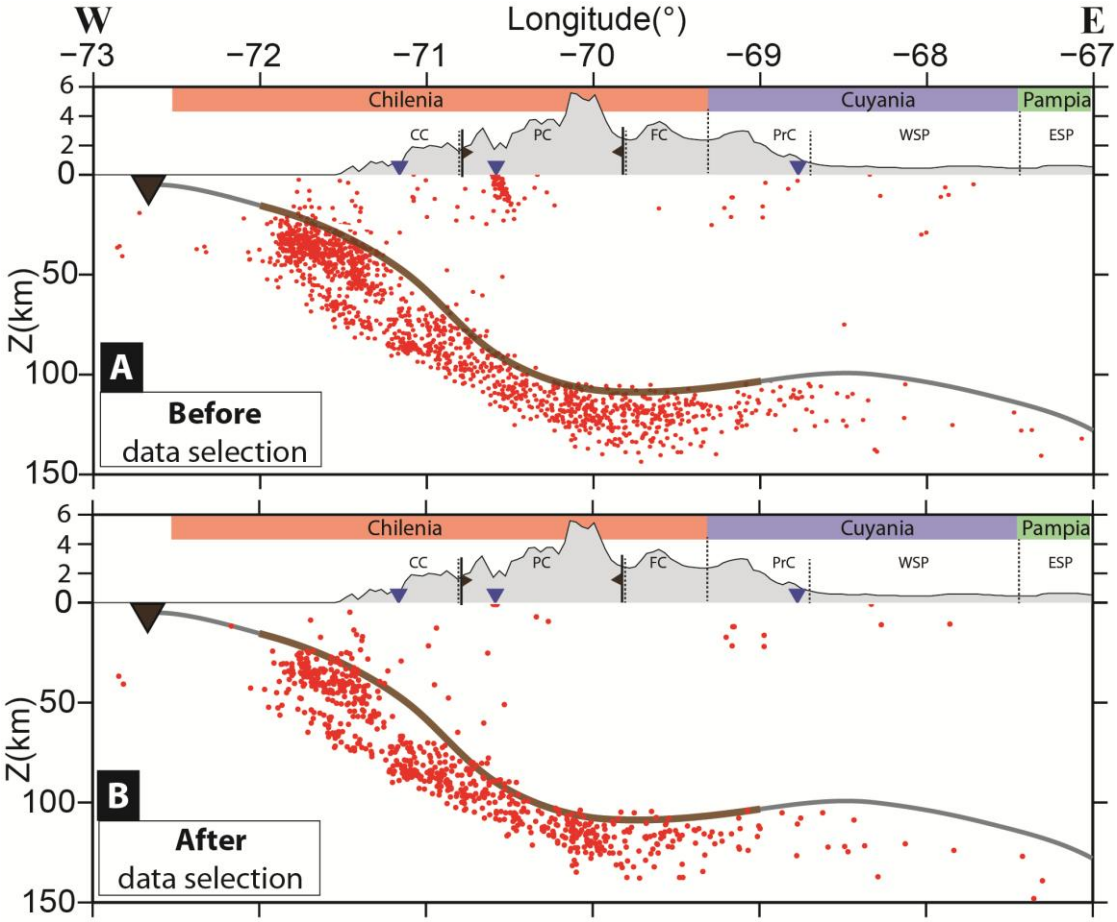


**Fig. 2.1.7:** *A comparison of the earthquake distribution along a vertical E-W profile at 32°S (A) before and (B) after event selection. Events used for the tomography inversion shown in (B).*

### *2.1.9 Our Damping Parameter*

The damping parameters are usually determined on the basis of a trade-off curve between the data variance and model variance, called the L-curve. Actually, this trade-off curve is a simplification, since under-determination strongly depends on the ray sampling of individual cells and, hence, on model parametrization. For the *TLR3* code, we find suitable damping values between 0.5 and 1 (chosen to be 0.7) that produce solution convergence with a minimum misfit error of ~ 0.2-0.3 s (Fig. 2.1.8C).

### *2.1.10 Assigning Quality Coefficients to our Data*

Quality weighting coefficients are assigned to the picking times of the observed P- (Cp) and S-waves (Cs) to give more importance to the most reliable data used and assure higher robustness of our final solution. We tested the influence on the final model solution when varying the Cp/Cs ratio. Likewise to the method used to determine the best damping value for the dataset, we fixed the damping value at 0.7 and tested for the best Cp/Cs ratio that minimizes the RMS misfit and converges rapidly to a stable solution (Fig. 2.1.8B). We tested for three combinations: (i) Cp/Cs = 0.5 (Cp:1, Cs:2), (ii) Cp/Cs = 2 (Cp: 2, Cs: 1), and (iii) Cp/Cs = 1 (Cp: 2, Cs: 2). Because the differences in the RMS misfit decay and solution convergence are negligible, we visually assessed the results for P-waves at their maximum velocity variations, at equivalent iteration number. Whereas, the location and

geometry of the velocity anomalies are similar regardless of the Cp/Cs ratio, the amplitudes vary in accordance to the relative importance assigned to P-arrival times, in this case. And since P-arrivals are usually picked with a higher precision than S-arrivals, we estimate appropriate to assign twice more significance to S-arrivals than P-arrivals, and hence, Cp/Cs = 0.5 is retained (Fig. 2.1.9A).

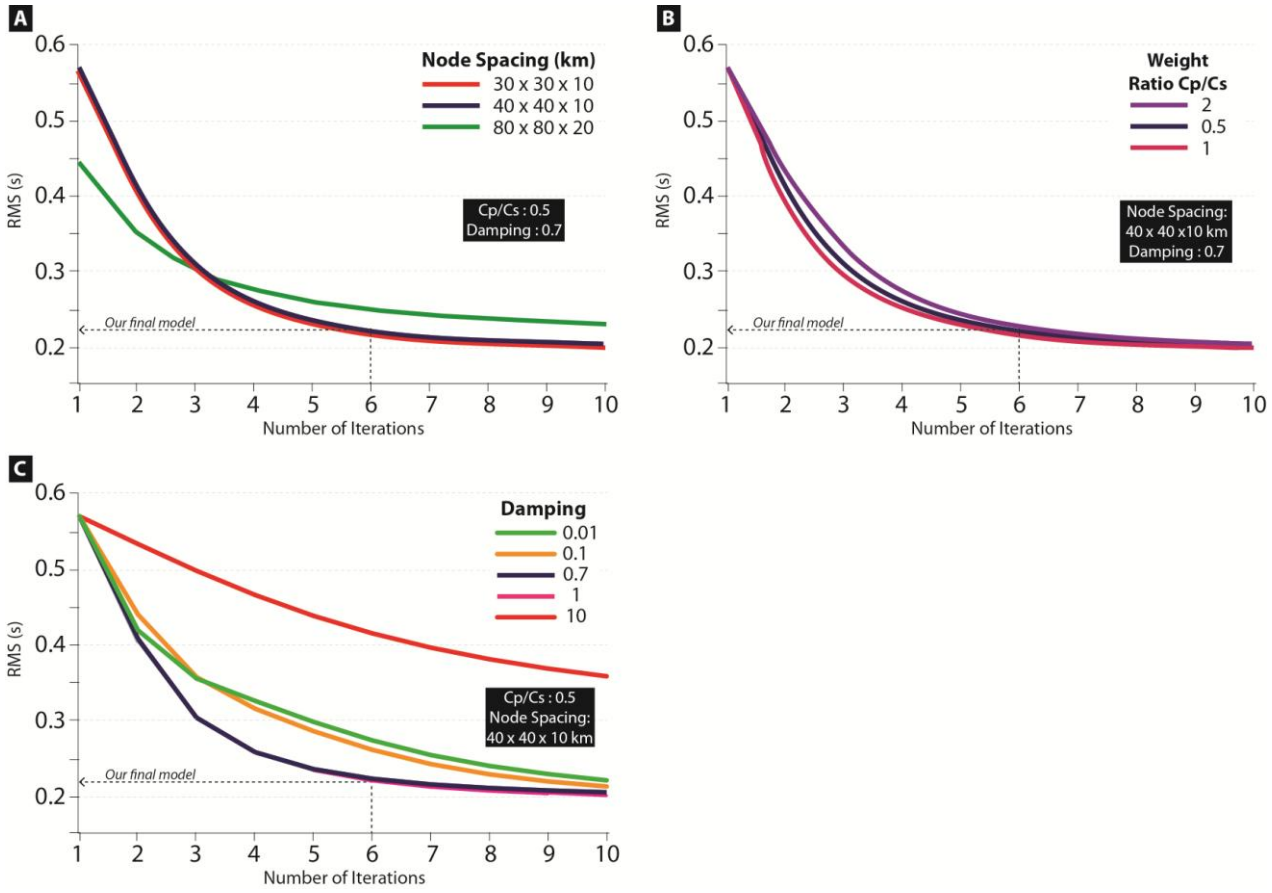


**Fig. 2.1.8:** *Determining the node spacing, iteration number, damping and Cp/Cs values for our final model solution, as a function of the minimum RMS misfit (normalized root mean square of residual times). The retained values are a node spacing of 40 x 40 x 10 km, a chosen iteration number of 6, a damping of 0.7, and a Cp/Cs of 0.5.*

### *2.1.11 Quality Assessment of the Final Solution Model*

Sketching out the well resolved areas of the tomography inversion is likely the most important task of assessing the resolution quality regarding result interpretation. Multiple techniques are available to *a posteriori* assess the quality of the solution: (1) ray density, which indicate the illumination properties of the data (Kissling and Haslinger, 2001), and (2) sensitivity tests, such as harmonic or spike checkerboard tests, which examine the restoration of amplitude, shape and extent of the velocity perturbations in the well resolved regions. All resolution estimates are assessed with synthetic data, using a characteristic 3-D model (Kissling and Haslinger, 2001). However, they only provide information about the solution quality, not the effectiveness of the model parametrization.

Artifacts can be produced in sensitivity tests due to the combination of model parametrization and ray-path deformations, and which are commonly observed as boundary effects and leakage issues, e.g. in regions of only mild or poor resolution, strict usage of ray theory may induce structure deformation. The spike test is applied to quantify these ray deformations for an initial velocity perturbation of controlled amplitude, emplacement and shape. Nonetheless, artifacts are difficultly distinguished *a posteriori* from real structures and attempts to eliminate them from tomography images involve smoothing and/or fancy filtering techniques (Kissling and Haslinger, 2001).

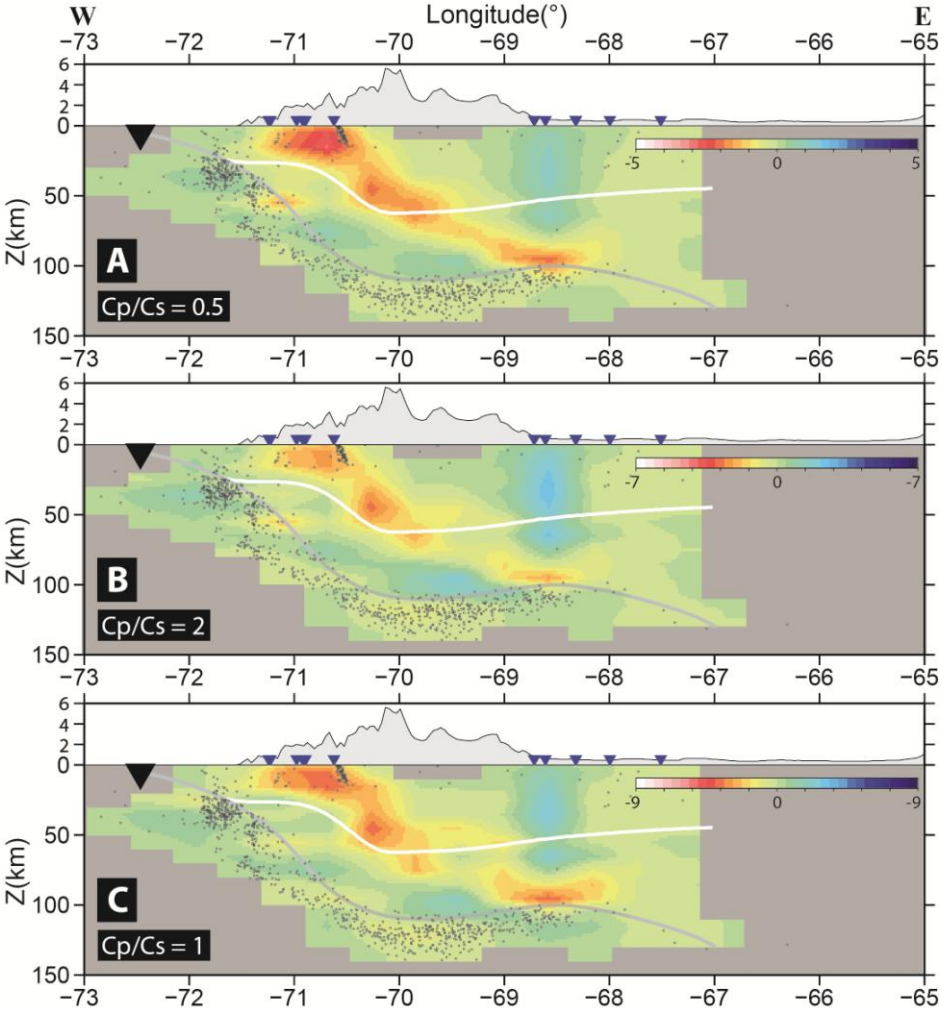


**Fig. 2.1.9***: Comparing different Cp/Cs values for Vp variations and an E-W cross-section through 31.5°S. (A) Cp is 1 and Cs is 2, (B) Cp is 2 and Cs is 1, and (C) Cp is 2 and Cs is 2. Note the variations in perturbation amplitude.*

**Fig. 2.1.10** : *Ray density for P- and S-waves, along horizontal cross-sections.*

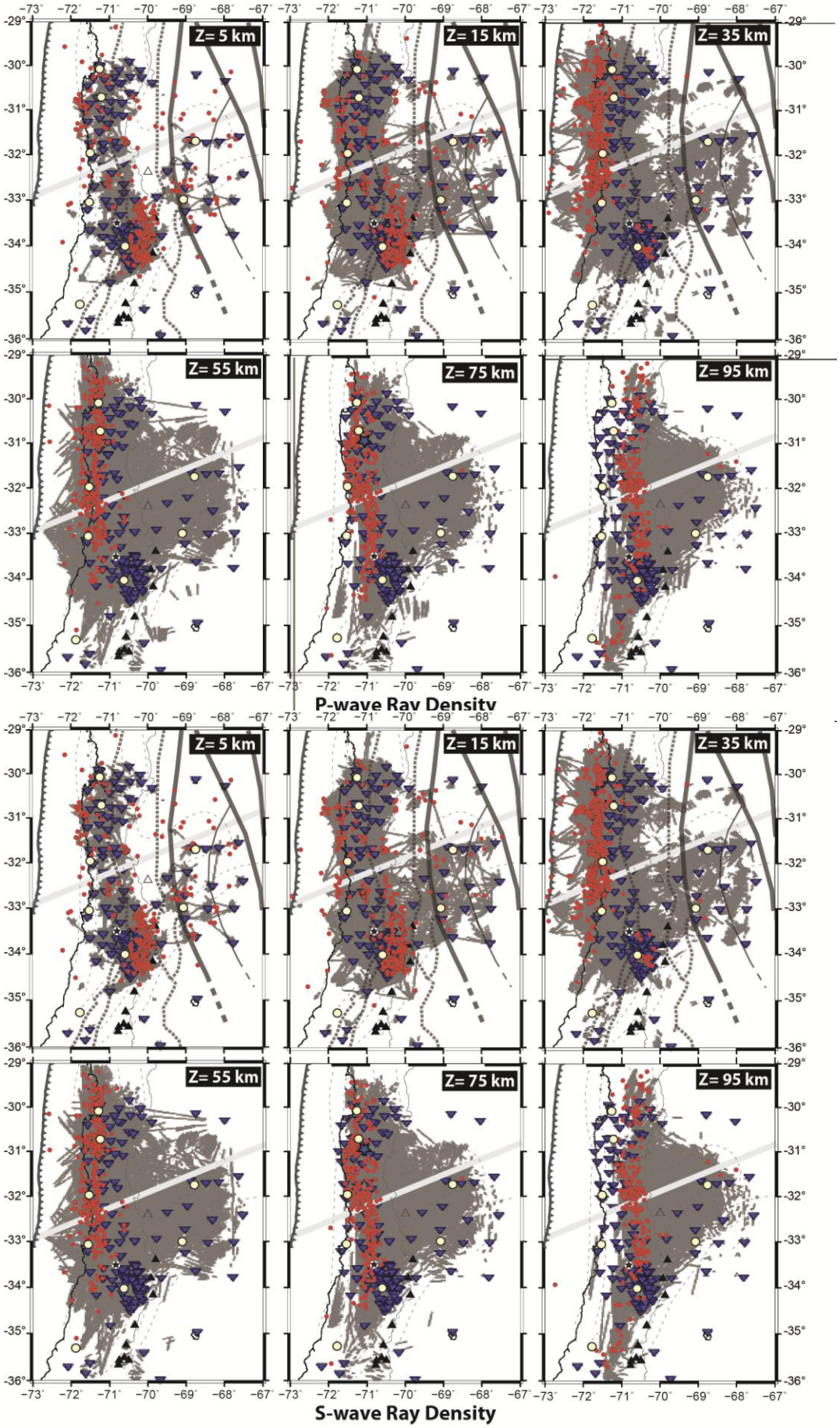
Z= 5 km
Z= 15 km
Z= 35 km
Z= 55 km
Z= 75 km
Z= 95 km
P-wave Ray Density
Z= 5 km
Z= 15 km
Z= 35 km
Z= 55 km
Z= 75 km
Z= 95 km
S-wave Ray Density

We used the checkerboard test to examine the spatial resolution of the data, based on ray coverage, testing for different node spacing for the coarser inversion grid. We tested for 80 x 80 x 20 km, 40 x 40 x 10 km and 30 x 30 x 10 km, the latter two bringing the best resolution of solution (Fig. 2.1.8A). Our preference is for a model where we can appreciate both the region's general trends as well as its fine structures. Hence, we chose to divide the inversion model into cells of 40 x 40 x 10 km, because 80 x 80 x 20 km is too coarse and 30 x 30 x 10 km is too detailed and complex. With an inversion model of node spacing 40 x 40 x 10 km and four grid nodes established at each corner of a cell, the number of nodes is 23 x 26 x 23 nodes (Fig. 2.1.2).

Our checkerboard test results show us that the overriding plate domain above the flat and normal slabs are well resolved, with a good recovery of both the amplitudes and geometry of the initial velocity perturbation (Fig. 2.1.11), indicating that the node spacing of 40 x 40 x 10 km for the inversion of our seismic data is a good choice (and can be further thinned to smaller scale, but will also increase the model complexity). Also, parts of the upper oceanic lithosphere, near to the dense seismogenic areas (~ 20-30 km inside the slab), are well recovered, including the flat slab segment (Fig. 2.1.11B). However, it also reveals a less well resolved backarc region, relative to areas closer to the convergence zone and to the highest seismic activity. The backarc region above the flat slab is not as reliable (Fig. 2.1.11A and C), and will be interpreted with caution. On the other hand, the backarc region above the normally-dipping slab is very poorly resolved, and will be disregarded in the discussion and interpretation of our results. Further checkerboard test results are shown in Appendix A.

We then constructed a "spike" test model for our final model solution, upon which we emplaced several seismic velocity perturbations (± 500 m/s), with the sign of the perturbation, location and geometry approximately representing the observed trends in our final velocity model (Fig. 2.1.12). These regions include (1) the seismically fast forearc crust, (2) the slow velocity Principal Cordillera, (3) the slow velocity Andean crustal root, (4) the seismically fast Punitaqui aftershock region, (5) the seismically fast Cuyania crust, and (6) the slow velocity anomaly above the flat slab. Further details about these regions are given in Chapter 3. Our spike test shows us that the regions closest to the subduction front, and where ray density is highest, are well resolved, with practically no distortion in the velocity structures. However, the backarc region, within the Cuyania terrane, is less well constrained and results in some horizontal smearing of the velocity structures and diminished amplitudes. Our spike test results for the rest of the region are shown in Appendix A.

**Fig. 2.1.11:** *The "Checkerboard" test results for our final velocity models of P- and S-waves in (A) plan view at 5, 35 and 95 km depths, (B) E-W vertical cross-section along 31.5°S (flat slab) and (C) N-S vertical cross-section along 71°W. The rest of the checkerboard tests at different depths, latitudes and longitudes are shown in Appendix A. The initial synthetic velocities perturbations for P- and S-waves are 500 and 300 m/s, respectively, and are shown on the left or in the upper panel of each representation. The horizontal and vertical node spacing distances are chosen to be 40 and 10 km, respectively. Grey shaded cells reflect areas of poor ray density, determined by fixing a certain threshold value for the total ray-length crossed in each cell. Also shown are the topography and geological and tectonic terrane boundaries, the location of the active volcanoes (red triangles) and of the seismic stations used in this study (inverted blue triangles), the inferred slab interface based on our relocated seismicity (dark gray line) and the expected location of the subducting Juan Fernandez Ridge material (thick brow line segment), the continental Moho calculated from gravity studies by Tassara et al. (2006), and the position of the 1997 Punitaqui event (blue star).*

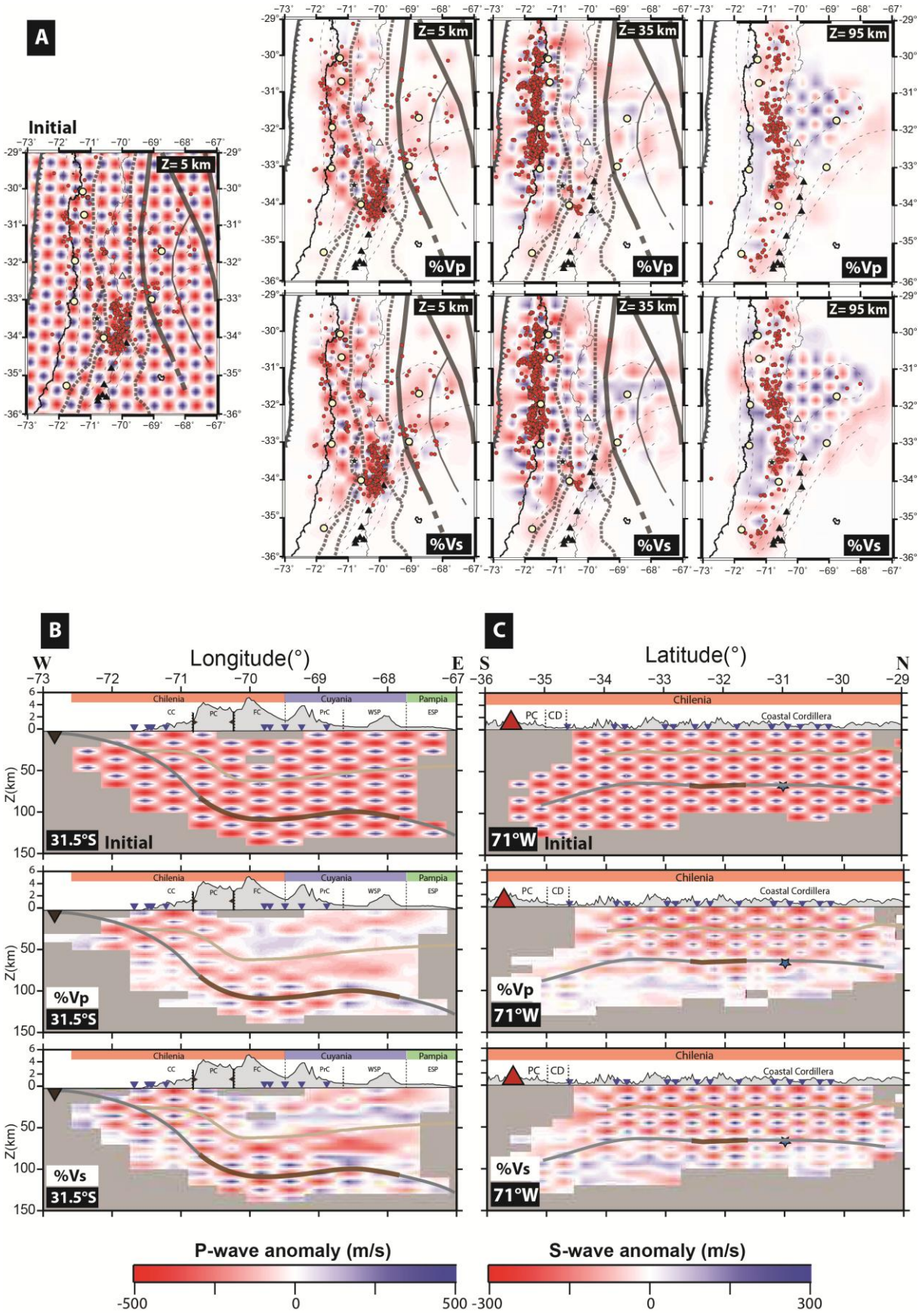
A
Initial
Z= 5 km
Z= 35 km
Z= 95 km
%Vp
%Vs
B
C
Longitude(°)
Latitude(°)
W
E
S
N
Chilenia
Cuyania
Pampia
Coastal Cordillera
Z(km)
31.5°S Initial
71°W Initial
%Vp 31.5°S
%Vs 31.5°S
%Vp 71°W
%Vs 71°W
P-wave anomaly (m/s)
S-wave anomaly (m/s)
-500
0
500
-300
300

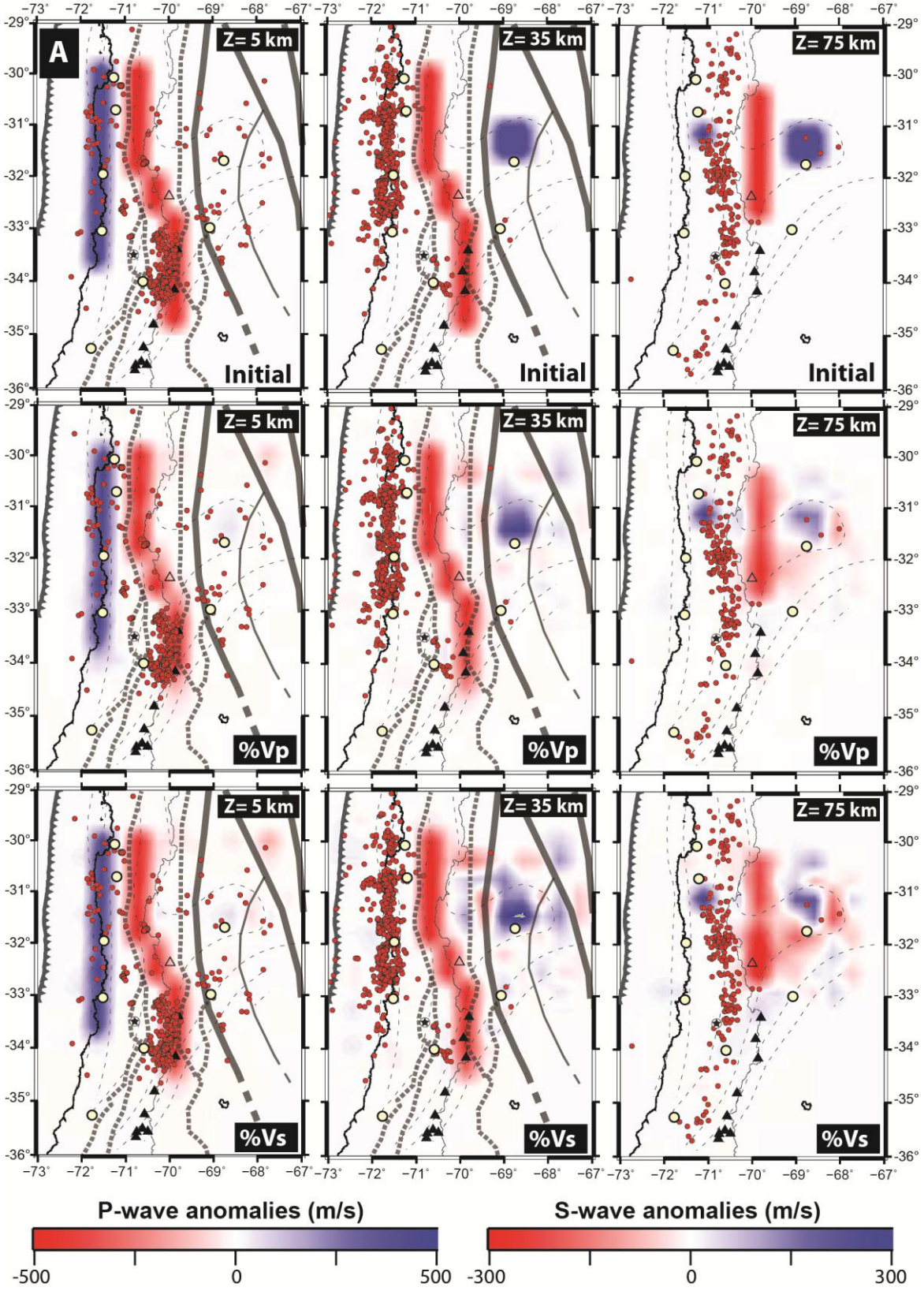
A
Z= 5 km
Z= 35 km
Z= 75 km
Initial
%Vp
%Vs
P-wave anomalies (m/s)
-500
0
500
S-wave anomalies (m/s)
-300
0
300

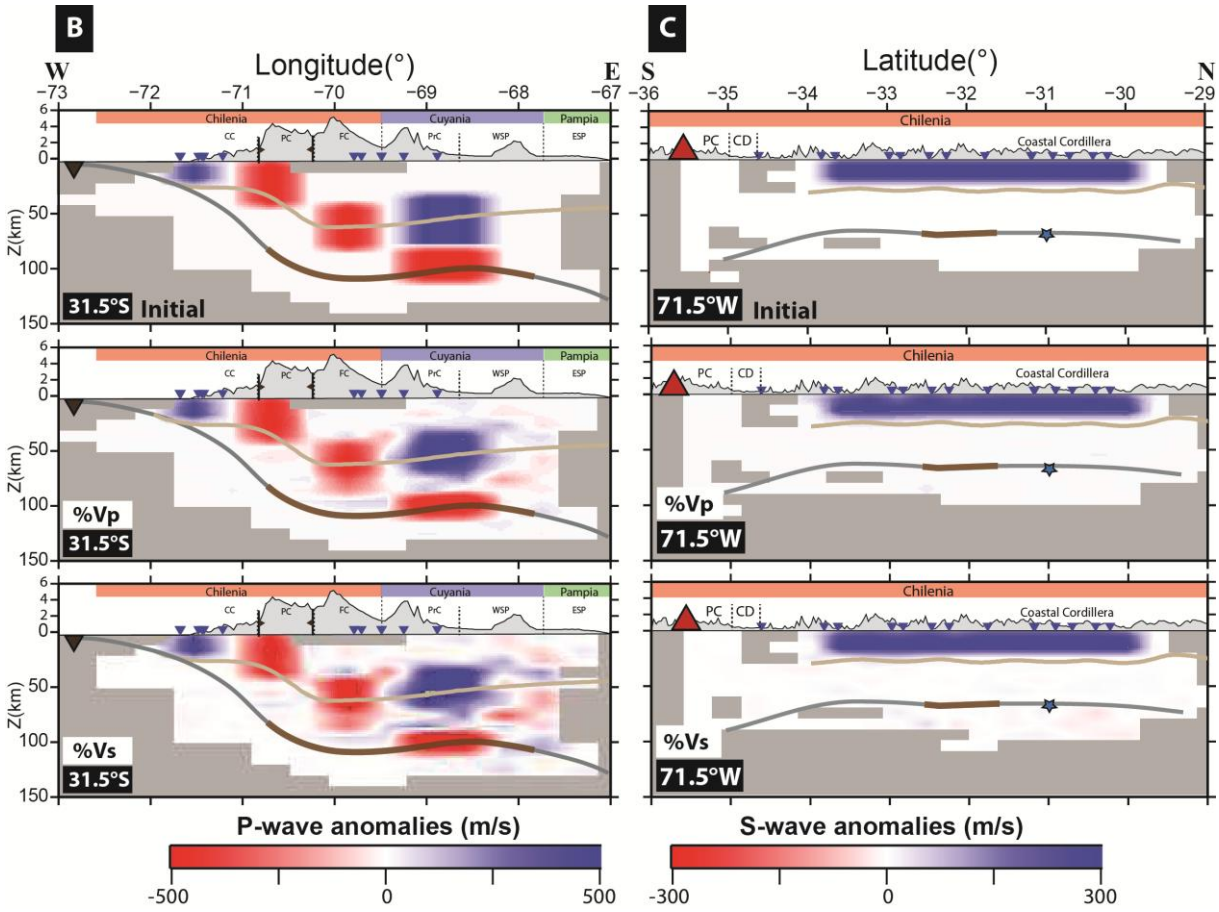


**Fig. 2.1.12 :** *Our "Spike" test results for P- and S-waves. (A) horizontal cross-sections at depth 5, 35 and 75 km, (B) E-W vertical cross-sections through the flat slab region at 31.5°S, and (C) N-S vertical cross-sections through the forearc crust at 71.5°S. Figure legend same as Fig. 2.1.11. The initial velocity perturbations imposed on our final velocity inversion model are shown in the upper panels by positive (blue) and negative (red) perturbations of amplitude ±500 m/s. We notice that We notice that, whereas, the region closest to the subduction front (i.e. the forearc) is well resolved with almost not distortions, the backarc region is less well constrained by the ray coverage, particularly in Vs, leading to some horizontal smearing, mostly in the continental mantle below Cuyania. The rest of the spike tests at other latitudes, longitudes and depths sections are shown in Appendix A.*

### *2.1.12 Conclusions*

To conclude, we modeled the velocity field by inverting for P- and S-wave travel-time residuals, based on ray theory, and solving for the finite-difference Eikonal equation (Podvin and Lecomte, 1991) using the *TLR3* algorithm. Our model volume is 960 x 880 x 220 km$^3$. Our seismic database was collected from four temporary campaigns (OVA99, CHARGE, CHARMSE and CHASE), and was consistently relocated in a 1-D velocity model of 17 layers, calculated previously for this region. We then applied strict quality selection criteria on our data, and incorporated a total of over 3603 earthquakes in our inversion, with 52 011 and 51 631 travel-times for P- and S-waves, respectively. The quality of our data enabled us to choose a damping of 0.7, a quality weighing coefficient Cp/Cs of 0.5. The quality of our final chosen model was assessed using the checkerboard and spike tests that show that the final model is well resolved for a node spacing of 40 x 40 x 10 km in a large part of its volume space, except mostly in the backarc region.

## 2.2 Approximating the Pressure-Temperature Conditions of the Flat and Normal Subduction Systems: Two-Dimensional Thermo-Mechanical Forward Modeling

In order to calculate the predicted seismic properties of rocks at depth, the pressure and temperature (P-T) field must be estimated. We chose to use a two-dimensional (2-D) thermo-mechanical forward modeling method, performed by Muriel Gerbault, to approximate the P-T conditions at depth for two 2-D cross-sections (for the normal and flat subduction zones), based on an initial synthetic setting and as much *a priori* data as possible for the area. These models run with self-consistently defined elasto-visco-plastic P-T dependent rheologies, and for a duration that can be hypothesized as representing the present transient equilibrium of the subduction zones (at the scale of several millions of years). Details are given below.

### *2.2.1 The Numerical Method*

The numerical code used is the plane-strain finite-differences Parovoz algorithm (Poliakov and Podladchikov, 1992), which is based on the FLAC method (Fast Lagrangian Analysis of Continuum, Cundall and Board 1988). It is funded on a 2-D plane-strain Lagrangian approach, and an explicit forward time-marching scheme. A Newtonian equation of motion and the temperature equation are both resolved iteratively at each time-step, incorporating elasto-visco-plastic rheologies. This code has been (and is still) widely used in a number of geodynamical contexts, such as lithospheric compression (e.g. Gerbault, 1999), continental collision (e.g. Burov et al., 2001; Burov and Yamato, 2008), extension (Buck et al., 2005) and subduction (e.g. Gerbault et al., 2009). Although the present version of this code does not account for the density variations that arise from mineral phase reactions, it is not necessary for our purpose, since we are only interested in retrieving information on the equilibrium P-T field for an already determined slab geometry, rather than simulating the geodynamical evolution of the subduction zone.

### *2.2.2 Computing the Stress, Strain and Temperature Conditions*

Nodal velocities $\partial u/\partial t$ are solved in a large-strain Lagrangian formulation, with the following equation of motion:

$$\rho\partial\frac{\partial u/\partial t}{\partial t} - \ div\,\sigma - \ \rho g = 0, \qquad (1)$$

where $\rho$, $u$, $t$, $\sigma$, and $g$ indicate the density, displacement, time, stress, and gravitational acceleration, respectively. The model mesh moves with the material, in discrete time intervals, as the displacements are integrated from these nodal velocities.

The viscous-elasto-plastic constitutive equations that relate stress to strain are given by the general function, $F$:

$$\frac{D\sigma}{Dt} = F\left[\sigma, u, \frac{\partial u}{\partial t}, T, \ldots\right] \qquad (2)$$

where $\partial/\partial t$, $D/Dt$ and $T$ represent a time derivative, an objective time derivative and a temperature, respectively.

The elasto-visco-plastic stress tensor (Fig. 2.2.1A) is estimated from the elementary strain rate components. As is detailed below, the rheological behavior importantly depends on the first invariant

of the stress tensor, namely the pressure *P*, defined by the trace of its diagonal components, and the second invariant of the deviatoric stress ($\sigma^{II\,dev}$), given by:

$$\sigma_{ij}^{II\,dev} = \frac{1}{2}\sqrt{\sigma_{ij}\sigma_{ij}} \qquad (3)$$

Elastic deformation is described by Hooke's law which defines a linear relationship between stress, $\sigma$, and strain, $\varepsilon$. In a homogeneous and isotropic material, as is assumed for each lithological layer defined in the starting model, Hooke's law is defined in the equation:

$$\sigma = 2\mu\varepsilon + \lambda tr(\varepsilon)I \qquad (4)$$

where $\sigma$ is the stress tensor, $\varepsilon$ is the strain tensor, $\mu$ is the shear modulus (Lamé's second coefficient), $\lambda$ is Lamé's first coefficient, *tr* is the trace function and *I* is the identity tensor. Lamé's coefficients, $\mu$ and $\lambda$, are used to parameterize the mechanics of homogeneous and isotropic rocks in the elastic domain, and here are given values $\lambda = \mu = 3.10^{10}$ Pa. Plastic yield or brittle failure is described by the pressure-dependant Mohr-Coulomb yield criterion. The Mohr-Coulomb failure criterion predicts that rupture occurs when the shear stress, $\tau_s$, applied to a plane reaches the yield stress, $\sigma_y$, which is a function of the deviatoric normal stress, $\sigma_3 - \sigma_1$, the friction angle, $\varphi$, and cohesion, *C*, along that plane, given by the equation:

$$\sigma_3 - \sigma_1 = Sin\varphi\left[\sigma_3 + \sigma_1 - 2C\frac{1}{Tan\varphi}\right] \qquad (5)$$

Visco-elastic deformation in rocks was shown to satisfy Maxwell's rheology visco-elastic rheology (e.g. Turcotte and Schubert, 1982; Ranalli, 1995):

$$\sigma_{ve}^{II\,dev} = \left[\mu(\varepsilon_3 - \varepsilon_1)dt + \sigma^0\left[1 - \frac{\mu dt}{2\nu_{eff}}\right]\right]\left[1 + \frac{\mu dt}{2\nu_{eff}}\right] \qquad (6)$$

Laboratory experiments on rocks show that amongst all deformation processes, most rock types obey to a dominantly power-law creep, which is described by a relationship between stress and strain that is exponentially dependent on temperature. Therefore, the effective viscosity $\nu_{eff}$ above depends on the temperature, on the deviatoric strain-rate, $\varepsilon_3 - \varepsilon_1$, on the deviatoric stress from the previous time increment, $\sigma^0$, the material parameter, *A*, the effective stress exponent, *n*, the creep activation energy, *Q*, the universal gas constant, *R*, given by:

$$\nu_{eff} = \frac{1}{4}\sqrt[n]{\frac{4}{3A}}\sqrt[n-1]{\varepsilon^{II\,dev}}exp^{\frac{Q}{nRT}} \qquad (7)$$

In Parovoz, for each element and each time-step, the stress tensor is deduced from the minimum of the elasto-plastic stress and the visco-elastic stress:

$$\sigma = (\sigma_{ep}, \sigma_{ve})$$

Approximating correctly the temperature field is important to assess the most probable composition deduced from seismic wave velocities. It is also important for the evaluation of the temperature-dependent viscous rheology, or the identification of brittle-ductile transition zones. In Parovoz, the heat transfer equation is resolved and for each time increment:

$$\rho Cp\frac{\partial T}{\partial t} + \dot{u}\nabla T - \dot{k}\nabla T - H_r - H_s = 0, \qquad (8)$$

where $T$, $\rho$, $Cp$, $k$, $H_r$, $H_s$ and $\dot{u}$ denote temperature, density, specific heat capacity, thermal conductivity, internal heat production, shear heating, and velocity, respectively. The advective term $\dot{u}\nabla T$ is implicitly solved by the movement of the Lagrangian mesh. Internal radioactive heating depends on depth, following the classical exponential relationship $H_r = H_0 \exp\left(\frac{-y}{H_r}\right)$, where $H_r$ is set to 5 km, $H_o$ = 8E$^{-10}$ W/kg (e.g. Burov and Diament, 1995). Shear heating $H_s$ results from the product of viscous-plastic deviatoric stress and strain rate. Shear heating in the subduction channel is a condition pre-defined in the initial setting, evaluated with the applied boundary velocities and an average shear stress of 10 MPa within the 16 km thick subduction channel.

### *2.2.3 The General Initial Conditions*

The domain is 1800 km long and 300 km deep. The mesh grid is comprised of 400 x 400 elements, each 6 km wide and increasing from 2 to 4 km with depth. The starting model is constructed with the simple assumption that the flat and normal subduction regions are presently in a steady-state slab geometry (Fig. 2.2.1), an thermal and rheological compositions, justified by the fact that the slab appears to have reached its current configuration since at least 6 Myr (Kay and Abbruzzi, 1994). The 2-D models are constructed based on *a priori* information collected from geophysical, geological, and geodetic studies. We preliminary proceeded to a number of tests in order to achieve a geometry within about 2.5-4 Myr, that does not evolve too much afterwards and that closely resembles present-day lithological layer boundaries (deduced from geophysical information); hence, approaching relatively stable P-T conditions at this time-scale.

In the numerical model, the geometry of the subducting oceanic plate is defined by fitting at best the hypocenter distribution collected for this study. The radius of curvature of the slab, as it subducts at the trench, is defined equal to 450 km, a rather constant average along the Chilean subduction margin (Gerbault et al., 2009) until 110 km depth, at which point the slab's dipping angle becomes zero or 35°, for the flat and normal slab sections, respectively, down to 400 km depth. In the flat subduction zone, the angle of subduction as it re-subducts into the mantle, is also set constant and equal to 35° down to 300 km depth.

The modeled domain is sub-divided into several rheological/lithological units, as evaluated by Tassara et al. (2006) and Tassara and Echaurren (2012), of specific thermo-mechanical properties (

Table 2**.1**, Table 2.2 and Fig. 2.2.1). These are described further in Section 2.2.4.

**Table 2.1**: *Parameters for each layer defined in the model: density, ρ, composition, comp (refer to Table 2.2), conductivity, κ, and angle of friction, φ. Cohesion is set to 10 MPa. The continental mantle above the flat and normal slab is either DryOl or WetOl. Values are taken from Gerbault et al. (2009) and modified from Tassara et al. (2006).*

| | **Ocean mantle** | **Ocean crust** | **Astheno-sphere** | **Continent upper crust** | **Continent lower crust** | **Continent mantle** | **Sub-ducting sedi-ments** | **Subduc-tion channel** |
|---|---|---|---|---|---|---|---|---|
| **ρ** (kg/m$^3$) | 3360 | 3050 | 3350 | 2750 | 3050 | 3350 | 2850 | 3200-3400 |
| **Comp.** | DryOl | Mafgr | DryOl | Wetgr/Qz/ Plg | Plg/Mafgr | DryOl & WetOl | Plg | Wetgr/Plg |
| **K** (W/m.K) | 3.3 | 2.9 | 3.3 | 2.5 | 2.5 | 3.3 | 2.9 | 2.9 |
| **Φ** (°) | 20 | 20 | 10 | 20 | 10 | 10 | 5 | 1.43-2.86 |

**Table 2.2**: *Dislocation creep parameters used to evaluate the effective viscosity for different compositions of*

*Table 2***.1**. *Material constant is A, power exponent, n, activation energy, Q, after compilation from Ranalli (1995).*

| | **Dry olivine (DryOl)** | **Wet olivine (WetOl)** | **Mafic granulite (Mafgr)** | **Plagioclase (Plg)** | **Quartz (Qz)** | **Wet granulite (Wetgr)** |
|---|---|---|---|---|---|---|
| ***n*** | 3.0 | 2.5 | 4.2 | 3.2 | 2.0 | 1.9 |
| **A** (MPa n/s) | $7 \times 10^4$ | $3 \times 10^4$ | $1.4 \times 10^4$ | $3.3 \times 10^4$ | $1 \times 10^4$ | $2 \times 10^4$ |
| **Q** (J/mol) | $5.2 \times 10^5$ | $4.44 \times 10^5$ | $4.45 \times 10^5$ | $2.38 \times 10^5$ | $1.67 \times 10^5$ | $1.37 \times 10^5$ |

Boundary velocities are then imposed, within the gravity field. An absolute westward velocity for the South American Plate is defined at 2.5 cm/a (O'Neill et al., 2005), based on moving hotspots. With a convergence velocity of 7.5 cm/a (Somoza and Ghidella, 2005), the eastward slab velocity must be equal to 5 cm/a, which is applied at the left-side of both flat and normal slab modeled sections. An additional slab pull velocity of identical magnitude is applied at the base of the model domain at 300 km depth along the flat slab's limit. The application of this basal velocity, in a direction parallel to the slab's inclination (35°) results from the assumption that the slabpull force is still driving the subduction at least until the 300 km depth of the model domain (see Gerbault et al. (2009) for discussion).

Stress buildup and development of deformation are calculated for a chosen time scale of approximately 4 Myr. Within the first 2 Myr, the modeled structures are loaded mechanically and deform with regards to the initial conditions and imposed constraints. For the remaining ~ 2 Myr, only minor changes in the thermal, stress and deformation states occur (characteristic time-scales of diffusion processes are usually larger than 10 Ma). A relatively short time-scale is used here, because (i) we assume the current system is already near equilibrium, and (ii) the aim is to retrieve intermediate-scale structures and their physical connection from the surface to depth.

The lithospheric thermal state is initially conditioned based on oceanic and continental thermal ages (e.g. Burov and Diament, 1995). For the continental lithosphere, a thermal arc anomaly of arbitrary geometry is superimposed both in the normal and flat subduction systems (details in Gerbault et al. 2009), aiming at roughly approaching the few existing heat flow values (retrieved from the Heat Flow Map of South America, Hamza and Munoz, 1996; and the Global Heat Flow Database for the eastern Nazca Plate). There exist few heat flow values for the oceanic lithosphere in this region. However, these indicate very low values of 33-40 $mW/m^2$ immediately seaward of the trench (at 33°S) (Grevemeyer et al., 2003; 2005; 2006), with respect to the predicted values of ~ 60 $mW/m^2$ for its age (32-35 Ma) (Stein and Stein, 1992).

A diffusion law simulates erosion and sedimentary processes, which control the orogenic mass balance, with a constant diffusion coefficient of 200 $m^2/a$ (e.g. Gerbault et al., 2009).

### *2.2.4 The Initial Upper and Lower Plate Conditions*

The continental lithosphere, in both the normal and flat subduction systems, is modeled with a geotherm representing a lithosphere of age of 180 Myr, and the lithospheric thickness (Lithosphere-Asthenosphere Boundary, LAB), defined by the 1350°C isotherm, is set at 100 km depth for both flat and normal slab sections (Fig. 2.2.1).

The continental crust is originally defined with a 35 km thickness (Fig. 2.2.1), and because of its complex compositional structure, we simplify it with an upper and lower crust, of densities 2750 kg/m$^3$ and 3050 kg/m$^3$, and effective friction values of 20° and 10°, respectively (as in Gerbault et al. 2009, modified from Tassara et al. 2006). The rheology of this domain controls the location of crustal shortening (in domains of weaker strength), and the occurrence of decoupling stress levels (e.g. *décollements* and horizontal shear zones).

The oceanic crust is defined as 7 km thick and is described with a power-law creep parameter for mafic granulite and a density value of 3050 kg/m$^3$ (

Table 2.**1**). The oceanic sub-lithospheric mantle is given a thermal age of 35 Ma, determined from magnetic anomaly surveys of the Nazca Plate (Tebbens and Cande, 1997), and a density value of 3320 kg/m$^3$ and 3350 kg/m³, for the flat and normal slab sections, respectively. Both the oceanic lithospheric mantle and asthenosphere are assigned power-law creep parameters of dry olivine (Table 2.2), consistent with fresh harzburgite and fertile lherzolite, respectively, and are given a density of 3350 kg/m$^3$. Afonso et al. (2007) calculated that slabs become negatively buoyant at ages > 35 Ma.

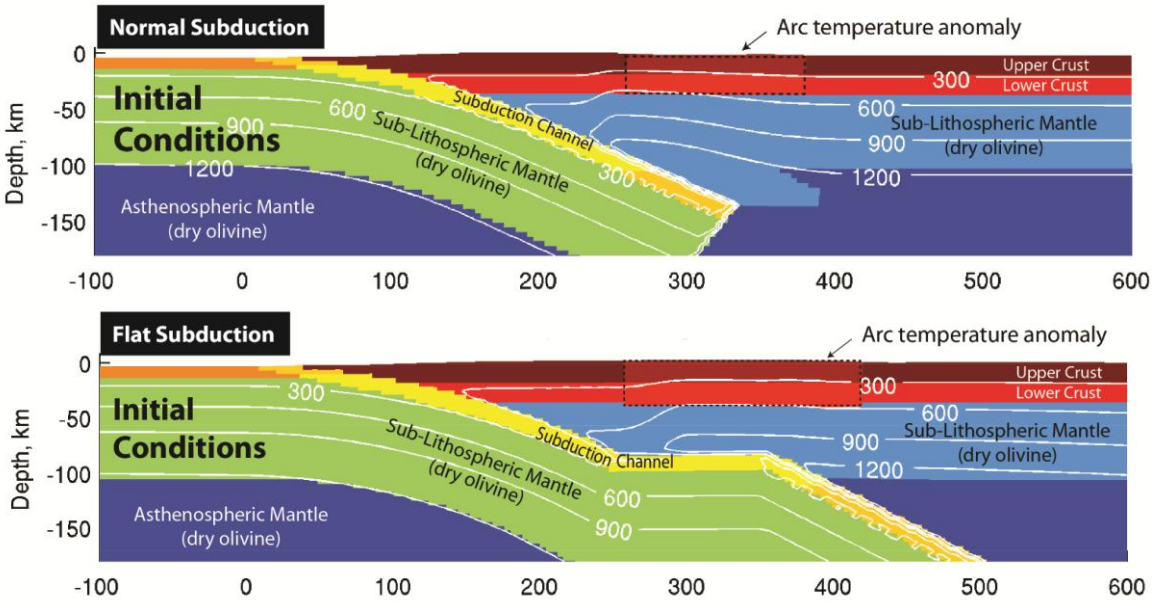


**Fig. 2.2.1**: *Initial temperature (isotherms) and rheology (colors and annotations) conditions for the construction of the (A) normal and (B) flat subduction zones, based on a priori data and representing the central Chilean convergence zone. More details in the text.*

The continental lithospheric mantle, below the active volcanic arc only, is initially characterized by a temperature anomaly which focuses deformation in the mantle. In reality, this thermal anomaly is the consequence of complex solid and fluid mass transfers and metamorphic reactions taking place throughout millions of years (Fig. 2.2.1).

The subduction channel is a thin layer that serves to accommodate the movements at the interface between the two converging lithospheric plates. Temperature gradient is locally high in this area. In the present thermo-mechanical models, this subduction channel is set as 16 km thick (linked to numerical resolution constraints), and sub-divided into three layers of different densities: (1) 0-10 km depth: $\rho$ = 2800 kg/m$^3$, angle of friction = 4.5°; b) 10-100 km depth: $\rho$ = 3100 kg/m$^3$; and c) > 100 km

depth: $\rho$ = 3370 kg/m$^3$, where the slab becomes denser than the surrounding asthenosphere. Because it only represents a relatively thin layer and is the result of complex metamorphic processes and material grinding, it has not yet been properly imaged seismically and is still misunderstood.

### *2.2.5 Our Chosen Final Models*

Two synthetic models of P-T conditions were built for the flat (Fig. 2.2.3A) and normal subductions (Fig. 2.2.3B). These two models are taken to represent an approximation of the true conditions characterizing the central Chilean subduction zone, and we have attempted to account for the variability in these models by applying rather large uncertainty ranges for the P-T conditions used in the future step of this study, which is petrological modeling (Part Three of this chapter).

In Fig. 2.2.2 we show the relative pressure, the thermal isotherms and the deformed rheologies after about 3 Ma of model calculation. We chose to retain these models as our basis for our petrological modeling; since not much improvement was achieved in the later modeling attempts (the number of combinations of more than 20 parameters is huge).

#### *2.2.5.1 Normal Subduction*

We retained two models for the normal dipping slab section, displayed in Fig. 2.2.2A and B. In the first model (Fig. 2.2.2A), the continental lithospheric mantle is given dry olivine power low creep parameters. This strong mantle rheology, together with a cold enough arc anomaly, impedes on compressional deformation and crustal thickening. Whereas, in Fig. 2.2.2B, a wet lithospheric mantle was assumed, and is displayed at a slightly later stage of the model calculation (3.2 Ma), indicating the development of a deep crustal root (up to nearly 70 km) because of the compliant (wet) mantle underneath. Wet olivine (serpentine/antigorite) weakens the rock strength, and depending on its extent, can change significantly subduction dynamics (e.g. Fumagalli et al., 2001; Fumagali and Poli, 2005; Reynard, 2010; 2013).

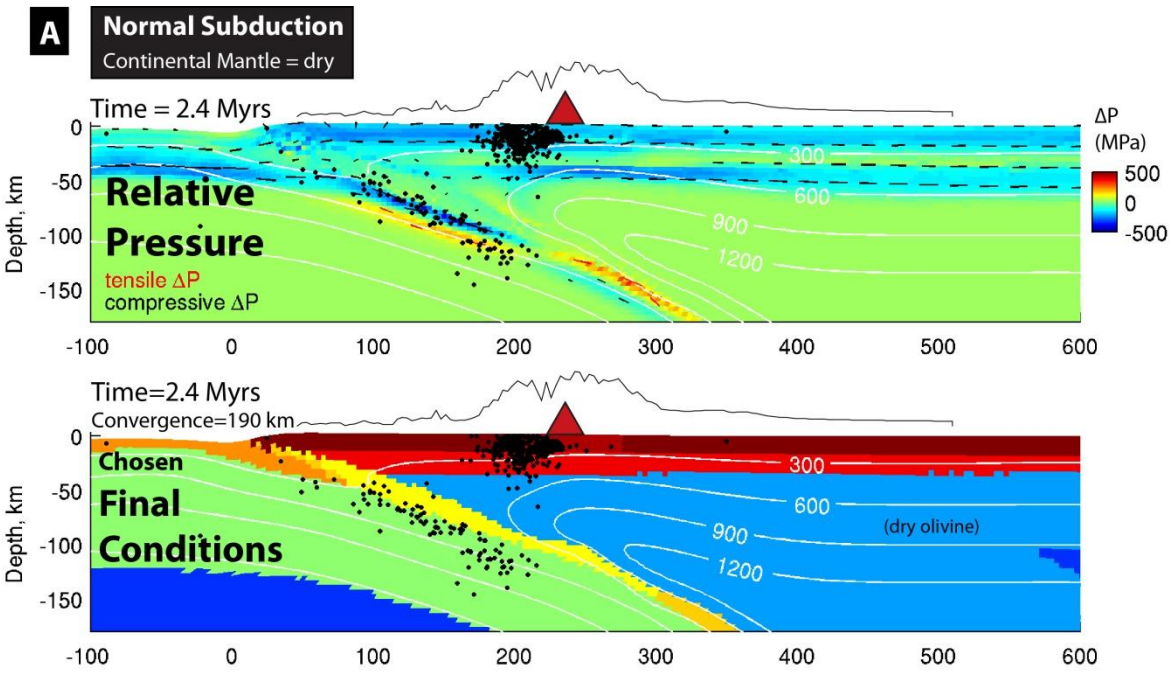

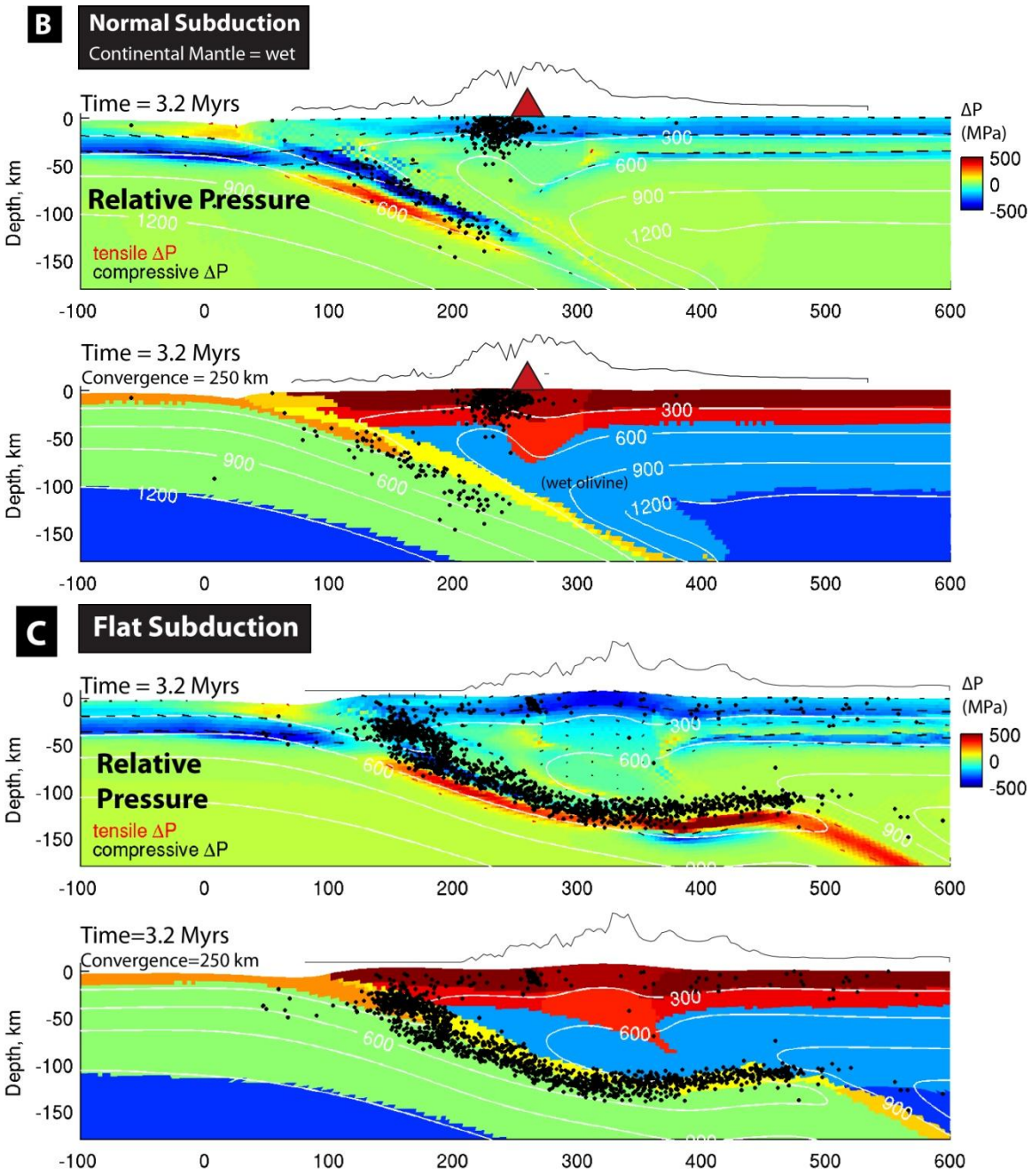


**Fig. 2.2.2**: *Thermo-mechanical models at given time-steps for the (A-B) normal and (C) flat subduction systems. For each of them, the upper panel shows the relative pressure of the system, calculated by subtracting the lithostatic pressure from the total pressure field, with units in megapascals (MPa). The small black lines of varying lengths, superimposed on the models, are the directions and magnitudes of principal stress (most compressive □1 and less compressive □3 for compressional and tensile domains, respectively. Red colors show the areas in tension and in blue of compression (relative to lithostatic pressure). In the lower panels are displayed the deformed*

*rheological layers at the given time-step. The true topography is shown at representative latitudes of the normal and flat subduction systems at 33.5°S and 31.5°S, respectively. The location of the active volcanic arc is shown by the red triangle. The temperature field T is shown by the white isotherms at 300°C increments. The black dots represent the earthquake catalog used in this study, assuming that they locate along the slab interface. Convergence values represent the total amount of plate convergence between both ends of the modeled plate.*

What this model of wet continental mantle also shows (Fig. 2.2.2B), is that the slab lithosphere endures more intense compressive and tensional bending stresses than in dry conditions in Fig. 2.2.2A. However, the pattern is the same for both, forming a double-planned structure that runs parallel to the slab surface at depth, and down to about 120 km depth (consistent with the down-dip limit of earthquakes). Compressional bending stresses occur at 40 km depths below the ocean floor and west of the trench. Below, the continental Moho-slab intersection and between 50 and 120 km depth, unbending compressional stresses shift to the upper 10-15 km of the slab surface, coinciding with the slab seismicity and the crust/subduction channel rheologies (yellow layer in figures), and slab-parallel tension becomes dominant in the oceanic mantle. This lower depth of 120 km coincides with (i) the maximum depth extent of the slab seismicity, below which, no more earthquakes occur (confirmed by independent studies), and (ii) the occurrence of a moderate-size earthquake (Mw 5.7, January 2003) and its multiple aftershocks, whose temporal and spatial distributions enabled us to interpret it as a reactivated pre-existing fault originating from the outer rise region. The earthquake analysis of the main- and aftershocks were published in the journal Earth and Planetary Science Letters in February 2012, and is included later in this sub-chapter.

This pattern of slab stress is particularly relevant because it mimics very well the geometry, depth extent and stress field observed for most Double Seismic Zones (DSZ). The link of DSZ with unbending stresses has previously been proposed and often discussed (Wang, 2002, Dorbath et al., 2008). Marot et al. (in submission) report a DSZ for the flat slab region of central Chile, with a width characteristic of the distance between the two planes of stress shown in Fig. 2.2.2B. However, the DSZ is located slightly above the high compressional/tensional modeled domains, i.e. the upper seismic zone seems to be located within the weak subducting channel, and the lower seismic zone seems to be located in between the compressional and tensional modeled domains. This result is consistent with that of Dorbath et al. (2008) for northern Chile. This observation has been interpreted as the presence of trapped free fluids in between both stressed domains, triggering seismicity (Dorbath et al., 2008, Faccenda et al., 2012). Marot et al. (submitted) also noticed that the DSZ disappears when the slab returns to a normal angle of subduction further south, which they attempted to explain either by the lack of data or a change in rheology (of the lower or upper plate). This is consistent with the disappearance of unbending stresses.

Furthermore, no other seismic studies located more southerly report such a DSZ, suggesting that its absence to the south of 33°S may be reality. We suggest that this absence of DSZ might also be linked with the absence of unbending stresses in the normal slab, simply due to the absence of a slab continuing at greater depths (tomographic signals vanish deeper, and further south).

The “unbending” model works well for the DSZs beneath Japan and most other western Pacific occurrences, where the upper and lower seismic planes are also dominated by compression and extension, respectively, and are explained with plate unbending mechanisms (Wang, 2002, Faccenda et al., 2012, and reference list in Marot et al., submitted at JGR). In more detail, DSZs have been explained with dehydration embrittlement and phase change processes (e.g. Yamasaki and Seno, 2002), however, the simple code used here, cannot account for these.

A major difference between both normal-dipping slab models displayed Fig. 2.2.2, is that in the first case (with a dry continental mantle Fig. 2.2.2A), the mantle wedge remains hot, a feature consistent with common knowledge of normal-dipping and relatively young slabs (e.g. Currie et al.,

2004). In contrast, the second model (with a wet continental mantle Fig. 2.2.2B) sees its mantle wedge cooled down rapidly, due to the thickening of the overriding crust, which advects temperatures downward. In reality, both processes of thickening crust and heat maintenance in the mantle wedge occur coevally, but the present numerical model does not account for the phase transformations, latent heat, nor fluid mass transfers that would allow to reproduce them. Since our study is rather focused on mantle properties, we opted for the first model of Fig. 2.2.2A, to carry out the future steps of our study (see next chapters).

Mantle wedge serpentinization occurs in most 'normal' subduction zones as a consequence of slab dehydration processes, shown by seismic tomography and direct field observations of ophiolite belts. However, in flat slab configurations, the consequent lower geotherm is expected to greatly reduce these slab dehydration reaction rates, leading to a drier overriding mantle conditions. For this reason, a dry continental sub-lithospheric mantle was assigned in the flat subduction model.

#### *2.2.5.2 Flat Subduction*

In the flat subduction model, shown in Fig. 2.2.2C, a thick continental crust is generated within 3.2 Ma, with a crustal root that remains thin beneath the high Andes. Many studies in central Chile indicate a similar deep crustal root of 60-70 km thick. In this model, a similar double-plane stress pattern results along the subducting slab in between 50 and ~ 100 km depth, with the zone in compression located under the oceanic crust and the zone in tension yet deeper inside the mantle. The intensity of the stress field is even higher than that for the normal slab under wet conditions.

When superimposing the slab seismicity of the DSZ found in central Chile above the flat subducting slab, we observe that the zone in tension is located a few tens of kilometers below the lower seismic plane, and that the layer of compression is either located along the lower seismic plane (e.g. > 70 km depth) or in between the seismic planes (e.g. between 50 and 60 km depth). Since the distance between the seismic planes decreases with depth to merge together (Marot et al., in submission), we are unable to justify with precision its position with respect to the seismicity. Hence, we test both hypotheses, for the DSZ and for the flat slab segment.

Dorbath et al. (2008) and Faccenda et al. (2012) agreed that the lower seismic plane is a result of fluid accumulation and migration along the plane of neutral pressure gradient, located between the compressional and tension domains. In that case, the location of the compressional layer observed in our flat slab model could well be located in between the seismic planes. However, the types of stresses do not match the focal mechanism and stress tensor solutions calculated for the DSZ (Pardo et al., 2002; Marot et al., 2013). Since the model was constructed based on data for this region, we deduct that these plate-bending stress conditions are likely to occur, at least to some degree; however, other more dominant factors must influence the apparent stress field at these depth. Further information on the Chilean DSZ is given in our article in submission at JGR at the end of this sub-chapter.

The flat slab portion is dominated by a wide band of tensional stresses, located within the oceanic mantle. Along this segment, no compression would occur. Comparing with the position of the slab seismicity, when assuming that they locate along the slab interface, the layer of tensional stresses yet locates deeper than the seismicity. A general look at our focal mechanism solutions for this segment, and confirmed by previous studies (e.g. Pardo et al., 2002; Anderson et al., 2007), show that tension is by far the dominant rupture mechanism here, indicating tensional stresses. The good fit between these two observations lead us to suppose that earthquakes might occur in regions of highest stress field in the lithospheric mantle. However, we are conscious that this assumption remains debatable, e.g. see discussion in Burov and Watts (2006). We explore this possibility by attempting to match the locations of the seismicity and the layers of maximum tensional and compressional tensional stresses. For this, we must lower the seismicity dataset everywhere by about 10-15 km. In

doing so, the upper and lower seismic planes of the DSZ match the compressional and tensional layers of stress, respectively, at these intermediate-depths, although still contradicted by the measured data. Then, the dense and thick flat slab seismicity would match the strong tensional stresses there.

Two comments are to be made at this point: (1) the modeled flat slab was setup with an initial depth of the flat lying subduction channel (yellow layer) that would fit the depth of the observed flat seismicity. It could be set initially shallower, so that instead, the tensile stresses built up after ~ 3 Myr would fit the depth of the observed flat seismicity; (2) One of the limitations of the 2-D plane-strain code used here is that, by definition, the third inplane direction corresponds to the intermediate stress component, and the inplane strain component is null. We are thus unable to test, nor reproduce, in the appropriate 3-D stress and strain tensors.

In fact, Anderson et al. (2007) showed that the direction of tension here is not parallel to slabdip but perpendicular and horizontal to slabdip. If this is a reality, two important points can be made: (1) the slab seismicity occurs in the oceanic mantle, starting at the base of the oceanic crust (when considering a subduction channel thickness of 16 km) and not in the oceanic crust; and (2) the 20 km shallower earthquake locations obtained using the IASEP-91 velocity model, and used many times as the basis of previous seismic studies in this region, are likely to be a clear underestimation of the much deeper earthquake locations, assuming that the seismic velocity, or numerical thermo-mechanical model, is correct and that the earthquakes do occur within zones of maximum stresses. To conclude, we advocate that there seems to be a good correlation with the seismic distribution and the tensile stress field in our region.

### *2.2.6 Conclusions*

To resume, the use of the numerical code Parovoz helps to predict the mechanical stress field of the subducting lithospheres, based on known data and first-order assumptions. In the case of central Chile, we are able to correlate the depth extent and geometry of the observed Double Seismic Zone with the double-planned stress pattern. In addition, we show that by displacing the earthquakes about 10-15 km deeper in the slab, there is a correlation with the layers of maximum tensile stresses. For the normal slab region, we chose a model for which the continental lithospheric mantle, adjacent to the slab, is dry rather than wet because preliminary seismic investigation of the mantle wedge shows that there is no significant hydration, and also because of the warm temperatures associated to the nose of the mantle wedge. In addition, the modeled strong double-planed stresses occurring in the slab are nearly as high as for flat subduction, which is incoherent with the single-planed, low seismic rate structure observed.

Fig. 2.2.3 shows the pressure and temperature distribution of Fig. 2.2.2A, which we used for our analysis of the composition of the flat and normal subduction zones, given in the next chapter, Part Three.

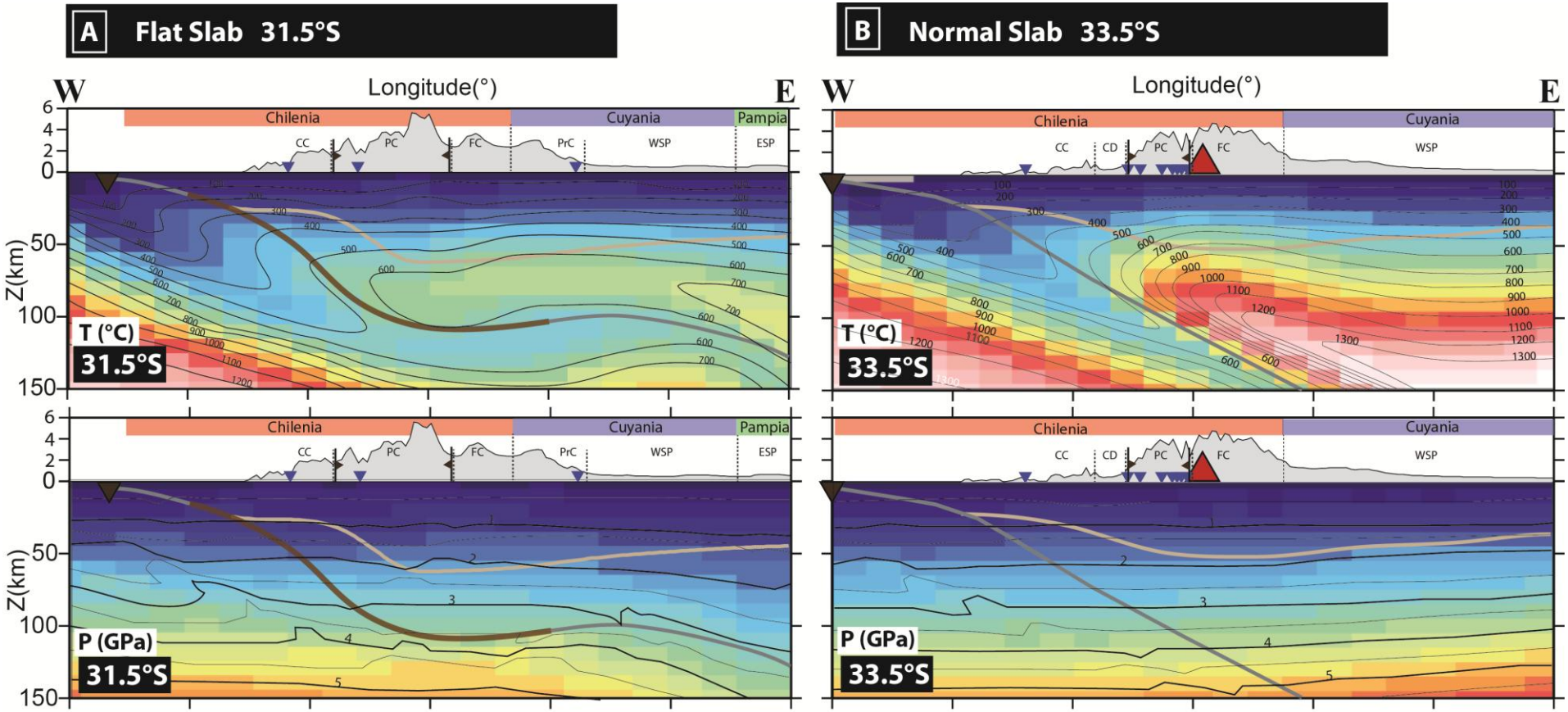


**Fig. 2.2.3**: *The estimated temperature and pressure field (shown by the isotherms and in colors) for the (A) flat and (B) normal subductions, based on geophysical, gravimetric and geological a priori information available for this region, as explained in more details in the text.*

### *2.2.7 A Reactivated Pre-Existing Fault Plane within the 'Normal' Subducting Nazca Slab*

Earth and Planetary Science Letters 327–328 (2012) 9–16

Contents lists available at SciVerse ScienceDirect

Earth and Planetary Science Letters

journal homepage: www.elsevier.com/locate/epsl

## An intermediate-depth tensional earthquake ($M_W$ 5.7) and its aftershocks within the Nazca slab, central Chile: A reactivated outer rise fault?

Marianne Marot [a,*], Tony Monfret [a], Mario Pardo [b], Giorgio Ranalli [c], Guust Nolet [a]

[a] Université de Nice Sophia-Antipolis, Centre National de la Recherche Scientifique (UMR 6526), Observatoire de la Côte d'Azur, Géoazur, 250 av Albert Einstein 06560 Valbonne, France
[b] Departamento de Geofísica, Universidad de Chile, Blanco encalada 2002, Santiago, Chile
[c] Department of Earth Sciences, Carleton University, 1125 Colonel By Drive, Ottawa, Canada K1S 5B6

## Abstract

An intermediate-depth earthquake (7 January 2003, $M_w$ 5.7) occurred within the subducting Nazca plate at longitude 70.3°W, latitude 33.8°S and depth 113 km. Its focal mechanism shows normal faulting with a slight strike-slip component. We detected 50 aftershocks within January 2003 using a temporary seismic network installed in the zone. Their local magnitudes $M_l$ range between 1.9 and 3.5, with the strongest events occurring around the mainshock. Their spatial distribution, including the mainshock, defines an area of ~ (35 ± 5) x (10 ± 2) $km^2$, cutting through almost half of the slab's total thickness at an angle of ~ 60° to the slab's surface. This area agrees well with one of the mainshock nodal planes. However, the total seismic area, as defined by the aftershock distribution, is larger than the rupture area normally expected for an earthquake of moderate magnitude. We compare the orientation of the seismic plane with the outer rise fault pattern offshore central Chile and find a correlation with the strike of the seafloor spreading fabric. The seismic sequence shows similarities with other intermediate-depth cases, notably the 13 June 2005 Tarapacá earthquake in northern Chile and similar cases in the Pacific slab beneath Japan. In all these cases, the inferred reactivated fault planes probably originate from the outer rise region, in agreement with the hypothesis that intermediate-depth seismicity is linked to inherited faults. Consequently, even moderate-sized earthquakes can reactivate large areas of inherited faults within slabs at depths > 100 km. Furthermore, the occurrence of multiple other local events ($M_w$ > 5), with similar focal mechanism and depth to the January 2003 event, appear to indicate that the slab becomes mechanically weak ~ 100 km depth. The depth extent in the slab of the reactivated pre-existing faults is likely governed by the slab's bending/unbending stress regime, i.e. the depth to the neutral plane. Dehydration embrittlement is a possible factor for triggering the seismic sequence.

## Keywords

Subduction, intermediate-depth seismicity, fault reactivation, outer-rise faults, dehydration embrittlement

### 2.2.7.1 Introduction

On January 7, 2003 at 00:54 GMT, an $M_w$ 5.7 earthquake occurred within the subducting Nazca slab in central Chile (70.3°W, 33.8°S) with focal depth 113 km. The mainshock was followed by a sequence of shocks whose spatial distribution forms a plane which penetrates within the slab. This seismicity is located near a transition zone between flat subduction, where the Juan Fernandez Ridge (JFR) enters the Chilean trench, and a steeper ~ 30° dipping segment (Fig. 1a). It is the first time that such an aftershock sequence aligning transverse to the slab surface is observed in the slab beneath central Chile despite permanent seismic monitoring provided by the seismic network of the University of Chile since the middle 1980s.

Similar seismic sequences at intermediate-depths and also at the outer rise region, penetrating deeply into the oceanic lithosphere in a direction approximately perpendicular to its surface, have been reported in several subduction zones, notably in the Pacific plate (Japan and New Zealand), in the Nazca plate (northern Chile), and in the Cocos plate (Costa Rica).

It is commonly suggested that the link between intermediate-depth seismicity and flexure-related outer rise faults is the release of fluids, by means of slab dehydration at depth. Bending of the oceanic lithosphere at the outer rise results in normal faulting and deep hydration via ocean water infiltration of the upper brittle part of the lithosphere (Faccenda et al., 2009; Contreras-Reyes and Osses, 2010). In most outer rise regions, seafloor bathymetry and seismic reflection surveys show dense networks of extensional faults cutting across the oceanic Moho by tens of kilometers (e.g. Ranero et al., 2005; Grevemeyer et al., 2005; Contreras-Reyes et al., 2007, 2008). Furthermore, the occurrence of double Benioff zones (DBZs), can also be accounted for by fluid release derived from dehydration transformation reactions, since their geometry correlate well with dehydrating reaction P,T-fields for various hydrated minerals present in the oceanic lithosphere (Seno and Yamanaka, 1996; Kirby et al., 1996; Peacock, 2001; Hacker et al., 2003, Dorbath et al., 2008).

In this study, we analyze the spatial distribution, magnitudes and focal mechanisms of the January 2003 seismic sequence which cut through almost half of the slab thickness (Fig. 1b). We suggest that the seismic plane, defined by the focal mechanism of the mainshock and the spatial distribution of aftershocks, represents an intermediate-depth reactivation of a fault with strike parallel to the seafloor spreading fabric formed by lithospheric flexure at the outer rise.

### 2.2.7.2 Tectonic Setting

Below central Chile and western Argentina (29°-34°S), the Nazca plate subducts beneath the South American plate at a rate of 6.7 ± 0.2 cm/a in the N78°E direction as constrained by GPS measurements (Kendrick et al., 2003). The Andes formed by the high convergence rate causing back-arc compression and crustal thickening up to 55 km beneath the Sierras Pampeanas (Beck et al., 2005) and 70 km beneath the Principal Cordillera (Heit et al., 2008), as well as trench retreat (Lallemand et al., 2008).

The region is seismically and tectonically characterized by along-strike variations in slab dip angle (Fig. 1a) (Barazangi and Isacks, 1976; Jordan et al., 1983; Cahill and Isacks, 1992). The slab subducts everywhere along the trench with initial eastward dip ~ $30^o$. However, between latitudes 27°-32°S, at ~ 100 km depth the slab becomes horizontal, underplating the overriding continental lithosphere for ~ 250 km eastward, before re-subducting into the mantle (Barazangi and Isacks, 1976; Cahill and Isacks, 1992; Engdahl et al., 1998; Pardo et al., 2002; Ramos et al., 2002). To the south of 32°S, the slab changes geometry along strike over a very short distance, returning to a constant angle of subduction of ~30°. The southern transition zone is sharp, and whether rupture or flexure occurs, remains uncertain (Swift and Carr, 1974; Barazangi and Isacks, 1976; Cahill and Isacks, 1992; Araujo

and Suarez, 1994). In contrast, the northern transition zone is gentler (Cahill and Isacks, 1992; Pardo et al., 2002; Anderson et al., 2007).

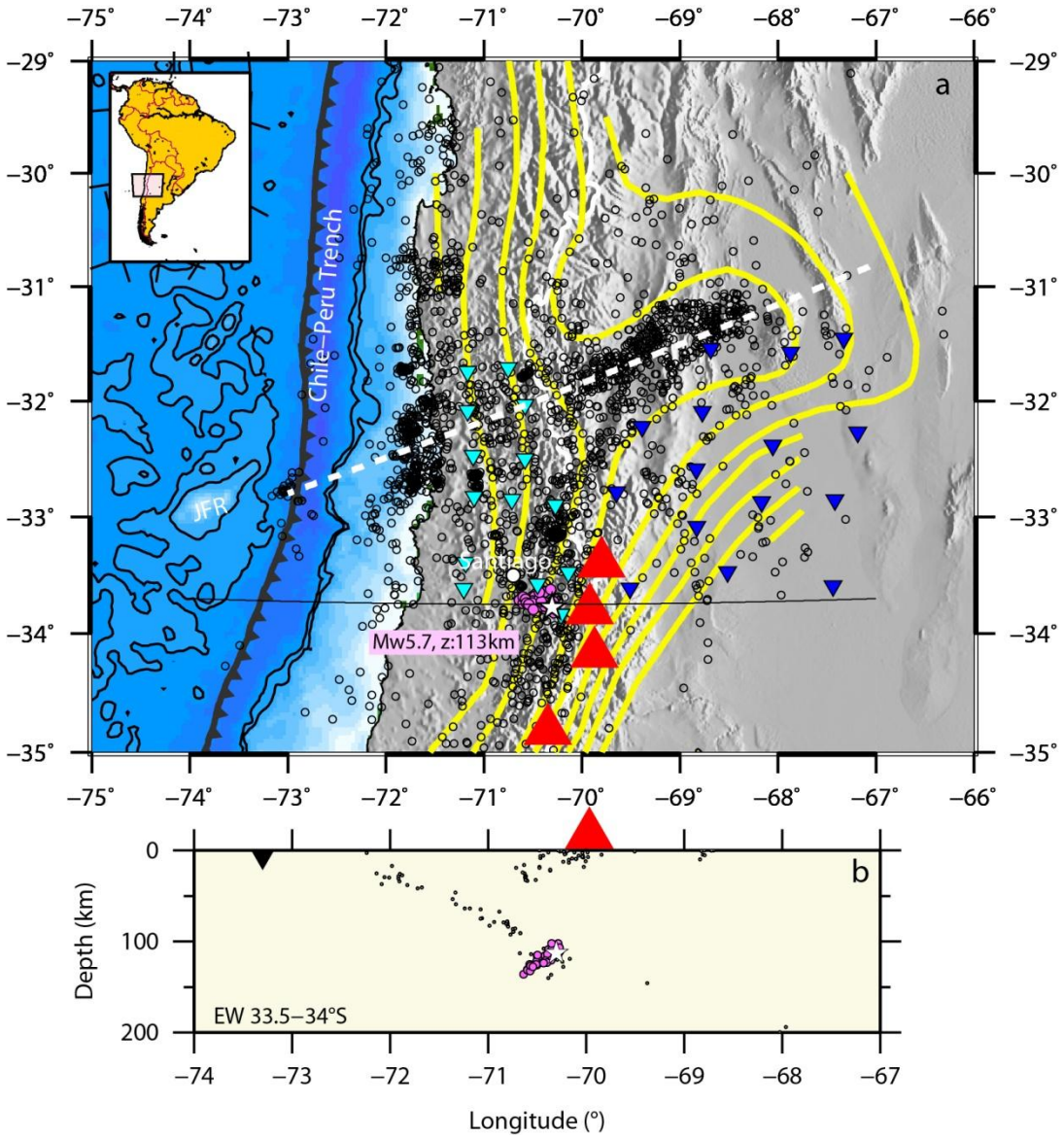


**Fig. 1***: Regional setting of seismicity in central Chile-western Argentina. Black circles: background seismicity; white star, 7 January 2003 mainshock; pink circles: aftershocks recorded by the CHARSME seismic network (light and dark blue inverted triangles: temporary stations in Chile and Argentina, respectively). Yellow contour lines (interval 10 km): isodepths of the slab upper surface (Anderson et al., 2007). Red triangles: Quaternary active volcanoes. Dashed white line: Juan Fernandez Ridge (JFR) subduction path. (a) Plan view; (b) EW-profile along 33.7°S.*

### 2.2.7.3 Data Analysis

The temporary seismic campaign CHARSME (CHile ARgentina Seismological Measurement Experiment) was carried out in central Chile and western Argentina between November 2002 and March 2003, with the purpose of analyzing the regional seismotectonic features and to map the shift in subduction geometry of the Nazca slab. It comprised 29 portable three-component broadband stations

(27 CMG-40T & 2 CMG-3T Guralp sensors) that continuously recorded seismicity. In an effort to increase coverage and improve hypocenter determination, particularly near coastal areas, 15 permanent short period seismic stations of the Chilean Seismological Service were added (Fig. 1a). A total of ~ 6000 regional events with $M_w < 6$ were recorded and analysed using the Seisan package (Havskov and Ottemöller, 2001).

*2.2.7.3.1 Hypocenter Location*

A seismic 1D velocity distribution, based on a 17-layer model, was compiled using arrival times from copper mining blasts for the first 20 km depth, and the VELEST program for larger depths (Kissling et al., 1994). The average $V_p/V_s$ ratio is 1.76. Hypocenter location was performed by manually picking body wave first arrival times and using the program HYPOCENTER (Lienert and Havskov, 1995). Only shocks with at least 9 seismic phase readings, including at least 2 S-phases, and RMS travel time residuals $\leq 0.6$ sec, were considered. Local magnitude ($M_l$) was determined taking into account maximum amplitude and hypocentral distance (Lay and Wallace, 1995) and was calculated for all events, calibrating $M_l$ such that its value for the mainshock is the well established $M_w$. We located the 7 January 2003 mainshock at 70.30°W, 33.77°S and 113 km depth, with a standard error of ~ 5 km in longitude and latitude and less than 10 km in depth.

The spatial distribution of the mainshock and its aftershocks defines an approximate planar feature which is described as the 'seismic plane' hereafter. The aftershocks are defined as events with smaller magnitude than the mainshock, occurring after the latter within in a 24 day window, and located on the seismic plane. We sampled only January events, since acquisition ended in early February, without any events located in the aftershock zone.

A total of 50 aftershocks were recorded between January 7$^{th}$ and 31$^{st}$, with $M_l$ ranging between 1.9 and 3.5 (Table 1). The aftershock locations show a rather well defined earthquake distribution along a plane of size ~ 40x10 km$^2$ oriented in the WNW direction and dipping ~ 30°W from the horizontal, with the mainshock located close to the slab surface (Fig. 1b).

About half of the aftershocks occurred within the first 24 hours after the mainshock (Fig. 2b). The strongest aftershocks ($M_l > 3$) clustered around the mainshock (Fig. 2a and Fig. 3), most of which occurred within the first two hours following the mainshock, succeeded in the next two hours by smaller events ($1.9 < M_l < 3$) randomly distributed along the entire length of the seismic plane. Over the next 24 days, continued clustering of events with more-or-less constant magnitude (average $M_l$ ~ 2.1) and occasional peaks ($M_l > 2.4$), occurred on the same plane. Wiens et al. (1997) noted that the maximum magnitude of aftershocks of deep earthquakes is ~ 2 units smaller than the mainshock magnitude (in contrast, for shallow California earthquakes the difference is 1.1), and that seems to be the case in this intermediate-depth sequence.

We also performed double-difference (DD) relative hypocenter relocation (Waldhauser and Ellsworth, 2000) for comparison with absolute hypocenter locations (HYPOCENTER). Forty-three events were relocated out of the total of 51 events, including the mainshock. The latter is relocated ~ 15 km lower along the seismic plane than the absolute location, and remains positioned at the shallow edge of the aftershocks. The DD method relocates the aftershock hypocenters towards the center of the plane, shortening both edges of the seismic plane and reducing its area to ~ 30x8 km$^2$. Since both methods give similar results and we manually evaluated the reliability of the absolute locations, we chose to retain the absolute hypocenter locations for our analysis. Thereafter, the seismic area considered is 35 ± 5 km long and 10 ± 2 km wide.

**Table 1**: *Hypocentral coordinates of the 7 January 2003 mainshock (#1) and its 50 aftershocks in chronological order. On the right-hand column, bold numbers shows the 6 events with focal mechanisms, whose bracketed numbers relate to their reference in Table 2 and Fig. 3.*

| | Long (°) | Lat (°) | Z (km) | $M_l$ | Year | Month | Day | hr | mn | sec |
|---|---|---|---|---|---|---|---|---|---|---|
| ***1 (1)*** | -70.304 | -33.775 | 113.0 | 5.7 | 2003 | 1 | 7 | 00 | 54 | 52.4 |
| ***2 (2)*** | -70.282 | -33.779 | 112.0 | 3.4 | 2003 | 1 | 7 | 01 | 00 | 55.8 |
| *3* | -70.308 | -33.789 | 113.6 | 2.4 | 2003 | 1 | 7 | 01 | 06 | 5.6 |
| *4* | -70.374 | -33.784 | 109.4 | 2.4 | 2003 | 1 | 7 | 01 | 09 | 1.1 |
| *5* | -70.307 | -33.809 | 113.4 | 3.5 | 2003 | 1 | 7 | 01 | 19 | 3.3 |
| ***6 (3)*** | -70.316 | -33.776 | 111.0 | 3.3 | 2003 | 1 | 7 | 01 | 19 | 3.6 |
| ***7 (4)*** | -70.294 | -33.793 | 114.9 | 2.6 | 2003 | 1 | 7 | 01 | 30 | 22.6 |
| *8* | -70.501 | -33.714 | 125.6 | 1.9 | 2003 | 1 | 7 | 02 | 10 | 49.6 |
| *9* | -70.636 | -33.712 | 135.9 | 2.2 | 2003 | 1 | 7 | 02 | 18 | 22.5 |
| *10* | -70.602 | -33.741 | 130.7 | 2.5 | 2003 | 1 | 7 | 02 | 26 | 53.6 |
| *11* | -70.301 | -33.750 | 115.2 | 2.5 | 2003 | 1 | 7 | 02 | 28 | 0.8 |
| *12* | -70.444 | -33.722 | 122.5 | 2.0 | 2003 | 1 | 7 | 02 | 44 | 55.8 |
| *13* | -70.564 | -33.704 | 129.8 | 2.2 | 2003 | 1 | 7 | 02 | 48 | 20.3 |
| *14* | -70.336 | -33.763 | 111.8 | 2.2 | 2003 | 1 | 7 | 02 | 50 | 40.1 |
| *15* | -70.532 | -33.737 | 125.0 | 2.1 | 2003 | 1 | 7 | 02 | 57 | 1.4 |
| *16* | -70.357 | -33.738 | 115.0 | 2.0 | 2003 | 1 | 7 | 03 | 03 | 59.3 |
| *17* | -70.295 | -33.774 | 110.4 | 3.1 | 2003 | 1 | 7 | 03 | 07 | 18.7 |
| *18* | -70.601 | -33.686 | 131.1 | 1.9 | 2003 | 1 | 7 | 04 | 51 | 35.0 |
| *19* | -70.493 | -33.717 | 118.8 | 1.9 | 2003 | 1 | 7 | 05 | 11 | 55.2 |
| *20* | -70.300 | -33.725 | 108.5 | 1.9 | 2003 | 1 | 7 | 05 | 42 | 0.2 |
| *21* | -70.500 | -33.708 | 115.6 | 1.9 | 2003 | 1 | 7 | 08 | 56 | 11.1 |
| ***22 (5)*** | -70.299 | -33.775 | 114.8 | 2.7 | 2003 | 1 | 7 | 09 | 18 | 14.8 |
| *23* | -70.428 | -33.718 | 119.5 | 2.0 | 2003 | 1 | 7 | 09 | 41 | 13.3 |
| *24* | -70.481 | -33.682 | 118.2 | 2.1 | 2003 | 1 | 7 | 10 | 35 | 21.2 |
| ***25 (6)*** | -70.364 | -33.763 | 110.2 | 2.4 | 2003 | 1 | 7 | 10 | 54 | 31.0 |
| *26* | -70.292 | -33.725 | 113.5 | 2.4 | 2003 | 1 | 7 | 15 | 17 | 35.2 |
| *27* | -70.285 | -33.820 | 102.1 | 2.0 | 2003 | 1 | 7 | 17 | 06 | 58.0 |
| *28* | -70.481 | -33.754 | 123.2 | 1.9 | 2003 | 1 | 8 | 03 | 33 | 20.0 |
| *29* | -70.470 | -33.726 | 122.1 | 2.1 | 2003 | 1 | 8 | 09 | 52 | 47.5 |
| *30* | -70.423 | -33.757 | 117.7 | 2.3 | 2003 | 1 | 9 | 06 | 03 | 46.6 |
| *31* | -70.507 | -33.720 | 125.5 | 2.1 | 2003 | 1 | 9 | 10 | 50 | 37.5 |
| *32* | -70.272 | -33.770 | 106.7 | 3.1 | 2003 | 1 | 9 | 12 | 15 | 37.0 |
| *33* | -70.386 | -33.646 | 120.3 | 2.2 | 2003 | 1 | 9 | 13 | 03 | 39.4 |
| *34* | -70.507 | -33.720 | 121.4 | 2.1 | 2003 | 1 | 10 | 03 | 45 | 25.4 |
| *35* | -70.559 | -33.744 | 126.3 | 2.1 | 2003 | 1 | 10 | 04 | 48 | 25.8 |
| *36* | -70.388 | -33.729 | 108.6 | 2.2 | 2003 | 1 | 10 | 13 | 56 | 25.6 |
| *37* | -70.354 | -33.761 | 108.9 | 2.1 | 2003 | 1 | 11 | 06 | 08 | 55.4 |
| *38* | -70.576 | -33.704 | 125.2 | 2.1 | 2003 | 1 | 11 | 08 | 40 | 15.7 |
| *39* | -70.443 | -33.733 | 119.8 | 2.4 | 2003 | 1 | 11 | 13 | 06 | 40.7 |
| *40* | -70.432 | -33.701 | 122.5 | 2.3 | 2003 | 1 | 11 | 15 | 03 | 12.5 |
| *41* | -70.511 | -33.737 | 125.2 | 2.1 | 2003 | 1 | 12 | 13 | 12 | 14.6 |
| *42* | -70.569 | -33.738 | 126.7 | 2.2 | 2003 | 1 | 15 | 01 | 43 | 43.0 |
| *43* | -70.544 | -33.749 | 127.5 | 2.1 | 2003 | 1 | 15 | 13 | 11 | 10.3 |
| *44* | -70.418 | -33.763 | 115.3 | 2.5 | 2003 | 1 | 15 | 20 | 43 | 28.6 |
| *45* | -70.297 | -33.770 | 113.1 | 2.7 | 2003 | 1 | 17 | 02 | 39 | 0.3 |
| *46* | -70.375 | -33.763 | 112.1 | 2.1 | 2003 | 1 | 18 | 03 | 33 | 44.9 |
| *47* | -70.495 | -33.791 | 114.8 | 2.0 | 2003 | 1 | 18 | 06 | 02 | 41.4 |
| *48* | -70.412 | -33.725 | 121.0 | 2.1 | 2003 | 1 | 20 | 05 | 59 | 46.5 |
| *49* | -70.318 | -33.622 | 113.4 | 3.3 | 2003 | 1 | 21 | 07 | 06 | 57.9 |
| *50* | -70.308 | -33.754 | 114.9 | 2.2 | 2003 | 1 | 24 | 06 | 14 | 17.5 |
| *51* | -70.435 | -33.646 | 123.8 | 2.1 | 2003 | 1 | 31 | 06 | 39 | 47.4 |

*2.2.7.3.2 Focal Mechanisms*

Earthquake focal mechanisms are obtained from first P-wave polarities (minimum 8 readings) using FOCMEC (Snoke et al., 1984). Only 6 double-couple focal mechanisms (Fig. 3), including the mainshock, are obtained for events that occurred within the first day after the main event (Table 2 and Fig. 3). The mainshock focal mechanism agrees with the solution in the Harvard Centroid Moment Tensor (CMT) catalogue, shown in Fig. 3a, which represents mainly normal faulting with a slight strike-slip component, a sub-vertical compressional axis (P-axis) and a tensional axis (T-axis) approximately normal to plate convergence. The aftershock seismicity aligns well with the 154°-striking and 34°W-dipping nodal plane for the mainshock. In addition, the azimuth of the aftershock alignment agrees very well with the slip direction of the mainshock (136°). The aftershocks mostly show reverse faulting (n° 2, 4, 5 and 6 in Fig. 3 and Table 2) with just one normal focal mechanism (n° 3, Fig. 3 and Table 2), and generally sub-vertical and sub-horizontal P- and T-axes. Not enough focal mechanisms were obtained to permit the convergence towards a reliable stress tensor solution.

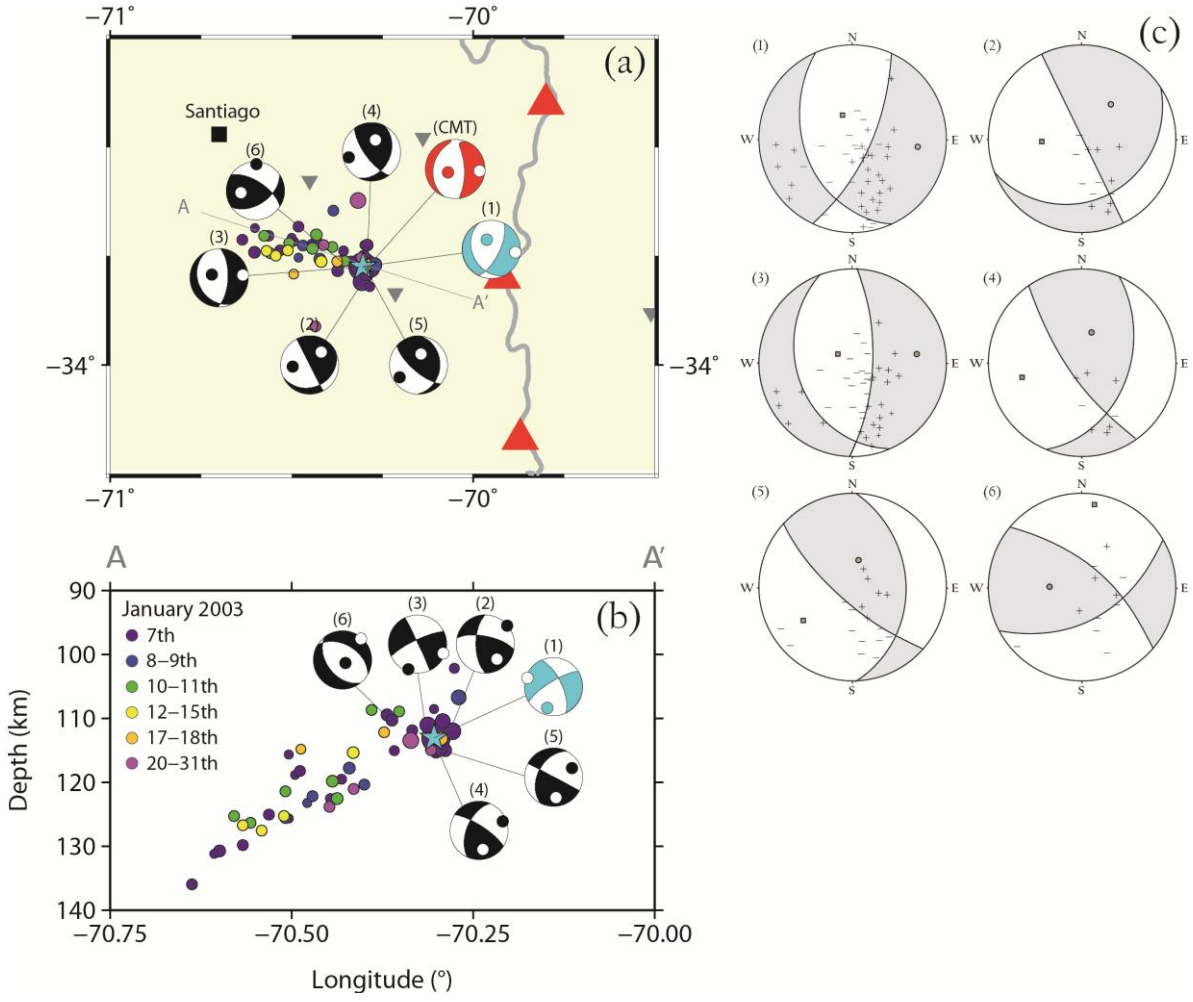


**Fig. 3**: *Earthquake focal mechanisms and aftershock time distribution (colored circles) Blue focal mechanism: January 2003 mainshock. Red focal mechanism: Harvard Central Moment Tensor (CMT) solution. Circles within focal mechanisms: P- (black) and T-axes (white). Numbers refer to the events in Table 2. Inverted grey triangles: nearby seismic stations. Red triangles: active volcanoes. Grey line: Chile-Argentina political boundary. (a) Plan view; (b) EW-cross-section view along A-A'; (c) Focal mechanisms with P-wave polarities (+: compression; -: dilatation), T-axis: grey circle, P-axis: filled square.*

**Table 2***: Focal mechanism solutions. Number (1) represents the mainshock, (2) to (6) are the aftershocks on Fig. 3. Hypocentral details of the events are in Table 1.*

| | Long (°) | Lat (°) | Z (km) | $M_l$ | Strike1 (°) | Dip1 (°) | Rake1 (°) | Strike2 (°) | Dip2 (°) | Rake2 (°) |
|---|---|---|---|---|---|---|---|---|---|---|
| **(1)** | -70.304 | -33.775 | 113.0 | 5.7 | 26 | 67 | -64 | 154 | 34 | -136 |
| **(2)** | -70.282 | -33.779 | 112.0 | 3.4 | 153 | 90 | 66 | 63 | 24 | -180 |
| **(3)** | -70.316 | -33.776 | 111.0 | 3.3 | 2 | 65 | -78 | 155 | 27 | -114 |
| **(4)** | -70.294 | -33.793 | 114.9 | 2.6 | 144 | 71 | 60 | 24 | 35 | 145 |
| **(5)** | -70.299 | -33.775 | 114.8 | 2.7 | 131 | 71 | 69 | 1 | 28 | 136 |
| **(6)** | -70.364 | -33.763 | 110.2 | 2.4 | 56 | 51 | 34 | 303 | 64 | 135 |

### *2.2.7.4 Discussion*

According to an empirical relation between seismic rupture area and moment magnitude for new normal faults (Wells and Coppersmith, 1994), the rupture area for an event with $M_w$ 5.7 should be ~ 60 $km^2$, one order of magnitude less than 240-400 $km^2$, the total area defined by the aftershock distribution in the present. The 7 January 2003 mainshock magnitude is thus too low to account for the observed seismic area. Hence, we suggest this plane was a pre-existing fault, reactivated by the main event. If aftershock distribution is taken as a good approximation of the size of the inherited fault plane, and the typical thickness of a ~ 40 Ma old oceanic slab is 80 km (Tassara et al., 2006), then the fault plane penetrated obliquely the subducting slab by ~ 40 km, that is, for almost half of its thickness (Fig. 4). If the slab is rotated back to horizontal, the dip of the fault plane becomes ~ $60^o$, typical of normal faults at Earth's surface (Twiss and Moore, 1992) and falling within the dip range of 45°-70° estimated by Ranero et al. (2003) for bend-faults offshore Middle America. Such large faults that penetrate deeply into oceanic lithosphere are observed at the outer rise region of subduction zones, where the plate bends before subducting beneath the overriding plate.

#### *2.2.7.4.1 Reactivation of Outer Rise Normal Faults*

Plate bending models for the Nazca plate indicate that most of the Chilean outer rise is subject to sharp plate curvature which results in widespread faulting once the yield strength is exceeded (Contreras-Reyes and Osses, 2010). Multibeam bathymetry in the outer rise region of central Chile shows three dominant patterns of structural damage: (i) reactivated seafloor spreading fabric striking ~ 145° (Kopp et al., 2004; Ranero et al., 2005; Contreras-Reyes et al., 2008); (ii) newly formed tensional bend-faults sub-parallel to the trench (Ranero et al., 2005); and (iii) fractures parallel to the JFR, striking ~ 60° and affecting a broader area of the sea floor than bend-faults (Kopp et al, 2004; Ranero et al., 2005). The best fitting mainshock nodal plane and the aftershock distribution strike 154°, matching the strike of the seafloor spreading fabric.

Seafloor spreading fabric consists of lineaments that affect all oceanic upper crusts and are formed parallel to mid-oceanic ridges, trending parallel to the magnetic anomalies (Ranero et al., 2005). As the fabric passes over the outer rise region of subduction zones, it also forms outer rise faults which are, however, not necessarily parallel to the trench axis. Offshore central Chile, the seafloor spreading fabric is clearly observed (F3 in Fig. 7 in Ranero et al., 2005), until ~32.5°S where the JFR's strong fault pattern (parallel to the offshore volcanic edifices) dominates.

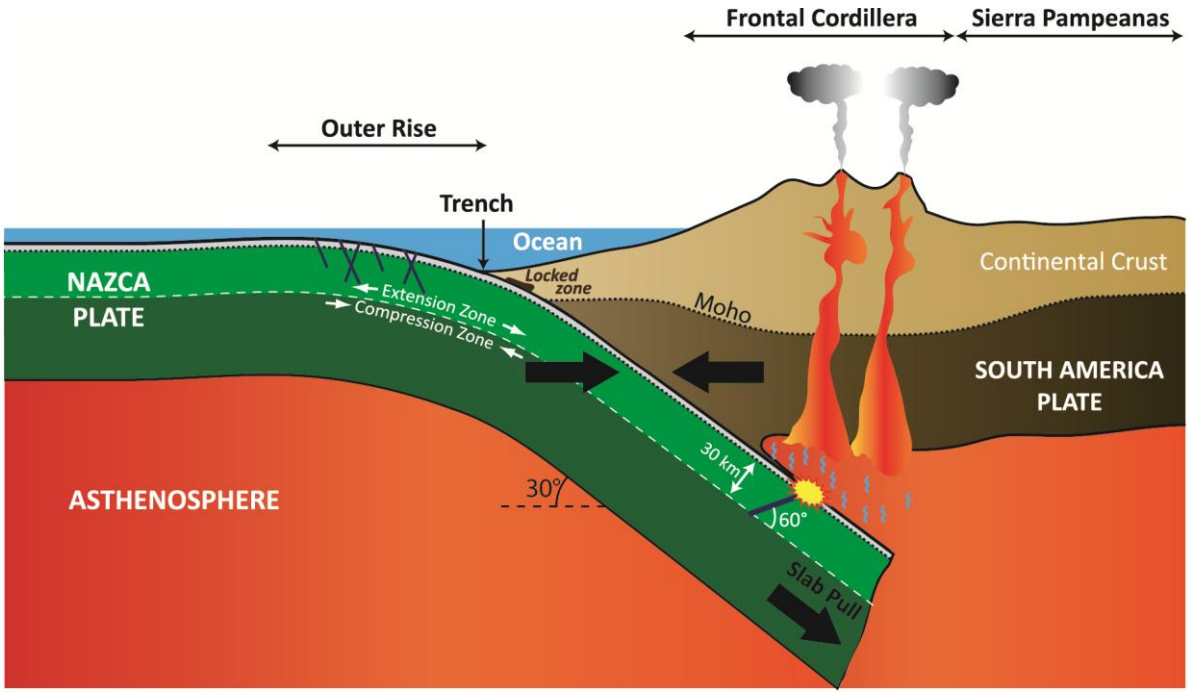


**Fig. 4**: *Schematic EW profile of the dynamical setting of the subduction zone along 33.7°S. Large yellow burst and dark blue line: 7 January 2003 mainshock and the associated rupture plane, respectively. Outer rise faults are shown by thin blue lines.*

At the outer rise, plate bending creates extensional conjugate faults, both trenchward- and oceanward-dipping. Warren et al. (2007, 2008) suggested that most trenchward-dipping faults can be reactivated at intermediate-depths. However, a few examples other than the present case show that oceanward-dipping faults also can be reactivated. For example, the tensional Mw 6.7 central Chilean outer rise earthquake of 9 April 2001 and its aftershocks (Fromm et al., 2006; Clouard et al., 2007) showed two fault dips of ~ 30°W and 60°E, and was interpreted as a JFR fault reactivation during its passage over the outer rise. The intermediate-depth Japanese event of 7 April 2011 (Mw 7.1) shows aftershocks limited to the upper 15 km of the slab and defining an area of 30x30 km2 (Nakajima et al., 2011) with an oceanward inclination of 60° from the slab surface, and was interpreted as a reactivated hydrated pre-existing outer rise fault. The Japanese 1993 Kushiro-oki (Mw 7.8, 90-110 km depth) and the 2003 Miyagi-oki (Mw 7.1, ~70 km depth) events generated aftershocks that aligned along 60°-dipping seismic planes, with a trenchward orientation for the latter seismic sequence (Nakajima et al., 2009b; Mishra and Zhao, 2004).

Within the Nazca slab in northern Chile, the intermediate-depth 13 June 2005 Tarapacá earthquake ($M_w$ 7.7; 69.24°W, 20.01°S) affords a very close comparison with our case study, as it is located in an area with similar subduction angle and slightly older slab age. The mainshock occurred near the slab surface at ~ 100 km depth with normal focal mechanism, and the rupture propagated through a large part of the slab. It was followed by a sequence of aftershocks defining a sub-horizontal fault plane of size ~ 50x40 $km^2$ (Peyrat et al., 2006; Delouis and Legrand, 2007; Peyrat and Favreau, 2010; Kuge et al. 2010). This event has also been interpreted as having ruptured a pre-existing plane of weakness that originally formed as a consequence of plate flexure at the outer rise. As in the present case, the original dip of the fault plane at the outer rise is consistent with this hypothesis.

Several earthquakes of $M_w > 5$ occurred in the area with similar focal mechanisms and depths as the 7 January 2003 mainshock (Fig. 5). The 16 June 2000 event ($M_w$ 6.4) is one of them and is located close to the 7 January mainshock. Did the 16 June earthquake newly create the fault that was

reactivated 3 years later by the January 2003 mainshock? The NEIC earthquake catalogue does not show any aftershock sequence, linked to the June 2000 earthquake and other events shown in Fig. 5, that would outline a fault plane transverse to the slab surface, although its magnitude corresponds to a rupture area of ~ 240 $km^2$, as observed for the January seismic sequence (Wells and Coppersmith, 1994). A fault plane identification and slip distribution by waveform inversion should be performed for the $M_w$ 6.4 event to constrain the rupture plane, however, it is out of the scope of this paper. Those similar focal mechanisms may signify that, since the slab in central Chile is highly and deeply fractured prior to subduction, it becomes strongly mechanically weakened ~ 100 km depth by reactivated faults, as observed in several subduction zones, described previously in this paper.

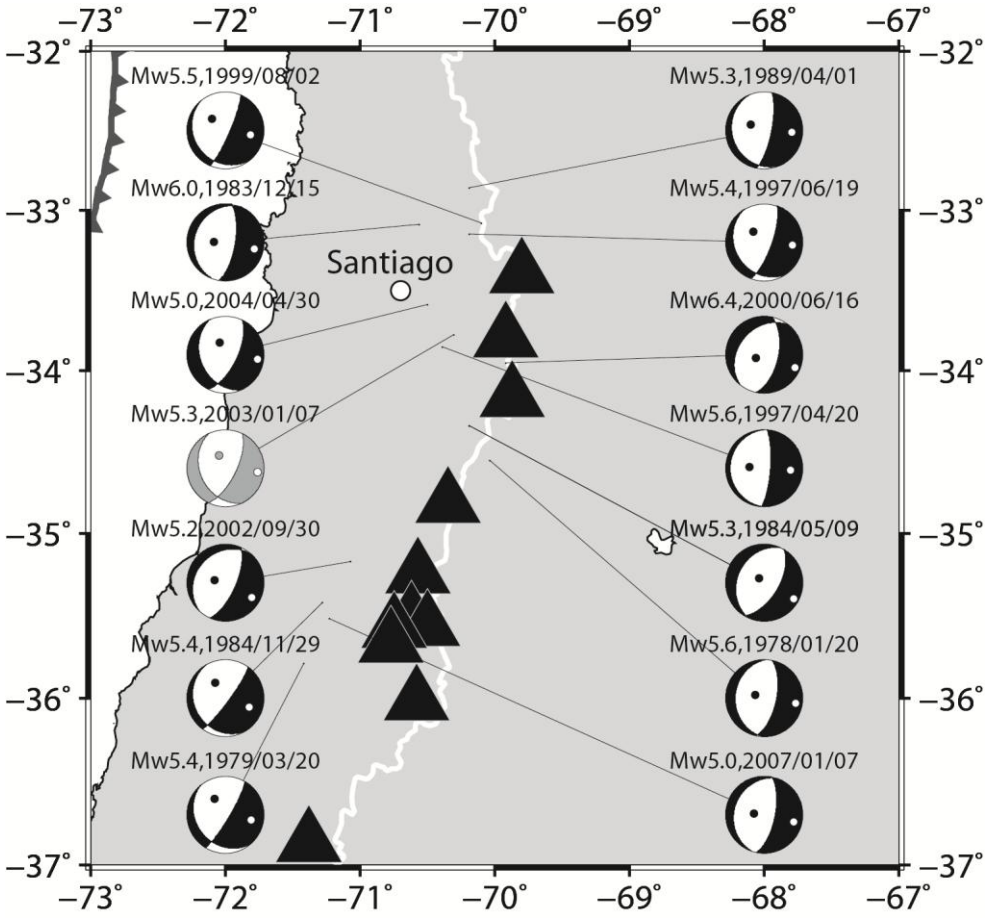


**Fig. 5**: *Earthquakes with $M_w$ > 5 at ~ 100 km depth in central Chile, from the Harvard CMT catalogue from 1987-2011, showing similar focal mechanisms than the 7 January 2003 event (grey). Black triangles denote active volcanoes. Moment magnitude ($M_w$) and date of occurrence are referenced above each focal mechanism.*

Fault reactivation at intermediate-depths has been proposed to account for the similarities in fault orientations and focal mechanisms with the outer rise fault pattern (Jiao et al., 2000; Ranero et al., 2003). The tensional nature of the January mainshock agrees with the hypothesis that the central Chilean intermediate-depth subduction seismicity is controlled by slab pull forces, rather than by slab unbending forces which predict a compressional state of stress at intermediate-depths in the upper part of the slab. The aftershock reverse focal mechanisms are probably related to fault re-equilibration or local variations of the stress field. The seismic plane is located within or very close to the southern

transition zone of the flat slab to the north, where complex slab stresses are expected. Normal faulting is predominant at intermediate-depths all along the Nazca slab (Astiz et al., 1988; Araujo and Suarez, 1994; Pardo et al., 2002). Double Benioff Zones in northern Chile show downdip tension in the upper plane (Comte and Suarez, 1994; Rietbrock and Waldhauser, 2004), and the same occurs in central Chile along the flat part of the slab (Marot et al., in preparation).

A study of intermediate-depth focal mechanisms in the Middle America and Tonga-Kermadec subduction zones (Warren et al, 2007; 2008) suggests that outer rise fault reactivation does not occur below 75 km and 100 km of depth, respectively, in these subduction zones. If reactivation of outer rise faults is a valid interpretation for the present case and the Tarapacá earthquake sequence (Peyrat et al., 2006; Delouis and Legrand, 2007, Kuge et al., 2010), then reactivation occurs to depths of at least ~ 100 km for the central and northern parts of the Nazca slab.

*2.2.7.4.2 Mechanisms of Fault Reactivation*

An important question concerning the intermediate-depth seismicity in subduction zones is the mechanism of frictional sliding at high pressure. Strong evidence suggests that dehydration reactions can increase significantly the P,T-field where frictional sliding can occur, and consequently dehydration embrittlement is considered a viable mechanism for intermediate-depth earthquakes in subducting slabs (Hacker et al., 2003). Experiments with materials containing only 1% of fluid produced by dehydrating water-bearing minerals have shown that frictional sliding can be triggered to P,T-conditions equivalent to ~ 300-400 km of depth (Jung et al., 2004). There is also some evidence that the presence of hydrated minerals such as serpentine in the mantle is sufficient to reactivate pre-existing fractures to depths of ~ 180 km even in the absence of dehydration (Jung et al., 2009).

Many observations indicate that oceanic plates and subducting slabs contain $H_2O$ and hydrated minerals. A systematic reduction in seismic velocities in the crust and upper mantle at the outer rise, shown by seismic wide-angle refraction surveys worldwide, is interpreted as the consequence of seawater infiltration and hydration (Contreras-Reyes et al., 2007). The depth of the reduced seismic velocities increases towards the apex of the plate flexure, indicating increased outer rise fault penetration and plate weakening in this area (Contreras-Reyes and Osses, 2010). Slow crustal and upper mantle P-wave velocities < 7 km $s^{-1}$ measured at the JFR are an indication of rock hydration (Kopp et al., 2004). The occurrence of circulating fluids at the outer rise, as well as at depth in the subduction zone, is further confirmed by electromagnetic (Worzewski et al., 2010), heat flow (Grevemeyer et al., 2005), and gravity (Tassara, 2006) studies. Velocity anomalies related to the presence of $H_2O$ have been observed all along the Peru-Chile trench: offshore Antofagasta (22°S, Ranero and Sallares, 2004); Valparaiso (33°S, Kopp et al., 2004); Concepcion (38°S, Contreras-Reyes et al., 2008); and Chiloé (43°S, Contreras-Reyes et al., 2007).

Outer rise heat flow measurements between 32.5°-33.5°S yield very low values of 24-31 mW $m^{-2}$, and extremely low heat flow values of 12 mW $m^{-2}$ have been measured at 36°S (Grevemeyer et al., 2005) compared to a global expected value of ~ 90 mW $m^{-2}$ for a crustal age of ~32 Ma (Stein, 2003). Low heat flow values are indicative of hydrothermal circulation systems that cool the upper oceanic lithosphere via the injection of cold seawater in faults. Similar values were observed in Peru (13°S) and Nicaragua (10°N) (Burch and Langseth, 1981). All these outer rise regions show pervasive faulting patterns. Thick sedimentary layers over the oceanic basement can reduce the interaction with ocean water and reduce heat flow variations (Grevemeyer et al., 2005; Contreras-Reyes et al., 2007). However, the pelagic sediment cover is only ~ 100 m thick offshore central Chile (Kopp et al., 2004; Ranero et al., 2005), while fault offsets in the same area are of the order of 500-1000 m (Grevemeyer et al., 2005), allowing full interaction between the fracture systems and ocean water.

Teleseismic and local seismic tomography investigations from around the globe reveal a narrow, inclined low velocity layer extending to ~ 150 km depths (e.g. beneath Japan, Nakajima and Hasegawa, 2006; Nakajima et al., 2009a), which coincides with the upper slab boundary and is interpreted as hydrated oceanic crust (Peacock and Wang, 1999; Hacker et al., 2003). Such seismic anomalies have been observed in the Pacific slab (e.g. Peacock & Wang, 1999; Nakajima et al, 2009a), the Aleutian slab (e.g. Helffrich and Abers, 1997), the Philippines slab (e.g. Hori et al., 1985), and recently in the Nazca slab as well (e.g. Haberland et al., 2009). At intermediate-depths below south-central Chile (37-39°S), evidence of hydrated subducting oceanic crust down to 80 km depth is shown by an inclined thin, low Vp layer with P-velocity ~ 7 km $s^{-1}$ , with seismicity located mainly inside it (Haberland et al., 2009).

The depth of hydration inside the lithosphere appears to coincide roughly with the 450°-500°C isotherm, which is close to the estimated slab neutral plane (Seno and Yamanaka, 1996; Contreras-Reyes et al., 2008). As a consequence of bending at the trench, the upper part of the plate should be in tension above a neutral plane, defining the limit between tensional and compressional stress regimes. The neutral plane for the Nazca slab, in the vicinity of the JFR, is estimated to be ~ 30 km from slab surface (Clouard et al., 2007). This roughly agrees with depth limits of the aftershocks for the 9 April 2001 outer rise event and the 13 June 2005 Tarapacá event (Fromm et al., 2006; Delouis and Legrand, 2007; Peyrat and Favreau, 2010), as well as with our present case (Fig. 4). The compressional regime can be envisaged as providing a barrier for normal fault propagation (Clouard et al., 2007). In this framework, the rupture that originally formed the 2003 seismic plane may have been limited to the topmost 35 ± 5 km of the slab by the stress regime.

Because active volcanism is observed vertically above the seismic sequence, indicating partial melting of the mantle wedge, we propose that the slab starts dehydrating near 100 km depth, and that the mainshock results from the dehydration embrittlement of the oceanic crust. A possible dehydrating candidate at ~ 100 km depth is lawsonite-eclogite, which undergoes continuous dehydration with increasing pressure from ~ 75-300 km depth (Yamasaki and Seno, 2003).

### *2.2.7.5 Conclusions*

The January 7, 2003 $M_w$ 5.7 normal faulting event (70.30°W, 33.77°S; focal depth ~ 113 km) and its aftershocks define a fault plane of (35 ± 5) x (10 ± 2) $km^2$ in the top half of the subducting Nazca slab underneath central Chile, with strike parallel to the seafloor spreading fabric, dipping ~ 60° from the slab surface, and cutting the oceanic mantle by 35 ± 5 km (Fig. 3 and 4). A comparison with outer rise tensional events leads to the hypothesis that this and similar seismic sequences at intermediate-depths in subducting slabs are related to the reactivation of outer rise faults formed during plate flexure. The spatial distribution of the aftershocks inside the slab appears to be controlled by the tensional stress regime in the upper part of the slab. The frequent occurrence of events with similar focal mechanisms at ~ 100 km depth shows that the slab is mechanically weakened at these depths. The proposed triggering mechanism for the January 2003 mainshock is dehydration embrittlement of the oceanic crust.

### *2.2.7.6 Acknowledgements*

The authors are grateful to Benoît Derode, Swann Zerathe and Flore Barat for their constructive comments and help in processing figures. Local data were obtained thanks to projects FONDECYT 1020972-1050758 and IRD-Géoazur. Marianne Marot and Guust Nolet are supported by the GlobalSeis project (ERC 226837). Giorgio Ranalli's participation in this project is supported by a

grant by NSERC (Natural Sciences and Engineering Research Council of Canada). The careful comments of two reviewers were very useful in preparing the final version of this paper.

### *2.2.8 The Double Seismic Zone of Central Chile: Details Revealed for the First Time*

JGR | Journal of Geophysical Research AGU American Geophysical Union

JOURNAL OF GEOPHYSICAL RESEARCH: SOLID EARTH, VOL. 118, 1–14, doi:10.1002/jgrb.50240, 2013

# A double seismic zone in the subducting Juan Fernandez Ridge of the Nazca Plate (32°S), central Chile

M. Marot,[1] T. Monfret,[1] M. Pardo,[2] G. Ranalli,[3] and G. Nolet [1]

Received 8 January 2013; revised 31 May 2013; accepted 5 June 2013.

## Abstract

The region of central Chile offers a unique opportunity to study the links between the subducting Juan Fernandez Ridge, the flat slab, the Double Seismic Zone (DSZ) and the absence of modern volcanism. Here, we report the presence and characteristics of the first observed DSZ within the intermediate-depth Nazca slab using two temporary seismic catalogues (OVA99 and CHARSME). The lower plane of seismicity (LP) is located 20-25 km below the upper plane (UP), begins at 50 km depth and merges with the lower plane at 120 km depth, where the slab becomes horizontal. Focal mechanism analysis and stress tensor calculations indicate that the slab's state of stress is dominantly controlled by plate convergence and overriding crust thickness: Above 60-70 km depth, the slab is in horizontal compression, and below, it is in horizontal extension, parallel to plate convergence, which can be accounted for by vertical loading of the overriding lithosphere. Focal mechanisms below 60-70 km depth are strongly correlated with offshore outer rise bend faults, suggesting the reactivation of pre-existing faults below this depth. The large interplane distances for all Nazca DSZs can be related to the slab's unusually cold thermal structure with respect to its age. Since LPs globally seem to mimic mantle mineral dehydration paths, we suggest that fluid migration and dehydration embrittlement provide the mechanism necessary to weaken the rock and that the stress field determines the direction of rupture.

**Keywords***:*
Nazca subducting slab; Central Chile; Double Seismic Zones; focal mechanisms; stress tensor

### 2.2.8.1 Introduction

In central Chile, the Nazca plate and Juan Fernandez Ridge subduct beneath the South American continental lithosphere. Two temporary local seismic campaigns were carried out over central Chile-western Argentina (29°-34°S) and enabled the detection of a Double Seismic Zone (DSZ) in the region (Fig. 1). The DSZ is most noticeable along the Juan Fernandez Ridge (JFR) track, an aseismic volcanic chain subducting beneath South America. This DSZ was first mentioned by *Pardo et al.* [2004].

DSZs consist of two planes of seismicity, more or less parallel to one another, located within the subducting oceanic slab at intermediate depths (50-200 km). An exception is *McGuire and Wiens*'s [1995] apparent recognition of one at ~ 600 km of depth within the Tonga slab. In all cases, the upper seismic plane (UP) locates within or near the oceanic crust, as verified by seismic tomography, while the lower seismic plane (LP) locates at variable depths within the oceanic mantle. The planes are separated by a region of reduced seismicity. They are observed at least once in every subduction zone, and are therefore suggested as ubiquitous features of subduction zones [*Brudzinski et al.,* 2007]. The first and best occurrence of a DSZ and also the much rarer Triple Seismic Zone (TSZ), are found in the Pacific slab beneath northern Honshu, Japan, with 30-40 km and ~ 10 km of separation distances between the planes, respectively [*Hasegawa et al.,* 1978; *Seno and Pongsawat,* 1981; *Kawakatsu and Seno,* 1983].

Recent improvements in station coverage and data processing tools have enabled DSZs to be increasingly and more accurately detected, with separation distances as small as 9 km, such as in northern Chile [*Rietbrock and Waldhauser,* 2004]. Previous studies also suggest their presence when layers of different focal mechanisms are observed (e.g. *Comte and Suarez* [1994]). However, hypocentral locations have uncertainties that sometimes are larger than the suggested separation between UP and LP, rendering their recognition and measurement difficult. A list of global DSZ occurrences and their reported characteristics is shown in Table 1.

There are a few global characteristics common to all DSZs that can be recognized: (i) LPs begin beneath the plate interface at ~ 50 km depth; (ii) UPs and LPs usually merge between 100-150 km depth; and (iii) UPs are composed of more events with smaller magnitudes than LPs [*Fujita and Kanamori,* 1981]. An attempt to classify DSZs into three classes according to their focal mechanism distributions was made by *Kao and Rau* [1999]: (a) 'Type I': compression along UPs and tension along LPs (e.g. Japan, Kurile); (b) 'Type II': tensional UPs and compressional LPs (e.g. beneath southern North Island in New Zealand, north of the Cape Mendocino Triple Junction in Cascadia, and Cook Inlet in Alaska); and (c) 'Type III': lateral compression in the shallowest part of the DSZ (due to plate convergence), and downdip tension in the deeper part (due to slab pull) (e.g. Philippine Sea plate beneath Taiwan).

Earthquakes reflect the state of stress of the lithosphere. A subducting plate accumulates stress via several mechanisms: plate interaction, slab pull, mantle viscous drag, thermal stresses, slab bending and unbending, and basalt-eclogite transformations in the crust [*Fry et al.,* 2009]. These are in turn influenced by convergence rate, subduction angle, slab age, subduction rollback, mantle viscosity structure and deeper mantle phase transitions [*Fry et al.,* 2009]. *Brudzinski et al.* [2007] described a positive correlation between separation distances in seismic planes in DSZs and slab ages from global observations. This, however, does not match our data, which show a larger separation distance. What controls DSZ global occurrence, widths, depth limits, tendencies for merging at depth and stress distribution is still a subject of debate.

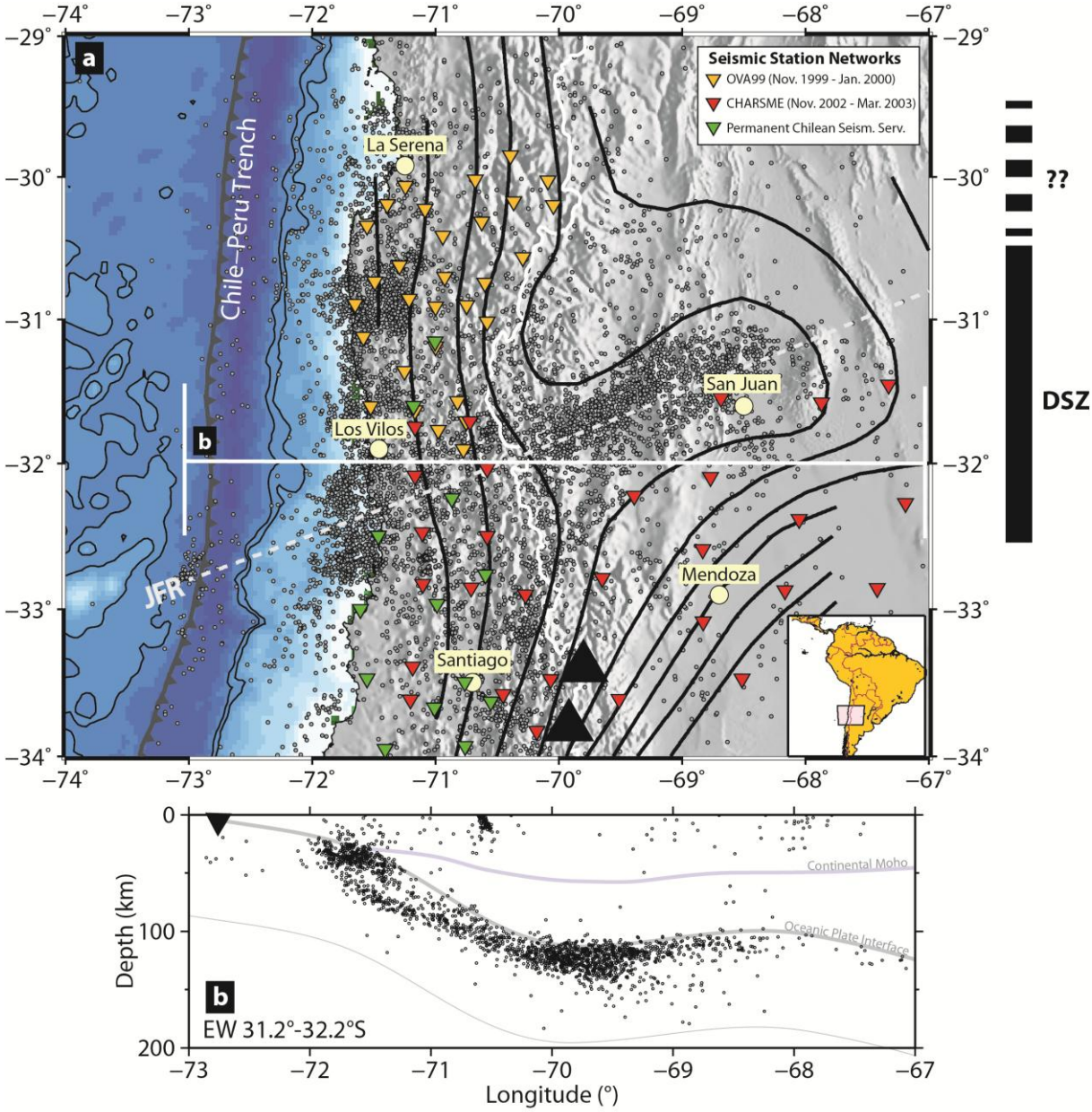


**Fig. 1**: *Regional seismic context. a) Plan view: Yellow and red inverted triangles represent the OVA99 and CHARSME temporary seismic station network, respectively; circles are the recorded seismicity. Dashed white line indicates the subduction track of the Juan Fernandez Ridge (JFR). Solid lines are isodepth contours (every 20 km) featuring the shape of the slab's surface [Anderson et al., 2007]. Black triangles denote the location of active volcanoes. Thick solid and dashed black lines, on the right, indicate the latitudes where the DSZ is clearly observed and where it is questionable, respectively. b) Vertical profile of the seismicity between 31.2°S and 32.2°S, where the Double Seismic Zone (DSZ) is well observed. Hypocenter uncertainty here is 15 km in all directions. Inverted black triangle locates the trench axis, and solid grey lines indicate the positions of continental Moho [Fromm et al., 2004], slab surface [Tassara and Echaurren, 2012] and modelled Lithosphere-Asthenosphere Boundary (LAB) [Tassara et al., 2006].*

Here, we describe the central Chilean DSZ, with an interplane distance of 20-25 km, in terms of its seismic distribution, focal mechanism solutions and their P- and T-axes orientations, as well as our stress tensor calculations for the UP and LP, in order to better understand the DSZ's occurrence and origin in this region's complex subduction dynamics. We assess the influence of the varying slab geometry and the subducting JFR on the occurrence of the DSZ, and consider possible controlling mechanisms. We also compare our observations with other known DSZs in the Nazca slab and worldwide, and conclude that the Central Chilean DSZ is a rare 'type III' case, where both seismic planes are affected by the same stress regime, which however change at a critical depth. This observation also enables us to rule out plate bending or sagging as a possible mechanism for the DSZ. Finally, our focal mechanisms indicate that subducted outer rise faults become dominantly reactivated below 60-70 km depth.

### 2.2.8.2 Regional Context

Below central Chile and western Argentina (29°-34°S), the Nazca plate subducts beneath the South American plate at a convergence rate of 6.7 ± 0.2 cm/a in the N78° direction as constrained by GPS measurements [*Kendrick et al.,* 2003]. The slab age at the trench is 33-38 Ma [*Clouard et al.,* 2007]. High plate convergence and strong plate coupling are characteristic of the region and result in back-arc compression and trench retreat [*Heuret and Lallemand,* 2005; *Heuret et al.,* 2007; *Lallemand et al.,* 2008]. Continental crustal thickness reaches 70 km below the Principal Cordillera and 55 km below the Sierras Pampeanas (Fig. 1b) [*Gilbert et al.,* 2006; *Heit et al.,* 2008, *Tassara and Echaurren,* 2012].

The slab geometry exhibits the world best observed 250 km-long ("Pampean") flat slab segment [*Isacks and Barazangi,* 1977; *Ramos et al.,* 2002; *Pardo et al.,* 2004]. The Nazca slab initially subducts everywhere along the Peru-Chile Trench at ~ 25º-30° dip, until 100 km of depth where, in central Chile between 27°-32.5°S, it becomes horizontal and underplates the overriding lithosphere [*Barazangi and Isacks,* 1976; *Cahill and Isacks,* 1992; *Araujo and Suárez,* 1994; *Pardo et al.,* 2002; *Ramos et al.,* 2002]. The Pampean flat slab is bounded to the south by a sharp transition zone (> 32.5°S) whereby the slab dip returns to normal (~ 30°) over a short distance, with a yet unconstrained along-strike mode of deformation (rupture vs. flexure). Smalley and Isacks [1987] used data from the local permanent Argentinean network INPRES to observe a flexure rather that a tear at depth < 125 km. This conclusion was later supported by Araujo and Suarez [1994] using teleseismic focal mechanisms and recently by Pesicek et al. [2012] from a tomographic model of the mantle. The northern transition zone (~ 27°S) is broader and gentler [Cahill and Isacks, 1992; Pardo et al., 2002; Anderson et al., 2007].

The causes for slab flattening are yet unclear. However, there appears to be a strong influence from the subducting Juan Fernandez Ridge (JFR) track, which should provide extra buoyancy to the already young slab. Similarly, the Peruvian flat slab segment is also correlated to the extensive Nazca Ridge plateau. In both cases, the flat slab segments are reflected on the surface by an absence of Quaternary arc volcanism, and in the case of the Pampean flat slab, also by a narrowing of the central Chilean valley for the past 9-10 Ma [*Barazangi and Isacks,* 1976; *Jordan et al.,* 1983; *Kay et al*., 1987; *Yáñez et al.*, 2002].

**Table 1**: *Global Double Seismic Zone (DSZ) observations. Plate ages at the trench are estimated from digital isochron measurements [Müller et al., 1997]. Also shown are starting and finishing depths of the lower seismic planes, maximum separation distances (width) between seismic planes, and stress regimes inferred from focal mechanisms (T: tension, C: compression).*

| Locality | Plate Age (Ma) | Starting Depth (km) | End Depth (km) | Width (km) | UP Stress | LP Stress | Reference |
|---|---|---|---|---|---|---|---|
| **Northeast Japan** Northern Honshu – Hakkaido | 133 | 50 | 160 | 30-40 | C | T | *Hasegawa et al.* [1978] |
| **Southwest Japan** Kanto | 133 | 50 | 75 | 20 | C | T | *Seno et al.* [2001] |
| **Northeast Taiwan** Ruyku Trench | 45 | 40-50 | 150 | 10-20 | C | C | *Kao & Rau* [1999] |
| **Northern Chile** (18.5°-19.5°S) | 47 | 80 | 150 | 20-25 | Mixed | Mixed | *Comte et al.* [1999]; *Dorbath et al.* [2008] |
| **Northern Chile** (20°-24°S) | 43 | 80 | 150 | 15 | T | C | *Comte and Suárez* [1994] |
| **Northern Chile** (22°S) | 43 | 80 | 130 | 9 | T | T | *Rietbrock & Waldhauser* [2004] |
| **Central Chile** (30°-32°S) | 35 | 50 | 100-120 | 30 | T | T | This study |
| **Cape Mendocino** Cascadia Trench | 10 | 15 | 25 | 9 | T | C | *Wang and Rogers* [1994] |
| **Eastern Aleutian** Shumagin Islands | 50 | 70 | 175 | 30-40 | Mixed | Mixed | *Ratchkovsky et al.* [1997] |
| **Central Aleutians** | 56 | 100 | 175 | 25 | C | T | *Engdahl and Scholz* [1977] |
| **New Zealand** Wellington Region | 90 | 50 | 80-90 | 20 | T | C | *Robinson* [1986] |
| **Kurile-Kamchatka** | 125 | 50 | 170-180 | 40 | C | T | *Kao and Chen* [1994] |
| **New Britain** | 130 | 60 | 170 | 15 | C | T | *McGuire and Wiens* [1995] |
| **New Hebrides** Vanuatu Trench | 84 | 10-40 | 80 | 50-70 | C | T | *Prévot et al.* [1994] |
| **Northern Marianas** (17°-19°N) | 170 | 60 | 180 | 30 | C | T | *Shiobara et al.* [2010] |

The JFR subduction track is characterized by dense micro-seismicity ($M_w < 5$) (Fig. 1). The JFR is a volcanic seamount chain, showing a linear increase in age inferred from magnetic anomalies. It is observed by global seismic tomography as originating from a narrow deep-seated mantle plume extruding at 97.5°W and 34°S [*Montelli et al.*, 2004; *Kopp et al.*, 2004, *Zhao*, 2007]. It extends 900 km on the seafloor, in ~ EW direction, and enters the Chilean trench near-normally at 32.5°S, subducting beneath the overriding continental plate.

The ridge migrated southward along the Peru-Chile Trench over the past 22 Ma to its current location [*Yáñez et al.*, 2002]. Its interaction with the overriding plate resulted in marginal erosion, shoreline indentation, crustal uplift and thickening on the continental side [*Fromm et al*., 2004], and a seaward shift in outer rise events on the oceanic side [*Clouard et al.*, 2007]. It also participated to the formation of a sediment barrier at 32.5°S, with a sediment-poor trench to the north, and a sediment-rich trench to the south, lasting since ~ 16 Ma [*Lowrie and Hey*, 1981], as well as probably provoking

the change of slab geometry in conjunction with the high overriding plate trenchward motion [*Pilger,* 1981; *Cahill and Isacks,* 1992; *Ramos et al.,* 2002; *Yáñez et al.,* 2002; *Martinod et al.,* 2005; 2010]. Hence, the interaction of this feature with the continental plate generates important disturbances despite its moderate size. Since the central Chilean DSZ is observed within and around the subducting JFR track, understanding whether a relationship exists between them could provide additional insight on the mechanisms that control the double-planed seismicity pattern inside a subducting slab (e.g. mechanical and compositional controls).

### 2.2.8.3 Data Analysis and Results

The regional seismicity was recorded by the two temporary seismic campaigns OVA99 (Ovalle 1999) and CHARSME (CHile ARgentina Seismological Measurement Experiment) in central Chile and western Argentina (Fig. 1a). Both networks were installed and maintained by a collaborative group from GéoAzur laboratory, France, and the Departamento de Geofísica of the University of Chile. For the CHARSME campaign, the collaboration of the University of San Juan and logistical support of INPRES in Argentina were also available.

The OVA99 seismic network was deployed in the region of Ovalle (30°-32°S, 72°-70°W) in central Chile during the period mid-November 1999 to mid-January 2000. Thirty-seven short-period three-component receivers (2 Hz and 4.5 Hz), about 30 km apart, recorded continuously the local micro-seismicity ($0.5 < Ml < 5.5$) with a sampling rate of 125 sps.

The CHARSME campaign was carried out from mid-November 2002 to March 2003 for the purpose of analyzing the regional seismotectonic features and to map the shift in subduction geometry of the Nazca slab. It comprised 29 portable broadband three-component stations (27 CMG-40T and 2 CMG-3T Guralp) that continuously recorded seismicity with a sampling rate of 125 sps. In an effort to increase station coverage and improve hypocenter determination, particularly near coastal areas, 15 permanent seismic stations (short period and broadband) from the Chilean Seismological Service of the University of Chile were also used (Fig 1a).

#### *2.2.8.3.1 Hypocenter Location*

Hypocenter location was performed by manual picking of first arrivals of P- and S-waves [*Pardo et al.,* 2004]. Initial velocity models were calculated from mining blasts for the first 20 km of depth and using the VELEST algorithm [*Kissling et al.,* 1994] for larger depths. The average 1D velocity model of least-square fit that best describes the arrival times is a 17 layer model with Vp/Vs of 1.76. Local magnitudes (Ml) were calculated (Fig. 2) for all events, accounting for maximum amplitude and hypocentral distance [*Lay and Wallace,* 1995], and calibrated such that the Ml values remain close to the Mw values available from the ISC catalog [Marot et al., 2012].

Only the most reliable events were selected with strict criteria: (i) In Fig. 1b, we show only events with maximum hypocenter uncertainties of 10 km in horizontal coordinates and 5 km in depth; and (ii) in Fig. 3, we further restrict the selection to minimum 10 seismic phases including at least 2 S-phases, and maximum RMS misfit ($\sqrt{\Sigma R_i^2}/N$ where $R_i$ is the time residual at the $i^{th}$ station) $\leq 0.6$ s. The DSZ is more noticeable when all the recorded seismicity is shown, indicating that even the events deemed ‘unreliable’ due to too few phase pickings, concentrate along the seismic planes, emphasizing the accuracy of the DSZ’s inferred geometry. Nevertheless, we chose to show only the most accurately determined events (Fig. 3). Also, we have performed the relative earthquake relocation method *HypoDD* [*Waldhauser and Ellsworth,* 2000], and found it inconclusive, with no significant difference with the initial hypocenter locations. Therefore, we deemed sufficient to show the earthquake distribution obtained with the classical location method.

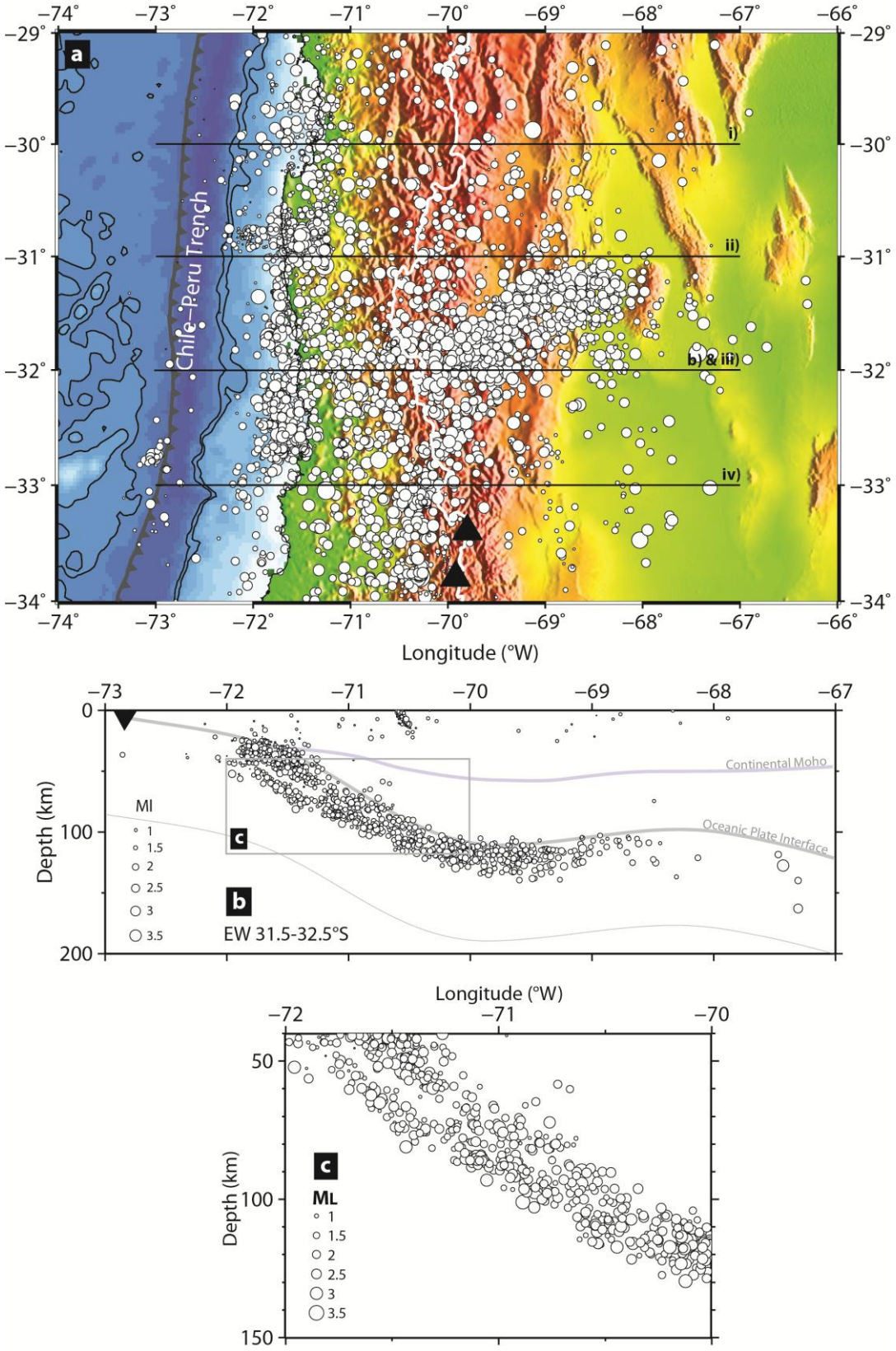


**Fig. 2**: *Earthquakes (circles) scaled on the basis of their local magnitude. a) Plan view. Horizontal lines, i) to iv), refer to the vertical profiles in Fig. 3. b) Vertical profile (also shown in Fig. 3iii). Refer to legend in Fig. 1. c) Close-up of the DSZ's seismicity and magnitude distribution.*

The DSZ clearly occurs between latitudes 30.5°S and 32.5°S (Fig. 1b), and may also be present between 29.5°S and 30.5°S, where station coverage is lacking (Fig. 3i). However, where station coverage is adequate at ~ 33°S, we have difficulty attesting it presence (Fig. 3iv).

Where we observe it clearly, the LP begins below the plate interface at 50 km of depth, as in other case studies (Table 1). Some events also locate below the trench axis at depths ~ 25-40 km (Fig. 1b and 3), possibly forming the western extension of the LP within the slab. The LP has a slightly higher seismic activity than the UP and extends downward until merging with the UP at ~ 100-120 km of depth, where the slab bends upward into horizontal subduction. The maximum interplane distance, as measured by the perpendicular distance between the two peaks in seismic activity, is 20-25 km beneath the plate interface. The magnitude distributions and standard deviations are similar along the UP and LP with an average $M_l$ of 2.3 (± 0.9) and 2.4 (± 0.6), respectively (Fig. 2b and 2c).

*2.2.8.3.2 Focal Mechanisms*

Equal-area projections of earthquake double-couple focal mechanisms were obtained from first P-wave polarities using program FOCMEC (SEISAN package; *Snoke et al.* [1984]) for the earthquakes that meet the selection criteria. In total, 1,065 focal mechanisms were calculated for the entire region. *Pardo et al.* [2004] used these results to infer the slab's state of stress at different depth intervals, but did not account for the DSZ. We show DSZ focal mechanisms across a 100 km wide profile between 31.2°S and 32.2°S (Fig. 4), where the slab geometry is constant and seismic density is highest. To increase accuracy and reliability of our results, we visually assessed every first P-wave arrivals and polarity readings, and determined nodal planes based on a minimum of 9 polarity readings allowing 1-5° increment of solution variation. We obtained 13 and 23 reliable focal solutions for the UP and LP, respectively (Table 2).

Both seismic planes indicate the same variations in normal and reverse focal mechanisms, with a clear dominant extensional faulting trend: (i) UP: 70% normal faulting, 30% reverse faulting, and (ii) LP: 80% normal faulting, ~ 20% reverse faulting. Contrary to most global observations for DBZs, there appears to be no partition in focal mechanism type between the seismic planes of the central Chilean DBZ (compare with Table 1).

However, a partitioning with depth can be noticed between normal and reverse focal mechanisms (Fig. 4b). Although a strong strike-slip component is pervasive at any depth, events with reverse mechanisms tend to be separated from normal mechanisms at the 60-70 km depth limit, with normal mechanisms occurring almost exclusively below this limit. Focal solutions above this depth show no particular strike pattern, but tend to have dip angles of 60°E (Fig. 4c). Below this depth a remarkable change in strike pattern occurs, strongly trending NS, parallel to the trench axis, and dipping 40°W, indicating a dip angle of ~ 70° from the slab surface.

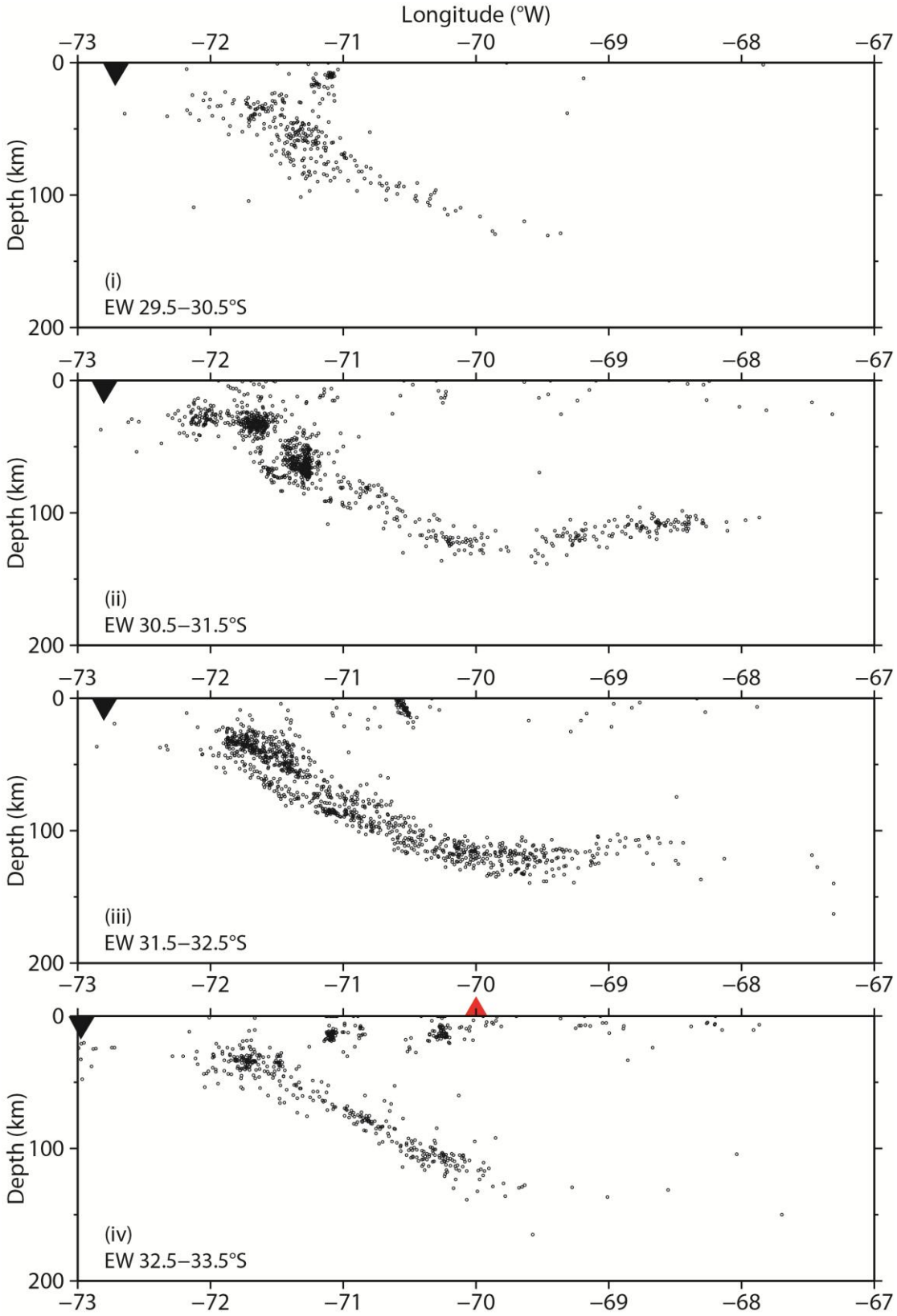


**Fig. 3**: *EW vertical cross-sections of the earthquake distribution (see Fig. 2 for locations), illustrating the NS extent of the DSZ (also shown in Fig. 1). Hypocenter uncertainty here is 5 km in the vertical and 10 km in the horizontal direction, respectively. Inverted black triangles and red triangle show the trench axis and active volcanoes, respectively.*

#### *2.2.8.3.3 P- and T-axes*

The discrepancy between the types of focal mechanisms at the 60-70 km depth limit can be observed also from the variations in azimuth and plunge orientations of the P- and T-axes (Fig. 5). Above 60-70 km, P-axes strike mainly with an EW component and a slabdip plunge oscillating between 0° and 30°E (Fig. 5a). Below 60-70 km, their strike is variable with sub-vertical predominant plunge angles between 60° and 90° (Fig. 5b). On the contrary, T-axes above 60-70 km have variable strikes with essentially high plunge angles between 60° and 80° (Fig. 5a), while below 60-70 km they have a well defined EW strike tendency, similar to P-axes above 60-70 km (Fig. 5a), with slabdip plunge angles between 0° and 30°E (Fig. 5b). *Anderson et al.*, [2007] demonstrated, using local earthquake focal mechanisms, that T-axes along the flat slab are sub-horizontal but trend normal to the directions of subduction and the JFR track. This shows that the slab is being stretched sideways as a consequence of the slab's kinematics. In addition, they show that P-axes are sub-horizontal and parallel to the direction of subduction and the JFR path. These strong differences in P- and T-axes orientations between the flat slab and the DSZ suggest that, despite their proximity, they are not influenced by the same tectonic regime. The slab is in slabdip compression down to 60-70 km depth, in slabdip extension between 60-70 km and 100-120 km depth, and in slabdip compression but laterally stretched along the flat part.

#### *2.2.8.3.4 Stress Tensor*

The stress tensor was calculated based on the code developed by Delouis [*Delouis et al.*, 2002]. Considering the average scalar product of the differences between the slip vectors, determined by the focal mechanisms, and those predicted by the stress tensors, our solutions are presented in Fig. 6 at three levels of confidence: (1) the best fitting model (the highest score) denoted by colored circles, (2) the second best solutions (grey circles), situated between the best score and 97% of the best score, and (3) the third best solutions (white circles), situated between 94% and 97% of the best score. Initially, we attempted to find a stress tensor accounting for the UP and LP separately, as is commonly shown in other studies. This attempt generated a poorly constrained solution with low scores (UP: 63%; LP: 59%). This suggests that there are perhaps insufficient data to well constrain the solution or that the central Chilean DSZ seismicity is not dominated by a stress regime such as bending/unbending, which would tend to dissociate the seismic planes into two separate stress regimes (e.g. numerous examples in the Pacific slab; Table 1).

The focal mechanisms that do not fit well the models for the UP and LP are located in the 60-70km depth range. We also calculated stress tensors for the UP and LP above and below 60-70 km depth ("UP < 60-70 km", "UP > 60-70 km", "LP < 60-70 km" and "LP > 60-70 km" in Fig. 6). The only solutions that give good results (best score > 95%) are those for the UP > 60-70 km and the LP < 60-70 km. However, a constraint on these results lies in the few data used in each group, particularly for UP > 60-70 km. Since stress tensor solutions for above 60-70 km of depth are similar for the two planes, regardless of their score, and likewise for those below 60-70 km, we chose to group them together in the two depth ranges. Because we find both types of focal mechanisms between 60 and 70 km, in order to identify which group they belong to, we incorporated them individually into our stress tensor calculations, and verified that a good fit was maintained. Although we are restricted to a number of 9 focal mechanisms for above 60-70 km, and 18 for below 60-70 km, we obtained two coherent and well constrained stress tensor solutions for this area (Fig. 6).

**Table 2**: *Focal mechanism solutions obtained for the profile 31.2°-32.2°S. Focal mechanisms 1-9 refer to events above 65 km of depth (red beach balls in Fig. 4), and 10-36 to those below this depth (blue beach balls in Fig. 4). Symbol * refers to UP events.*

| | Long (°) | Lat (°) | Z (km) | Ml | Strike1 (°) | Dip1 (°) | Rake1 (°) | Strike2 (°) | Dip2 (°) | Rake2 (°) |
|---|---|---|---|---|---|---|---|---|---|---|
| **1*** | -71.375 | -31.319 | 57.8 | 2.2 | 251 | 14 | 45 | 117 | 80 | 100 |
| **2*** | -71.302 | -31.737 | 59.8 | 2.9 | 145 | 47 | 69 | 354 | 47 | 111 |
| **3*** | -71.147 | -31.674 | 62.8 | 1.5 | 148 | 60 | 35 | 39 | 60 | 145 |
| **4*** | -71.358 | -31.881 | 52.5 | 1.0 | 206 | 30 | 80 | 38 | 61 | 96 |
| **5** | -71.510 | -32.033 | 66.5 | 2.7 | 174 | 26 | 78 | 7 | 65 | 96 |
| **6** | -71.595 | -32.189 | 57.5 | 1.6 | 345 | 75 | -89 | 161 | 15 | -94 |
| **7** | -71.664 | -32.138 | 52.9 | 2.2 | 190 | 56 | 72 | 40 | 38 | 115 |
| **8** | -71.541 | -31.394 | 68.6 | 1.5 | 177 | 81 | 70 | 64 | 22 | 155 |
| **9** | -71.455 | -31.388 | 67.0 | 2.4 | 262 | 56 | 53 | 135 | 49 | 132 |
| **10*** | -70.952 | -31.394 | 78.7 | 3.0 | 1 | 58 | -60 | 134 | 43 | -1 |
| **11*** | -71.375 | -31.319 | 57.8 | 2.2 | 251 | 14 | 45 | 12 | 81 | -105 |
| **12*** | -71.067 | -31.887 | 74.8 | 1.7 | 193 | 51 | -76 | 351 | 41 | -107 |
| **13*** | -70.938 | -31.916 | 71.4 | 1.2 | 191 | 75 | -84 | 349 | 16 | -111 |
| **14*** | -70.642 | -32.088 | 87.0 | 1.5 | 180 | 80 | -89 | 354 | 10 | -96 |
| **15*** | -70.553 | -31.554 | 91.0 | 1.3 | 187 | 65 | -84 | 353 | 26 | -103 |
| **16*** | -70.648 | -31.604 | 83.0 | 1.5 | 187 | 65 | -84 | 353 | 26 | -103 |
| **17** | -70.725 | -31.747 | 100.5 | 1.9 | 180 | 40 | -89 | 359 | 50 | -91 |
| **18** | -70.692 | -31.965 | 98.1 | 1.9 | 350 | 25 | -89 | 169 | 65 | -90 |
| **19** | -71.138 | -32.064 | 87.2 | 3.2 | 166 | 81 | -46 | 265 | 45 | -167 |
| **20** | -71.238 | -31.868 | 82.9 | 2.5 | 180 | 46 | -75 | 339 | 46 | -105 |
| **21** | -71.051 | -31.852 | 92.4 | 2.9 | 346 | 59 | -15 | 84 | 77 | -148 |
| **22** | -70.534 | -31.673 | 111.5 | 2.8 | 196 | 78 | -50 | 300 | 41 | -162 |
| **23** | -70.541 | -31.687 | 109.1 | 2.8 | 196 | 36 | -89 | 15 | 54 | -91 |
| **24** | -71.524 | -32.020 | 70.1 | 2.9 | 218 | 4 | 90 | 38 | 86 | 90 |
| **25** | -71.525 | -31.397 | 71.9 | 3.1 | 50 | 90 | 84 | 320 | 6 | 180 |
| **26** | -71.251 | -32.044 | 77.2 | 1.9 | 185 | 35 | -89 | 4 | 55 | -91 |
| **27** | -71.374 | -31.544 | 74.6 | 1.7 | 39 | 35 | -41 | 164 | 68 | -118 |
| **28** | -71.019 | -31.446 | 90.4 | 1.9 | 196 | 42 | -66 | 345 | 52 | -110 |
| **29** | -71.323 | -31.483 | 77.9 | 1.5 | 216 | 80 | 18 | 123 | 72 | 169 |
| **30** | -71.006 | -31.521 | 95.0 | 1.0 | 185 | 45 | -82 | 354 | 46 | -98 |
| **31** | -71.140 | -31.420 | 84.3 | 1.3 | 60 | 48 | -47 | 186 | 57 | -127 |
| **32** | -71.022 | -31.536 | 89.0 | 1.8 | 198 | 83 | 45 | 101 | 45 | 170 |
| **33** | -71.171 | -31.457 | 81.8 | 1.6 | 47 | 14 | -44 | 180 | 80 | -100 |
| **34*** | -71.014 | -31.702 | 67.0 | 2.2 | 235 | 32 | -35 | 356 | 72 | -117 |
| **35*** | -71.139 | -31.777 | 61.4 | 1.2 | 34 | 88 | -29 | 125 | 61 | -178 |
| **36** | -71.556 | -31.970 | 65.0 | 3.1 | 328 | 68 | -83 | 130 | 23 | -107 |

Our preferred stress tensor solution for the central Chilean DSZ is the one shown in Fig. 6. In both cases (above and below 60-70 km of depth), the σ3 axis is very well determined, with azimuth consistently parallel to direction of convergence (N78°), and plunging sub-vertically above 60-70 km depth and sub-horizontally below 60-70 km depth. The solutions for the σ1 and σ2 axes for both above and below 60-70 km depth, indicate that they interchangeable, reflecting heterogeneity in the main acting forces in the region. However, if we consider only the best fitting models with the best scores for each case (colored dot in Fig. 6), we observe that: (i) above 60-70 km of depth, σ1 is sub-horizontal and σ3 is sub-vertical, both trending parallel to the direction of convergence with a shape factor of -1.41 which indicates predominant reverse faulting [Rivera and Cisternas, 1990]. The σ2 axis is horizontal and oriented NS. This solution of convergence-parallel compression is in good agreement with the region's tectonic context of high convergence rate and degree of interplate coupling. Furthermore, similar stress tensor solutions were obtained for the backarc crust (Fig. 7) [Pardo et al., 2002; Alvarado et al., 2005]. (ii) Below 60-70 km of depth, the σ1 axis is sub-vertical and σ3 is sub-horizontal trending parallel to the direction of convergence, and the shape factor indicates predominant normal faulting (1.13). The σ2 axis is identical to that above 60-70 km depth. This suggests that the slab is in sub-horizontal extension below 60-70 km depth. These results are in agreement with Pardo et al. [2002] and Salazar [2005] results for this region.

### 2.2.8.4 Discussion

In this work, we present evidence for a DSZ in central Chile with an interplane distance of 20-25 km. The LP is best identified between latitudes ~ 30.5° and 32.5°S, coincident with the location of the JFR subduction track, where seismic activity is highest, but is still noticeable at latitude 29.5°S, amounting to a total trench-parallel length of ~ 300 km. The uneven seismic coverage of the region renders its relationship with the JFR unclear. Nevertheless, if we consider the width proposed by *Kopp et al.* [2004] and assume that it remains constant with depth, the DSZ is found in a geographical range that is broader than the JFR track, suggesting that it is perhaps not directly related to the JFR properties.

Our observation of the DSZ ends at ~ 32.5°S, close to the southern transition zone, where good station coverage existed during our data recording but seismic rate falls. This means that either it exists further south but is concealed by low seismicity, or it is truly non-existent due to local factors causing the reduction in seismicity and the LP to vanish. Other seismic studies southward of our region [e.g. *Campos et al.,* 2002; *Haberland et al.,* 2009] have not reported any DSZ. Since the geographical extent of the central Chilean DSZ appears to be constrained by the regions bounding the flat slab, one can suppose that it is affected by changes in slab geometry. Indeed, the return to normal subduction creates increased slab stresses, due to localized lateral deformations, as demonstrated by *Anderson et al.,* [2007], and changes in the system's thermal state, as hot asthenosphere is re-introduced into the corner wedge [*Wada and Wang,* 2009; *Syracuse et al.,* 2010], a process witnessed by the return of active volcanism at the surface. Therefore, we expect the contrast in slab temperature and rheology that arises between flat and normal subduction regions to affect the viability of the central Chilean DSZ, particularly along its more abrupt southern margin.

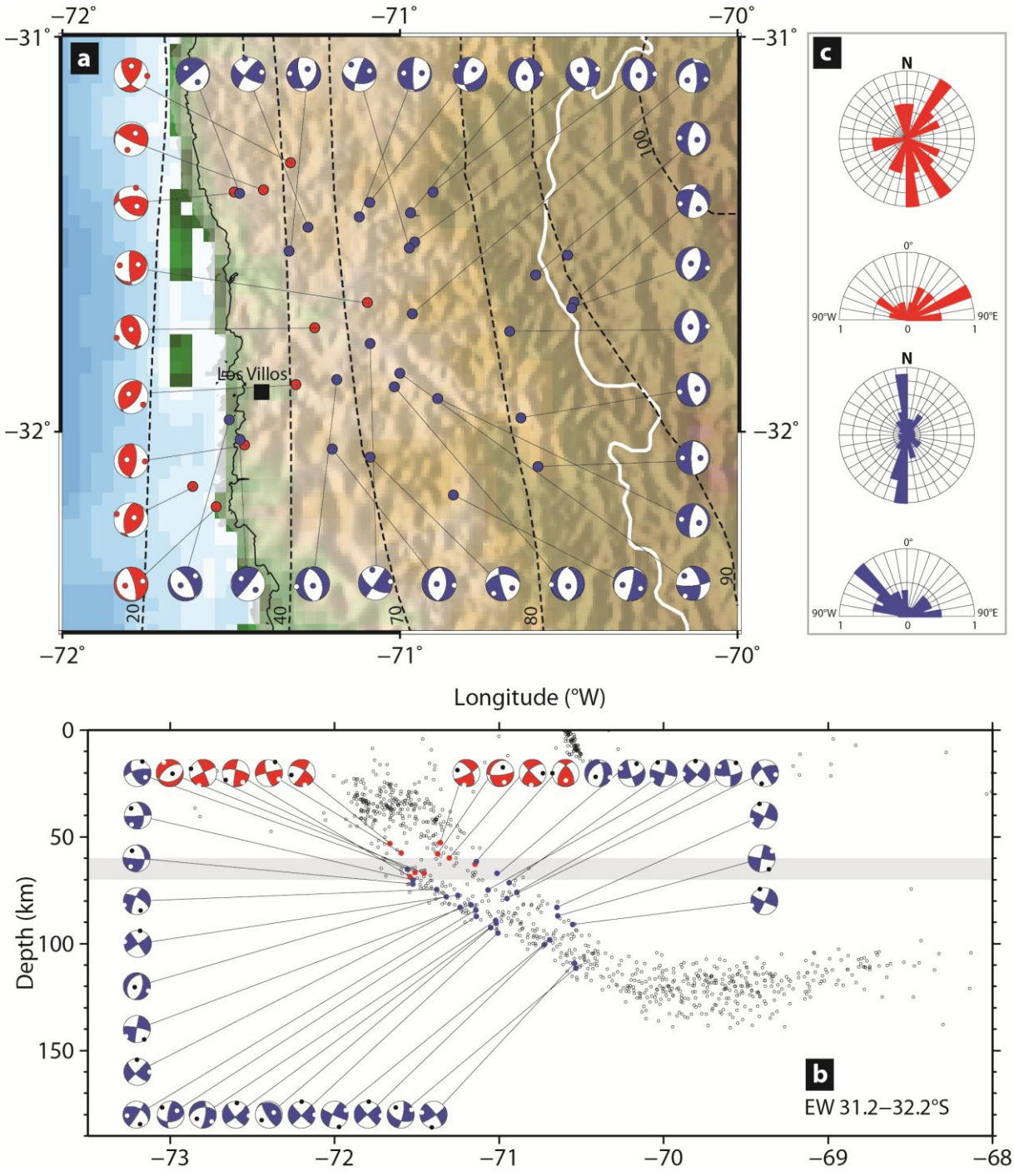


**Fig. 4**: *Focal mechanism solutions along profile 31.2°-32.2°S (also shown in Fig. 1b). a) Plan view: Red and blue focal mechanisms represent those above and below the depth limit of 60-70 km, respectively. Dotted lines indicate the isodepth contours. Thick white line is the political border between Chile and Argentina. b) Vertical profile: Colour code as in (a). Thick grey line shows the 60-70 km depth limit. c) Strike and dip rose diagrams of the focal mechanism solutions with focal depth < 60-70 km (red) and > 60-70 km (blue).*

Within the Nazca slab, two other DSZs have been reported to date, both in northern Chile. They are located side by side, one at 18.5-19.5°S [*Comte et al*., 1999; *Dorbath et al*., 2008] and the other at 20-24°S [*Comte and Suarez,* 1994; *Rietbrock and Waldhauser*, 2004]. They exhibit two different stress patterns and interplane distances (see Table 1). This rapid change in DSZ characteristics along strike suggests that they reflect changes in ambient stresses and are complex features of slabs that do not necessarily connect smoothly with one another.

Several other studies of global DSZs recognized their sensitivity to slab age, particularly in regard to their interplane distances. The interplane distance observed for the central Chilean DSZ is 20-25 km, and is unexpectedly large compared to *Brudzinski et al.*'s [2007] estimate of 0.14 km/Ma, deduced from global earthquake catalogue EHB [*Engdahl et al.,* 1998]. The central Chilean DSZ could not be detected using this database, because of the region's too dense seismicity. According to *Brudzinski et al.* [2007] a plate of age of ~ 40 Ma, as in our case, should correspond to an interplane distance of ~ 6 km, and not 20-25 km. The same discrepancy applies for northern Chile: for a slab age of 50 Ma, the expected interplane distance is ~ 7 km, and not 20-25 km [*Comte et al*., 1999; *Dorbath et al.*, 2008].

*Dorbath et al.* [2008] proposed that the slab's unusually low thermal structure relative to its age accounts for the northern Chilean DSZ interplane distances. Heat flow studies offshore central Chile show much lower values than predicted (24-31 $mW/m^2$ [*Grevemeyer et al.,* 2003; 2005] compared to the expected ~ 90 $mW/m^2$ for a lithosphere age of ~ 32 Ma; (*Stein,* [2003]). Since the northern and central Chilean DSZs are far away from another, but located within the same slab, all showing unexpectedly large widths, we suggest that, in the case of the Nazca slab, its age is not the direct cause to its DSZs' interplane distances, but rather other factors, such as thermal state, dehydration reactions and consequent fluid migration, may play an important role.

**Fig. 5**: *Strike and dip orientations of P- and T-axes, determined from the focal mechanisms at a) < 60-70 km depth (red), and b) > 60-70 km (blue). The strike and dip orientations are shown by (1) stereonet representations, as lower hemisphere projections, with the slab orientation shown by the thick grey great circle at the DSZ's depth, (2) rose diagrams, and (3) EW vertical profiles of the dip angles, projected in the EW direction in order to show the relation with the slab dip.*

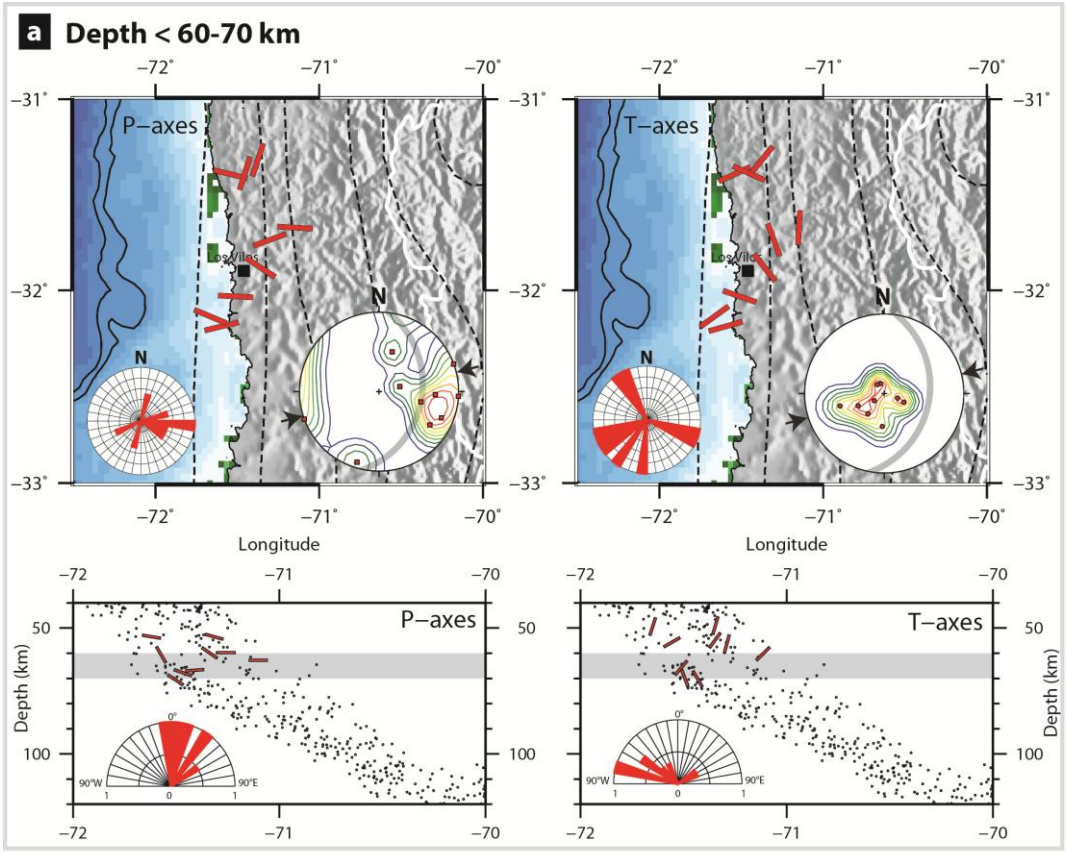
a Depth < 60-70 km
P–axes
T–axes
N
Longitude
Depth (km)
b Depth > 60-70 km

Considering the impact of plate convergence on the slab, as emphasized by *Fujita and Kanamori* [1981], the central Chile DSZ belongs to what *Kao and Rau* [1999] termed the 'type III' model for the Philippine Sea plate DSZ, characterized by compression in the shallow part and extension in the deeper part. In our case, the depth limit of 60-70 km corresponds to the maximum depth of the continental crustal root jamming into the subducting plate. The estimated stress tensor for these depths shows that the slab is undergoing horizontal compression in the upper 60-70 km depth, and affecting at least 20-25 km of the slab from its upper surface. The same stress tensor solutions fit the backarc crust (Fig. 7), ~ 800 km eastward from the trench, emphasizing the large-scale and dominant role of plate convergence in the resulting compressional regime. On the other hand, inferred P- and T-axes for the DSZ below 60-70 km depth until the slab fold hinge, where the DSZ seems to disappear, indicate that the slab is dominated by horizontal and slabdip tension. The flat slab segment is in horizontal/slabdip compression with sideways extension influenced by the slab geometry [*Anderson et al.,* 2007]. The Nazca slab's extensional regime between 60-70 km and the depth of horizontal subduction can be explained by the fast westward motion of the overriding plate that results in trench retreat [*Lallemand et al.,* 2008], and by its downward loading on the subducting plate, inducing slab stretching which is likely accommodated by reactivation of pre-existing faults, as suggested by the dominance in normal focal mechanisms and focal plane striking parallel to the trench axis at these depths. In turn, the slab's compressive regime above 60-70 km depth can be explained by the rapid horizontal plate convergence, strong plate coupling, rapid subduction rate, buoyant lithosphere and subducting JFR topography.

Dehydration reactions are commonly proposed as a triggering mechanism to explain the presence and characteristics of DSZs (e.g. *Yamasaki and Seno,* [2003]; *Hacker et al*., [2003]; *Hacker,* [2008]; *van Keken et al.,* [2011]). The central Chilean DSZ shows several characteristics compatible with dehydration reaction patterns: (i) unexpectedly large interplane distance with respect to slab age, (ii) merging of both seismic planes with depth, and (iii) deep-seated seismicity beneath the trench axis at ~ 40 km depth (Fig. 3), as predicted by dehydration paths. If dehydration embrittlement, fluid migration or local weakening [*Dorbath et al.,* 2008; Because dehydration paths for mantle phases do not match the UP seismicity band, it is widely acknowledged that UPs represent the breakdown of oceanic crust (meta-basalts and meta-gabbros; e.g. amphibolites and blueschists) to anhydrous eclogite facies [*Kirby et al.,* 1996; *Peacock,* 2001; *Hacker et al.,* 2003; *van Keken et al.,* 2011]., associated to the presence of fluids, are the effective generators of seismicity for the central Chilean DSZ, the Nazca lithosphere must be hydrated down to at least 20-25 km, where we observe the LP. The continuous and denser seismicity along the LP, compared to the UP, suggests that the role of fluids is more prominent than along the UP, and that dehydration reactions and/or fluid migration are continuously ongoing in time and space.

Evidence of plate hydration in the region is revealed by the low heat flux values offshore central Chile, which reflect active hydrothermal convection along the outer rise [Grevemeyer et al., 2003; 2005]. The region's bathymetry indicates that the outer rise is intensely fractured, as shown by the presence of: (i) reactivated seafloor fabric, (ii) trench-parallel faults, and (iii) JFR-parallel faults [*Ranero et al.,* 2005]. Widespread reduced upper mantle velocities beneath and around the JFR axis further indicate that the Nazca plate is already hydrated before its passage over the outer rise [*Kopp et al*., 2004]. We have indicated earlier in the discussion that the JFR may be an influencing factor for the DSZ in this region and, because of the similarities with dehydration reaction paths, we suggest that there is a possible relationship with the JFR's degree and depth of hydration.

Our focal mechanisms for the DSZ below 60-70 km depth indicate a strong tendency for trench-parallel strike orientations (~ NS) consistent with the region's outer rise bend-faults [*Ranero et al.,*

2005]. Furthermore, their dominant dip is 40°W, amounting to 70°W when accounting for slab dip, which is representative of typical normal faults at Earth's surface. This observation provides evidence that outer rise faults are preserved in the subducting slab and become reactivated around 60-70 km depth in this region (see *Marot et al.* [2012]). In Middle America, *Warren et al.* [2008] reported the reactivation of outer rise faults at depth ranges of 35-85 km. Dehydration embrittlement, fluid migration and local weakening [*Dorbath et al.,* 2008; *Faccenda et al.,* 2009*;* 2012] could be the triggering mechanism for fault plane reactivation at intermediate-depths [*Jung et al.,* 2004].

How fluids manage to penetrate the lithosphere to depths of 20-40 km may be accounted for by a model by *Faccenda et al.* [2009] invoking a mechanism of 'seismic pumping' which takes place during an event along bend faults, and which enhances water migration to deeper levels, down to ~ 50-70 km depth. The association of plate unbending with dehydration reactions is a hypothesis that was also put forward by *Dorbath et al.* [2008] to explain the northern Chilean DSZ between 18.5°-19.5°S, and by *Faccenda and Mancktelow* [2010] for global models. These authors propose that fluids trapped in the oceanic mantle are released from the tensile lower part of the slab due to slab unbending, and then ascend due to buoyancy, and accumulate at the base of the compressional upper part of the slab. This would create a fluid-rich layer, where pore fluid pressure exceeds a critical threshold and produces seismic failure, accounting for the LPs of DSZs. However, we do not observe the effects of slab unbending along the central Chile DSZ, where the LP is under tension for most of the DSZ's depth extent, probably because the influence of plate interaction is stronger.

The three most commonly evoked dehydrating mantle minerals when discussing global LP occurrences are antigorite, chlorite and 10Å-phase. *Fumagalli and Poli* [2005] proposed that antigorite breakdown is responsible for the LPs in water-saturated colder slabs, and chlorite-10Å-phase breakdown in under-saturated hotter slabs. *Fumagalli et al.* [2001] demonstrated that the dehydration of 10Å-phase, from the breakdown of chlorite and/or talc as P-T conditions increase, results in continuous volatile release rather by discrete fluid pulses, and this process could possibly be responsible for the LP's higher and uninterrupted seismicity. Also, the merging depth between UP and LP depends on the slab's thermal structure and water content. *Yamasaki and Seno* [2003] and *Brudzinski et al.* [2007] matched most DSZs with the breakdown of antigorite, and merely a few with chlorite dehydration. The latter cases are associated with anomalously large interplane distances. Furthermore, *Babeyko and Sobolev* [2008] observed that dehydration reactions are mainly temperature driven, rather than pressure dependent. This is further evidence that the distance of separation is primarily controlled by the slab's thermal structure rather than absolute age. Hence, the large interplane separation of the central Chilean DSZ could be explained by the slab's thermal structure and consequent preference for the breakdown of chlorite minerals. The depth of merging (~ 120 km), would be where complete devolatization of the slab occurs [*Fumagalli et al.,* 2001].

Because dehydration paths for mantle phases do not match the UP seismicity band, it is widely acknowledged that UPs represent the breakdown of oceanic crust (meta-basalts and meta-gabbros; e.g. amphibolites and blueschists) to anhydrous eclogite facies [*Kirby et al.,* 1996; *Peacock,* 2001; *Hacker et al.,* 2003; *van Keken et al.,* 2011]. These reactions provoke a 10% bulk volume reduction [*Kirby et al.,* 1996], which could explain the UP's extensional nature below 60-70 km with crustal stretching and normal faulting.

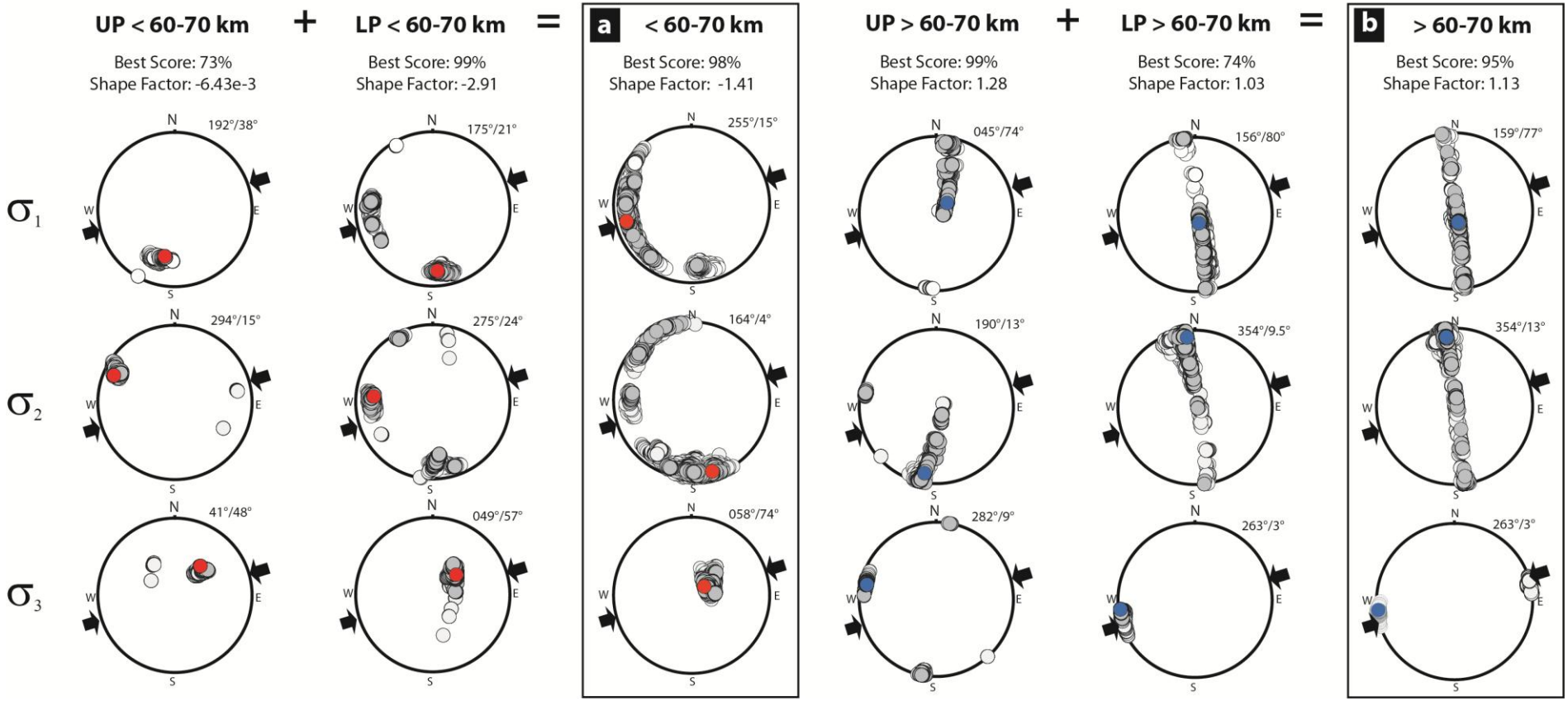


**Fig. 6**: *Stress tensor solutions ($\sigma_1$, $\sigma_2$, $\sigma_3$-axes, azimuth/plunge orientations, best score and shape factor) projected on lower hemispheres, calculated for the focal mechanisms shown in Table 2 and Fig. 4. Black arrows indicate the direction of convergence of Nazca Plate. The best solutions (best score) are indicated by red (< 60-70 km depth) and blue (> 60-70 km depth) circles. All other solutions found at levels > 97% and > 94% of the best score are shown in grey and white circles, respectively. Our selected stress tensors for the region above and below the 60-70 km depth limit, and used for our interpretation, are shown in a) and b), respectively. A shape factor < 0 corresponds to a compressional regime, between 0 and 1 to a strike-slip regime, and > 1, to an extensional regime [Rivera and Cisternas, 1991*

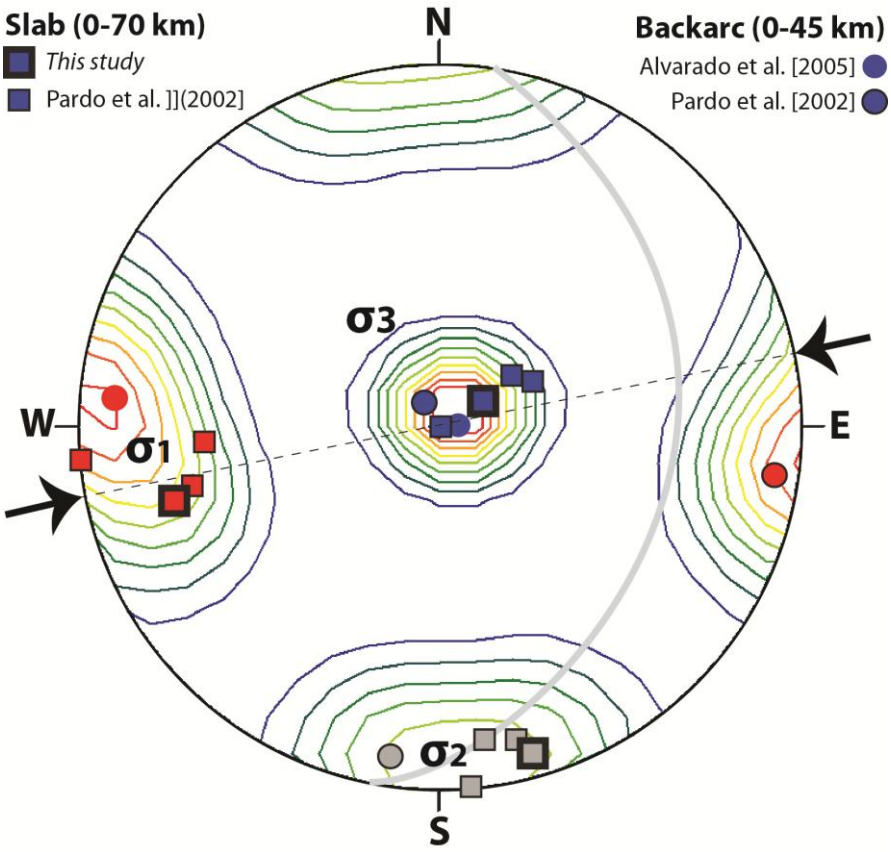


**Fig. 7**: *Stress tensor orientations ($\sigma_1$: red, $\sigma_2$: grey, $\sigma_3$: blue) calculated by different studies, projected on a lower hemisphere, showing the similarity in solutions between the slab and the backarc continental crust. Thick squares represent the stress tensor calculated in this study (shown in Fig. 6) for the depth range of 50 to 60-70 km depth. Thin squares represent the stress tensor solutions calculated by Pardo et al. [2002] for earthquakes located between 0 and 70 km depths at different latitudes along the flat slab. Circles represent the solutions calculated by Pardo et al. [2002] and Alvarado et al. [2005] for the continental crust between 0 and 45 km depth. The slab orientation at these latitudes and depths is shown by the thick grey great circle. The black dotted line and arrows denote the azimuth of the plate convergence.*

### 2.2.8.5 Conclusions

We have reported the geometry and characteristics of the Central Chilean DSZ. Its LP extends continuously 300 km along strike from 29.5°S to 32.5°S, initiates at 50 km depth, has an interplane maximum distance of 20-25 km and merges with the UP at 100-120 km depth, coincident with the flat slab's fold hinge. Its detection in this region is due to the installation of local seismic networks, and its occurrence is probably related to the subducting JFR and its degree of hydration. However, the relation between the JFR and the DSZ is not entirely clear. The latter southward geographical span appears to end at the abrupt southern transition zone, which we suggest is due to the slab's change in geometry. Its unusually large interplane distance, as for the other DSZs in the Nazca slab, is probably related to the slab's relatively cold thermal structure, compared to its absolute age.

Focal mechanisms show that the slab changes regime at 60-70 km of depth, with predominant compression and tension above and below, respectively, affecting at least the top 20-25 km of the slab from its upper surface. The estimated stress tensors show that both seismic planes of the DSZ are subjected to compression above 60-70 km of depth, due to high plate convergence, and are dominated

by horizontal extension parallel to the convergence direction below this depth, due to heavy continental loading of the overriding lithosphere. This depth limit corresponds to the depth of the overriding continental crustal root. These observations allowed us to discredit plate sagging or unbending as the causal mechanisms for this DSZ, since these result in stress partitioning between both seismic planes. Instead, we consider the Central Chilean DSZ another rare example of 'type III' DSZ proposed by *Kao and Rau* [1999] for the Philippine Sea plate, where strong convergence with a thick continental crust dominates the slab's stress regime at intermediate depth.

The DSZ shape, like all other global occurrences, shows strong resemblances with dehydration reaction paths. Evidence that the central Chilean Nazca slab is hydrated prior to subduction comes not only from offshore seismic surveys indicating reduced mantle velocities and high electrical conductivity, but also from our observation that focal mechanism strike orientations below 60-70 km of depth strongly correlate with regional outer rise fault strikes. This suggests that reactivation of inherited outer rise faults dominates below ~ 60-70 km depth until at least 120 km depth, where merging of the two seismic planes occurs.

In agreement with other hypotheses, we propose that dehydration embrittlement, fluid migration or local weakening provide the mechanism necessary to weaken rocks/faults, while the ambient stress field controls the occurrence and orientation of rupture. In this context, global DSZ occurrences and interplane distances can be explained by the slab's thermal structure and volatile content.

### 2.2.8.6 Acknowledgements

We are grateful to Bertrand Delouis for his collaboration and help in the use of his code of stress tensor inversion. We thank Perrine Deshayes for notifying the central Chilean DSZ in her PhD thesis. We are equally thankful to all people who have participated in active discussions on the subject with us, and have brought us new insights into the topic. Local data were obtained thanks to projects FONDECYT 1020972-1050758 and IRD-GéoAzur, and the unconditional logistic support of INPRES in the field trips in Western Argentina. Marianne Marot and Guust Nolet are supported by the GlobalSeis project (ERC 226837). Giorgio Ranalli's participation in this project is supported by a grant by NSERC (Natural Sciences and Engineering Research Council of Canada). We thank two anonymous reviewers whose thoughtful comments have helped us to prepare the final version of this paper.

## 2.3 Predicting the Rock Compositions of the Flat & Normal Subduction Systems: Two-Dimensional Petrological Modeling

In this final step of my study, I computed predicted rock seismic properties for the normal and flat subduction zones, at relevant pressure and temperature (P-T) conditions calculated in the Part Two of this chapter. We chose two representative vertical E-W profiles (2-D) of the normal and flat subduction zones at 33.5°S and 31.5°S, respectively. For every cell of each profile (size 40 x 10 km), seismic velocities were computed from Hacker et al. (2004)'s database, assuming MORB-type crust and mantle rocks, at the previously calculated P-T conditions. These values were then compared with the seismic velocities obtained from our tomography inversion, based on pre-defined ranges of uncertainty (in P, T, and seismic Vp and Vs).

The rock compositions used from the Hacker and Abers (2004) database, are used to calculate their seismic properties. The available rock compositions in this database limit us to analyzing only ultramafic and mafic rocks, and not felsic compositions. However, the aim of this exercise is not to find a specific rock composition, but to observe whether trends in similar compositions exist (e.g. eclogites vs. blueschists). We are also limited by the resolution of our seismic tomography model, which depends on the ray coverage and recovery of the synthetic sensitivity tests, as described in Part One of Chapter 2. Consequently, I was able to analyze quite well the composition of the continental mantle above the flat slab and near to the convergence interface, however, to the east of our model, along the normal subduction zone, the model is limited in resolution the further we go south and away from the center of our study area. For this reason, a vertical profile at 33.5°S was used to represent the normal subduction zone. Nevertheless, we are conscious that these conditions are probably a mixture of the "transition" from flat to normal conditions (for further detail, see Discussion in Chapter 3), rather than the absolute normal conditions typical of the southern Chilean subduction zone.

We have not used more complete or self-consistent mineral databases, such as Perplex (Connolly, 2005) and Theriak/Domino (Capitano and Petrakakis, 2010), since these methods generally require that detailed rock and mineral compositions be known (obtained from field sampling and laboratory analyses), which is not our case here. Nevertheless, we have verified the seismic wave speeds predicted by Hacker and Abers (2004) for our rock solutions in the continental mantle with those predicted by PerpleX (Connolly, 2005), and demonstrate a close correlation and a good reliability of the Hacker and Abers (2004) result database used. Furthermore, the resolutions associated to our thermo-mechanical and tomographic data are too large to justify the use of more complex and precise methods, which furthermore are best applied to crustal domains than to mantle domains. The Hacker and Abers (2004) database, in turn, has been quite well developed for mantle domains, which is our principal interest in this study.

We afore describe the basic principles of the Hacker and Abers (2004) macro spreadsheet for the calculation of rock seismic properties.

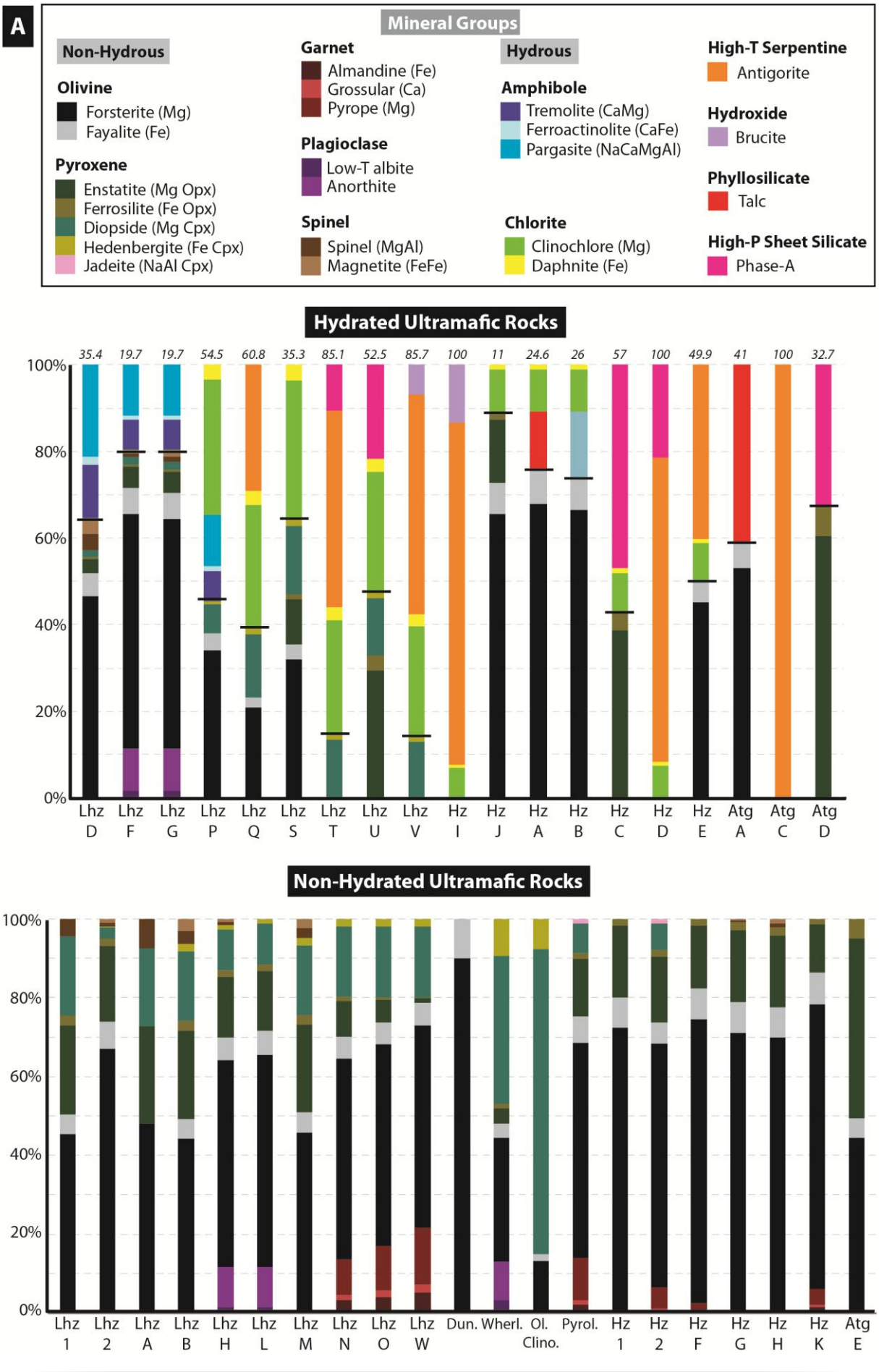
A
Mineral Groups
Non-Hydrous
Olivine
Forsterite (Mg)
Fayalite (Fe)
Pyroxene
Enstatite (Mg Opx)
Ferrosilite (Fe Opx)
Diopside (Mg Cpx)
Hedenbergite (Fe Cpx)
Jadeite (NaAl Cpx)
Garnet
Almandine (Fe)
Grossular (Ca)
Pyrope (Mg)
Plagioclase
Low-T albite
Anorthite
Spinel
Spinel (MgAl)
Magnetite (FeFe)
Hydrous
Amphibole
Tremolite (CaMg)
Ferroactinolite (CaFe)
Pargasite (NaCaMgAl)
Chlorite
Clinochlore (Mg)
Daphnite (Fe)
High-T Serpentine
Antigorite
Hydroxide
Brucite
Phyllosilicate
Talc
High-P Sheet Silicate
Phase-A
Hydrated Ultramafic Rocks
35.4 19.7 19.7 54.5 60.8 35.3 85.1 52.5 85.7 100 11 24.6 26 57 100 49.9 41 100 32.7
100%
80%
60%
40%
20%
0%
Lhz D
Lhz F
Lhz G
Lhz P
Lhz Q
Lhz S
Lhz T
Lhz U
Lhz V
Hz I
Hz J
Hz A
Hz B
Hz C
Hz D
Hz E
Atg A
Atg C
Atg D
Non-Hydrated Ultramafic Rocks
100%
80%
60%
40%
20%
0%
Lhz 1
Lhz 2
Lhz A
Lhz B
Lhz H
Lhz L
Lhz M
Lhz N
Lhz O
Lhz W
Dun.
Wherl.
Ol. Clino.
Pyrol.
Hz 1
Hz 2
Hz F
Hz G
Hz H
Hz K
Atg E

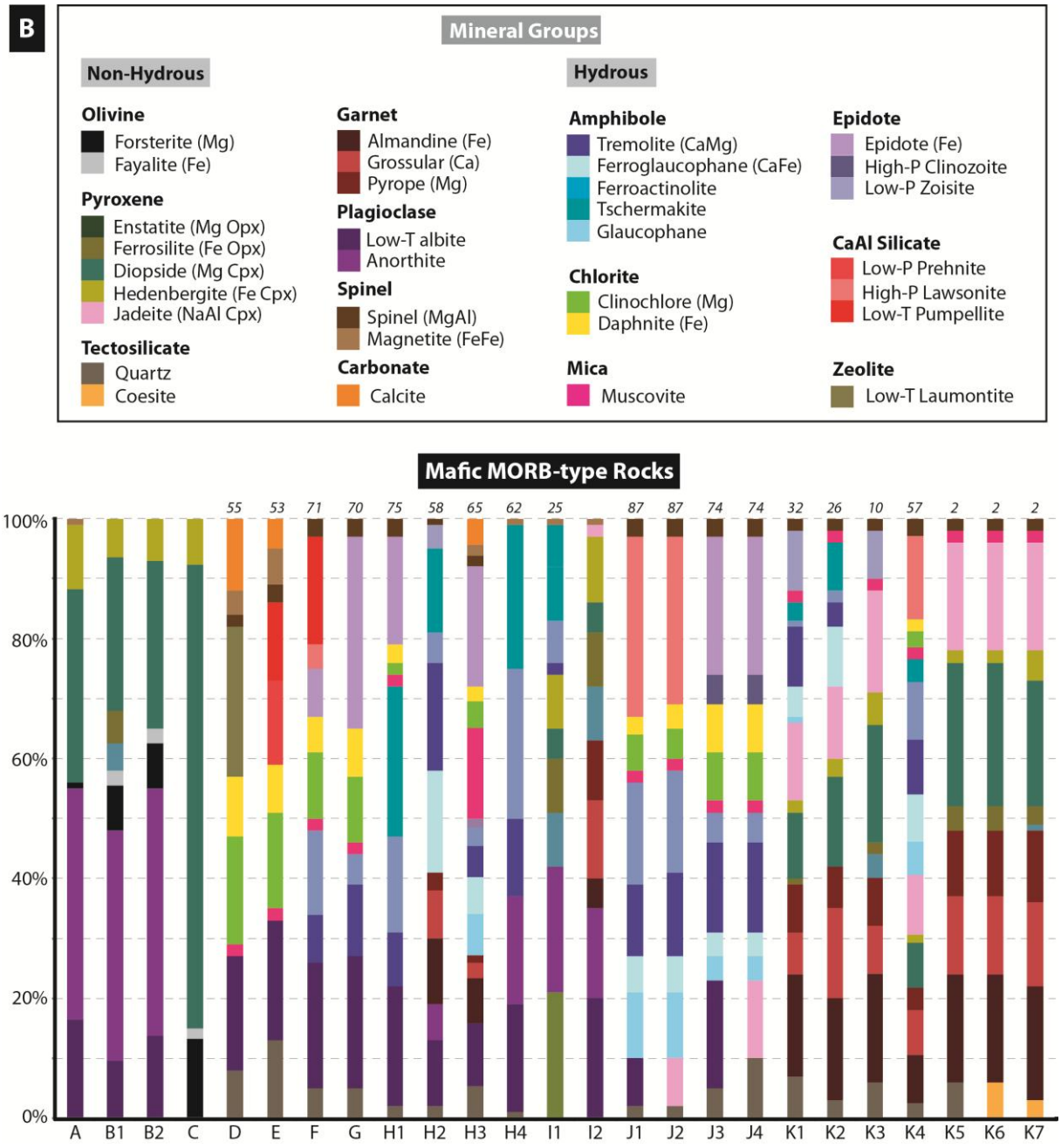


**Fig. 2.3.1**: *Rock compositions used for our petrological modeling, from Hacker and Abers (2004), showing minerals (colored) and total water volume percentage (top of column). (A) Ultramafic mantle rock types. Lhz and Hz and Atg stand for lherzolites, harzburgites and antigorites. Details of composition in Table C.2 and Table C.3 of Appendix C. (B) Mafic crustal rocks. Rock composition and facies names are in Table C.1 and Table C.4 of Appendix C.*

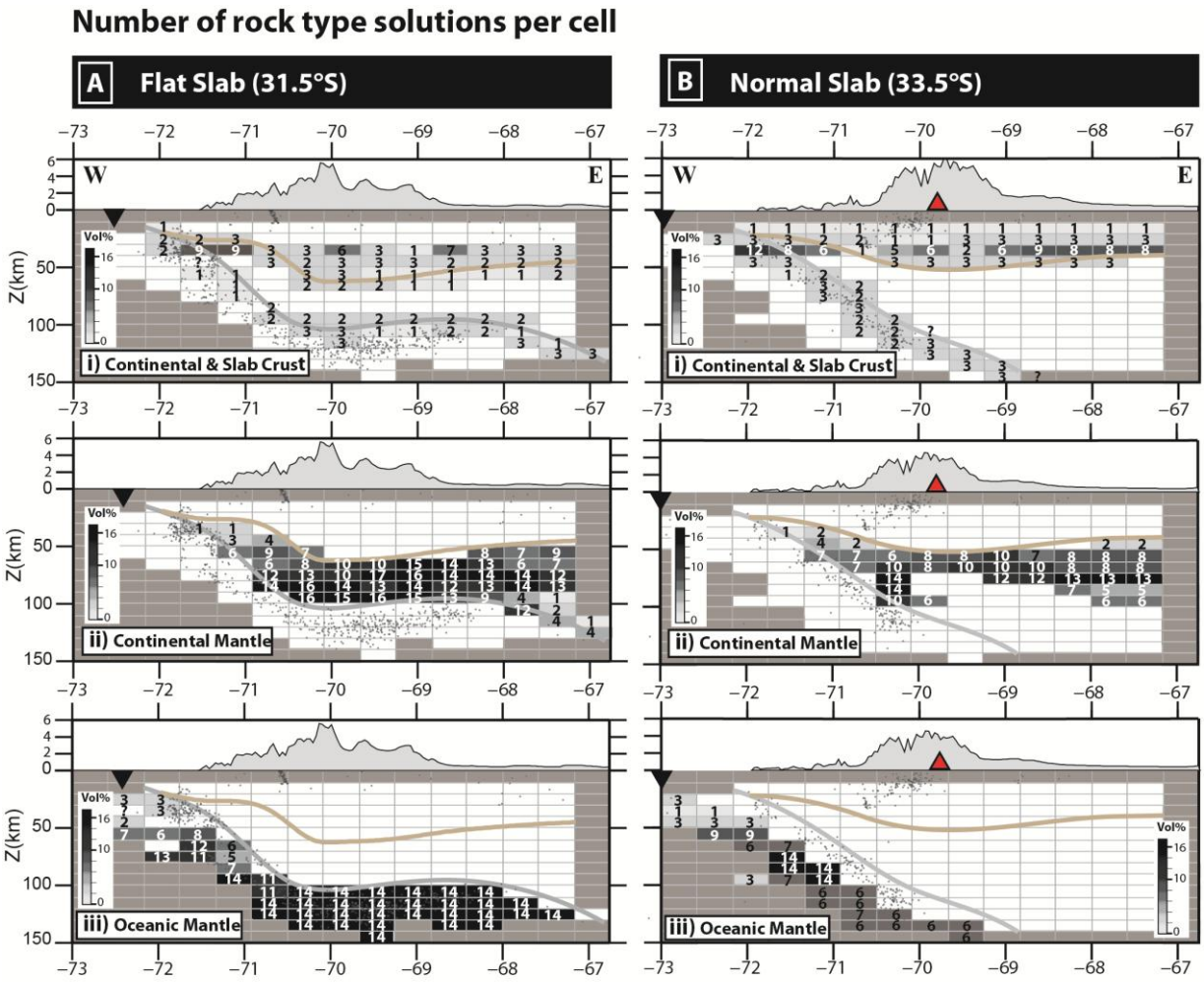


**Fig. 2.3.2**: *Number of rock solutions per cell found to match our absolute seismic velocities. Seismic properties of rock types calculated using Hacker and Abers (2004) rock and mineral physical properties database.*

### *2.3.1 The Hacker and Abers (2004) Worksheet and Macro*

In order to estimate of rock densities and seismic velocities at high P-T conditions, the physical properties of minerals and bulk rocks are necessary. The physical properties for common minerals include the formula weight, molar volume, $H_2O$ content, thermal expansivity (variable with temperature), isothermal bulk modulus, shear modulus, and first and second thermodynamic Grüneisen parameters (details and values in Table 1 of Hacker et al. 2003). Most of these parameters have not been measured, but estimated from a series of scaling relationships (Helffrich, 1996). According to Hacker and Abers (2004), the most important approximations are the shear moduli of hydrous mineral phases, where few data exists. They palliated to this problem by assuming that the Poisson (or Vp/Vs) ratio matches that of another mineral with similar molecular structure and known shear modulus.

Physical properties of minerals, including P- and S-wave velocities and Poisson's ratio, are reported for single-crystals and measured at high P-T conditions, which are extrapolated from standard room P-T conditions (STD). The rock's (defined as a mineral aggregate) physical properties include the model or volume percent of minerals in rocks, and their high P-T behavior is also extrapolated

from STD. The rock densities are computed by summing the individual densities of each mineral in the constituting aggregate.

These physical properties of minerals and rocks are compiled in an Excel macro table, in which the physical properties can be computed automatically following a few simple steps:

(1) One first enters the volume proportions (vol %) of the mineral phases comprising the rock of interest, into the "rocks" worksheet. If total percentage does not amount to 100%, the volume proportions will be automatically re-normalized. The "rock mineral models" worksheet provides a list of rock compositions, but one may also modify or enter his own composition of rock. Several rocks can be entered at a time.

(2) Entering the P (GPa) and T (°C) conditions, in the rows underneath, desired for the calculation.

(3) Once the macro is executed, the computed values for each rock are shown in the green-shaded rows.

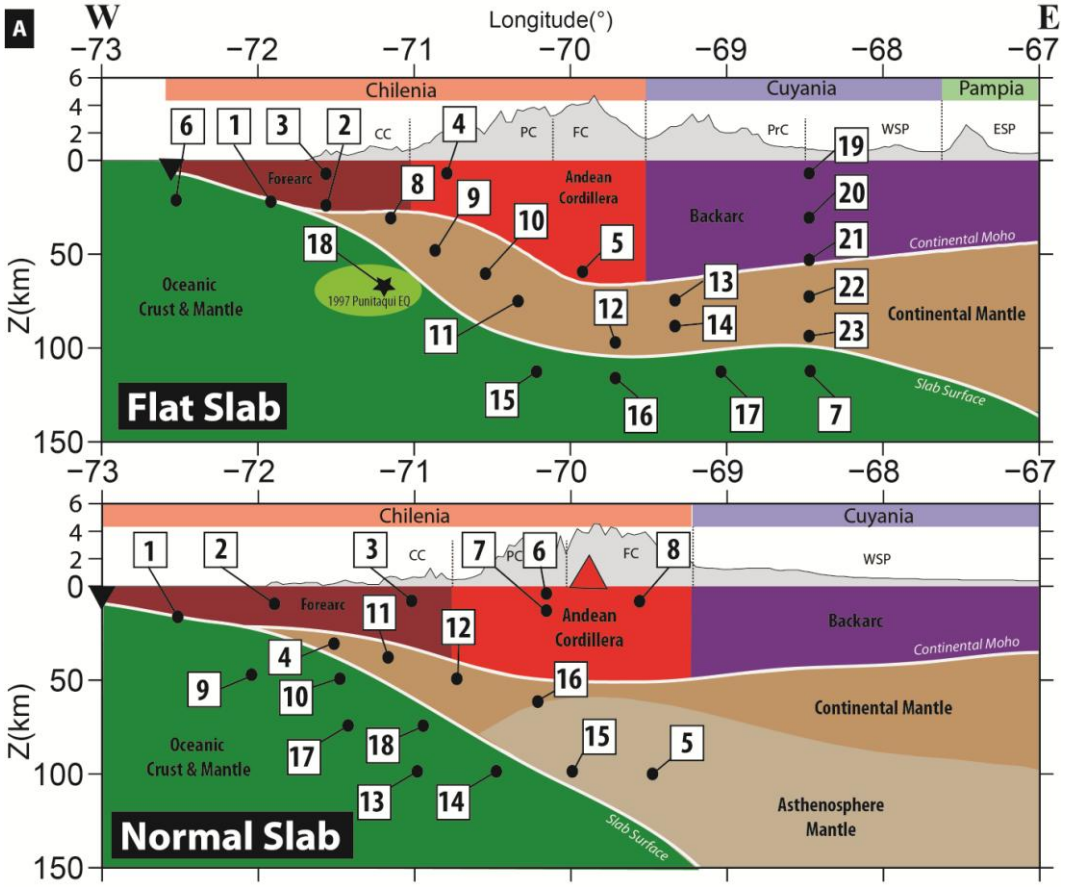


**Fig. 2.3.3**: *The subduction domains and numbered areas are displayed at specific locations where the predicted seismic properties of rocks were calculated, whereas every cell was analyzed (see text). The thermal and seismic values at each of these points are described in Table 2.3.1.*

It is worth noting that the macro is oblivious to mineral stability within the specified P-T conditions, and so, it is important to have basic knowledge of the occurrence of the type of mineral polymorphs present at the required P-T conditions. To palliate to this problem, we calculated, using PerpleX (Connolly, 2005), the stability fields of the rock compositions from Hacker and Abers (2004) found to match our seismic velocities for the continental mantle, over a wide range of P-T.

### *2.3.2 Our Rock Database*

The Hacker and Abers (2004) rock and mineral database provided us with a listing of many common rock compositions typical to subduction zones. Amongst them, we tested 25 MORB-type rocks for the crustal domain, and 19 hydrated (10 harzburgites, 9 lherzolites) and 21 non-hydrated (10 lherzolites, 7 harzburgites, 1 dunite, wherlite, olivine clinopyroxenite, and pyrolite) peridotites for the mantle domain. Their compositions are shown in Fig. 2.3.1, and details are described in Tables C.2 and C.3 of the Appendix C.

The rock and mineral compositions used by Wagner et al. (2005) (see Fig. 3.11 and its caption) to explain their calculated seismic velocities for the continental mantle above the flat slab for this region, were also analyzed and compared with those of Hacker and Abers (2004). See Chapter 3 for detailed discussion.

### *2.3.3 Our Proceeding*

As mentioned above, the calculation of the rock seismic properties for the 65 different rock types was performed for each cell, one by one, and for the normal and flat subduction 2-D cross-sections. Our analysis consisted of two main steps: (1) matching the predicted seismic velocities of rocks with our seismic tomography values, (2) assessing statistically the results for each cell of the two models, and, (3) mapping the distributions of our results.

Step 1 required accounting for the uncertainties, defined at: (i) ± 0.1 km/s in Vp and Vs, (ii) ± 100°C in temperature, and (iii) ± 0.5 Gpa in pressure, given that the values used here are only estimates amongst other model solutions. We did not compare the predicted rock Vp/Vs ratios with the Vp/Vs values obtained from our seismic velocities, since small variations within the uncertainty constraints of either Vp or Vs resulted in misleading substantial differences in the resulting Vp/Vs ratios. Hence, we only acknowledged for absolute velocities.

Step 2 consisted in determining the average volume proportions of: (i) $H_2O$ content, (ii) individual hydrous minerals, and (iii) individual anhydrous minerals, in the rocks found for each cell. We further analyzed the volume percentage of magnesium (Mg) and iron (Fe) end-members of minerals. Because these values are averages, we stress the importance to consider the number of solutions obtained per cell, shown in Fig. 2.3.2, as it statistically quantifies the reliability of our results.

### *2.3.4 Results*

Fig. 2.3.3 and

Table 2**.3.1** show the physical properties (Vp, Vs, P, T) at specific locations in the models, deduced from our seismic tomography and thermo-mechanical calculations, and used for the calculation of the predicted seismic properties for the different rock types.

We mapped our results of the distribution of the average volume percentages (vol %) for each cell of the continental mantle, as it is the main scope of our study. The total proportion of hydrated rocks and the average volume percent of H2O per cell are shown in Fig. 2.3.4. The average volume percent of non-hydrous, hydrous and Mg end-member minerals are shown in Fig. 2.3.5 to Fig. 2.3.7. We also superposed the distributions of the hydrated mantle and crustal regions (both oceanic and continental) (Fig. B3 to B6 of Appendix B) over our seismic velocity perturbation results at these

latitudes (flat and normal subduction regions), in order to correlate eventual variations in the seismic properties with rock or mineral compositions.

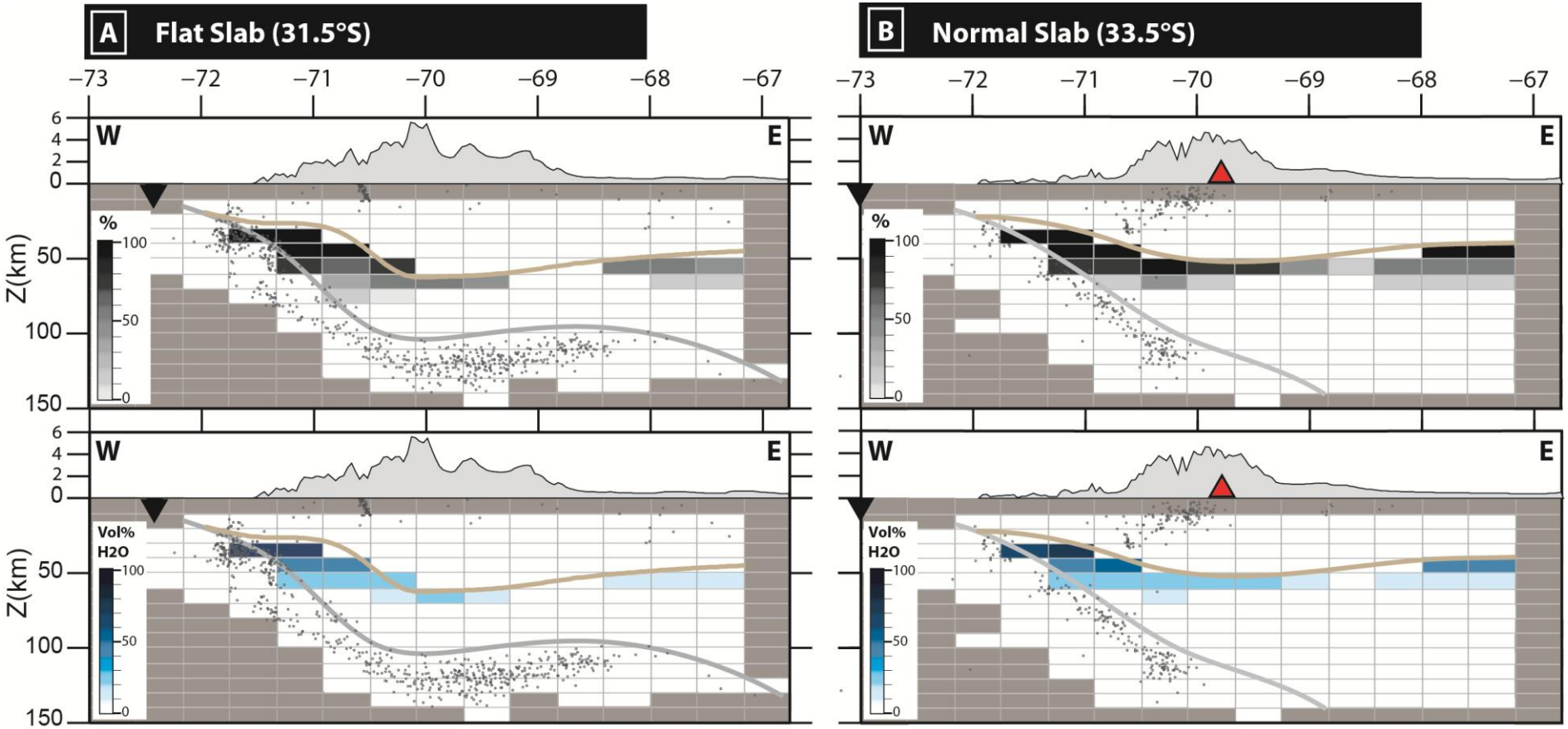


**Fig. 2.3.4**: *Water distribution for the (A) flat and (B) normal subduction zones. The upper panel describes the percentage of rocks which are hydrated to some degree within the group of rock solutions that define each cell. The lower panel shows the average volume percentage of hydration per cell. It is important to consider the number of rocks per cell in Fig. 2.3.3, as the darker colors describing higher proportions of hydration may lead to confusion because maybe only one rock type describes the cell. The reasons for the poor quantity of solutions per cells in some areas, is discussed in Chapter 3.*

**Table 2.3.1**: *Thermo-mechanical and seismic properties for the locations in Fig. 2.3.3, and used our petrological modeling of the (A) flat and (B) normal subduction zones. Depth, Z, pressure, P, temperature, T, and our seismic tomography results for P- and S-wave velocity, Vp and Vs, respectively, and Vp/Vs ratio. The allowed uncertainty for Vp and Vs is ± 0.1 km/s, 100°C in temperature, ± 0.5 GPa in pressure.*

| A | 1 | 2 | 3 | 4 | 5 | 6 | 7 | 8 | 9 | 10 | 11 | 12 | 13 | 14 | 15 | 16 | 17 | 18 | 19 | 20 | 21 | 22 | 23 |
|---|---|---|---|---|---|---|---|---|---|---|---|---|---|---|---|---|---|---|---|---|---|---|---|
| **Z (km)** | 25 | 25 | 15 | 15 | 60 | 25 | 110 | 35 | 50 | 65 | 45 | 100 | 100 | 95 | 110 | 110 | 110 | 70 | 15 | 35 | 55 | 75 | 95 |
| **P (GPa)** | 1.0 | 1.0 | 0.5 | 0.5 | 2.0 | 1.0 | 3.0 | 1.0 | 2.0 | 2.0 | 2.0 | 3.5 | 3.5 | 3.0 | 4.0 | 4.0 | 4.0 | 3.0 | 0.5 | 1.0 | 2.0 | 25 | 3.0 |
| **T (°C)** | 250 | 300 | 150 | 100 | 600 | 150 | 500 | 350 | 450 | 500 | 600 | 600 | 550 | 600 | 550 | 550 | 550 | 400 | 200 | 300 | 600 | 700 | 600 |
| **Vp (km/s)** | 6.9 | 6.6 | 6.2 | 6.1 | 7.9 | 6.9 | 8.25 | 7.0 | 7.7 | 8.0 | 8.25 | 8.45 | 8.45 | 8.4 | 8.4 | 8.4 | 8.35 | 8.0 | 6.4 | 7.2 | 8.0 | 8.25 | 8.25 |
| **Vs (km/s)** | 3.8 | 3.8 | 3.6 | 3.3 | 4.4 | 3.9 | 4.55 | 4.2 | 4.4 | 4.55 | 4.65 | 4.85 | 4.85 | 4.7 | 4.8 | 4.8 | 4.85 | 4.8 | 3.6 | 4.0 | 4.6 | 4.6 | 4.55 |
| **Vp/Vs** | 1.82 | 1.75 | 1.75 | 1.80 | 1.78 | 1.8 | 1.77 | 1.74 | 1.77 | 1.79 | 1.73 | 1.76 | 1.76 | 1.78 | 1.77 | 1.75 | 1.76 | 1.71 | 1.75 | 1.75 | 1.75 | 1.75 | 1.76 |

| B | 1 | 2 | 3 | 4 | 5 | 6 | 7 | 8 | 9 | 10 | 11 | 12 | 13 | 14 | 15 | 16 | 17 | 18 |
|---|---|---|---|---|---|---|---|---|---|---|---|---|---|---|---|---|---|---|
| **Z (km)** | 15 | 15 | 15 | 25 | 100 | 10 | 20 | 15 | 50 | 50 | 35 | 50 | 100 | 100 | 100 | 75 | 75 | 75 |
| **P (GPa)** | 0.5 | 0.5 | 0.5 | 1.5 | 3.5 | 0.5 | 0.5 | 0.5 | 1.5 | 1.5 | 2.0 | 2.0 | 3.5 | 3.5 | 3.5 | 2.5 | 2.5 | 2.5 |
| **T (°C)** | 100 | 150 | 150 | 300 | >900 | 100 | 100 | 200 | 400 | 350 | 400 | 400 | 550 | 550 | >700 | 900 | 500 | 600 |
| **Vp (km/s)** | 6.7 | 6.4 | 6.2 | 7.0 | 8.45 | 5.8 | 6.2 | 6.4 | 7.7 | 7.6 | 7.5 | 7.7 | 8.4 | 8.4 | 8.4 | 8.0 | 8.0 | 8.0 |
| **Vs (km/s)** | 3.8 | 3.6 | 3.6 | 4.0 | 4.75 | 3.3 | 3.5 | 3.6 | 4.3 | 4.2 | 4.1 | 4.25 | 4.75 | 4.75 | 4.7 | 4.5 | 4.5 | 4.5 |
| **Vp/Vs** | 1.77 | 1.75 | 1.79 | 1.77 | 1.77 | 1.8 | 1.73 | 1.77 | 1.77 | 1.77 | 1.76 | 1.79 | 1.74 | 1.74 | 1.74 | 1.79 | 1.75 | 1.75 |

We also mapped the distribution of eclogites (Fig. C.5, Fig. 3.10, Fig. 3.3 and Fig. 3.14), with the assumption that the continental Moho model which we use is correct. The thickness and location of the oceanic crust is much more debated, as no studies have yet managed to describe it unambiguously at depth (see previous Chapter 1). Therefore, we considered that the slab seismicity is located near the surface of the slab, and that the cells encountered by the slab interface sample either oceanic crust or continental mantle.

Our results are further discussed in full detail in Chapter 3 and argued with, or against, other studies for the region.

### *2.3.5 Conclusions*

To resume, we used our previously determined seismic tomography and thermo-mechanical models of Vp and Vs and P-T conditions, respectively, to model the composition of the subduction zones along two representative cross-sections of the flat and normal subduction zones (31.5°S and 33.5°S, respectively), using the Hacker and Abers (2004) mineral and rock physical property worksheet. The Hacker and Abers (2004) database comprises 65 mafic and ultramafic rock types that enabled us to analyze the compositions of the continental lower crust and its mantle, as well as the oceanic lithosphere. For each cell in the model, we compared our seismic tomography results with the seismic velocities predicted for these rocks. We then analyzed the distributions and volume percentages of the rocks and minerals for each cell, with particular emphasis on the continental mantle. The aim of this method is to acknowledge the location and quantity of fluids present (if any) for the flat and normal subduction zones, to compare them together, and to better understand their observed subduction dynamics and deformation styles.

Here, we show that the continental mantle wedge is moderately hydrated (average of 30%) in a narrow depth range (50-60 km) above both the normal and flat slabs, a sign that the slab is dehydrating and that there is no significant difference between both subduction settings. The oceanic lithosphere in the flat slab region, and particularly along the lower part of the plate interface, is deeply hydrated down to 50-70 km depth. The oceanic slab beneath that depth is composed either of dry peridotite and/or dense eclogites (whether in the mantle or crustal domain, respectively), forming a paradox to the flat subduction dynamics. The normal slab could be eclogitized below 50 km depth, based on our seismic velocities obtained. Eclogite could also exist below 50 km depth in the Cuyania lower crust, however, it is not found in the deepest parts of the Andean crust, where the total thickness of the crust reaches 70 km depth, well within the eclogite stability field.

The next chapter is a synthesis of this PhD research, including a complete description of our results and my interpretations to their significance, in article format for future submission.

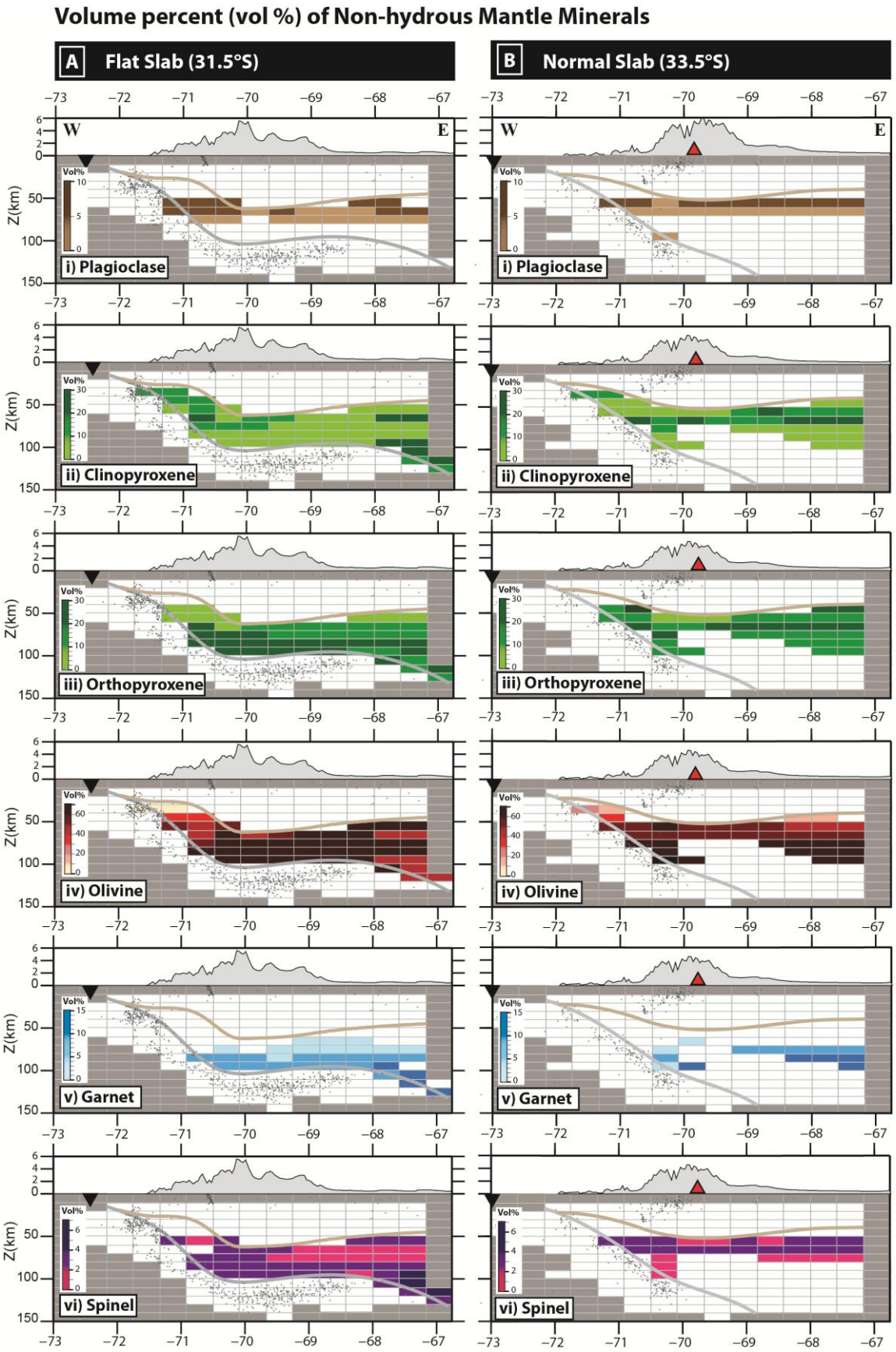


**Fig. 2.3.5**: *Average volume percentage (vol %) distribution of anhydrous continental mantle minerals.*

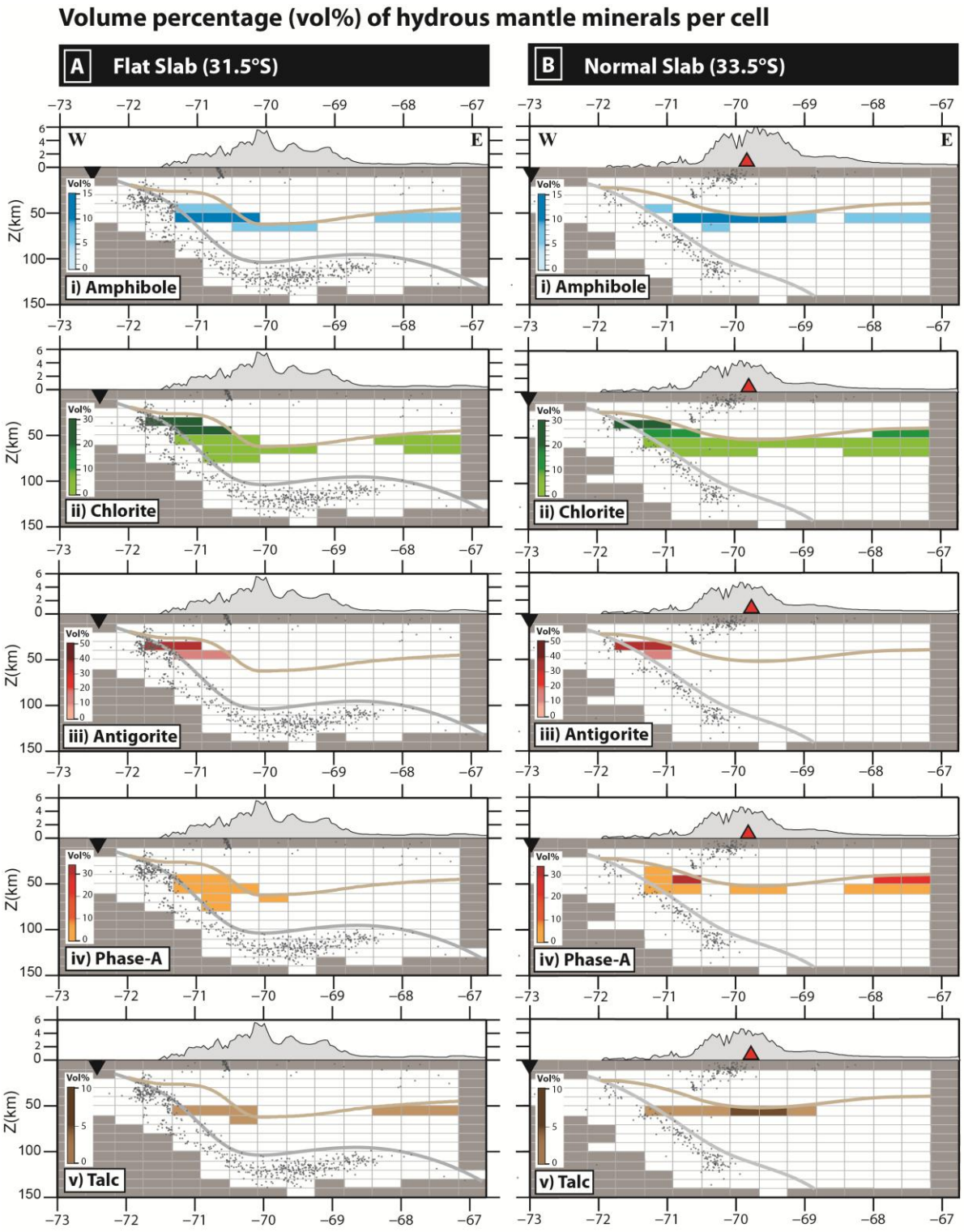


**Fig. 2.3.6**: *Average volume percentage (vol %) of hydrous continental mantle minerals.*

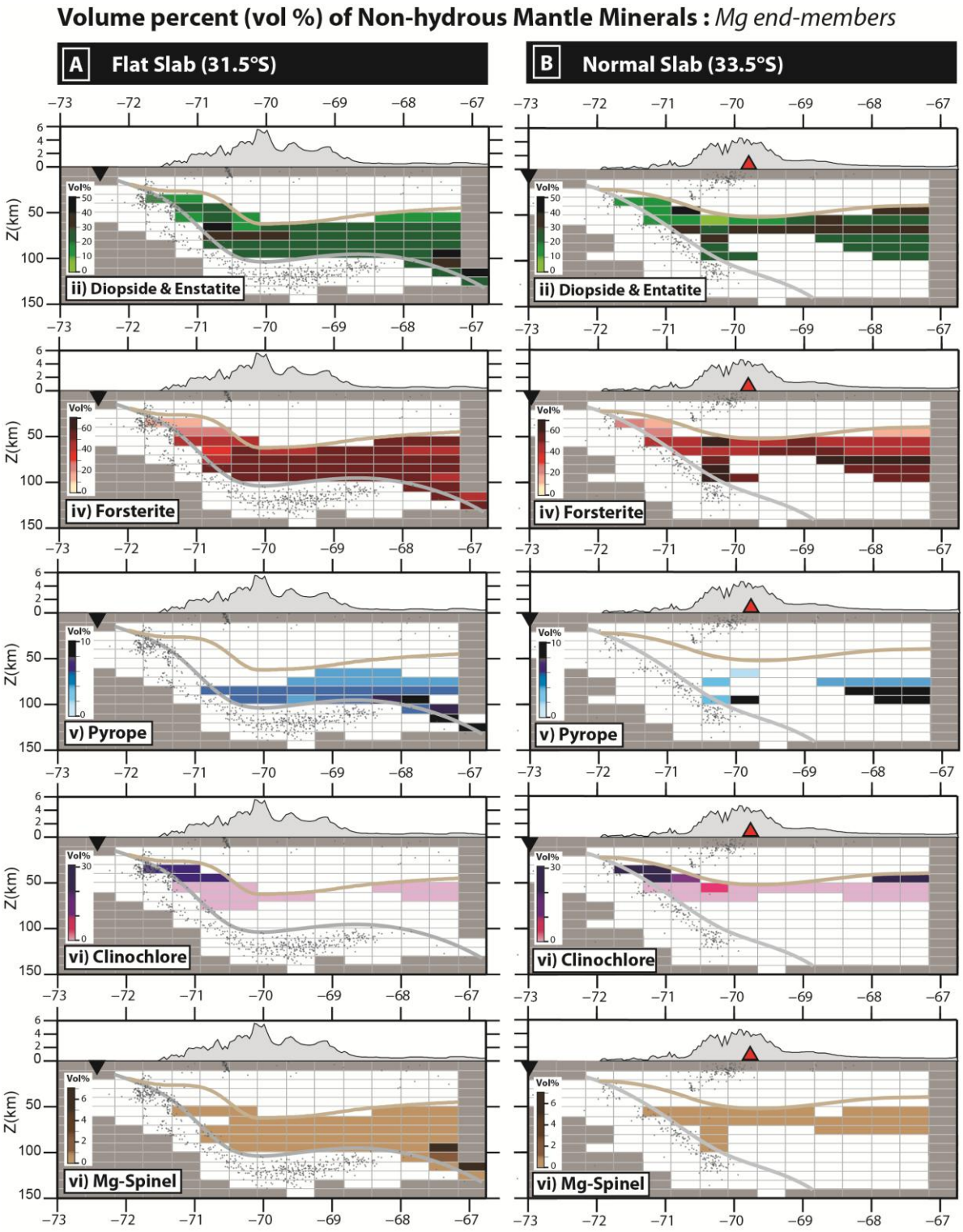


**Fig. 2.3.7**: *Average volume percentage (vol %) of Mg end-member minerals for the continental mantle.*

# Chapter 3

# 3 A Thermo-Petrological-Seismological Interpretation of the Central Chilean Normal & Flat Subduction Zones: Results and Interpretations

# Flat vs. Normal Subduction Zones: A Comparison Based on 3-D Regional Travel-Time Tomography & Petrological Modeling of Central Chile & Western Argentina (29°-35°S)

M. Marot[(1)], T. Monfret[(1)], M. Gerbault[(1)], G. Nolet[(1)], G. Ranalli[(2)], M. Pardo[(3)]

*[(1)] Géoazur, UNSA, IRD, CNRS, OCA, (UMR 7329), 250 Albert Einstein, 06560 Valbonne, France*
*[(2)] Department of Earth Sciences, Carleton University, 1125 Colonel By Drive, Ottawa, ON, K1S 5B, Canada*
*[(3)] Departamento de Geofisica, Universidad de Chile, Blanco encalada 2002, Santiago, Chile*

## Abstract

Beneath central Chile and western Argentina, the oceanic Nazca slab drastically changes geometry from dipping at an angle of 30-35° to horizontal, and correlates with the subduction of the Juan Fernandez seamount ridge. The aim of our study is to assess the differences in the seismic properties of the overriding lithosphere of these two regions, in order to better understand the deep structure of the continental lithosphere above the flat slab, and the links between the deformations at the surface and at depth. Here, we show the first most complete regional 3-D seismic tomography images of this region, whereby, in comparison to previous studies, we use (1) a much larger seismic dataset compiled from several short-term seismic catalogs, (2) a much denser seismic station network which enables us to better resolve the subduction zone from the trench to the backarc and into the upper ~ 30 km of the slab, and (3) a starting 1-D background model calculated for this region specifically and refined over the years. We assess and discuss our seismic tomography results with (i) supporting unpublished models of seismic attenuation for this region, and (ii) predicted rock types which we calculated using the Hacker and Abers (2004) mineral/rock database and approximations of the pressure and temperature conditions at depth using thermo-mechanical modeling. We show significant seismic differences between the flat and normal subduction zones: As expected, the flat slab region is impacted by colder temperatures imposed by the slab geometry, and is characterized by faster seismic velocities and more intense seismic activity, both within the descending and overriding plates, compared to the normal slab region. We show evidence that the flat slab dehydrates within the mantle wedge, but also along the subducting ridge prior to re-subducting. Also, the forearc region above the flat slab area is subject by unusual seismic properties correlated either to the slab geometry at depth and/or to the aftershock effects of the Mw 7.1 1997 Punitaqui earthquake, which occurred several years before the recording of our events. The continental crust above the flat slab has very heterogeneous seismic properties which correlate with important deformational structures and geological terranes at the surface. We confirm previous studies that have shown that the Cuyania terrane, in the backarc region, is more mafic and contains an eclogitized lower crust; whereas to the west, the thick lower crust of the present day Andean arc is non-eclogitized and could represent the felsic Chilenia terrane. We also suspect well identified major crustal faults (or shear zones) to extend towards the plate interface and channelize slab-derived fluids into the continental crust.

**Keywords**: Central Chile; Flat subduction; Seismic tomography; Rock composition; Thermo-mechanical modeling; Eclogite crust; Dehydration/hydration

## 3.1 Introduction

All along the South American-Nazca convergence zone, there exists a positive correlation between subducting oceanic features (ridges, plateaus, fracture zones) and flat subductions (Skinner and Clayton, 2013), volcanic arc gaps and backarc basement uplifts. However, this correlation is still thoroughly debated and poorly understood.

The central Chilean (~ 27°-32.5°S) "Pampean" flat subduction is perhaps the best documented so far, because of the region's very high seismic activity, the geology of the region exhibits higher structural evolution and exposure levels, and it has been impacting the region for a relatively long period of time (15-18 Ma) (Kay and Mpodozis, 2002; Ramos et al., 2002). It is associated with the convergence between the subducting Juan Fernandez seamount ridge, lying atop the relatively young (35-40 Ma) and hydrated Nazca Plate (Kopp et al., 2004), and the continental South American Plate, whose crustal thickness (70 km) beneath the main Cordillera is one of the greatest on Earth (Fromm et al., 2004; Gilbert et al., 2006; Heit et al., 2008).

Drastic tectonic changes occur between the "normal" and "flat" slab regions (Fig. 3.1). Above the normal slab, the magmatic arc domain is active, the geothermal gradient is higher and heat is supplied from the asthenospheric corner flow, resulting in conventional slab dehydration, arc volcanism and seismicity, and a weaker continental crust. In comparison, above the flat slab, the asthenosphere is believed to have been expelled eastward during slab flattening, significantly cooling the subduction environment (Kay and Mpodozis, 2002; Ramos et al., 2002; Grevemeyer et al., 2003) and provoking increased (i) degree of plate coupling, (ii) compressional stresses, expanding further inland, (iii) topography, (iv) seismicity in the backarc, forearc, plate interface and in the slab (including a Double Seismic Zone, Marot et al. 2013), and also in a (v) lack of arc magmatism (Kay and Abbruzzi, 1996; Kay and Mpodozis, 2002; Ramos et al., 2002). Furthermore, the colder geotherm is also reflected by a small Moho impedance contrast (Fromm et al., 2004; Gilbert et al., 2006; Alvarado et al., 2007; Gans et al., 2011) and fast mantle velocities (Wagner et al., 2005). The latter were further interpreted to correspond to dry conditions, leading to the question of whether or not the slab is dehydrating. Low temperatures tend to inhibit dehydration chemical reactions, acting to retard the eclogite formation in the oceanic crust, hence, sustaining positive slab buoyancy. Magnetotelluric studies (Brooker et al., 2004) and the occurrence of relatively recent volcanism above the re-subducting slab to the east (65°W) (~ 2 Ma, Kay and Abbruzzi, 1994), provide good evidence that partial melting and slab dehydration are ongoing processes; however, in smaller quantities than expected for a normal subduction zone and given the relatively high degree of plate hydration interpreted by offshore seismic (Kopp et al. 2004), heat flow (Grevemeyer et al., 2005) and gravity (Yáñez et al., 2001) surveys along the Juan Fernandez ridge at proximity of the subduction zone.

The region's characteristic high seismic rate and rapid along-strike transition in slab geometry (between 32.5°S and 33.5°S and ~ 100 km wide) make it an ideal place to study the earthquake distribution and the seismic wave perturbations associated to deformations at depth.

Whereas the timing of backarc basement core uplifts and the eastward migration of the volcanic arc are well constrained and provide good insights into the processes of slab shallowing (Ramos et al., 2002; Alvarado et al., 2007), the dominant factor(s) that triggered flat subduction and maintained it since 6 Myr (when today's crustal thickness was attained, Kay et al., 1991; Kay and Abbruzzi, 1996) are misunderstood; so are its effects on the upper plate composition (thermal, petrological, structural) and deformation below the surface. While properties of the lower plate (heat flux, age, structure, fluid content) are suggested important factors influencing variations in the slab geometry, there is a good consensus that the westward upper plate motion and the thick Rio de La Plata craton, to the east, also play a non-negligible role in promoting the Pampean flat slab (e.g. van Hunen, 2001; 2004; Manea et al., 2012).

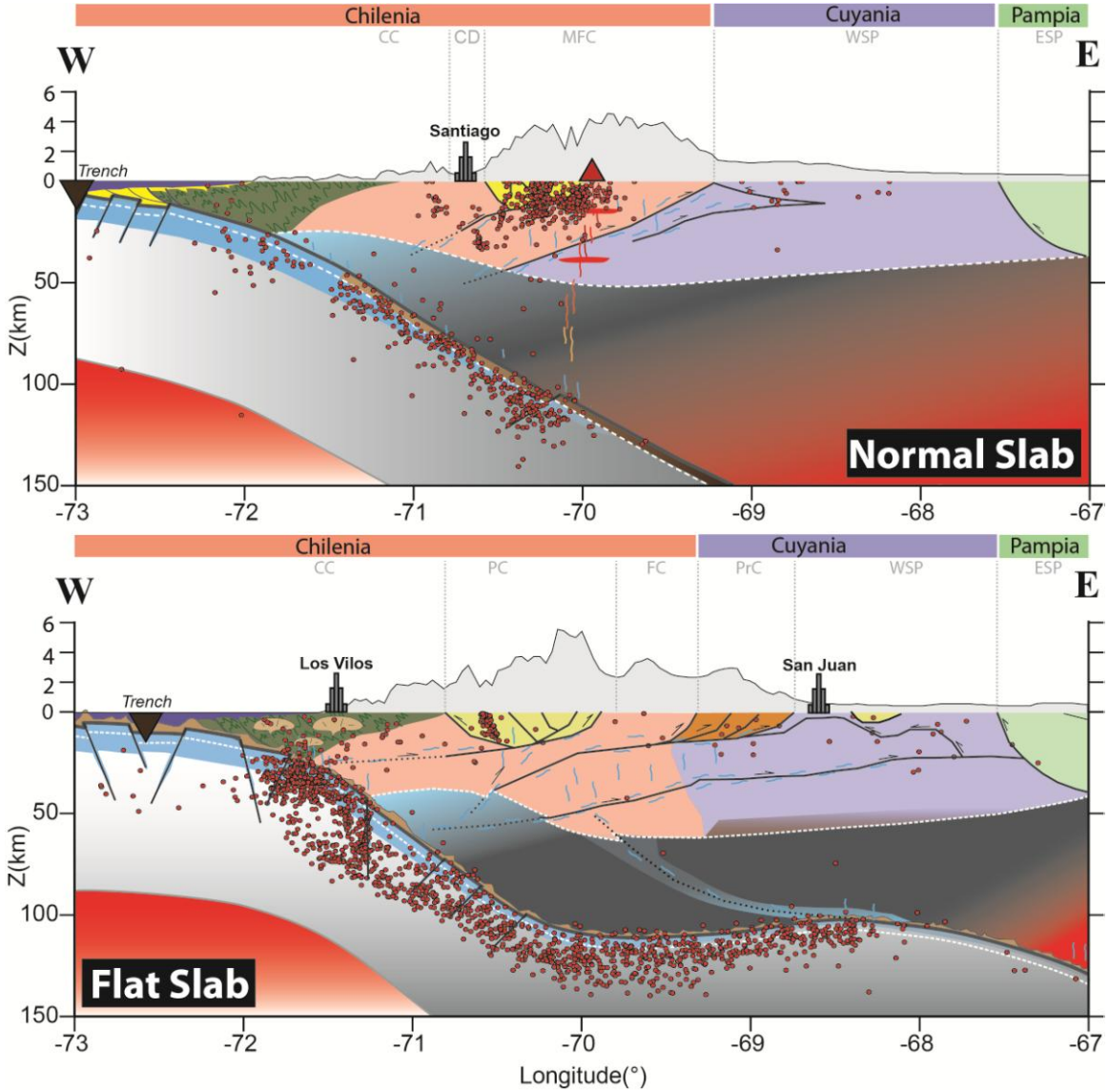


**Fig. 3.1***: Schematic diagram of the normal and flat subduction in central Chile. Seismicity is shown in red dots, geological terranes are the Pampia (green), Cuyania (purple), Chilenia (pink), and the forearc paleo-accretionary wedge (green with intruded batholiths). The subducting Juan Fernandez ridge material is shown as brown topography on the slab surface. Blue areas near the slab surface are zone of expected hydration, decreasing with depth and persisting in the flat slab segment. Straight lines in the slab are normal faults cross-cutting the lithosphere. Solid lines in the continental crust are suspected faults/shear zones from Ramos et al. (2002) and Farias et al. (2010). The La Ramada-Aconcagua fold-thrust-belt is shown in light yellow. Dotted lines are their hypothetical extensions (see text) In dark red color is the hot asthenosphere, in dark grey is the cold lithospheric mantle and in light blue is the hydrated portion of the continental mantle wedge. The white dotted line is the continental Moho (Fromm et al., 2004), which we deepened at the plate interface from 35 km to 50 km depth, as proposed in the text.*

This study aims at enlarging the comprehension of the central Chilean flat subduction dynamics, its impacts on the overriding plate and to qualify the style of deformation at depth. This is done by comparing it with the normal-dipping (30-35°) slab immediately to the south, taken to represent conventional subduction conditions. We used the local seismicity recorded by four temporary seismic

campaigns (OVA99, CHARGE, CHARSME, CHASE) to perform 3-D regional ray-tracing residual seismic tomography of P- and S-wave travel-times.

We image with a good resolution the overriding lithosphere above the flat slab region, from the coast to the backarc, including the upper parts of the oceanic slab where seismicity is densest. We then compared our seismic absolute velocities (Vp and Vs) with those predicted for rocks, at appropriate pressure and temperature (P-T) conditions that were evaluated from thermo-mechanical modeling.

We also compare our tomography results with those of Wagner et al. (2005), who performed a similar analysis for this region using only the CHARGE database. Our work incorporates of much larger earthquake catalog comprising different time periods and resulting in greater ray coverage, increased resolution to the north and south of the region, and a more complete temporal view of the seismic properties of the lithospheres. Furthermore, our results include the continental crust and the upper portion of the slab lithosphere, which could not be interpreted in their models due to lack of data and poor resolution. We also supplemented unpublished seismic attenuation models calculated by Deshayes (2008) for the region using the OVA99 and CHARSME catalogs, to reinforce our interpretations of the nature of the velocity perturbations observed. Our work hopes to bring a finer, broader and more complete view of the region's subduction system.

Our results show significant seismic differences between the normal and flat subduction zones. The seismic perturbations near the surface correlate with geological terranes or major fault zones. We confirm two previous interpretations: (1) for a generally cold, dry, and Mg-rich continental mantle (e.g. Wagner et al., 2005; 2006; 2008), which, nevertheless, appears to be locally hydrated; and (2) for a likely eclogitized continental lower crust within the Cuyania terrane, however absent within the thick Andean crust. Eclogite or dense peridotite may also constitute the oceanic lithosphere below 70 km, contradicting slab buoyancy processes. We also notice that localized slow velocity anomalies appear to correlate with extensions of major basement detachment faults, and that similar abnormal seismic properties describe the aftershock region of the 1997 Punitaqui earthquake and the forearc crust, which may be associated together or with the flat slab geometry at depth.

## 3.2 Tectonic and Geological Settings

The Nazca Plate subducts beneath central Chile and western Argentina (27°-35°S) at a current convergence rate of 6.7 ± 0.2 cm/a in the N78°E direction (Fig. 3.2A) (Kendrick et al., 2003), with absolute velocities of 3.2 and 4.6 cm/a, respectively, based on the fixed hotspot reference frame (Gripp and Gordon, 2002) (2.5 cm/a westward for the South American continent based on moving hotspots, O'Neill et al. 2005).

Five morpho-tectono-structural-geological provinces have developed in the flat slab region over the past ~ 25 Ma of compression which was lead by the breakup of the Farallon Plate, progressive slab flattening and eastward arc and orogeny migrations (Ramos et al., 2002). These provinces are (from west to east) the Coastal, Principal and Frontal Cordilleras, the Precordillera and the Sierra Pampeanas. The Sierra Pampeanas represents the backarc region, the Precordillera forms the Andean foothill, the Principal and Frontal Cordilleras make up the present-day active Andean belt, and the Coastal Cordillera is the forearc region (Fig. 3.2A).

Here, the flat slab region is defined as the area north of the subducting Juan Fernandez ridge path, i.e. between ~ 27°S and 32.5°S. Its northern transition zone is larger (~ 27°-30°S, ~ 100 km wide) and displays a much gentler slope (Cahill and Isacks, 1992; Giambiagi and Ramos, 2002) than the southern transition zone (~ 32.5°-33.5°S, ~ 100 km wide) (Fig. 3.2B), whose nature of deformation is still unclear, however, more often interpreted as a sharp bend than a tear (Wagner et al., 2005; Pesicek et al., 2012). Around 100-120 km depth, the slab becomes horizontal and underplates the continental lithosphere for 250-300 km eastward before tilting back into the deep mantle at 68°W and

at a 30° dip angle (Fig. 3.1) (Barazangi and Isacks, 1976; Cahill and Isacks, 1992; Anderson et al., 2007). At the surface, the flat slab region is associated with a volcanic arc gap since ~ 9 Ma (Kay and Mpodozis, 2002) and strong tectonic shortening estimated between 130 and 150 km (Allmendinger et al., 1997; Alvarado et al., 2007).

South of 33°S, the Nazca slab returns to a normal dip of 30-35° (Fig. 3.1 and 3.2B), and is associated with significant changes, to mention only a few: (i) the strike of the trench rotates from N20°E to N5°E (Fig. 3.2B), (ii) the geothermal gradient increases (Miranda, 2001), (iii) the slab becomes younger (Fig. 1.14A) (Yáñez and Cembrano, 2000), (iv) arc magmatism resumes, (v) the Central Depression valley re-appears (Fig. 3.2A), (vi) backarc basement uplift no longer occurs, and the Precordillera and Sierra Pampeanas blocks become absent (Ramos, 2009), (vii) topography decreases from an average elevation of 4500 m (max. 6700 m, Aconcagua, ~ 70°W/32.5°S) to < 2000 m at 38°S, (viii) crustal thickness decreases from 70 to 35 km (Tassara et al., 2006; Alvarado et al., 2007), (ix) total lithospheric thickness also decreases from 80-100 km (Tassara et al., 2006) to 60 km south of 36°S (compared to > 140 km in Peru and > 160 km in the eastern Brazilian shield, the thickest in South America), and finally, (x) crustal seismic rates decrease in the slab and backarc regions, however increase along the active volcanic arc.

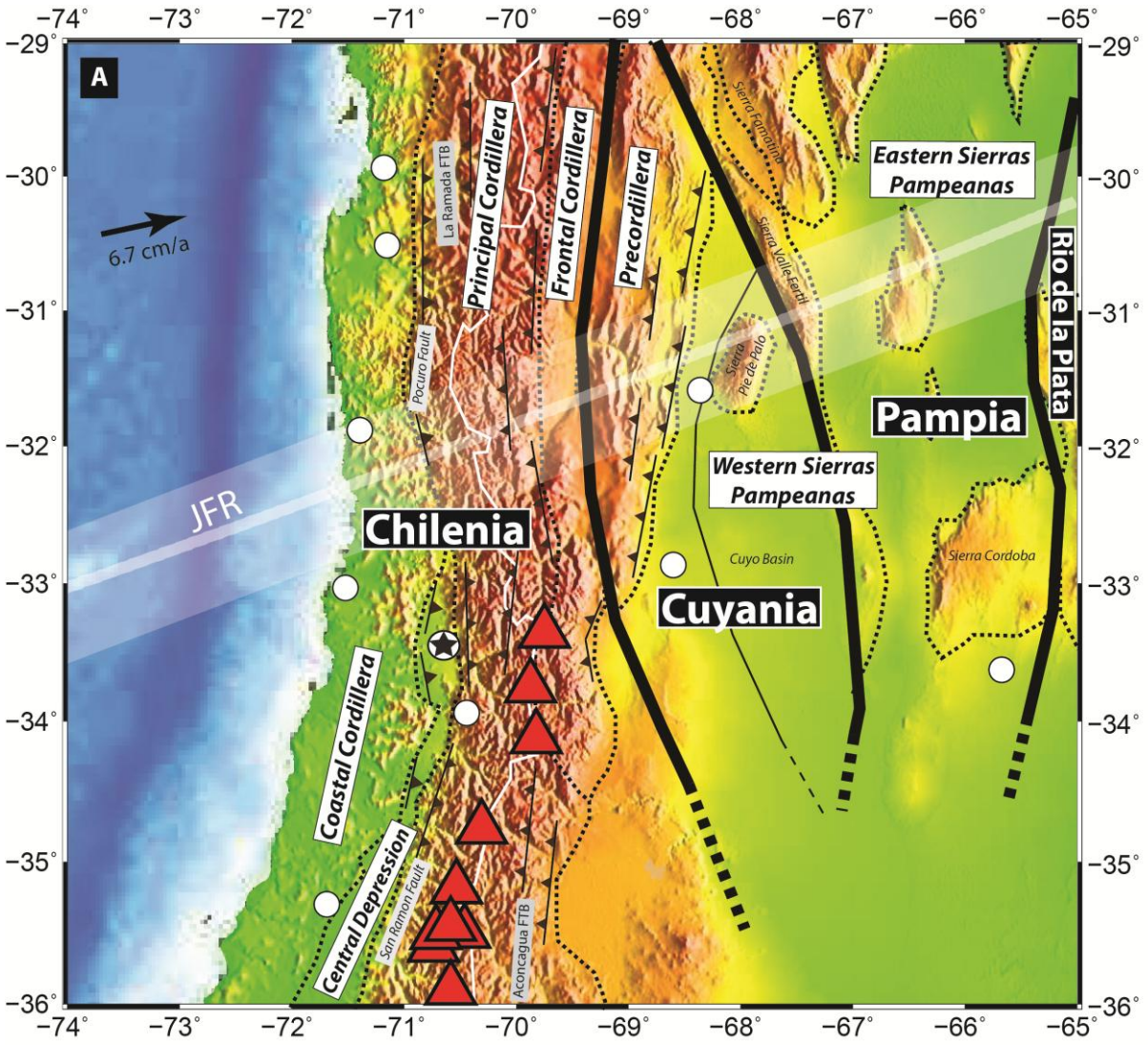

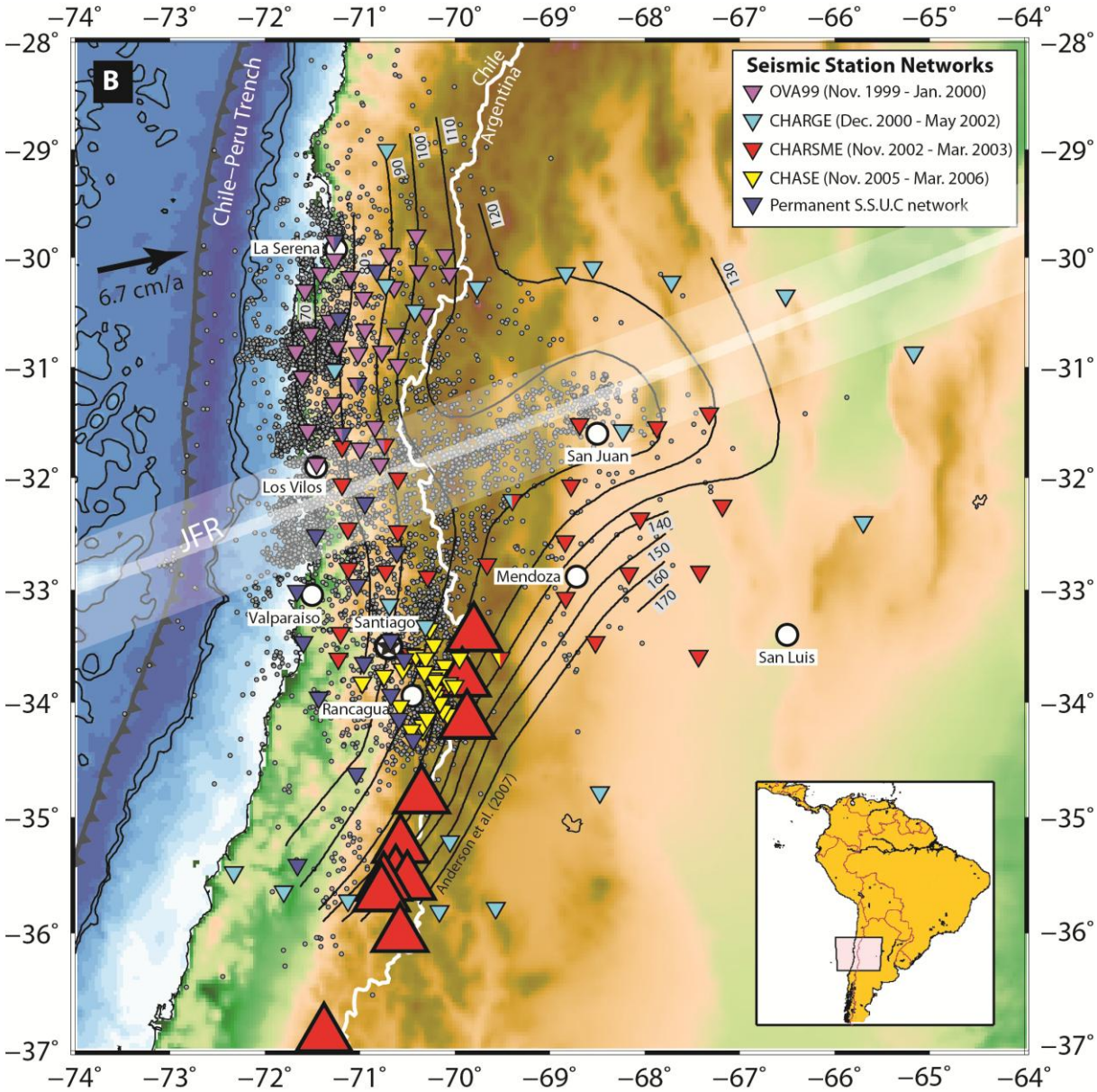


**Fig. 3.2***: Regional tectonic setting of central Chile. (A) Tectono-structural-geological context. Thick black lines are major suture zones. Dotted lines are the geological provinces and their uplifted outcrops. Lines with triangles are the approximate location of thrust faults forming the La Ramada-Aconcagua fold-and-thrust belt. (B) Seismological context of the seismic networks (inverted triangles) and its recorded seismicity (small circles). Shown are: active volcanoes (red triangles), main cities (white circles, capital city Santiago with a star), slab contours from Anderson et al. (2007) and the political border between Chile and Argentina (white line).*

The compositional variations in the crustal basement rocks (Fig. 3.1), west of Rio de la Plata craton, results from three major episodes of terrane accretion over the past 600 Ma, which have strongly influenced the structure and tectonic evolution of the region (Fig. 3.2A) (Ramos et al., 1986; Ramos et al., 2002; Alvarado and Ramos, 2011). These terranes, of various provenances, compositions and ages, include (i) the para-autochthonous Pampia terrane, amalgamated at ~ 530-515 Ma, (ii) the allochthonous Cuyania terrane, accreted at ~ 460 Ma, and (iii) the allochthonous Chilenia terrane, whose existence is debated, added at ~ 420-315 Ma, and believed to form the Andean basement and parts of the forearc crust (Ramos, 2004). At the surface, the Pampia, Cuyania and Chilenia terranes

comprise the foundations of the eastern Sierra Pampeanas and Sierra Cordoba, western Sierra Pampeanas and Precordillera, and the Andean and perhaps also the forearc regions, respectively. However, the distributions at depth of these terranes and the suture zones that separate them have never been resolved.

Many episodes of varying stress regimes and deformation styles have reactivated these suture zones as major faults, and created anisotropy and further fracturing of the region (Ramos, 2009). These faults have controlled the neo-tectonic style of deformation in the region, significantly influencing the thick-skinned basement uplift of the Sierra Pampeanas backarc region, up to ~ 800 km from the trench (Ramos et al., 2002; Alvarado et al., 2009). A similar style of deformation is observed for the modern Peruvian flat subduction zone (James and Snoke, 1994) and in the old Laramide Orogeny of western North America (DeCelles, 2004) characterized by several hundreds of kilometers of backarc basement uplift. The central Chilean flat subduction is in fact considered a modern example of the ancient flat subduction of the Farallon Plate beneath western North America.

## 3.3 Seismic Data

### *3.3.1 Our Seismic Catalog*

Our seismic tomography inversion is based on a set of local passive sources, recorded during four short-term seismic campaigns, and a regional 1-D background model specific to the region. The recorded seismicity and station coverage are shown in Fig. 3.2B.

OVA99 was deployed in the region of Ovalle (30°-32°S, 72°-70°W) during the period of mid-November 1999 to mid-January 2000. Thirty-seven short-period three-component receivers, about 30 km apart, recorded continuously the local micro-seismicity ($0.5 < M_l < 5.5$) with a sampling rate of 125 pts/s.

CHARGE (Chile-Argentina Geophysical Experiment, an American project of the University of Arizona) continuously recorded seismicity from December 2000 to May 2002, and consisted of 22 broadband seismic sensors (10 STS-2, 10 Guralp CMG-3ESPs and 2 Guralp-40T) deployed along two profiles at 30°S and 36 °S, with some stations positioned in between. Sampling rate was 40 pts/s.

CHARSME (CHile ARgentina Seismological Measurement Experiment) was carried out from mid-November 2002 to March 2003 in the purpose of analyzing the regional seismo-tectonic features and to map the shift in subduction geometry of the Nazca slab. It comprised 29 portable broadband three-component stations (27 CMG-40T and 2 CMG-3T Guralp) that continuously recorded seismicity with a sampling rate of 125 pts/s.

CHASE (CHile-Argentina Seismic Experiment) recorded seismicity from mid-November 2005 to March 2006 included, and was composed of 14 broadband and 12 short period seismometers. It focused around the area of Santiago (33.5°-34°S and 70°-71°S) with the main goal of locating shallow seismicity along fault systems and quantifying the seismic hazard of the capital region, and also recorded slab events which were used in this study.

In an effort to increase receptor coverage and to improve hypocenter determination near coastal areas, earthquakes recorded by 15 permanent seismic stations from the Chilean Seismological Service of the University of Chile were supplemented. The OVA99, CHARSME, and CHASE station networks were installed and maintained by a collaborative group of experts from Géoazur laboratory, France, the IRD and the Geophysical Department of the University of Chile.

### *3.3.2 Event Location in a 1-D Background Model*

All events were consistently relocated, using HYPOINVERSE (Klein, 2000), within a ‘minimum’ average 1-D velocity model of least-square fit that best describes the region, constructed

using passive and active sources, and the VELEST program (Kissling et al., 1994) for depths greater than 20 km. The average velocity model represents a 17 layer model with average Vp/Vs ratio of 1.76. In comparison to the IASEP-91 global average model, which is used in Wagner et al. (2005)'s tomography inversion, our model produces generally faster velocities and a deeper average continental Moho (Fig. 2.1.4).

To ensure stability and reliability of our tomography results, we selected only the highest quality events with the following selection criteria for P- and S-waves, respectively: (a) maximum error of manual picking of ± 0.25 s and ± 0.4 s, (b) maximum pick quality index of 2 and 3 (0 being excellent, 4 being discarded), (c) maximum hypocenter uncertainty of 5 km in all directions, (d) maximum RMS misfit ($\sqrt{\Sigma R_i^2}/N$, where $R_i$ is the time residual at the $i^{th}$ station) of < 0.6 s, and (e) minimum 8 and 4 station observations. We retain a total of 3 603 events for the inversion process, including 52,011 and 51,631 P- and S-wave arrival times, respectively.

## 3.4 Methods

### *3.4.1 3-D Tomography Inversion*

We apply the tomography code *TLR3* (Tomography, Localisation, Relocalisation) (Latorre et al., 2004; Monteillet et al., 2005) which calculates the damped least-square 3-D velocity field for P- and S-waves. Source-receiver ray tracing is calculated using the finite-difference algorithm developed by Podvin and Lecomte (1991). The geographical limits of our model are defined between longitudes 73.5°W and 64.5°W, latitudes 28.5°S and 37.5°S, and depths 0 to 215 km, representing a total volume of 960 x 840 x 220 $km^3$. It is discretized into a regular grid system of mesh size 40 x 40 x 10 $km^3$. Synthetic ray trajectories are calculated within a finer model of mesh size 2 x 2 x 2 $km^3$ to allow ray-path smoothness, and body wave travel-times are computed in the coarser model, for computational efficiency.

The least-square 3-D velocity structure is progressively retrieved through a set of iterations that solve for small velocity perturbations, in order to linearize the problem and reduce computational time constraints due to the large dataset, simultaneously relocating hypocenters at each step. The initial 1-D velocity model and its relocated seismicity provide the starting iteration for the inversion.

Damping and the weighed ratio of P- versus S-travel-times (Cp/Cs) were adjusted separately by fixing one parameter at a time, and allowing the other to vary, in order to obtain the values that minimize the RMS misfit solution. The parameters that led to best results were a damping value of 0.7 and a Cp/Cs value of 0.5.

Mesh spacing and robustness of the final velocity model were examined using the checkerboard and spike tests. The well resolved regions of the model have a spatial resolution representative of the mesh spacing used, and represent areas where the seismicity is densest.

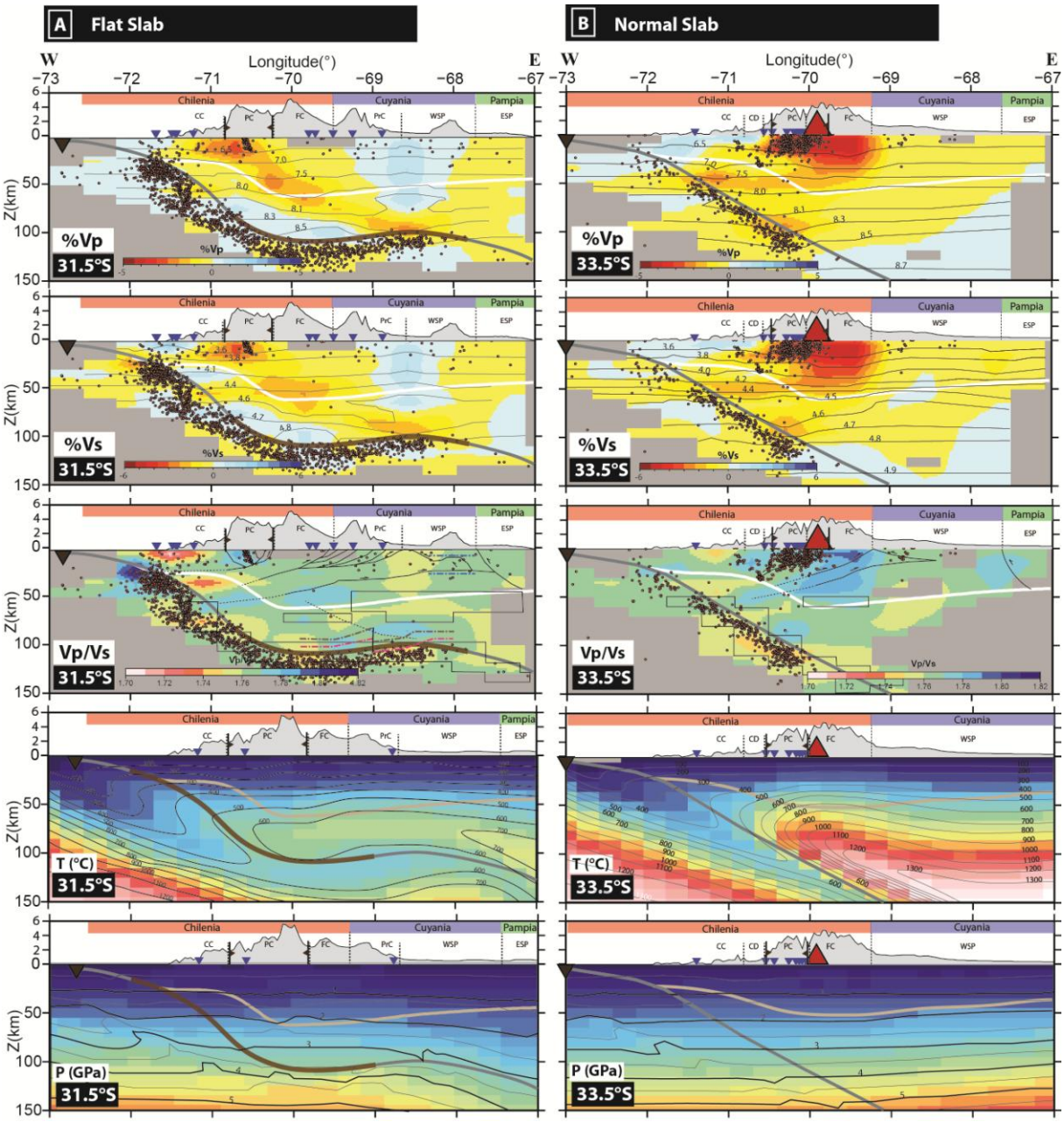


**Fig. 3.3***: Seismo-tectono-thermo-mechanical models of the (A) flat and (B) normal subduction zones along 31.5°S and 33.5°S, respectively, used to model the rock compositions of the systems. The seismic velocities are shown in P- and S-wave perturbations with respect to our reference model, and superimposed contour lines represent the absolute values, respectively. The seismicity is shown in black dots, and represents the entire catalog, and not just those chosen for the tomography inversion. Boxes superimposed on the Vp/Vs ratio figure, in the center, represent the fields where eclogite can be present. Curved solid and dotted lines in the continental crust (defined above the thick white or light brown line) indicate the approximate geometry at depth of inferred major detachment faults (from Ramos et al., 2002 and Farias et al., 2010), and our speculation of their westward extension into the mantle wedge or slab interface, which remains purely hypothetical, and based on our seismic tomography results and other independent studies (see text). The slab surface (thick grey line) is inferred from the slab seismic distribution, and the suspected location of the subducted Juan Fernandez ridge material (brown line segment). Topography, location of active volcanoes (red triangle), geological provinces and terranes and seismic station location (inverted blue triangles) are shown in the upper quadrant of each profile. Grey regions represent areas of insufficient ray coverage. The bottom two panels show the calculated temperature and pressure fields, with absolute values shown by the isocontour lines, used for the basis of our petrological models.*

### *3.4.2 Thermo-Mechanical State of the Subduction Lithospheres*

In order to link the superficial geology with the lithospheric-scale mechanisms of deformation, we compared the seismic properties of different rock types, at appropriate P-T conditions, with our calculated seismic velocities. In order to do so, we numerically estimated the P-T field along 2-D cross-sections of the flat and normal subduction zones, by modeling the thermo-mechanical behavior of the lithospheres. The plane-strain finite-differences code "Parovoz" (Poliakov and Podladchikov, 1992) was used to do so. This code is based on the FLAC method (Fast Lagrangian Analysis of Continuum, Cundall and Board, 1988) and has been widely used for a variety of geodynamic contexts (see ref. list in Chapter 2). The version of Parovoz used here is the same as that used in Gerbault et al. (2009). The equations of motion and heat transfer are explicitly solved in a time-marching scheme, and allow to account for self-consistent elasto-visco-plastic rheologies.

The modeled domain is sub-divided into rheological units of different thermo-mechanical parameters (describing elastic behavior, Mohr-Coulomb failure, and power-law viscous creep; see details in Gerbault et al. 2009) that describe the different portions of the continental and oceanic lithospheres. The computational time is chosen to span ~ 4 Ma, at which point we assume that the initial setup finds a transient thermo-mechanical equilibrium where it does not evolve much, and considering that only the major processes are significant at this time-scale (thermal diffusion and isostatic balance). Two synthetic models are constructed, for the normal and flat-dipping slab sections.

The slab geometries of our starting models are constructed using the earthquake distribution from our catalog, and complemented by seismic reflection and wide-angle data for depths less than 10 km (Flueh et al., 1998). The thermal ages of the oceanic and continental lithospheres are set to 35 Ma and 200 Ma, respectively, calculated as in Burov and Diament (1996), who attempt to best fit surface heat flow data (Hamza and Muñoz, 1996). The thickness of the continental lithosphere (LAB) is set at 100 km and 150 km depths above the flat and normal slab, respectively (close to LAB values determined by Tassara et al. 2006), determined by the 1350°C isotherm. In addition, radiogenic heating ($8 \times 10^{-10}$ W/kg, with an exponential decay set to 10 km) is imposed to the continental crust, which has a reference thickness of 35 km. Plate convergence rate is applied at 7.5 cm/yr, based on long-term predictions by Somoza and Ghidella (2005) and O'Neill (2005). Other details of the setup are provided in Gerbault et al. (2009). The final pressure-temperature (P-T) models are shown in Fig. 3.3.

### *3.4.3 Petrological Modeling*

For a 2-D representative cross-section through the flat (31.5°S) and normal (33.5°S) subductions zone of central Chile, and for each cell in the model and also at discrete regions (Fig. 2.3.3), we analyzed which rock types matched best our calculated seismic velocities for the continental mantle and lower crust, and the upper portion of the slab for which we have resolution. We based our analysis on experimentally measured isotropic properties of mafic and ultramafic rock compositions, representative of subduction zones (Hacker et al., 2003). The Hacker and Abers (2004) rock and mineral database provides a listing of such rock compositions, common to subduction zones. Hence, we tested 25 MORB-type rocks, 19 hydrated peridotites (10 harzburgites, 9 lherzolites) and 21 non-hydrated peridotites (10 lherzolites, 7 harzburgites, 1 dunite, wherlite, olivine clinopyroxenite, and pyrolite). We accounted for an uncertainty of ± 0.1 km/s in Vp and Vs, ± 100°C in temperature and ± 0.5 GPa in pressure. We did not compare with the predicted rock Vp/Vs ratios, since small velocity variations within the uncertainty constraint resulted in misleading substantial differences in the resulting Vp/Vs ratios. Therefore, we only acknowledge absolute velocities.

We have not used more complete or self-consistent mineral databases, such as Perplex (Connolly, 2005) and Theriak (Capitano and Petrakakis, 2010), since these methods generally require that detailed rock and mineral compositions be known (obtained from field sampling and laboratory analyses), which is not our case here. Furthermore, the resolutions associated to our thermo-mechanical and tomographic data are too large to justify the use of more complex and precise methods, which furthermore, are best applied to crustal domains than to mantle domains. In turn, we have used PerpleX (Connolly, 2005) to test the coherency in the results obtained with Hacker and Abers (2004)'s worksheet, proving to be a reliable method to use. And, Hacker and Abers (2004) is quite well developed for mantle domains, which is our principal interest in this study.

Finally, we have compared our results with Wagner et al. (2005)'s seismic velocities and their proposed rock/mineral compositions for the continental mantle above the flat slab, using Hacker and Abers (2004), to show important differences in our seismic values and consequent petrological interpretations.

The aim of this exercise is *not* to find a specific rock composition that best matches the seismic wave field at a certain depth, but instead to observe whether trends in rock type exists, such as recurring rock facies (e.g. eclogites vs. blueschists) or in the case of mantle rocks, hydrated vs. non-hydrated, garnet vs. plagioclase peridotites. And also to compare these trends between the flat and normal subduction zones. We therefore mapped the distributions and average volume percents (vol %) of water and individual minerals of the rocks that matched the seismic velocities for each cell. However, it is important to consider the number of solutions obtained for each cell, as it statistically quantifies the reliability of our results (Fig. 2.3.2).

## 3.5 Results

Our complete seismic tomography results, for several E-W, N-S and horizontal cross-sections of the region, are shown in Appendix C, and in Fig. 3.3. The flat and normal slab regions are defined as the area to the north and south of the subducting Juan Fernandez ridge path (~ 32.5°S), respectively.

### *3.5.1 The Forearc Crust: the Coastal Cordillera*

Between 15 and 25 km depth, the forearc crust (Coastal Cordillera) is described throughout the region with faster seismic velocities than our background model (Fig. 3.4), and is limited between the subduction and the western Andean fronts. Its eastern boundary is in good agreement with the location of the western limit of the La Ramada-Aconcagua fold-and-thrust belt in the western Andean front, at the boundary between the Coastal and Principal Cordilleras. To the north of the intersection between the subducting ridge and the trench (< 32.5°S), this anomaly is 120-160 km wide, compared to 180-230 km above the normal-dipping slab, to the south (e.g. Fig. 3.3 and Fig. 3.5).

In the flat slab region (< 32.5°S) and between 0 and 10 km depth, Vs is higher (3.6-3.7 km/s) (Fig. 3.4), as well as the seismic activity, relative to the normal-dipping slab region (> 32.5°S, 3.4-3.5 km/s), whereas Vp remains constant, resulting in very low Vp/Vs ratios of 1.70-1.73 (Fig. 3.4 and Fig. 3.5). At this depth, the Vp throughout the region is more-or-less constant (6.2 km/s). Directly below it, a narrow 10 km thick layer of reduced Vp and Vs, and higher Vp/Vs ratios (1.78) connects the plate interface with the Principal Cordillera crust (Fig. 3.3 and Fig. 3.4 and Fig. 3.7).

South of the subducting Juan Fernandez ridge subducting path (> 32.5°S) and near the surface, two distinct areas of reduced seismic velocities and high Vp/Vs ratios occur (Fig. 3.5), with unknown origin: (1) northeast of Valparaiso city (70°W/33°S), down to ~ 25 km depth, and associated with a cluster of deep seismicity, and (2) beneath Rancagua city (~ 70.5°W/34°S), down to ~ 10 km depth, and where the Vp/Vs ratio is very high (1.82). These localized high Vp/Vs areas suggest important

concentrations in fluids, with a possible superimposed thermal influence inherited by the relatively recent (4-9 Ma) magmatism in this area (responsible for the famous porphyry copper deposits of El Teniente and Rio Blanco-Los Bronces) or due to the proximity with the current volcanism in the eastern Principal Cordillera (Farias et al., 2010). However, it may be of interest to re-evaluate the seismic risk for these localities, given these new observations.

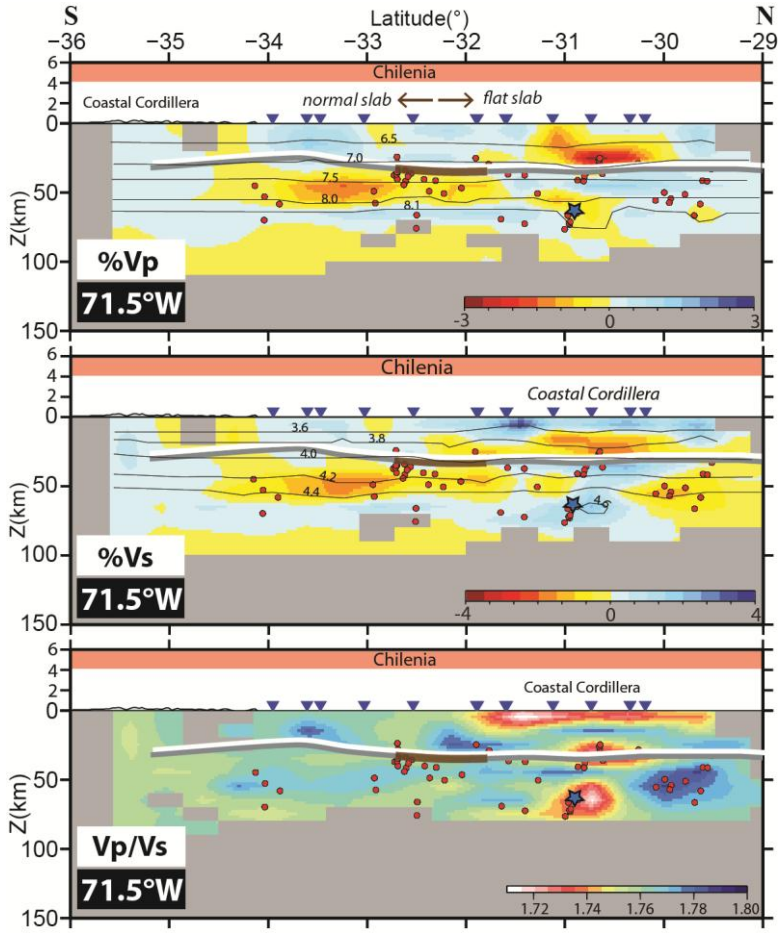


**Fig. 3.4** *: N-S cross-section through the forearc region along 71.5°W. The continental Moho, slab interface and subduction Juan Fernandez ridge material are shown in thick white, grey and brown lines, respectively. Seismicity is shown by the red circles. The seismic stations at the surface are the inverted blue triangles. Iso-contour lines are absolute seismic velocities. Blue star denotes the hypocenter of the Punitaqui earthquake. Note the change in color scale between %Vp and %Vs. Grey areas represent insufficient ray coverage.*

### *3.5.2 The Main Andean Arc Crust: the Principal and Frontal Cordilleras*

The entire Andean crust shows reduced seismic velocities and moderately high Vp/Vs ratios (~ 1.78-1.79) (Fig. 3.3 and Fig. 3.5).

Beneath the active and inactive volcanic arcs, until 25-30 km depth, the Principal Cordillera experiences strong reductions in both Vp and Vs, and moderately high Vp/Vs ratios (1.78-1.80), with a width of ~ 100 km (e.g. Fig. 3.5). This anomaly affects a broader area of the crust south of the subducting ridge path, and it becomes stronger ~ 50 km west (not directly beneath) of the active volcanic arc (> 33°S) in association with intense and deep seismicity. Directly above the inferred Juan Fernandez ridge path, at 5 km depth (~ 32.5°S/70.5°W), the seismic velocities are less reduced and

this area correlates with the location of the highest peak (Aconcagua, 6700 m, empty triangle in Fig. 3.5). The orientation and dimension of this anomaly mimic those of the La Ramada-Aconcagua fold-and-thrust belt. Only between 33°S and 34°S, does the anomaly spread into the Frontal Cordillera, stopping at the suture zone between Cuyania and Chilenia (Fig. 3.5). These observations suggest a strong structural influence on the shallow crustal seismic velocities.

Below ~ 35 km depth, this slow velocity anomaly propagates eastward deeper, penetrating the underlying mantle (Fig. 3.3) and progressively narrowing in its N-S extent. The seismic continental Moho has Vp ~ 8.0 km/s and Vs ~ 4.5 km/s.

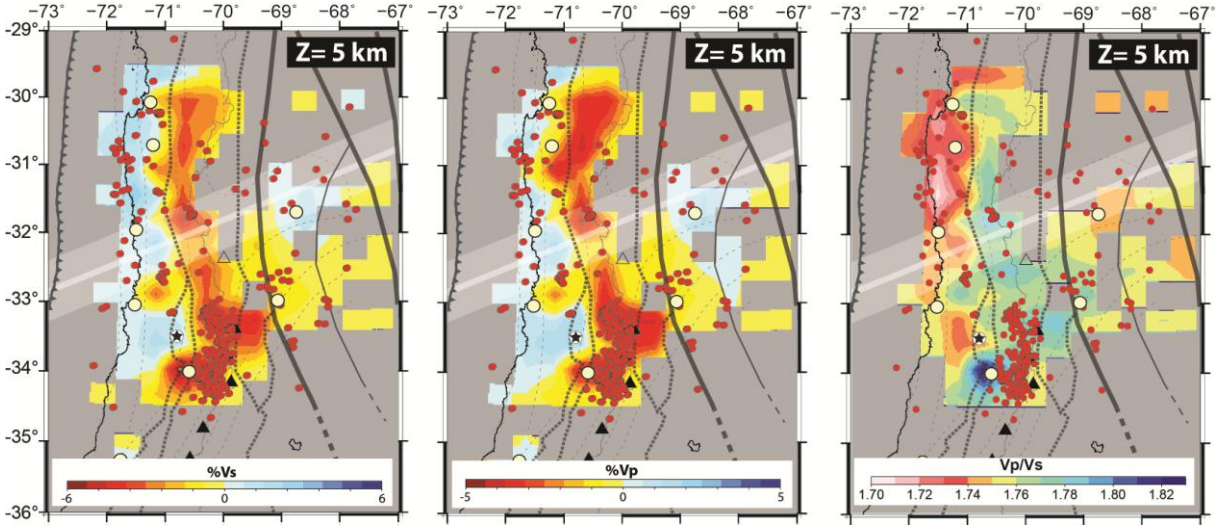


**Fig. 3.5***: Horizontal cross-section through 5 km depth in central Chile. Left, center and right figures show the velocity perturbations in S-waves, P-waves and the Vp/Vs ratio, respectively. Red circles are the earthquakes, solid grey lines are the major faults/sutures from Fig. 3.2A, dotted grey lines are the boundaries between the geological-tectonic provinces, white circles are the major cities with the capital city Santiago with a star, and the volcanoes are shown by black triangles. Empty triangle is the Aconcagua mountain, the highest in the region. Grey areas represent insufficient ray coverage.*

### *3.5.3 The Backarc Crust: the Precordillera and Western Sierra Pampeanas*

The backarc crust above the flat slab (< 32.5°S), comprising the Cuyania terrane (Precordillera and western Sierra Pampeanas), exhibits similar increases both in Vp and Vs, with relatively low Vp/Vs ratios (1.75-1.76) that affected the continental mantle down to 75-80 km depth (~ 20 km above the slab seismicity) (Fig. 3.3 and Fig. 3.6). The low Vp/Vs ratios suggest either a compositional or low temperature effect. On the contrary, previous results based on 1-D velocity forward modeling describe the Cuyania crust with high Vp/Vs ratios over 1.80 (Gilbert et al., 2006; Alvarado et al., 2007).

Unfortunately, as indicated by our checkerboard and spike tests, our results for the backarc region above the normal-dipping slab do not present sufficient resolution to provide any detailed discussion.

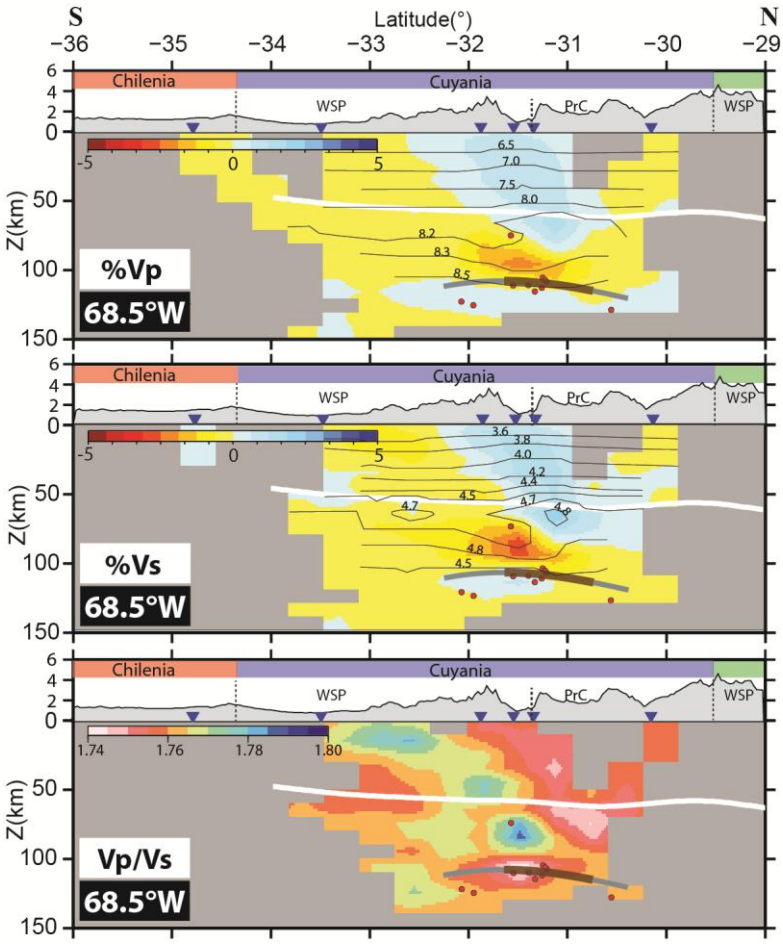


**Fig. 3.6***: N-S cross-section through the Cuyania terrane and above the eastern edge of the flat slab portion, at 68.5°S. Upper, middle and lower panels show the velocity perturbations in P- and S-waves and the Vp/Vs ratios, respectively. The white, grey and brown lines indicate the continental Moho, slab interface and subducting Juan Fernandez ridge material, respectively. Grey regions represent insufficient ray coverage.*

### *3.5.4 The Continental Mantle: beneath the Forearc and Principal Cordilleras (> 70.5°W)*

Throughout the region, the continental mantle's seismic velocity gradient is highest above 70 km depth (Fig. 3.3), which we define hereafter as the mantle wedge.

Above the normal slab, the seismic velocities in the mantle wedge (< 70.5°W) are slightly lower, with moderately higher Vp/Vs ratios (1.76-1.78), than our background model and the flat slab region (1.76-1.77) (Fig. 3.3 and Fig. 3.10), possibly reflecting a higher fluid or temperature content.

Above the flat slab, the mantle wedge is noticed as more heterogeneous, with horizontal variations in seismic velocities and Vp/Vs ratios. Between 35 and 50 km depth, the mantle below the seismic continental Moho (Fromm et al., 2004) has a higher Vs (4.2-4.4 km/s) compared to the normal slab region (4.0-4.2 km/s), whereas Vp is more-or-less constant (7.0-7.75 km/s) throughout the region (Fig. 3.3 and Fig. 3.7). In consequence, the Vp/Vs ratio above the flat slab region (to the north of the subducting ridge path) is significantly lower (1.70-1.74) in this depth range, analogous to the shallow forearc crust (Fig. 3.3-3.4, Fig. 3.7, Fig. 3.9 and Fig. C.3 in Appendix C). Since this anomaly lies within the seismic Moho's uncertainty depth range, it may either represent either continental crust or mantle. Between 50 and 70 km depth, the mantle exhibits reduced seismic velocities and higher Vp/Vs ratios (1.78-1.79), indicating possible local hydration (Fig. 3.3 and Fig. 3.7).

### *3.5.5 The Continental Mantle: beneath the Frontal Cordillera and Cuyania (< 70.5°W)*

Below 70 km depth, the continental mantle is generally characterized by increased Vp (8.0 to 8.5-8.6 km/s) and Vs (4.5 to 4.8-4.9 km/s) and relatively low Vp/Vs ratios (1.75-1.77) (Fig. 3.3, Fig. 3.6 and Fig. 3.10). However, this trend is interrupted beneath the Frontal Cordillera by a slow east-dipping velocity region that extends downwards to the slab's interface at 68.5°W, beneath the Cuyania terrane, and connects with the surface of the Principal Cordillera (Fig. 3.3), forming a curved plane, in 3-D. This slower region is mostly characterized by slightly higher Vp/Vs ratios (1.77-1.79) (Fig. 3.3), and is locally strongest in the 10-20 km above the slab's interface, before re-subduction occurs (Fig. 3.7 and Fig. 3.8).

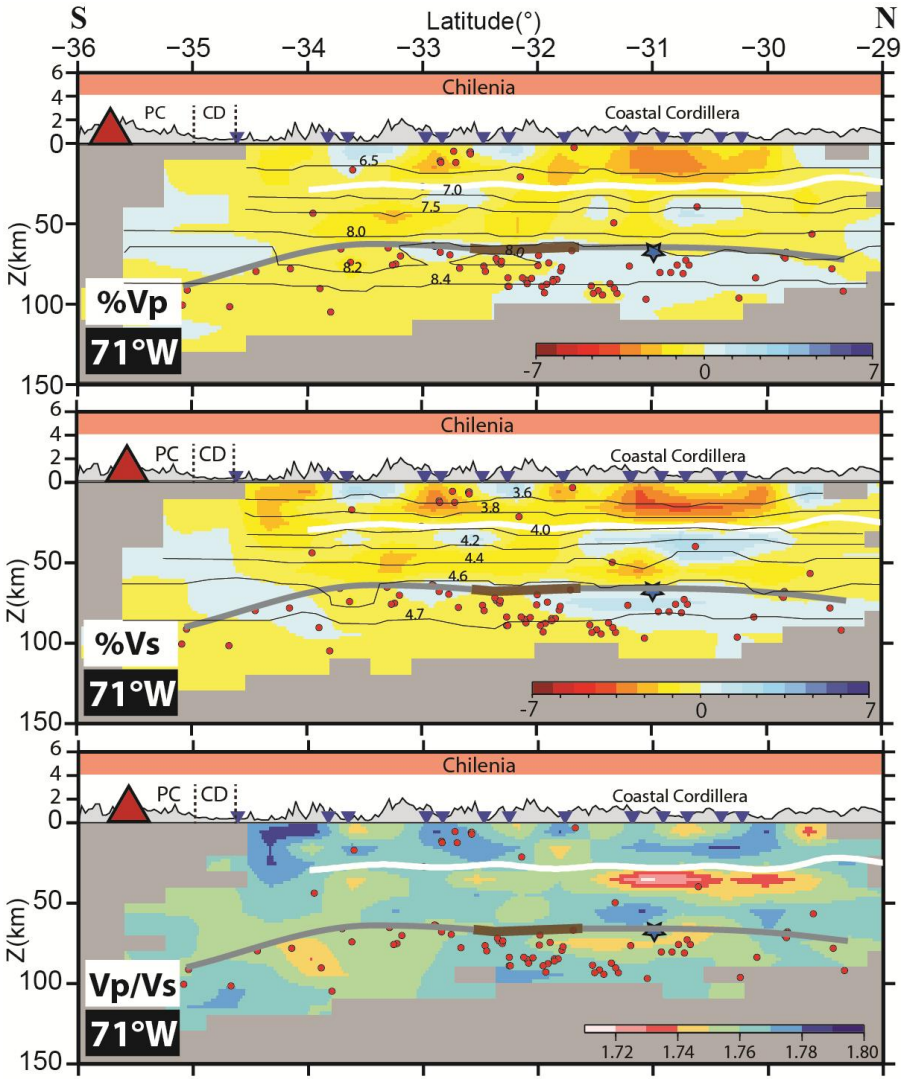


**Fig. 3.7***: N-S cross-section through the forearc crust and continental mantle wedge at 71°W, showing the very low Vp/Vs ratios directly beneath the continental Moho. Legend, as in other previous figures. Grey regions represent areas of insufficient ray coverage.*

### *3.5.6 The Subducting Plate: Flat Slab Region*

Down to ~ 50 km depth, the upper portion of the subducting slab in the flat slab region (< 32.5°S) is highly seismogenic and corresponds to reduced Vs with high Vp/Vs ratios (1.80-1.82), suggesting possibly fluids (Fig. 3.9 and Fig. 3.10). Deeper, between 50 and 75 km depth, the Vp/Vs ratios decrease, as well as the seismicity along the upper seismic plane of the Double Seismic Zone (DSZ) (Fig. 3.3).

The western part of the flat slab segment, between 69°W and 70.5°W, is expressed by higher Vp (8.5-8.6 km/s) and Vs (4.8-4.9 km/s) than the eastern part (8.4-8.5 and 4.7-4.8 km/s, respectively), however, the Vp/Vs is relatively low (1.75-1.77) and constant (Fig. 3.10). The eastern part of the flat slab at 31.5°S (Fig. 3.3A), before it re-subducts and where the Juan Fernandez ridge is expected to occur, experiences the strongest reductions of ~ 0.2 km/s in both Vp and Vs.

At 31°S, 71°W and 50-80 km depth, the slab is imprinted by unusual seismic properties that define the 1997 Punitaqui (Mw 7.1) aftershock region (Fig. 3.9), with strongly decreased Vp (8.0-8.1 km/s) and increased Vs (4.5-4.7 km/s) that result in very low Vp/Vs ratios (1.71-1.73). The highest Vs value is observed near the lower seismic plane of the Double Seismic Zone, uncorrelated with the most seismogenic aftershock area.

### *3.5.7 The Subducting Plate: the Normal Slab Region*

Contrary to the flat slab, the normal slab is less seismically active above 50 km depth, including the plate interface, and corresponds to normal Vp/Vs ratios of 1.76-1.77 (Fig. 3.10). The slab seismicity becomes denser below 50-60 km depth and is associated to lower Vp/Vs ratios of 1.74-1.76. Beneath 125-150 km depth, seismic activity becomes rare.

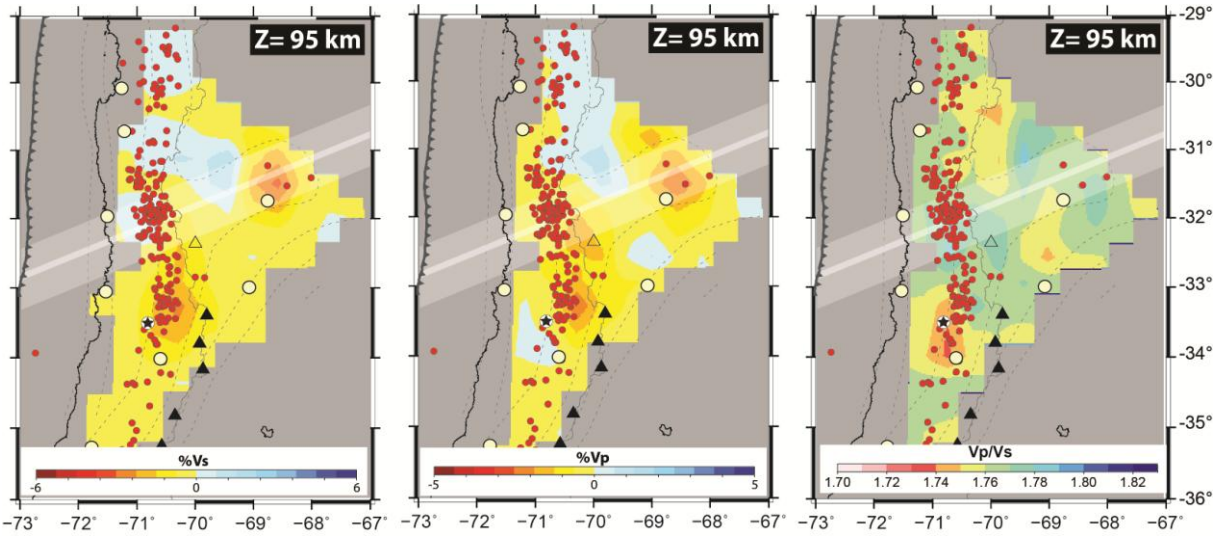


**Fig. 3.8***: Horizontal cross-section through the continental mantle at 95 km depth of the P- and S-wave perturbations and Vp/Vs ratios, showing the localized region of reduced seismic velocities above the inferred Juan Fernandez ridge subduction path. Grey regions represent areas of insufficient ray coverage.*

## 3.6 Discussion

Variations in the seismic properties of a medium can be attributed to changes in (i) temperature, (ii) pressure, (iii) composition, (iv) texture (e.g. pore geometry), (v) fabric (e.g. preferred mineral orientation, faults, fractures), and (vi) fluid content (water and magma) (Soustelle, 2010; Hacker and Abers, 2012). Although, there are disagreements amongst the scientific community of their affects on the seismic behavior of rocks, I list a few generally accepted concepts: Increases in temperature and fluid concentrations result in decreased seismic velocities and increased the seismic attenuation (e.g. Soustelle, 2010). Magma (partial melt) has the effect of decreasing more strongly Vs than Vp and resulting in higher Vp/Vs ratios, however, P- and S-waves are not much attenuated when the magma volume is less than 5% (Soustelle, 2010). Water in peridotites, even in small quantities, results in decreased seismic velocities and increased seismic attenuation (Karato and Jung, 1998; Karato, 2003). However, seismic attenuation can behave similarly for high temperatures and in the presence of fluids, leading to confusion between them in the absence of more data (Soustelle, 2010). Jacobsen et al. (2008) stated that water in rocks has the same effect on both Vp and Vs, and consequently provokes little change in the Vp/Vs ratio. However, many other studies associated high and very high Vp/Vs ratios to the presence of fluids, assuming different effects on Vp and Vs (e.g. Takei, 2002; Wang and Zhao, 2012). We will consider the later and more popular interpretation for the analysis of our results. Finally, rock composition (besides water content) has a limited impact on seismic attenuation or velocity (Sobolev and Chaussidon, 1996), and instead can be detected by analyzing the Vp/Vs ratios, as Vp and Vs are impacted differently for different rock types (Soustelle, 2010).

Since the seismic variations linked to texture and fabric are outside the scope of this study, we have concentrated mainly on possible variations in compositions and water content. However, knowing at first-order the surface locations of major faults and other forms of structural damage, we can extrapolate their influence at depth and end up considering fabric effects as well, but to a second degree.

### *3.6.1 The Forearc Crust: the Coastal Cordillera*

The higher seismic velocities and low Vp/Vs ratios in the forearc crust, particularly to the north of the subducting ridge (< 32.5°S), relative to the Andean crust, suggest denser rocks and negligible water content. Rock density increases with decreasing temperature and increasing the magnesium and iron content of rocks (i.e. more mafic).

Since the eastern limit of the fast forearc anomaly coincides with the western boundary of the La Ramada-Aconcagua fold-and-thrust-belt, it suggests that the forearc Coastal Cordillera and the Principal Cordillera may be compositionally distinct from one another, a contrast which is often associated with fault zones (Twiss and Moores, 1992). This trend is also observed in northern Chile (at 15°S and 23°S), where sharp density contrasts exists between the forearc and the Altiplano-Puna crusts (Tassara, 2005). The north Chilean forearc reflects high gravity and resistivity values and low P-wave attenuation, interpreted as cold and rigid material which acts as an indenter into the weaker Altiplano-Puna lithosphere (Tassara et al., 2006; Gerbault et al., 2009). In central Chile, the forearc crust also reflects high gravity anomalies (A. Tassara, personal communication); however, seismic attenuation models by Deshayes (2008) do not reveal any particular trend. The forearc in the flat slab region experiences increased basal and surface erosion than the southern forearc, due to higher compression and plate coupling induced by the slab's buoyancy and the ridge's indentation effect (Yáñez and Cembrano, 2000; Ramos et al., 2002; Marquardt et al., 2004; Tassara et al., 2005; Espurt et al., 2008; Alvarado et al., 2009; Gerbault et al., 2009). This causes exposure of deeper and denser basement rocks at the surface, as confirmed by the gravity studies (Tassara et al., 2006). However

increases in rock density imply a simultaneous increase in both Vp and Vs, and not only Vs. The same can be said for the lower geotherm, induced by the flat subduction.

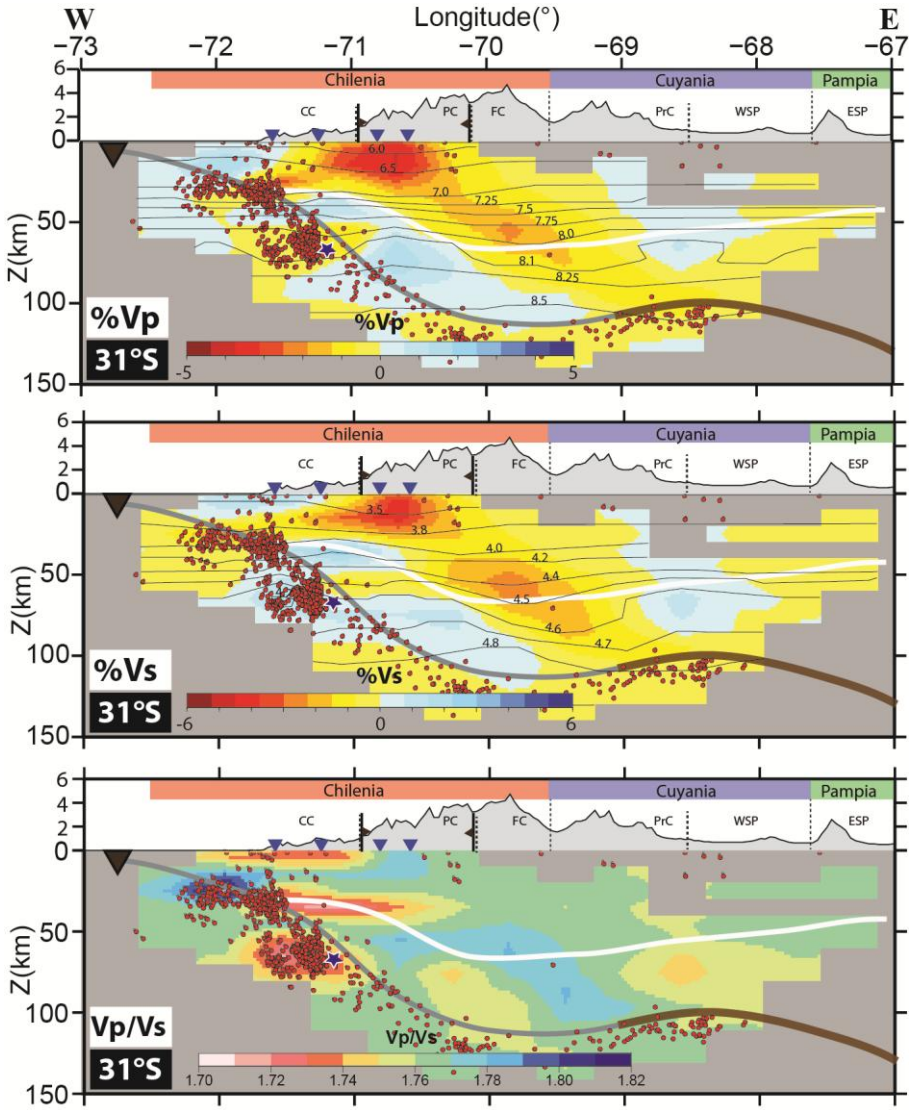


**Fig. 3.9***: E-W cross-section at 31°S showing the 1997 (Mw 7.1) Punitaqui hypocenter (blue star), its aftershocks and the region affected (very low Vp/Vs ratios).*

Similar to our observations, Sallares and Ranero (2005) also noted that the central Chilean forearc, contains faster Vs (> 4.0 km/s) north of 33°S than to the south (~ 3.5 km/s), which they attributed to a compositional change, since the forearc basement to the north is more affected by plutonism and metamorphism, whereas the southern part is more meta-sedimentary and less intruded (Ramos et al., 1986). Comparing our forearc's seismic velocities to the north (at 5 km depth, Vp: 6.2 km/s, Vs: 3.6 km/s) with those predicted for mafic rocks using the Hacker and Abers (2004) worksheet, we notice that our Vp and Vs are much lower than most rocks at these depths (average ΔVp: -1.25 km/s, ΔVs: -0.66 km/s), suggesting that more felsic rocks should be instead considered. Unfortunately, the Hacker and Abers (2004) rock database does not provide felsic rock compositions to compare our seismic results with. Therefore, the forearc crust to the north of the subducting ridge is faster and denser than the forearc crust to the south, however cannot be explained by more mafic

compositions. Therefore, temperature and composition do not seem to be the leading parameters influencing the seismic velocities of the shallow forearc to the north of 32.5-33°S, though they may have a minor influence.

Directly beneath it, between 35 and 50 km depths, we notice identical seismic characteristics as the shallow forearc, with similar increases in Vs, constant Vp, and very low Vp/Vs ratios. Also, their geographical distributions are the same (i.e. exclusively above the flat slab region, to the north of the subducting ridge's path) (Fig. 3.3, Fig. 3.4, Fig. 3.7 and Fig. C.3 at 5 km), suggesting a relationship either with the flat slab geometry at 100 km depth, or by being affected by the same independent factor, or by comprising the same rock entity which exhibits such seismic characteristics.

Because the deeper anomaly is located along the seismic continental Moho (Fromm et al., 2004) and within its depth uncertainty range, we wonder whether it represents the lower forearc crust or the mantle wedge corner? Its lower limit (50 km) coincides with the downdip extent of the dense seismogenic interplate zone (Fig. 3.9), suggesting that the deeper anomaly comprises the forearc crust and that the seismic Moho is probably a too shallow estimation. Comparing our seismic velocities for the deeper anomaly (at 35-50 km depth) with those predicted for mantle rocks at appropriate P-T conditions (P: 1-2 GPa and T: 200-400°C) (#8 in Fig. 2.3.3 and

Fig. 3.11), we note that our Vp and Vs are generally much lower (Vp: -0.41 to +1.18 km/s, Vs: -0.27 to +0.82 km/s) and that mafic crustal rocks match much better. However, no rock type matches our low Vp/Vs values of 1.70-1.73. Furthermore, all our seismic velocities over 50 km depth match those for mantle rocks (> #9, Fig. 3.11), supporting the idea that the deeper low Vp/Vs anomaly represents the lower forearc crust, that the continental Moho is probably positioned at ~ 50 km depth instead of 35 km (in Fig. 3.10, we show our suggested new Moho in thick dotted white line), and that the entire forearc crust above the flat slab is characterized by these unusual seismic properties that result in very low Vp/Vs ratios for the region.

The lower forearc crust of the Cascadia subduction zone also exhibits very similar low Vp/Vs ratios (1.65) due to increased Vs (4.1-4.2 km/s), and also decreased Vp (6.6-6.8 km/s), between 25 and 35 km depth (Ramachandran and Hyndman, 2012). In comparison, our Vp are significantly higher (7.0-7.1 km/s), but our Vs is similar. The only common mineral that can explain very low Vp/Vs ratios is silica. Takei (2002) indicated that adding only 5% of silica to a rock can significantly decrease the Vp/Vs ratio. For the Cascadian forearc, Ramachandran and Hyndman (2012) explained their seismic anomaly with 20% pure silica precipitated from silica-saturated slab-derived fluids, which form when significant amounts of sediments are subducted. We have tested using the Hacker and Abers (2004) worksheet that increasing the silica content of a rock decreases Vp more than Vs; and since our Vp is constant throughout the region, we consider that our Vs, in the flat slab region, must be abnormally high and that a higher silica content is unlikely the cause our low Vp/Vs ratios in the shallow and deep forearc crust. Furthermore, practically no sediments are expected to enter the subduction zone in central Chile, since the subduction channel at these latitudes is shown to be too narrow (0.2 km at 31°S, ~ 1 km at 33°S) (Gross and Micksch, 2008; Contreras-Reyes et al., 2010) and the exposure of basement rocks in along the subduction margin (due to basal erosion and lack of channel lubrication) suggests that no sediments enter the subduction zone since the Jurassic (Marquardt et al., 2004). Therefore, the accumulation of silica-rich sediments at the base of the forearc crust is not a possible compositional change that can explain answer our low Vp/Vs ratios.

Since composition and temperature fail at explaining our low Vp/Vs ratios in the shallow and deep forearc crust above the flat slab, we now consider seismic anisotropy. Shear wave splitting studies by MacDougall et al. (2012) in the continental mantle of this region indicate that seismic anisotropy is strong in the mantle wedge (below the forearc), with olivine a-axes oriented parallel to the slab-strike, i.e. perpendicular to the direction of convergence, analogous to the expected orientations of foliation, faulting, fracturing, or veining which form normal to the principal stress axis

(Twiss and Moores, 1992). For this reason, we suspect that the unusual forearc seismic properties of the flat slab region are caused by seismic anisotropy, which in turn could be created by the compression induced by indentation of the Juan Fernandez ridge into the forearc (Yáñez and Cembrano, 2000). However, this does not explain why the eastern boundary of the forearc anomaly, throughout the region, is restricted to the boundary between the Coastal Cordillera and the Principal Cordillera, which also suggest a structural influence, however not impacting the Principal Cordillera.

Because we notice that the aftershock area of the 1997 Mw 7.1 Punitaqui intraslab earthquake (70 km depth, Fig. 3.9), also located in the flat slab region, describes a similar seismic behavior as the forearc crust, we consider that a relationship with the forearc may exist. Our seismic catalog, which recorded events between 2 and 7 years after the mainshock, describes the aftershock area as a large and highly seismogenic region, with strongly reduced Vp, increased Vs, and very low Vp/Vs ratios of the same order as those in the forearc. This anomaly also cannot be explained by a high silica concentration simply because quartz cannot exist in big quantities in the oceanic lithosphere (olivine and quartz minerals are incompatible together), and the lower density of quartz/coesite over such a large volume would create drastic gravimetric instabilities, modifying the subduction dynamics. And, for the same reasons as those described for the forearc crust, we infer that the unusual seismic parameters of the Punitaqui aftershock region can be associated to structural damage induced by the mainshock and producing seismic anisotropy. However, we do not have the tools necessary to analyze the seismic anisotropy in our region, and we suggest it purely by the process of elimination.

Finally, it appears that the two low Vp/Vs anomalies of the forearc crust are not physically connected to together, and are separated by a region, between 20 and 35 km depths, of higher Vp/Vs (1.80-1.82) and reduced Vs (Fig. 3.4 and Fig. 3.7). The plate interface adjacent to it also shows strongly reduced Vs and very high Vp/Vs ratios (> 1.82). Westward-dipping detachment faults, from the Andean belt, cross the forearc crust and reaching the subduction interface around these depths around 34°S and in northern Chile also (Farias et al., 2010). Fig. 3.10 shows Farias et al. (2010)'s interpretations, based on surface and seismic observations, of the deep shear zone configuration for the Aconcagua fold-and-thrust belt at 34°S, which I have superimposed on the more northern latitudes. Also shown is Ramos et al. (2002)'s deep shear zone interpretation for the backarc region. Using these fault geometries, we remark that by extending the main detachment faults towards the subducting interface, there is a good correlation with regions of high Vp/Vs ratios in the forearc and mantle wedge regions. This sudden increase in the Vp/Vs ratio in the forearc (surrounded by low Vp/Vs ratios), suggests the presence of fluids, especially at the plate interface. This is supported by the knowledge that pore fluids, from the oceanic crust, are expelled around such depths, by the increasing lithostatic pressure and consequent pore closure, in addition to the activation of primary dehydration reactions (e.g. Kirby et al., 1996; Peacock, 2001; Hacker et al., 2003). Therefore, we suggest that a major crustal shear zone crosses the forearc crust at ~ 30 km depth, reaches the subduction interface, and channelizes slab-derived fluids into the continental crust. Nevertheless, there is little conclusive data on the geometry and extent of these faults at depth.

To resume, the shallow and deep forearc anomalies appear linked to a common origin, as well as being correlated to the occurrence of the flat slab at depth. We assessed that temperature and mafic rock compositions are insufficient to explain the increases in Vs (and not Vp) that characterize the forearc crust. The strong compression induced by the ridge and flat subduction, suggest that seismic anisotropy in the forearc crust may be the leading factor that explains these anomalies, however, we do not have the means to analyze this hypothesis. There may also be a link between the identical seismic behavior shared by the forearc and the slab Punitaqui earthquake, and in that case, the forearc anomalies could represent relatively short-lasting features. In conclusion, the forearc and Punitaqui aftershock seismic anomalies remain mysterious to us.

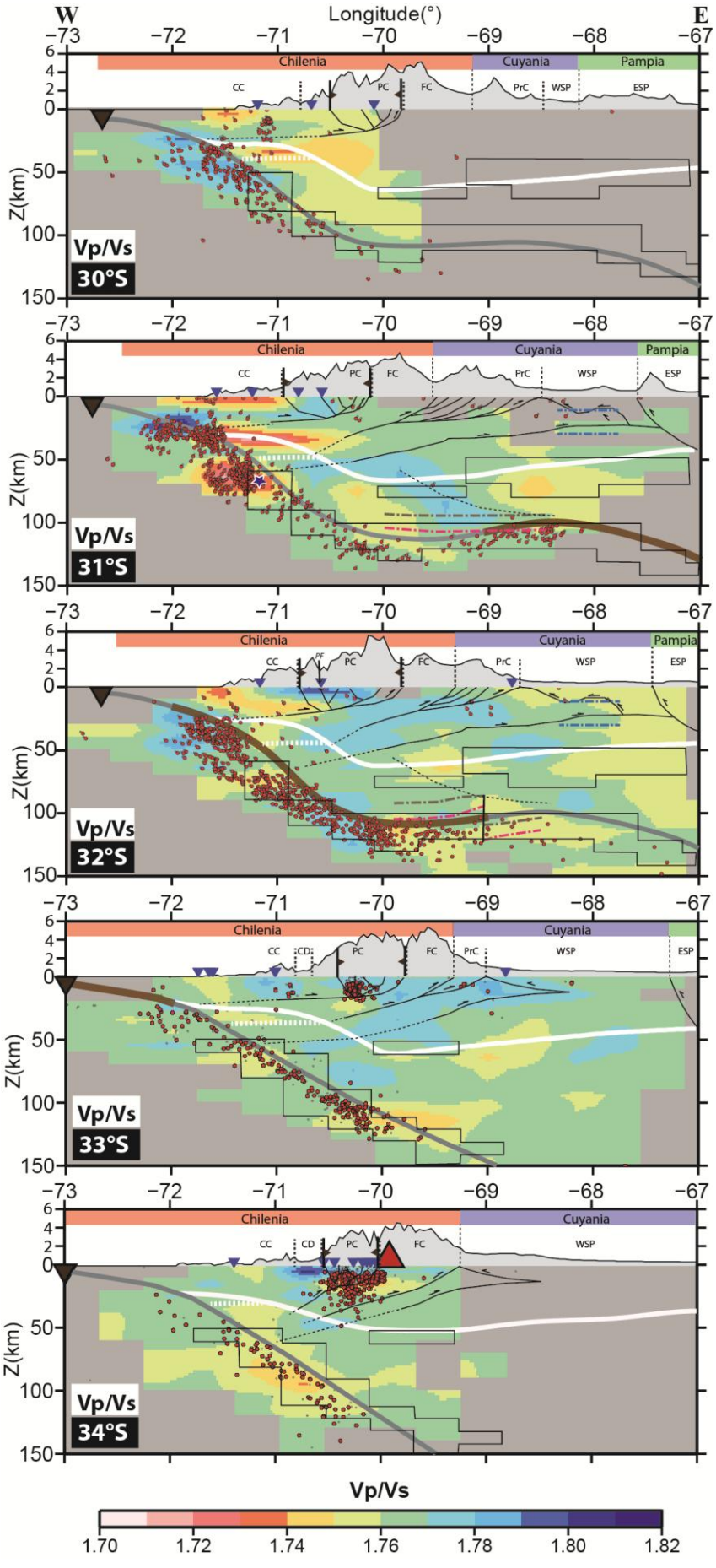
W
Longitude(°)
E
−73
−72
−71
−70
−69
−68
−67
Chilenia
Cuyania
Pampia
CC
CD
PF
PC
FC
PrC
WSP
ESP
Z(km)
0
50
100
150
Vp/Vs
30°S
31°S
32°S
33°S
34°S
Vp/Vs
1.70
1.72
1.74
1.76
1.78
1.80
1.82

**Fig. 3.10** *: E-W cross-sections of the region, from north to south, at 1°S latitude increments, showing the correlations between our Vp/Vs field, the earthquake distribution, and the possible geometry of faults at depth from Ramos et al. (2002) in the backarc, and from Farias et al. (2010) in the forearc region. Dotted black lines are our proposed fault extensions, made to regions of high Vp/Vs ratio Thick dotted white line denotes our suggested new continental Moho depth, based our rock type modeling. Boxes indicate the possible locations of eclogite rocks which we modeled in our petrological analysis (Chapter 2 Part Three). The grey, blue and pink "line-dot-lines" are the location and shape of seismic reflectors imaged by Gans et al. (2011), using the IASEP-91 model, and are interpreted as the oceanic interface (grey line) with its underlying oceanic Moho (pink), and the other lines are crustal discontinuities, also imaged by Alvarado et al. (2007) and other workers. Grey areas represent regions of insufficient ray coverage.*

### *3.6.2 The Main Andean Crust: the Principal and Frontal Cordilleras*

The upper ~ 30 km of the Principal Cordillera crust is characterized by strongly reduced Vp and Vs, with relatively high Vp/Vs ratios, which match well the location, geometry and dimension of the La Ramada-Aconcagua fold-and-thrust belt (~ 100 km wide). And it also correlates with the most seismogenic zone of the Andes, particularly adjacent to the active volcanic arc (> 33.5°S) (Fig. 3.5). This fold-and-thrust belt is composed dominantly of thrust and strike-slip faults that join together at depth with a basement detachment shear zone at ~ 20-30 km depth (Fig. 3.10) (Ramos et al., 2002; Giambiagi et al., 2003; Farias et al., 2010). Therefore, the correlation between the fold-and-thrust belt and the slow velocity anomaly seems to indicate that structural damage is responsible for this perturbation, in addition to the association of meta-sedimentary rocks and higher water content (reflected by the higher Vp/VS ratios), typically characteristic of fault zones. If a deep detachment shear zone connecting the slab's surface to the La Ramada-Aconcagua fold-and-thrust belt exists in reality, as stated in section 3.6.1, then we may consider that the fluids in the Principal Cordillera crust are partly derived from the dehydrating slab.

In opposition to the Principal Cordillera, the Frontal Cordillera to the east appears relatively unaffected by these strong velocity variations, suggesting stronger, less fractured crust (Ramos et al., 2002), in agreement with its lower seismicity. The only exception is the Cordon del Plata region, strongly reduced in seismic velocities down to 35 km depth, located between 33°S and 34°S, beyond the eastern limit of the Aconcagua fold-and-thrust belt and west of Mendoza city. The Cordon del Plata region is also affected by structural damage, though to a lesser degree than the Aconcagua fold-and-thrust belt to the west (Alvarado et al., 2009). In addition, the higher geothermal gradient associated to the arc volcanism could contribute somewhat to these velocity reductions.

Little is known about the compositional affinity of the Andean basement rocks, since there is little evidence left of the existence of Chilenia, obliterated by abundant intrusions, volcanism and sedimentation. The oldest rocks in the Frontal Cordillera (~ 500-508 Ma, Caminos et al., 1982) are located in the Mendoza region (33°-34°S), and are believed to document the metamorphic event of its accretion rather than its age of formation. Nevertheless, these old rocks have continental (felsic) compositions that support the existence of another terrane (Chilenia) accreted against the mafic and ultramafic Cuyania terrane. Currently, there is no knowledge of the suture zone location at depth that separates Chilenia from Cuyania (Ramos et al., 1986); i.e. the deep Andean crust could either be old and mafic such as Cuyania, or, old and felsic like Chilenia.

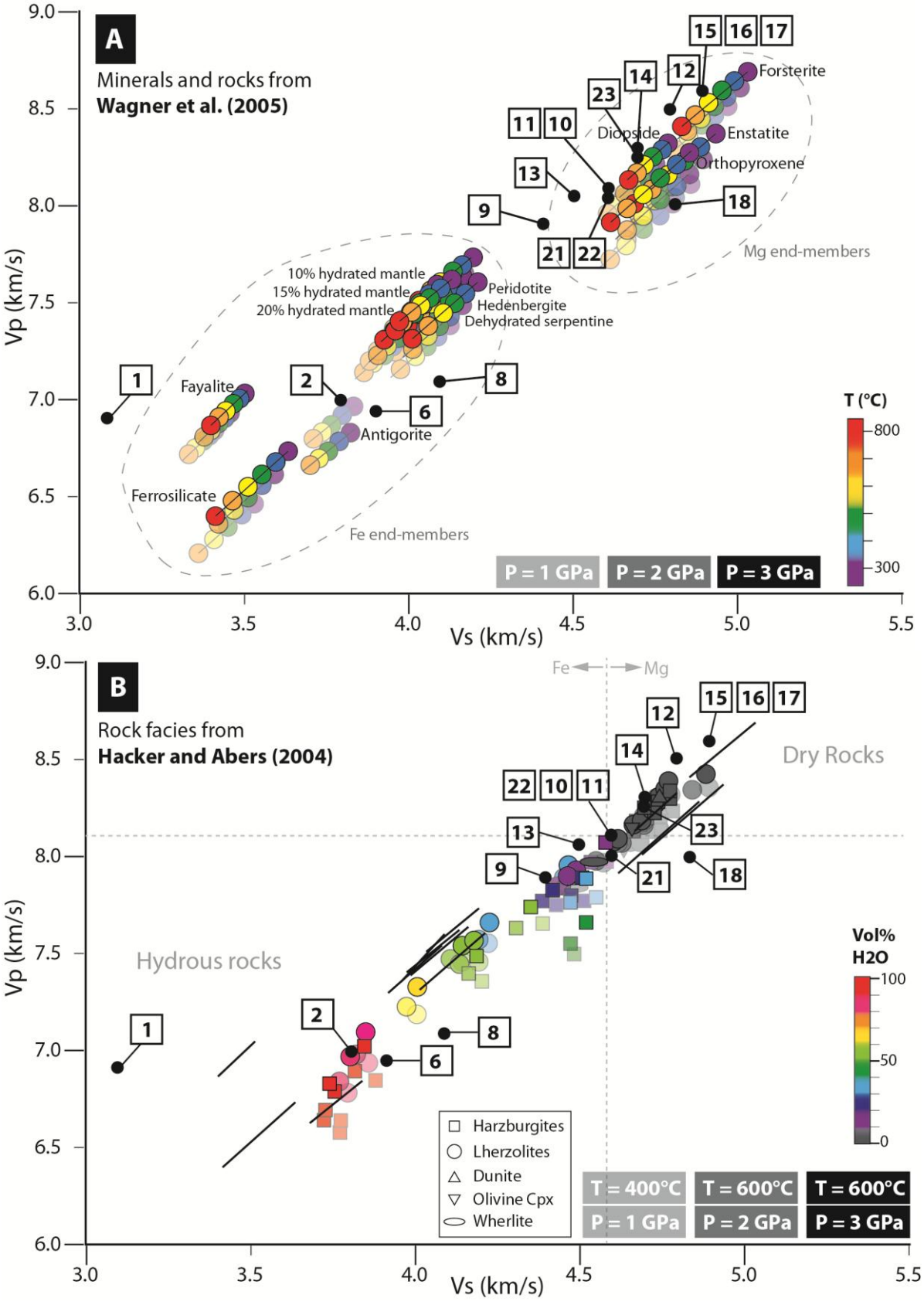
A
Minerals and rocks from
Wagner et al. (2005)
Forsterite
Enstatite
Orthopyroxene
Diopside
Mg end-members
10% hydrated mantle
15% hydrated mantle
20% hydrated mantle
Peridotite
Hedenbergite
Dehydrated serpentine
Fayalite
Antigorite
Ferrosilicate
Fe end-members
T (°C)
800
300
P = 1 GPa
P = 2 GPa
P = 3 GPa
Vp (km/s)
Vs (km/s)
B
Rock facies from
Hacker and Abers (2004)
Fe
Mg
Dry Rocks
Hydrous rocks
Vol% H2O
100
50
0
Harzburgites
Lherzolites
Dunite
Olivine Cpx
Wherlite
T = 400°C
P = 1 GPa
T = 600°C
P = 2 GPa
T = 600°C
P = 3 GPa

**Fig. 3.11***: Rock and mineral seismic behaviors at varying pressures, temperatures and fluid content for the continental mantle above the flat slab. (A) Minerals and rock compositions taken from Wagner et al. (2005) for which we calculated the seismic properties from Hacker and Abers (2004) spreadsheet, at different temperatures and pressures. These minerals are fayalite, forsterite, ferrosilicate, enstatite, hendenbergite, diopside, orthopyroxene (95% enstatite, 5% ferrosilite); and the rock compositions are peridotite (90% olivine, 8% orthopyroxene, 2% garnet), dehydrated serpentine (49% olivine, 51% orthopyroxene), 20% hydrated mantle (80% olivine, 15% antigorite, 5% chlorite), 15% hydrated mantle (85% olivine, 12% antigorite, 3% chlorite), and 10% hydrated mantle (90% olivine, 8% antigorite, 2% chlorite). Each mineral and rock is represented by a circle, whose color is according to the temperature conditions. Each was calculated at three different pressures. Increasing the temperature decreases the seismic velocities, and increasing the pressure increases the seismic velocities. We have surrounded the regions where Mg- and Fe-rich rocks and minerals occur, indicating that most of our sampled regions (Fig. 2.3.3) are located in the Mg-rich section. (B) Ultramafic rock compositions from Hacker and Abers (2004) database, including harzburgites and lherzolites and others, representative of subduction zones. The rocks are color coded according to their volume percent of water. The higher it is, the lower its seismic velocities. We have also calculated their seismic properties at varying pressures and temperatures, since the uncertainty range used in our petrological modeling is quite large. To compare the differences with Hacker and Abers (2004) rock trends, we superimposed on them the mineral and rocks trends (black lines) from Wagner et al. (2005) at pressure 3 GPa (in (A)).*

Our seismic tomography results show that the lower Andean crust contains decreased seismic velocities relative to our background model, with relatively high Vp/Vs ratios (1.77-1.79) (Fig. 3.3 and Fig. C.6 at 70°W). Gravity data for the Andean crust indicates that it is isostatically compensated (Tassara et al., 2006; Alvarado et al., 2009), and its 60-70 km deep crustal root suggests that it lies within the eclogite stability field (Hacker et al., 2003; Hacker and Abers 2004), hence, expect eclogite to occur. However, our seismic velocities for the deep crust are too low to represent eclogitic rocks (Fig. 3.3 and Fig. 3.10). Our seismic velocities at 50-60 km depth can be explained mostly by hydrated mafic rocks: jadeite epidote blueschist (74% H2O), garnet granulite, and lawsonite amphibole eclogite (57% H2O). However, between 60 and 70 km depth, and within the uncertainty range of the seismic Moho, zoisite and zoisite-amphibole eclogites (32% and 10% H2O, respectively) could occur, as well as continental mantle rocks with an average hydration of 10-30%. In both cases, the Andean crust is most likely to be hydration, but non-eclogitized (at least until 60 depths). Therefore, we wonder why not more eclogite occurs, especially because it is located well within the eclogite stability field and significant amounts of water seem to be present, which have the effect of reducing further the seismic velocities and accelerating the process of eclogite formation (Artemieva and Meissner, 2012).

In general, the absence of an eclogitized crustal root can be explained by the following: (1) the rock composition is too felsic to transform to eclogite. Felsic rocks further decrease the seismic velocities by their smaller densities and their higher radiogenic heat production (Muñoz, 2005); (2) the ambient temperature is too low for transformation to occur rapidly (even in the presence of large quantities of fluids) (Artemieva and Meissner, 2012). Flat subductions result in the expulsion of its asthenosphere, strongly reducing the regional geotherm; and (3) crustal delamination of the previously eclogitized lower crust occurred (DeCelles et al., 2009). This gravitational instability is dependent on the rheology contrasts between the crust and underlying mantle (Lenardic and Moresi, 1999). Depleted mantle compositions, such as cratonic lithospheres, increase the mantle viscosity and are able to sustain thick and dense crust, rendering the processes of crustal detachment or "drooping" difficult (Doin et al., 1997). Detachment of the Andean lower crust was proposed by Kay and Gordillo (1994) to explain the deep and old crustal signatures found in the Pocho lava rocks above the re-subducting slab (65°W, 32°S). A late Neogene crustal delamination was also suggested for the central Puna region

in northern Chile to explain its 1 km higher topography and ~ 20 km thinner crust, compared to the Altiplano (> 75 km thick) (Kay and Kay, 1993; Schurr et al., 2006).

Therefore, the slow seismic behavior of the Andean crust can be explained either by a silica-rich composition (felsic) and/or by the presence of fluids, either by non-eclogitized mafic rocks.

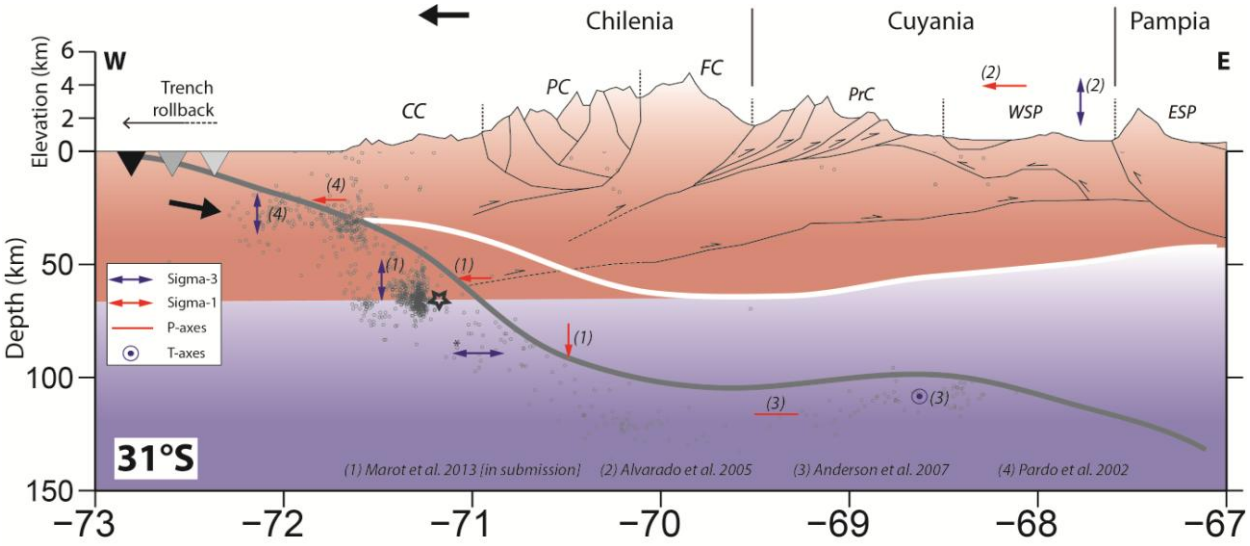


**Fig. 3.12***: State of stress of the upper and lower lithospheres at 31°S, based on stress tensor calculations (Pardo et al., 2002; Alvarado et al., 2005 and Marot et al., 2013) and P- and T-axes orientations of focal mechanism solutions (Anderson et al., 2007). The P- (red) and T-axes (blue) are shown as line segments along the flat slab portion (dot and circle around it denotes an orientation perpendicular to the plane of view). Principal stresses, σ1 (red) and σ3 (blue) are shown by arrows. Number next to arrows and lines are the references. Structural composition of the overriding plate is based on Ramos et al. (2002) and Farias et al. (2010), and our inferred fault extensions (see text). The continental Moho and slab interface are shown by thick white and grey lines, respectively. Seismicity is shown in thin circles. The star locates the Punitaqui hypocenter. Thick arrows are the direction of plate motion. Accreted terranes and the geological provinces are shown (CC: Coastal Cordillera; PC: Principal Cordillera; FC: Frontal Cordillera; PrC: Precordillera; WSP: Western Sierra Pampeanas; ESP: Eastern Sierra Pampeanas). Areas in compression are shaded in red, and in tension in blue. Both lithospheres are in horizontal compression, and sub-horizontal compression above and below 70 km depth, parallel to convergence, respectively. The flat slab portion is dominated by extension, however in a direction normal to convergence direction.*

### *3.6.3 The Backarc Crust: the Cuyania Terrane*

The Cuyania terrane (Precordillera and western Sierra Pampeanas) is described by our seismic tomography model as a fast seismic velocity region, with relatively low Vp/Vs ratios, throughout its crustal thickness (Fig. 3.3, Fig. 3.6 and Fig. C.1 and C.2 of Appendix C). The exposed rocks of the Precordillera are meta-carbonates in composition, and the western Sierra Pampeanas rocks are a mixture of crystalline calcites, amphiboles, mafic and ultramafic rocks (Ramos et al., 1986; 2002; Ramos, 2004). Their Grenville ages (1.0-1.1 Ga) are over-printed by scarce younger granitic rocks. Gravity studies mapped the Cuyania terrane as a high density anomaly and a low geothermal gradient until 37°S and 67°W (Tassara et al., 2006), including the Bermejo and Mendoza basins. In our model, we only observe the resulting high seismic velocities until ~ 33°S, though our model resolution

continues further south. The peak of intensity of this anomaly is situated beneath San Juan city, directly above the inferred subducting ridge track (Fig. 3.5), and the reason for their spatial correlation is unclear.

The low average elevations of the Precordillera (~ 2000 m) and western Sierra Pampeanas (~ 1000 m) with respect to their gravity measurements suggest that some excess density in their lower crusts or underlying mantle is required (Miranda, 2001; Alvarado et al., 2005; 2007; Gilbert et al., 2006). Multiple seismic (global and regional) and gravity studies measured a crustal thickness of 60 km beneath the Precordillera, and 50-55 km beneath the western Sierra Pampeanas. Below 35 km depth, the crust is described with a higher Vp gradient (Reigner et al., 1994; Fromm et al., 2004; Alvarado et al., 2005; 2007; Gilbert et al., 2006, Calkins et al., 2006; Corona, 2007; Alvarado et al., 2009).

Our seismic velocities in the Precordillera and western Sierra Pampeanas crusts from 40 to 70 km depth describe: (i) between 40 and 50 km depth: jadeite epidote blueschist (74% $H_2O$, 3.21 g/cm$^3$), garnet granulite (0% $H_2O$, 3.33 g/cm$^3$) and lawsonite amphibole eclogite (57% $H_2O$, 3.34 g/cm$^3$), (ii) between 50 and 60 km depths: amphibole eclogite (26% $H_2O$, 3.51 g/cm$^3$), (iii) between 60 and 70 km depth (around the crust-mantle boundary): zoisite eclogite (10% $H_2O$, 3.52 g/cm$^3$). These rock distributions confirm the presence of eclogites in the backarc lower crust below 50 km depth, with an average hydration of 10-25% and densities of 0.1-0.2 g/cm$^3$ (~ 3.50 g/cm$^3$) greater than mantle rocks becoming progressively drier with depth. The distribution of possible eclogites is summarized in Fig. 3.10. Since eclogite is not seismically distinguishable from mantle rocks, we are unable to provide information about maximum thickness of this eclogite layer.

The presence of eclogite attests for the presence of mafic crust, indicating that Cuyania (and not Chilenia) rocks occur in the backarc region, suggesting that the suture between these terranes probably does not lie beneath the Precordillera or western Sierra Pampeanas, as proposed by Armijo et al. (2010), but instead locates further west.

How long such dense eclogites can be preserved in the eclogite field before becoming gravitationally unstable is uncertain, since experimental data lack on this topic (Artemieva and Meissner, 2012). It is known that the transformation from basalt/gabbro to eclogite crust is critical of temperature and fluids, whereby in cold and dry environments, metamorphic reactions are very slow (Hacker et al., 1996; Austrheim et al., 1997; Jackson et al., 2004; Artemieva and Meissner, 2012). In central Chile, the current flat slab configuration is thought to have been achieved since ~ 6 Ma (Kay and Mpodozis, 2002; Kay and Abbruzzi, 1996). Therefore, assuming that the rate of the eclogite transformation is greatly reduced in these cold circumstances (though in the presence of fluids), we imagine that the likely present-day eclogite is a feature pre-dating 6 Ma, when temperatures were higher and more favorable for this process to occur.

### *3.6.4 The Continental Mantle and Subducting Oceanic Lithosphere*

One of the questions we ask is whether the flat slab dehydrates? Fluids have an important influence on the buoyancy and rheology of rocks. Mapping their distribution helps us to better understand the mechanisms that maintain slab buoyancy as well as those deforming the overriding lithosphere. By studying the seismic behavior of the overriding mantle, relative to what we assume are 'normal' subduction conditions at ~ 34°S, we hope to qualify and quantify the hydration (linked to slab dehydration processes) and composition of the continental mantle above the flat slab.

### *3.6.4.1 The Continental Mantle: < 70 km depth (the mantle wedge) (> 70.5°W)*

As discussed in Section 6.1, we define the mantle wedge as starting below 50 km depth in the flat slab region (< 32.5°S) (thick dotted white line Fig. 3.10). Our seismic velocities, only down to 60 depth, match hydrated mantle rocks (Fig. 3.13 and #9-11 in Fig. 2.3.3), indicating a serpentinitized layer of only ~ 10 km in thickness. Out of all these rock solutions, 70-80% of them are hydrated, and the average hydration is 30% (Fig. 3.13). This shows that the slab does dehydrates even though the low temperatures that are expected to inhibit these chemical reactions (e.g. Kirby et al., 2001). The hydrous minerals constituting the matching rocks are: amphibole (15%) and talc (< 5%) (found almost exclusively at this depth range), and chlorite and Å-phase (< 10%) (Fig. 2.3.6). Though our locally higher Vp/Vs ratios agree with a hydrated mantle at these depths, it is in turn contradicted by very low P-wave attenuation values and normal S-wave attenuation values (Fig. 3.14) (Deshayes, 2008).

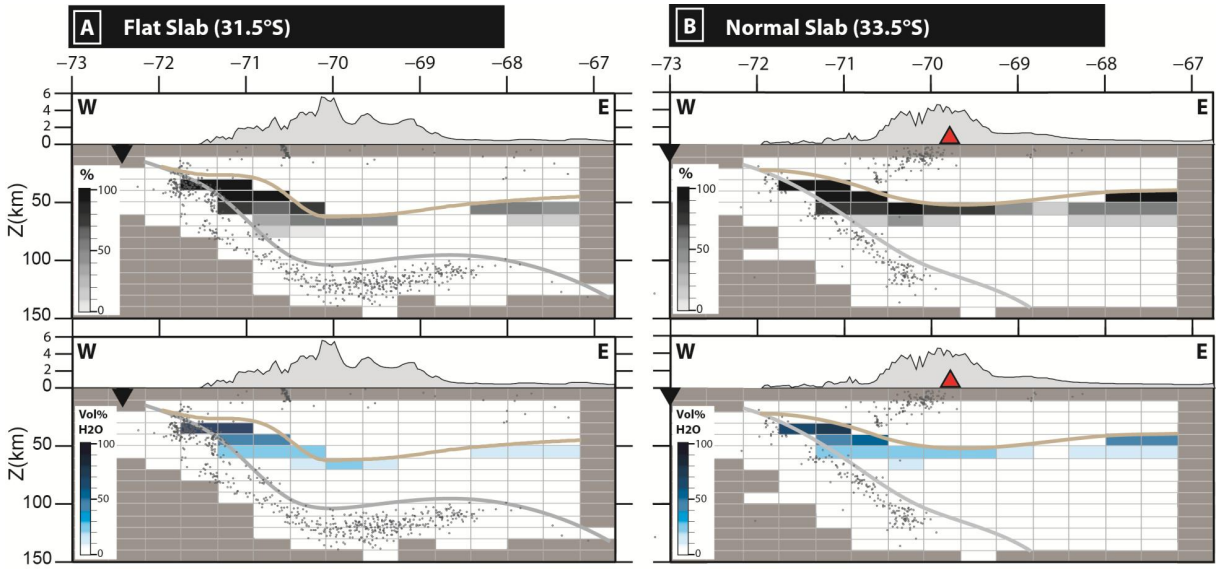


**Fig. 3.13***: Mantle wedge hydration for the (A) flat and (B) normal slab regions. Upper panel: percentage of hydrated rocks for all the solutions found for each cell. Lower panel: average (vol % $H_2O$) hydration for each cell. Because these are averages, it is important to consider the number of rock solutions per cell, shown in Fig. 2.3.2 of Chapter 2 Part Three.*

We notice that the 50-70 km depth range, where mantle hydration is expected to occur, coincides with four other trends/events (in the flat slab region): (1) the upper plane slab seismicity is strongly reduced between these depths and adjacent to the hydrated mantle wedge, corroborating serpentinization (e.g. Fig. 3.3), (2) the hypothetical westward extension of a deep basement shear zone originating from the backarc crust, cross-cut the mantle at this depth (Fig. 3.10), (3) a change in the slab's state of stress occurs at 60-70 km depth, from horizontal compressional to extensional (Fig. 3.12) (Pardo et al., 2002; Marot et al., 2013), (4) the hypocenter location of the 1997 Punitaqui mainshock (Mw 7.1) occurred at 70 km depth (Fig. 3.9 and Fig. 3.12) (Lemoine et al., 2002), and (5) the maximum continental crustal thickness lies somewhere between 60-70 km depth (Reigner et al., 1994; Fromm et al., 2004; Alvarado et al., 2005; 2007; Gilbert et al., 2006, Calkins et al., 2006). Therefore, this depth range appears to be an important area of locally strong stresses, affecting both the mantle wedge and the oceanic lithosphere, and the distribution of fluids, in the flat slab region.

The mantle wedge above the normal-dipping slab (> 33°S) reflects very similar hydration patterns as the mantle wedge above the flat slab (Fig. 3.13), implied by the seismic variations which are too small to be described by separate rock types. Yet, in a normal subduction configuration, the higher geothermal gradient and arc volcanism lead to the expectation that the mantle wedge is further hydrated. Hence, we wonder whether the mantle wedge above the normal slab is unusually dry, or, the mantle wedge above the flat slab is abnormally hydrated. Although the similar seismic velocity variations, Deshayes (2008) showed that both P- and S-waves are highly attenuated within the mantle wedge above the normal slab, between 50 and 75 km depth (Fig. 3.14). The erupted lavas at the surface, from the first three volcanoes of the Southern Volcanic Zone, between 33.5° and 35°S, reflect higher degrees of fractionation and crustal contamination caused by the longer magma ascent and residence times in the crust (Michael Dungan, personal communication). These effects can be explained by the higher compressive stresses in the overriding plate at these latitudes, compared to further south (> ~ 35°S), caused by the southward migrating ridge subduction trench (Ramos et al., 2002). On the other hand, these effects can also be the result of a small magma volume, reflecting poor slab dehydration reactions or too low mantle wedge temperatures (due to proximity to the flat slab) to trigger such reactions. Therefore, we suggest that the influence of the Juan Fernandez ridge overlaps by a few hundred kilometers the region directly to its south, rendering our assumed 'normal' subduction conditions closer to the transition state, between the 'absolute' normal and flat slab conditions.

#### *3.6.4.2 The Continental Mantle: > 70 km depth*

Within the flat slab region (< 32.5°S) and over 70 km depth, the continental mantle experiences increased seismic velocities (Vp > 8.1 km/s, Vs > 4.6 km/s), relative to our background model and to the mantle above the normal slab. Unfortunately, we are limited to the east by our model resolution of the normal slab, and are unable to compare the mantle with that of the flat slab region. Therefore, I will solely describe the mantle of the flat slab region.

The many rocks that match the seismic velocities of the mantle overlying the flat slab segment are mostly dry garnet peridotites (equally in lherzolites and harzburgites) (#12-14 and #22 and # 23 in Fig. 3.11), which are rich in orthopyroxene and magnesium minerals (enstatite, forsterite and pyrope), in agreement with Wagner et al. (2005; 2006; 2008)'s interpretation of a Mg-pyroxene-rich (enstatite) continental mantle (

Fig. 3.11 and Fig. 1.20). Only around the continental Moho depths (50-60 km), do the seismic velocities match rocks with some degree of hydration (10-20%) (#13, #21 in Fig. 3.13, and #22 in Fig. 3.11). Nevertheless, these can be confused with lower crust material, since the Moho signal here is not clearly mapped due to poor seismic impedance contrasts (Fromm et al., 2004; Alvarado et al., 2005; Gilbert et al., 2006; Heit et al., 2008). The higher seismic velocities of the continental mantle above the flat slab are in good agreement with previous work that have qualified it as cold and dry, due to flat subduction effects.

Directly above the eastern edge of the flat slab portion, between ~ 90 and 110 km depth, we notice a local reduction in the continental mantle's seismic velocities and an increase in the Vp/Vs ratios, a seismic signature for possible mantle hydration (Fig. 3.8 and Fig. 3.6). This relatively small area of 100 x 100 x 20 $km^3$ is focused above the suspected location of the subducting Juan Fernandez ridge material, and at the edge of re-subduction (68.5°W). This region is equally noticed by several other studies (Fig. 3.14), as a reduced P-wave velocity anomaly (Bianchi et al., 2013), attenuated in S-waves (Deshayes, 2008), with higher mantle conductivity values than its surroundings (Booker et al., 2004; Orozco et al., 2013). These data all support the notion of a hydrated mantle. In opposition, Wagner et al. (2005) correlated this region with very low Vp/Vs values, resulting from a decrease in

P-wave velocities, in agreement with our and others studies (Fig. 1.20). Another contradiction to mantle hydration is that our absolute seismic velocities only match dry mantle rocks (#23 in Fig. 3.11; more details in section 3.6.5).

This anomaly seems to be a deep continuation of the shallow and slow velocity anomaly located in the Principal Cordillera (see Section 5.2). The continental mantle beneath the Frontal Cordillera is also impacted by reduced seismic velocities (though less pronounced than at 68.5°W) (Fig. 3.3), increased Vp/Vs ratios, and this time, is attenuated in P-waves (instead of S-waves directly east) (Fig. 3.14) (Deshayes, 2008). The combination of seismic velocity reductions and attenuations leads us to assume that fluids are involved; however, we do not know how to interpret the alternations between P- and S-waves attenuations in the continental mantle. We hypothesize that slab fluids, released from the dehydrating Juan Fernandez Ridge before it re-subducts, migrate upwards into the Andean lower crust where the Vp/Vs ratios are also high. Because colder mantle temperatures increase the rock strength, shearing of the mantle due to stresses might have caused local weakening by faulting/fracturing, and hence, the ascent of fluids from the dehydrating slab can be facilitated along such shear zones. Crustal faults are believed to cross-cut the continental Moho and underlying mantle, although none have been mapped at these locations (e.g. Fromm et al., 2004).

### *3.6.5 The Oceanic Lithosphere*

Along the flat slab region (< 32.5°S) and between 0 and 50-70 km depth, the subducted oceanic lithosphere presents high Vp/Vs ratios. The seismic velocities of the oceanic mantle at these depths are near those for antigorite (#6 in Fig. 3.11A), i.e. close to 100% serpentinization (#6 in Fig. 3.11B), in agreement with the ridge's inferred deep lithospheric hydration, offshore (Kopp et al., 2004). The Nazca oceanic crust and possibly parts of its mantle, offshore, have been mapped by seismic and gravity investigations as deeply hydrated along fault systems which run parallel to the Juan Fernandez ridge axis (Yáñez et al., 2002; Grevemeyer et al., 2003; 2005; Kopp et al., 2004; Ranero et al., 2005; Clouard et al., 2007; Contreras-Reyes et al., 2010). Clouard et al. (2007) showed that hydration can reach over 20 km depth. We suggest that the higher Vp/Vs ratios of the flat slab region are the consequence of the deep and intense slab hydration that exists along the Juan Fernandez ridge.

At the plate interface of the flat slab region, the Vp/Vs ratio is particularly high (1.82) (e.g. 31°S, Fig. 3.9), and no rocks match its seismic velocities. Faccenda et al. (2008; 2012) and Dorbath et al. (2008) argued that compressional stresses, which impact the region of the slab above 70 km depth (Pardo et al. 2002, Marot et al., 2013), result in compaction and expulsion of fluids trapped in the slab. This mechanism might explain the plate interface anomaly, whereby fluids saturation conditions may exist. Deeper, between 70 km and ~ 100-120 km depth, Marot et al. (2013) showed that the slab is in downdip extension with dominantly reactivated outer rise faults (represented in Fig. 3.1). Faccenda et al. (2008; 2012) and Dorbath et al. (2008) also showed that tensional stresses along faults induce negative pressure gradients which attract fluids deeper inside the slab. According to us, this should have the effect of maintaining the hydration levels within the slab and hence, the high Vp/Vs ratios constant. However, the lower Vp/Vs ratios in this depth range are generally relatively low (1.76-1.77).

In the normal slab region and between 0 and 50-70 km depth, the Vp/Vs ratios are lower than for the flat slab region at the same depth range, indicating a lower degree (30-40% H20) of slab hydration (Fig. 3.10). Below 70 km depth, the slab's Vp/Vs ratios are even smaller (1.74-1.76), reflecting dry conditions, and correspond to an increase in the slab seismic activity (e.g. 34°S in Fig. 3.10).

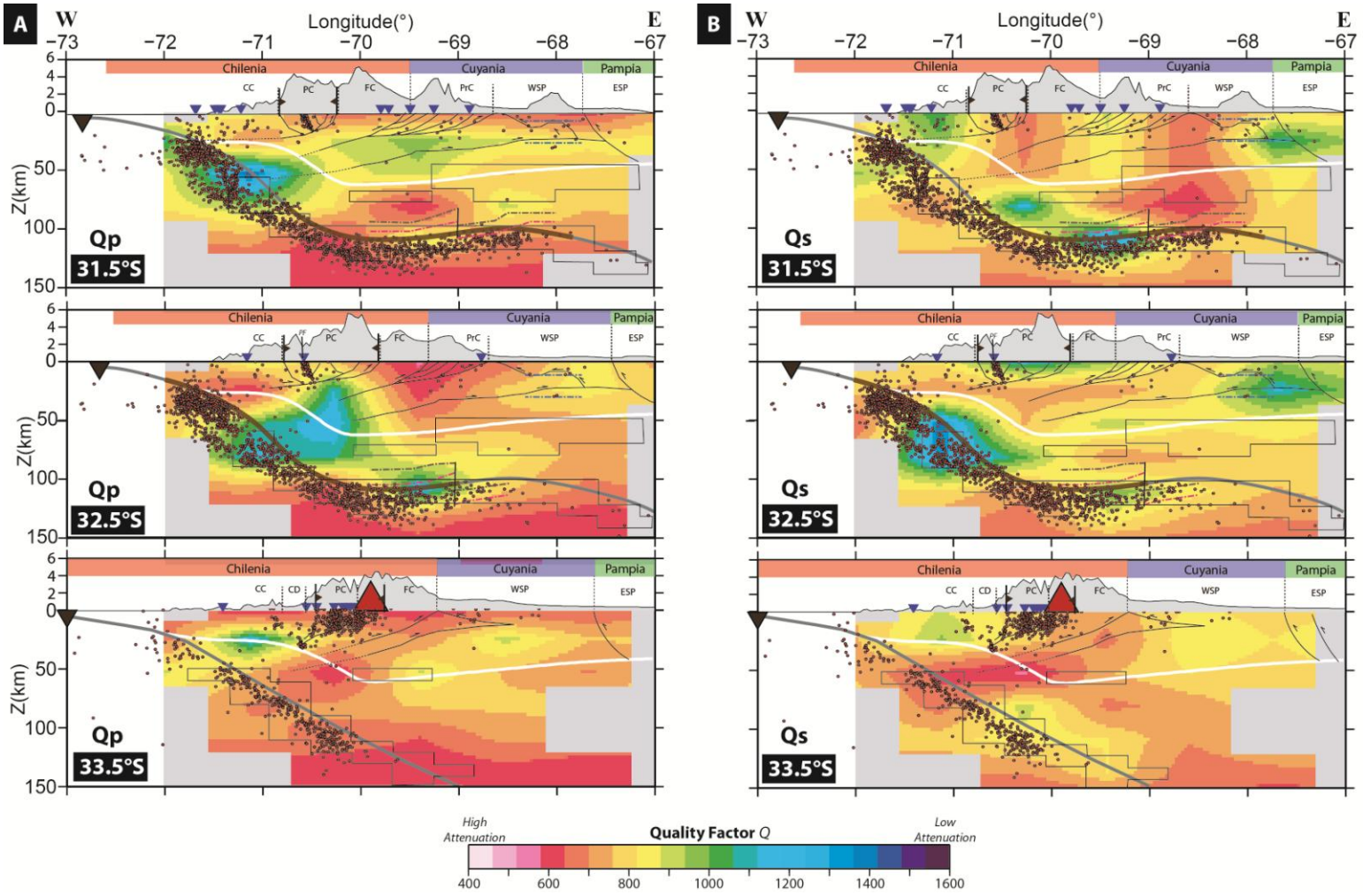


**Fig. 3.14**: *E-W cross-sections of the P- (left) and S-wave (right) seismic attenuation along the flat slab (upper panel), transition zone (lower panel) and normal slab (lower panel) regions, from Deshayes (2008). Superimposed are the speculative fault geometries at depth from Ramos et al. (2002) and Farias et al. (2010), as mentioned in the text; and the location of possible eclogite formation based on our petrological modeling. Same legend as other figures. White areas are outside the model.*

Offshore seismic and gravity studies argue that the Juan Fernandez ridge crust is moderately overthickened (by 1 km), with a thickness of only 8 km (Kopp et al., 2004). Its exact thickness at depth and its subduction path are still not fully known, neither is its precise involvement in the slab flattening process. Analogue subduction models showed that the narrowness and orientation of the ridge with respect to the trench cannot induce flat subduction (Espurt et al., 2008; Martinod et al., 2005; 2010). On the other hand, the location, width and orientation of the flat slab's seismicity coincide very well with the ridge's characteristics offshore. Also, the flat slab's focal mechanisms indicate sideways slabpull (normal to the ridge azimuth, i.e. 168°, Fig. 3.12) (Anderson et al., 2007), supporting the concept of buoyancy along this narrow band of seismicity. Using seismic receiver functions, Gans et al. (2011) found that the oceanic crust of the flat slab segment may be thicker than observed offshore, with an average of ~ 15 km (shown by the pink dotted lines in Fig. 3.10, representing their oceanic Moho), representing a much broader area than the 100 km width offshore (Kopp et al., 2004). With a thickness exceeding that of our model cell resolution of 10 km, a partially- or non-eclogitized oceanic crust should be perceived as a slow velocity anomaly, since basalt/gabbros are lighter than the surrounding mantle, and an eclogitized crust, whether 8 or 15 km in thickness, would not provide the buoyancy force necessary to sustain flat subduction for such long time periods. We now test the hypothesis that the oceanic crust is not eclogitized.

Normal average basaltic crust has Vp values between 7.2 and 7.6 km/s (Hacker et al., 2003) at the P-T conditions of flat subduction (400-800°C at 2-4 GPa, van Hunen et al., 2002). However, our seismic velocities are substantially higher in the section of the flat slab (Vp > 8.5-8.6 km/s and Vs > 4.8 km/s). Any slab hydration (causing reduced rock densities), below 50 km, is contradicted by our high seismic velocities and moderately low Vp/Vs ratios (1.75-1.77). The possible eclogite distribution is shown in Fig. 3.10 and Fig. 3.14. Eclogitic rocks with various degrees of hydration occur at (in brackets are the rock names, see Table B.4 of Appendix B): (i) 50-60 km depth: 30% H2O (K1), (ii) 60-80 km depth: 10% H2O (K3), and (iii) > 80 km depth: 1% H2O (K6, K7). Based on these results, the eclogites below 80 km depth have very high rock densities of 3.6 g/cm$^3$, which is ~ 0.2-0.3 g/cm$^3$ greater than dry mantle rocks (3.3-3.4 g/cm$^3$). This observation challenges the buoyancy of the slab and its long horizontal distance, posing a paradox of how can flat subduction occur when slab density is so high? Furthermore, in theory, a fully transformed eclogite crust, as our seismic velocities suggest below 80 km depth, should no longer be seismically active, despite our seismic distribution.

These discrepancies between our observations and the apparent slab buoyancy can be explained with three scenarios: (1) our model over-estimates the seismic velocities at depth: they are substantially faster ($\Delta$Vp ~ 0.5 km/s and $\Delta$Vs ~ 0.4 km/s) than the global IASEP-91 model along the flat slab depths (Fig. 2.1.4). However, this does not seem to be the case, as our checkerboard tests indicate that the flat slab segment is well resolved; (2) we do not resolve for the oceanic crust because it is thinner than our model resolution of 10 km. In this case, the oceanic crust along the flat slab portion is about the same thickness as offshore, and to maintain the slab buoyancy, it should be non-eclogitized. However, we do not have the means to investigate this option; (3) the oceanic crust along the flat slab portion is eclogitized, no matter its thickness, and it is 'stuck' to the base of the overriding lithosphere, forming a new subduction interface below it, locating the flat slab's seismogenic zone inside the oceanic mantle. This was proposed by Gans et al. (2011) to explain a seismic reflector ~ 20 km shallower than the seismogenic zone (Fig. 3.10 and Fig. 3.14).

The evidence that the continental mantle above the subducting Juan Fernandez ridge is likely hydrated (details in Section 6.4.2) signifies that the slab may be releasing fluids and storing them directly above it. The transformation of basalt/gabbro to eclogite is a fluid-releasing reaction. This suggests that the Juan Fernandez ridge crust is eclogitizing before re-subducting into the deeper mantle. The higher mantle temperatures in its vicinity could be triggering for dehydration reactions to

become effective again. If this is correct, we question whether eclogitization of the flat slab's eastern tip provokes its re-subduction, or, re-subduction triggers slab eclogitization due to slab steeping?

The upper portion of the flat slab where this is taking place is characterized by decreased seismic velocities but equally low Vp/Vs ratios (1.75-1.76) as the rest of the flat slab. Alvarado et al. (2007) noted that this region is seismically quieter than the rest of the flat slab (e.g. Fig. 3.14) and explained it by local fluid effects inhibiting earthquake nucleation. Relatively recent volcanism occurred further east (~ 65°W) beneath Sierra Cordoba at the San Luis volcanic fields about 2 Ma (Kay and Abbruzzi, 1996), providing incontestable evidence that fluids are retained during flat subduction and released further east as the temperature conditions become more appropriate deeper in the mantle.

Therefore, although our absolute seismic velocities suggest that the oceanic crust begins transforming to eclogite at 50 km depth and to very dense eclogites at 80 km, this scenario appears impossible to explain the observed flat slab configuration, and also contradicts the mantle hydration signatures above the eastern extremity of the flat slab. Therefore, we propose that the oceanic crust along the flat is smaller than our model resolution of 10 km and that it should be non-eclogitized to maintain slab buoyancy.

In the normal subduction zone (34°S), the higher geotherm in the volcanic arc domain (Grevemeyer et al., 2005) and the active volcanism are associated to slab dehydration and mantle partial melting processes (due to the presence of the asthenospheric wedge). Similarly to the flat slab region, the slab seismic velocities below 50 km depth concur with eclogites of varying hydration levels (Fig. 3.10) (in brackets: rock types; refer to Table B.4): (i) 50-60 km depth: 45% H2O (K1, K4), (ii) 60-80 km depth: 20% H2O (K1, K2, K3), (iii) 90-100 km depth: 6% H2O (K3, K6), and (iv) > 100 km depth: 2% H2O (K5, K6). The average water content in these eclogites indicates higher crustal hydration in the normal slab than the flat slab, opposing the fact that the normal oceanic lithosphere is generally less hydrated, based on our seismic values.

## 3.7 Conclusions

In conclusion, our results show that there are significant seismic differences in the continental lithosphere of central Chile and western Argentina between the flat and normal subduction zones (represented schematically in Fig. 3.1).

Above the flat slab, between 31°S and 32.5°S, the forearc crust shows abnormal velocity properties (very low Vp/Vs ratios) which we do not manage to explain. However, they appear consistent with the flat slab geometry at depth, and/or, the Punitaqui aftershock region exhibiting similar seismic trends, and/or, related to crustal deformation. It is possible that a major shear zone cross-cuts the centre of the forearc crust, connecting to the plate interface and channelizing fluids into the Andean crust, reflected by locally higher Vp/Vs ratios and seismic velocity reductions separating the shallow and deep low Vp/Vs anomalies of the forearc.

The entire Andean arc crust is characterized by slower seismic velocities with relatively high Vp/Vs ratios. Zones of fold-and-thrust belts are significantly reduced in seismic velocities, which we interpret structure damage and fluid content are the causes. It crustal root is described as non-eclogitized, and we explain it either by a felsic composition reflecting the Chilenia terrane, and/or, a well hydrated lower crust, and/or, the remains of a previously detached eclogitized crustal portion.

We image the Cuyania terrane in the backarc region as a fast seismic velocity anomaly with an eclogitized lower crust below 50 km, supporting many previous interpretations.

The continental mantle above the flat slab portion is expressed by faster seismic velocities, probably attributed to the lower geotherm and to drier conditions. This explains well the more intense deformation style at the surface, and the cessation of arc volcanism at the surface.

Above both the normal and flat slabs, the mantle wedge appears to be hydrated between 50 and 60 km, with similar levels of hydration, which suggests that the mantle wedge above the normal slab, at 33.5°-34°S, is unexpectedly dry compared to expectations, and that it reflects transitional conditions between the flat subduction to the north and the more 'normal' subduction zone further south.

We show evidence that the subducting Juan Fernandez ridge is locally dehydrating at the eastern edge of the flat slab (68.5°W/ 31.5°S), before it re-subducts, and fluids are stored in the continental mantle directly above it. We interpret the flat slab to become eclogitized near its eastern tip, where ambient temperatures are higher, triggering the eclogitization processes.

Throughout the region, the oceanic crust of the Nazca slab can be described with eclogite formation from 50 km depth, in contradiction with the apparent flat slab's buoyancy. An alternative explanation is that our model does not resolve for the oceanic crust because it is thinner than 10 km (the minimum depth resolution of our model), and to maintain buoyancy, it should be non-eclogitized.

## 3.8 Acknowledgements

Local data were obtained thanks to projects FONDECYT 1020972-1050758 and IRD-GéoAzur. Marianne Marot and Guust Nolet are supported by the GloablSeis project (ERC 226837). Giorgio Ranalli's participation in this project is supported by a grant by NSERC (Natural Sciences and Engineering Research Council of Canada). We are very grateful to all the members who have actively discussed and debated our subject with us, bringing us new insights and challenges to our topic. These include, Andres Tassara, Eric Ferre, Lara Wagner, Pablo Molina, Francisco Gutierrez, Samuel Angiboust, Scott Henderson, Stephan Rondenay, Manuele Faccenda, Flore Barat and Benoît Derode. We also would like to thank Perrine Deshayes who shared with us her seismic attenuation tomography results for this region, which she performed during her PhD thesis project.

# Conclusions

The region of central Chile and western Argentina (29°-33°S) is underplated by the well defined flat slab segment of the Nazca Plate for ~ 250-300 km eastward, and this has been ongoing for a period of ~15-18 Ma (Kay and Abbruzzi, 1996). At this latitude, the Juan Fernandez seamount ridge subducts beneath the continental lithosphere and its subduction track appears well correlated with the flat slab geometry, characterized by a dense cloud of micro-seismicity, about 30 km thick at 50 km depth, and 20 km thick along the flat slab portion. The overriding plate is also impregnated by a high seismic activity that impacts its crust up to about 800 km east (Alvarado et al., 2009) from the subduction front, above where the slab re-subducts into the mantle. Crustal uplift and shortening is particularly intense along this segment. To the south, over a short distance of only ~ 100 km (between 32.5°S and 33.5°S), the Nazca slab suddenly changes along-strike geometry, from flat to dipping 30°, resulting in drastic differences between the 'normal' and flat subduction regions, including the most obvious return of the arc volcanism at the surface.

Numerous studies were carried out in this region to better understand the dynamics of flat subduction, indicating that flat subduction depends on the kinematics of the interacting plates, their compositions and the pressure and temperature conditions of the lithosphere and asthenosphere (e.g. van Hunen et al., 2002; 2004; Espurt et al., 2008; Gerbault et al., 2009; Faccenda et al., 2012). However, according to me, none are completely satisfactory, and we focused our approach on the use of local seismological data to better constrain the geodynamical conditions at over the large-scale.

This work aims at imaging the seismic variations in the lithospheric physical properties between the flat and normal subduction zones, in order to better understand the regional seismic distribution and the link between the surface and deep deformations. My research was segmented into three steps: (1) finding the best model that describes the seismic velocity field for the normal and flat subduction zones, using seismic tomography; (2) approximating the pressure and temperature fields, using a 2-D thermo-mechanical approach for two cross-sections representative of the flat and normal subduction zones; and (3) estimating the rock and mineral compositions of the flat and normal subduction zones, based on step 1 and 2, using a list of published common rock compositions for subduction zones.

In step 1, we modeled the velocity field by inverting P- and S-wave travel-time residuals, based on ray theory. This was performed using the *TLR3* algorithm (Latorre et al., 2004; Monteillet et al., 2005). Our model volume is 960 x 880 x 220 $km^3$, and our seismic database is a collection of four temporary seismic campaigns (OVA99, CHARGE, CHARMSE and CHASE), which were consistently relocated in our 1-D velocity model used as our background model for our inversion. Strict quality selection criteria were imposed on our dataset prior to inversion, resulting in a total of 3603 earthquakes used, with more than 52 000 and 51 500 travel-times for P- and S-waves, respectively. The quality of our chosen final model was assessed using the checkerboard and spike tests. Our model has a node spacing of 40 x 40 x 10 km, and resolves well a large part of the subduction zone except a little less constraint on the backarc. Our tomography results are the first most complete regional 3-D images of central Chile compared to previous existing tomography studies: (1) we used a larger seismic dataset that represents different time intervals; (2) our seismic station distribution is more consequent, enabling us to resolve for the continental lithosphere over larger distances and the upper 30 km of the subducting lithosphere; and (3) we used a reference 1-D model that was calculated specifically for this region, providing us with a better initial approximation of the region. In addition, we assessed and discussed our results with supporting unpublished seismic attenuation models for this region (Deshayes 2008), providing stronger emphasis to our interpretations of fluid distribution, for instance. Here, we show significant differences in the seismic wave velocity

field of the converging lithospheres above the flat and normal subducting slabs. As expected, due to the colder temperatures imposed by the slab geometry, the flat slab region is characterized by faster seismic velocities in the continental's crust and mantle, relative to the normal subducting region (34°S). The continental crust above the flat slab has very heterogeneous seismic properties which correlate with important deformation structures and geological terranes at the surface. We show seismic evidence that the slab dehydrates along the subducting ridge axis prior to re-subducting, at ~ 100 km depth, and hydrating the above continental mantle. The forearc crust in the flat slab region is described with unusual seismic properties, which seem to be correlated with the extent of the flat slab at depth, and/or, the aftershock region of the 1997 Mw 7.1 Punitaqui earthquake which exhibits similar abnormal seismic properties, several years after the mainshock.

In step 2, the numerical code *Parovoz* (Poliakov and Podladchikov, 1992) was used to compute the predicted pressure and temperature conditions, based on the mechanical stress, *a priori* information and first-order assumptions (similar to Gerbault et al., 2009). A double-planed pattern of compression and tension is found for the normal and flat subductions zones, parallel to the angle of subduction, and reflecting bending/unbending slab effects. Within the normal slab, this pattern stops at 120 km depth, consistent with this maximum depth of the slab seismicity slab, and with propositions by others of slab break-off throughout the southern subduction zone (Li et al., 2008; Pesicek et al., 2012; M. Obayashi personal communication). Around the same depth (113 km), along the normal slab section, we relocated and analyzed a cluster of events triggered by a moderate-size mainshock (7 January 2003, Mw 5.7), which we interpreted in as a reactivated inherited outer rise fault plane (Marot et al., 2012). Along the flat slab, we describe the Double Seismic Zone (DSZ) fully for the first time (Marot et al., 2013), as a secondary band of seismicity located within the oceanic mantle, starting at 50 km depth and merging with the upper seismic plane at 110-120 km depth, correlated with the depth at which the slab becomes horizontal. Our analyzed focal mechanisms and calculated stress tensors for the DSZ show that around 65 km depth the slab's state of stress switches from horizontal compression to horizontal extension, a stress pattern which does not reflect bending/unbending stresses predicted by our thermo-mechanical models.

In step 3, we used our seismic tomography and thermo-mechanical models generated in steps 1 and 2 to analyze the compositions of the flat and normal subduction zones. To do so, we compared our absolute seismic velocities with those predicted for 65 rocks (mafic and ultramafic types), at appropriate P-T conditions using the Hacker and Abers (2004) database, for two 2-D cross-section representing the flat and normal subduction zones. We were able to analyze the distributions and volume percentages of minerals in our rock solutions for each cell of our model. The continental mantle was our principal focus, for which we show that the mantle wedges above the normal and flat slabs are similarly moderately hydrated (30%) along a limited depth range (50-60 km). This observation provides evidence that the slab is dehydrating and we qualify the 'normal' subduction zone at 34°S as an intermediate, or transition, region separating the flat and the more 'normal' subduction zones. Our seismic velocities for the thick Andean lower crust describe a lack of eclogite rocks, possibly represent a felsic composition (the Chilenia terrane), a hydrous state, or, a previously delaminated eclogite lower crust. We confirm previous studies (e.g. Gilbert et al., 2006; Alvarado et al., 2007; Corona, 2007) that the Cuyania terrane in the backarc region probably contains an eclogitized lower crust below 50 km depth. We also suspect that major crustal faults or shear zones reported at the surface extend deep towards the plate interface, cross-cutting the forearc crust and the mantle wedge, to channelize slab-derived fluids into the continental crust. The oceanic lithosphere in the flat slab region appears to be deeply hydrated down to 50-70 km depth, based on our high Vp/Vs ratios (1.80-1.82). The deeper part of the plate interface, around 25-30 km depth, exhibits very high Vp/Vs ratios and low seismic velocities, which no rock matches, interpreted as the presence of high levels of fluids. Below 70 km depth, the oceanic lithosphere along the flat slab region experiences

seismic velocities that correspond to either dry peridotites or dense eclogites (these are not seismically distinguishable). Our high Vp and Vs values for the flat and normal slabs above 70 km depth, suggest dry and dense rocks, which pose several paradoxes with the flat slab's buoyancy and our relative seismic trend for mantle hydration above the edge of the flat slab.

Linking seismic tomography data with a petrological perspective is a technique which has not yet been fully exploited in seismic studies, mainly because there are little direct observations of the true rock compositions that occur in subduction zones, and there are still many limitations to laboratory experiments and extrapolation of deep Earth conditions. This study shows that it is possible to extract useful information on the comparative compositions of the normal and flat subduction zones. It demonstrates the importance of performing interdisciplinary relationships, to better understand the observations.

# Perspectives

This region of central Chile and western Argentina has attracted many national and international scientific interests that have very well described the surface deformations associated to flat subduction, relative to other flat slab regions in the world. However, as this study shows, less is understood about the deep deformations and their links with the flat subduction or the surface deformations. In this study, we have used seismic tomography to suggest areas of the subduction zone where fluids might be present. However, this technique is not the most sensitive to detect the presence of fluids, which are an important proxy to understand the central Chilean flat subduction. Therefore, it would be very useful to map the region with magnetotelluric data, from the trench to the backarc, reaching down to the subducting slab, and making a comparison between the normal and flat subduction zones.

Regarding the seismic imaging of this region, one should complete our study's lack of data by adding (i) local temporary earthquakes, recorded during our database's temporal gaps, (ii) local permanent earthquakes, including those from the permanent Chilean and Argentinean networks, for a more continuous vision of the longer-term seismic velocity field, illuminating the subduction zone all the way into the backarc region, and (iii) teleseismic earthquakes, to better image the deeper parts of the subducting Nazca plate. For instance, a large number of seismic networks were deployed over the region after the 2010 Maule megathrust event (Mw 8.8) (34°-38°S), recording large quantities of data which could be used to ameliorate our comparison of the flat subduction with the 'normal' subduction conditions.

One might also wish to compare our ray-tracing seismic tomography results with other techniques, such as finite-frequency and double-difference methods, using local earthquake data. The analysis of the data at different frequency bands should bring further information on the seismic velocity variations and refine the shapes of the structures.

The double-difference seismic tomography tool could also be used to ameliorate our study of the Double Seismic Zone, in order to correlate the seismic planes with velocity variations, already performed for the northern Chilean DSZ (Dorbath et al., 2008).

The 1997 Punitaqui earthquake engendered our surprised interest due to its strong aftershock seismicity many years following the mainshock and by its unusual seismic properties revealed by this study. As a result, it would be particularly interesting to further investigate its possible seismic anisotropic character, using shear wave splitting techniques. Correlating areas of unusual earthquake activity with unusual seismic properties could be useful for earthquake forecasting and risk assessment, in these regions.

# **Conclusions** (in French)

La région du Chili central et de l'Argentine occidentale (29°-33°S) se caractérise par un sous-plaquage de la plaque Nazca en subduction horizontale (*flat slab*) sur une distance d'environ 250-300 km vers l'intérieur des terres, et cela depuis environ 15-18 Ma (Kay et Abbruzzi, 1996). À ces latitudes, la ride sous-marine de Juan Fernandez subducte sous la lithosphère continentale et sa trajectoire de subduction semble être bien corrélée avec la géométrie du *flat slab*, définie par la distribution des séismes. Ce *flat slab* est défini par un nuage dense de micro-sismicité, réparti sur environ 20 km d'épaisseur. La plaque chevauchante est également sujette à une forte activité sismique qui affecte sa croûte sur une distance de plus de 800 km vers l'est par rapport au front de subduction (Alvarado et al., 2009). Le soulèvement et le raccourcissement de la croûte sont particulièrement intenses le long de ce segment (*flat slab*), et liée à la géométrie de la plaque en profondeur. Vers le sud (entre 32.5°S et 33.5°S), le *slab* change brusquement de géométrie, allant d'un pendage horizontal à un pendage de 30° sur une courte distance d'environ 100 km, entraînant des changements radicaux, y compris le retour du volcanisme d'arc.

De nombreuses études ont été précédemment réalisés dans ce domaine d'application afin de mieux comprendre la dynamique d'une subduction plate, en relation avec la cinématique des plaques, la nature lithosphérique des plaques et des conditions pression-température (P-T) de la lithosphère et de l'asthénosphère (ex. van Hünen et al., 2002; 2004; Espurt et al., 2008; Gerbault et al., 2009; Faccenda et al., 2012). Toutefois, aucun argument ne satisfait entièrement les données, et nous avons donc concentré notre approche sur des données sismologiques locales nous permettant de mieux contraindre les conditions géodynamiques à grande échelle.

L'objectif de ce projet de thèse est d''imager les différences qui se produisent en profondeur entre la zone de subduction plate et normale, en intégrant les plaques chevauchante et en subduction, afin de mieux comprendre l'origine des déformations en surface, et les relations entre la distribution de la sismicité et les variations des propriétés physiques de la lithosphère. Mes recherches abordent trois approches: (1) une approche de tomographie sismique pour les premières arrivées d'ondes P et S pour trouver un modèle pertinent décrivant le champ de vitesse sismique de la région au-dessus du *slab* normal et plat, (2) puis une approche thermomécanique 2-D, modélisant deux sections représentant les zones de subduction normale et plate, pour décrire les champs approximatifs de P-T, et enfin (3) une approche pétrologique, afin de modéliser la composition des roches aux conditions de P-T estimées précédemment, pour les deux coupes en 2-D représentatives de la subduction normale et plate.

Dans l'approche tomographique, nous avons modélisé le champ de vitesse en inversant les résidus de temps de trajet des ondes P et S, basés sur la théorie des rais. Pour cela, nous avons utilisé l'algorithme *TLR3* (Latorre et al., 2004; Monteillet et al., 2005). Le volume de notre modèle est de 960 x 880 x 220 $km^3$. Nous avons construit une base de données sismique alliant quatre campagnes sismiques temporaires (OVA99, CHARGE, CHARSME et CHASE), dont les séismes ont été systématiquement relocalisés dans notre modèle de vitesse 1-D. Ce modèle a servit de modèle de base pour notre inversion. Des critères sélectifs de qualité stricts ont été imposés à notre ensemble de données avant l'inversion pour 3603 séismes, avec plus de 52 000 et 51 500 temps de trajets pour les ondes P et S, respectivement. La qualité de notre modèle final choisi a été évaluée par des tests de *checkerboard* et de *spike*. Ce modèle est bien résolu en grande partie de son volume, pour un espacement de nœuds de 40 x 40 x 10 km, avec quelques contraintes plus faibles dans la région arrière-arc.

Nos résultats tomographiques montrent des différences significatives dans le domaine des vitesses des ondes sismiques dans la lithosphère chevauchante, dans le cas d'une subduction de plaque

à faible pendage et à fort pendage. Nos résultats de tomographie sont les premières images les plus complètes par rapport aux précédentes études de tomographie existantes pour la région du Chili centrale en 3-D: (1) Nous avons utilisé un plus grand ensemble de données sismiques qui représente aussi différents intervalles de temps, (2) la distribution de nos stations sismiques est donc plus conséquente, ce qui nous permet de résoudre la lithosphère chevauchante sur une plus grande distance et aussi d'imager la partie supérieure (de 30 km) de la lithosphère en subduction, et (3) nous avons utilisé un modèle de référence 1-D qui a été calculé spécifiquement pour cette région nous fournissant une meilleure première approximation. De plus, nous avons évalué et discuté nos résultats à l'appui de résultats jamais publiés d'atténuation sismiques (Deshayes 2008) pour cette région, fournissant davantage de supports à nos interprétations de la distribution des fluides, par exemple. La croûte continentale à l'aplomb du *flat slab* possède des propriétés sismiques très hétérogènes en étroite corrélation avec des structures de déformation importantes et des terrains géologiques à la surface. En accord avec les prévisions, la région où se localise le *flat slab*, les vitesses sismiques sont plus rapides (dans la croûte et le manteau) par rapport à la région soumise à une subduction normale, en raison des températures plus froides imposées par la géométrie du *flat slab.* La croûte d'avant-arc située au-dessus du *flat slab* est décrite par des propriétés sismiques inhabituelles (rapport Vp/Vs très faibles et augmentation de Vs) corrélée à la distribution géographique du *flat slab* en profondeur, et/ou, aux effets de répliques du séisme de Punitaqui (Mw 7.1) de 1997, qui a eu lieu plusieurs années (2 à 9) avant l'enregistrement de notre jeu de données sismiques. Nous montrons la preuve sismique que le *flat slab* se déshydrate à des profondeurs proche de 100 km le long de l'axe de la ride en subduction, avant de re-subducter.

Dans l'approche thermomécanique, le code numérique *Parovoz* (Poliakov et Podladchikov, 1992) a été utilisé pour estimer le champ de P-T, sur la base d'informations a priori et d'hypothèses de premier ordre (similaire à Gerbault et al., 2009). Ces modèles montrent une structure en double-plan de stresse compressif et de tension, parallèle à l'angle de subduction, pour les zones de subduction normale et plate, et reflétant le mécanisme de flexion/inflexion du s*lab.* Dans le modèle de *slab* normal, cette tendance s'arrête à ~120 km de profondeur, compatible avec la profondeur maximale de la sismicité du *slab*, et avec des propositions par d'autres d'un *slab break-off* à cette latitude et tout au long de la zone de subduction sud (Li et al., 2008; Pesicek et al., 2012; M. Obayashi communication personnelle). Autour de cette même profondeur (113 km), notre base de données sismiques nous a permis d'observer et interpréter un plan de faille réactivé, cohérent avec les structures de failles observées dans le *outer rise*, et déclenché par un choc principal de taille modérée (Mw 5.7) en 2003, ainsi que de ses répliques. Dans la région de subduction plate, nous corrélons ce modèle de stress en double-plan avec la profondeur et la géométrie de la Double Zone Sismique observée (DSZ) (Pardo et al., 2002; Marot et al., 2013). Le DSZ décrit un deuxième plan de sismicité située à l'intérieur du manteau océanique de la plaque Nazca, débutant à partir de 50 km de profondeur et allant jusqu'à la rencontre avec le plan de sismicité supérieur à 110-120 km de profondeur, en corrélation avec la profondeur à laquelle le *slab* est horizontale. Nos mécanismes aux foyers analysés et nos tenseurs de contraintes calculés pour le DSZ montrent que près de 65 km de profondeur, l'état de stress du *slab* alterne d'une compression horizontale à une extension horizontale, ce qui contredit le modèle de stress en double-plan modélisé. Cette gamme de profondeur coïncide avec l'hypocentre du séisme de Punitaqui de 1997 (Mw 7.1) à 31°S et 71°W, qui connaît une activité sismique de répliques anormalement élevée par rapport au reste du *slab*. Nous montrons que par déplacement de tous les séismes du *slab* d'environ 10-15 km plus profonds, nous sommes en mesure de corréler les couches en tension avec le plan sismique inférieure de la DSZ ainsi que la sismicité le long du *flat slab*.

Aussi à l'étape 3, nous avons utilisé notre tomographie sismique préalablement déterminé et les modèles thermo-mécaniques pour analyser la composition lithosphérique dans les régions de subduction plate et normale. Pour ce faire, nous avons comparé nos valeurs de vitesse absolue avec

celles prédites pour 65 types de roches mafiques et ultramafiques, pour des conditions P-T appropriées, en utilisant la base de données de Hacker et Abers (2004). Cette base de données a permis l'analyse de la croûte inférieure et du manteau continental et océanique.

Nous avons pu analyser les distributions et les pourcentages de volume des minéraux dans nos solutions de roche trouvées pour chaque cellule, pour le manteau continental, qui est notre principal objectif. Ici, nous montrons que le coin mantellique continental est modérément hydraté (30%) le long d'une plage de faible profondeur (50-60 km) au-dessus du *slab* normal et plat, un signe que le *slab* se déshydrate, mais aussi que la zone de subduction normale, à 34°S, reflèterai d'avantage une zone intermédiaire séparant la subduction plate, vers le nord, des conditions plus «normales» plus au sud. Nous montrons que la croûte inférieure continentale de l'arc andin est non-eclogitized et pourrait représenter une composition felsique (du terrain accrété Chilenia), tandis que le terrain accrété Cuyania, dans la région backarc, à l'est, est plus mafiques et pourrait contenir une croûte inférieur éclogitizée à partir de 50 km de profondeur. Nous pensons également que des principales failles, ou zones de cisaillement, de la croûte continentale observée à la surface s'étendent en profondeur vers l'interface de la plaque en subduction et servent à canaliser les fluides dérivés du *slab* vers la croûte continentale. La lithosphère océanique de la région du *flat slab* semble être hydratée jusqu'à 50-70 km de profondeur, en particulier le long de la partie profonde de l'interface de plaque (~25-30 km de profondeur), basée sur nos valeurs élevées de Vp/Vs (de 1.80 à 1.82). À des profondeurs plus profondes (> 70 km), et selon notre analyse pétrologique, le *slab* pourrait être composé de péridotites sèches soit d'eclogites denses (elles ne sont pas distinguables sismiquement). Toutefois, ceci poserai plusieurs paradoxes avec le dynamisme de la subduction plate et de l'hydratation du manteau continental reflétée par nos signatures sismiques relatives. Pour cela, nous proposons que la croute océanique le long du *flat slab* à une épaisseur inferieure à la résolution verticale du notre model (10 km) et que celle-ci doit être non-éclogitisée ou partiellement éclogitisée pour maintenir la flottaison du *flat slab*. Quant à la subduction normale, les vitesses sismiques du *slab* pourraient être expliquées avec une croûte éclogitisée à des profondeurs de plus de 50 km.

L'approche d'interpréter des données de tomographie sismique en alliant des données pétrologiques est une technique qui n'est pas encore pleinement exploitée, freinée essentiellement par notre incapacité actuelle à observer les roches à de telles profondeurs, ainsi que de nombreuses autres limitations. Cependant, ma thèse montre qu'il est possible d'extraire néanmoins des informations utiles sur la composition pétrologique du manteau lithospheric, à partir de données indirectes. Ma thèse souligne l'importance d'une approche pluridisciplinaire afin de mieux aborder et comprendre la dynamique des zones de subduction.

# **Perspectives** (in French)

La région du Chili central et ouest d'Argentine attire de nombreux intérêts scientifiques nationaux et internationaux, qui ont suscité à beaucoup de découvertes par rapport à d'autres régions de subductions plate (e.g. le Pérou et le centre du Mexique). Cette étude de thèse suggère la présence et une distribution de fluides dans le manteau continentale qui s'avère importante pour la compréhension du dynamisme de la subduction plate. Par contre, la méthode de tomographie sismique n'est pas la mieux adaptée pour confirmer la présence de fluides. Une enquête magnétotellurique détaillées de la fosse à l'arrière arc, jusqu'à la surface du *slab*, pourrait apporter une pertinence significative à nos interprétations sur la distribution des fluides, la présence de failles (ou de zone de cisaillements) profondes hydratées, et de la composition du milieu.

En ce qui concerne cette étude, je propose plusieurs perspectives futures qui peuvent apporter à cette étude encore plus de robustesse. Par exemple, je propose d'améliorer notre image de la zone de subduction en complétant notre base de données sismique actuelle avec des informations supplémentaires: (1) des données locales enregistrées entre les gammes de temps des campagnes sismiques temporaires utilisées pour cette étude, afin d'obtenir une image plus continue des tendances à long terme de vitesse sismique. Cela pourrait être fait en incluant d'autres études à court terme mises en place au cours de nos écarts de temps d'enregistrement, et en ajoutant des séismes enregistrés non seulement par des réseaux permanents chiliens, mais aussi argentiniens, ce qui a rarement été fait auparavant. Cela aiderait à obtenir un meilleur éclairage de la région arrière arc et du *slab* en re-subduction. Nous pourrions obtenir une image de la zone de subduction sud (34°-38°S) qui représente des conditions plus «normales» que notre région à 34°S, en incluant les nombreux séismes enregistres suite a mégaséisme de Maule en 2010 (Mw 8.8); (2) des événements télésismiques, afin de mieux imager les parties plus profondes de la plaque en subduction.

Un autre point de vue qui serait bénéfique pour notre étude consisterait à effectuer la tomographie à fréquence-finies pour plusieurs bandes de fréquences, afin de mieux faire ressortir les formes et les structures les plus fines de la région, ainsi que de comparer les différences qui surgissent entre cette méthode et celle du tracé des rayons.

Outre l'imagerie sur l'ensemble de la région et d'affiner notre modèle avec une base de données élargie, nous proposons également d'accorder plus d'attention à la DSZ et à affiner notre analyse, par l'application du programme de relocalisation *HypoDD* des séismes avec la méthode de double-différence (Waldhauser et Ellsworth 2000) pour les événements définissant la DSZ, afin d'affiner et de clarifier la séparation entre les deux plans sismiques. De cette façon, nous serons en mesure de mieux observer l'interaction en profondeur de ces plans, car nous n'avons pas, dans notre premier essai, réussit à distinguer si les plans sismiques se confondent à la profondeur du *flat slab*, ou continuent à travers le segment de *flat slab* à une distance inter-plan beaucoup plus petit. Nous pourrions également effectuer simultanément une tomographie sismique par la méthode de double-différence de la DSZ, afin de mieux corréler la sismicité avec les variations de vitesse des ondes sismiques, comme cela a été déjà effectué, par exemple, pour le DSZ du nord du Chili (Dorbath et al., 2008).

Le séisme de 1997 de Punitaqui a surprit notre intérêt en raison de sa forte activité sismiques 2 à 9 ans après le choc principal, et surtout parce que nous sommes en mesure de corréler cette région de répliques avec des vitesses sismiques anormales, que nous montrons pour la première fois dans cette étude. En conséquence, il serait particulièrement intéressant d'étudier plus extensivement son possible caractère d'anisotropie sismique. La corrélation de zones à propriétés sismiques inhabituelles avec une forte activité sismique, pourrait fournir de plus grandes connaissances pour la prévision de séismes et l'évaluation des risques sismiques possibles dans ces régions.

# References


Abbruzzi, J. M., Kay, S. M., & Bickford, M. E. (1993). Implications for the nature of the Precordilleran basement from the geochemistry and age of Precambrian xenoliths in Miocene volcanic rocks, San Juan province. Actas, 3, 331-339.

Afonso, J. C., Ranalli, G., & Fernandez, M. (2007). Density structure and buoyancy of the oceanic lithosphere revisited. Geophysical Research Letters, 34(10). doi:10.1029/2007GL029515

Allmendinger, R. W., & González, G. (2010). Invited review paper: Neogene to Quaternary tectonics of the coastal Cordillera, northern Chile. *Tectonophysics*, *495*(1), 93-110. doi:10.1016/j.tecto.2009.04.019

Allmendinger, R. W., Jordan, T. E., Kay, S. M., & Isacks, B. L. (1997). The evolution of the Altiplano-Puna plateau of the Central Andes. *Annual Review of Earth and Planetary Sciences*, *25*(1), 139-174.

Alvarado, P., Beck, S., Zandt, G., Araujo, M., & Triep, E. (2005). Crustal deformation in the south-central Andes backarc terranes as viewed from regional broad-band seismic waveform modeling. *Geophysical Journal International*, *163*(2), 580-598. doi:10.1111/j.1365-246X.2005.02759.x.

Alvarado, P., Beck, S., & Zandt, G. (2007). Crustal structure of the south-central Andes Cordillera and backarc region from regional waveform modeling. *Geophysical Journal International*, *170*(2), 858-875. doi :10.1111/j.1365-246X.2007.03452.x

Alvarado, P., Pardo, M., Gilbert, H., Miranda, S., Anderson, M., Saez, M., & Beck, S. (2009). Flat-slab subduction and crustal models for the seismically active Sierras Pampeanas region of Argentina. *MWR204: Backbone of the Americas: Shallow subduction, plateau uplift, and ridge and terrane collision: Boulder, Colorado, Geological Society of America*, 261-278. James, D. E., & Snoke, J. A. (1994). Structure and tectonics in the region of flat subduction beneath central Peru: Crust and uppermost mantle. *Journal of Geophysical Research: Solid Earth (1978–2012)*, *99*(B4), 6899-6912. doi:10.1130/2009.1204(12)

Alvarado, P., & Ramos, V. A. (2011). Earthquake deformation in the northwestern Sierras Pampeanas of Argentina based on seismic waveform modeling. *Journal of Geodynamics*, *51*(4), 205-218.

Anderson, M. L., Zandt, G., Triep, E., Fouch, M., & Beck, S. (2004). Anisotropy and mantle flow in the Chile-Argentina subduction zone from shear wave splitting analysis. *Geophysical Research Letters*, *31*(23), L23608. doi:10.1029/2004GL020906

Anderson, M., Alvarado, P., Zandt, G., & Beck, S. (2007). Geometry and brittle deformation of the subducting Nazca Plate, Central Chile and Argentina. *Geophysical Journal International*, *171*(1), 419-434. doi: 10.1111/j.1365-246X.2007.03483.x

Araujo, M., & Suarez, G., (1994). Geometry and state of stress of the subducted Nazca Plate beneath central Chile and Argentina: Evidence from teleseismic data. *Geophysical Journal International*, *116*, 283-303. doi: 10.1111/j.1365-246X.1994.tb01799.x

Armijo, R., Rauld, R., Thiele, R., Vargas, G., Campos, J., Lacassin, R., & Kausel, E. (2010). The West Andean Thrust, the San Ramón Fault, and the seismic hazard for Santiago, Chile. *Tectonics*, *29*(2). doi:10.1029/2008TC002427

Artemieva, I. M., & Meissner, R. (2012). Crustal thickness controlled by plate tectonics : A review of crust-mantle interaction processes illustrated by European examples. *Tectonophysics*, *530*, 18-49.

Astiz, L., Lay, T., & Kanamori, H., (1988**).** Large intermediate-depth earthquakes and the subduction process. *Physics of the Earth Planetary International*, *53(1-2)*, 80-166. Doi:10.1016/0031-9201(88)90138-0

Austrheim, H., Erambert, M., & Engvik, A. K. (1997). Processing of crust in the root of the Caledonian continental collision zone: the role of eclogitization. *Tectonophysics*, *273*(1), 129-153.

Babeyko, A.Y., & Sobolev, S. V. (2008). High-resolution numerical modeling of stress distribution in visco-elasto-plastic subducting slabs. *Lithos*, *103*, 205-216. Doi.org/10.1016/j.lithos.2007.09.015

Barazangi, M., & Isacks, B. L. (1976). Spatial distribution of earthquakes and subduction of the Nazca plate beneath South America. *Geology*, *4*(11), 686-692. doi: 10.1130/0091-7613(1976)

Barrientos, S., Vera, E., Alvarado, P., & Monfret, T. (2004). Crustal seismicity in central Chile. *Journal of South American Earth Sciences*, *16*(8), 759-768. doi:10.1016/j.jsames.2003.12.001

Beck, S., Barrientos, S., Kausel, E., & Reyes, M. (1998). Source characteristics of historic earthquakes along the central Chile subduction Askew et Alzone. *Journal of South American Earth Sciences*, *11*(2), 115-129.

Beck, S.L., Gilbert, H., Wagner, L.S., Alvarado, P., Anderson, M., Zandt, G., Araujo, M., & Triep, E., (2005). The lithospheric structure of the Sierras Pampeanas region of Argentina. *Geological Society of America Abstracts with Programs*, *37*(7), 553.

Bianchi M., Heit, B., Jakovlev, A., Yuan, X. , Kay, S.M. , Sandvol, E., Alonso, R.N. , Coira, B., Brown, L., Kind, R., Comte, D., (2013). Teleseismic tomography of the southern Puna plateau in Argentina and adjacent regions. *Tectonophysics*, *586*, 65–83.

Booker, J. R., Favetto, A., & Pomposiello, M. C. (2004). Low electrical resistivity associated with plunging of the Nazca flat slab beneath Argentina. *Nature*, *429*(6990), 399-403. doi:10.1038/nature02565.

Bourgois, J., Martin, H., Lagabrielle, Y., Le Moigne, J., & Jara, J. F. (1996). Subduction erosion related to spreading-ridge subduction: Taitao peninsula (Chile margin triple junction area). *Geology*, *24*(8), 723-726. doi:10.1130/0091-7613(1996)024<0723:SERTSR>2.3.CO;2.

Bown, J. W., & White, R. S. (1994). Variation with spreading rate of oceanic crustal thickness and geochemistry. *Earth and Planetary Science Letters*, *121*(3), 435-449.

Brasse, H., & Soyer, W. (2001). A magnetotelluric study in the Southern Chilean Andes. *Geophysical Research Letters, 28*, 3757-3760

Brooks, B. A., Bevis, M., Smalley, R., Kendrick, E., Manceda, R., Lauria, E., Maturana, R., & Araujo, M. (2003). Crustal motion in the Southern Andes (26–36 S): Do the Andes behave like a microplate?. *Geochemistry, Geophysics, Geosystems*, *4*(10). doi:10.1029/2003GC000505.

Brudzinski, M. R., Thurber, C. H. , Hacker, R.,& Engdahl, E. R. (2007). Global prevalence of double Benioff zones. *Science*, *316*, 1472-1474. *doi:* 10.1126/science.1139204

Buck, C. (2005). An extension to the wide swath ocean altimeter concept. *Geosciences and Remote Sensing Symposium, 8*, 5436-5439

Burch, T. K., & Langseth, M. G., (1981). Heat-flow determination in three DSDP boreholes near the Japan trench. *Journal Geophysical Research, 86* (B10), 9411-9419. doi:10.1029/JB086iB10p09411

Burov, E., Jolivet, L., Le Pourhiet, L., & Poliakov, A. (2001). A thermomechanical model of exhumation of high pressure (HP) and ultra-high pressure (UHP) metamorphic rocks in Alpine-type collision belts. *Tectonophysics*, *342*(1-2), 113-136

Burov, E., & Yamato, P., (2008). Continental plate collision, P-T-t-z conditions and unstable vs. stable plate dynamics : insights from thermo-mechanical modeling. *Lithos*, *103*(1-2), 178-204

Burov, E. B., & Watts, A. B. (2006). The long-term strength of continental lithosphere:" jelly sandwich" or" crème brûlée"?. *GSA today*, *16*(1), 4. doi: 10.1130/1052-5173(2006)016<4:TLTSOC>2.0.CO;2)

Burov, E. B., & Diament, M. (1995). The effective elastic thickness (Te) of continental lithosphere: What does it really mean?. *Journal Geophysical Research*, *100*, 3905–3927. doi:10.1029/94JB02770.

Burov, E., & Diament, M. (1996). Isostasy, equivalent elastic thickness, and inelastic rheology of continents and oceans. *Geology*, *24*(5), 419-422. doi:10.1130/ 0091-7613(1996)024<0419:IEETAI>2.3.CO;2.

Cahill, T., & Isacks, B. L. (1992). Seismicity and shape of the subducted Nazca plate. *Journal of Geophysical Research*, *97*(B12), 17503-17. doi:10.1029/92JB00493

Calkins, J. A., Zandt, G., Gilbert, H. J., & Beck, S. L. (2006). Crustal images from San Juan, Argentina, obtained using high frequency local event receiver functions. *Geophysical Research Letters*, *33*(7). doi:10.1029/2005GL025516.

Caminos, R., Cingolani, C. A., Hervé, F., & Linares, E. (1982). Geochronology of the pre-Andean metamorphism and magmatism in the Andean Cordillera between latitudes 30 and 36 S. *Earth-Science Reviews*, *18*(3), 333-352.

Campos, J., Hatzfeld, D., Madariaga, R., López, G., Kausel, E., Zollo, A., S. Barrientos & Lyon-Caen, H. (2002). A seismological study of the 1835 seismic gap in south-central Chile. *Physics of the Earth and Planetary Interiors*, *132*(1), 177-195. doi:10.1016/S0031-9201 (02)00051-1

Cande, S. C., Leslie, R. B., Parra, J. C., & Hobart, M., (1987). Interaction between the Chile Ridge and Chile Trench: Geophysical and geothermal evidence. *Journal Geophysical Research,* 92*(*B1*),* 495–520. doi:10.1029/JB092iB01p00495

Cande, S. C., & Haxby, W. F. (1991). Eocene propagating rifts in the southwest Pacific and their conjugate features on the Nazca plate. *Journal of Geophysical Research: Solid Earth*, *96*(B12), 19609-19622. doi:10.1029/91JB01991

Capitano, C., de, & Petrakakis, K. (2010). The computation of equilibrium assemblage diagrams with the Theriak/Domino software. *America Mineralogist*, *95*(7), 1006-1016. doi:10.2138/am.2010.3354

Cattermole, P. J. (2000). *Building Planet Earth: Five Billion Years of Earth History*. London: Cambridge University Press. ISBN 978-0-521-58278-0. OCLC 317422973

Cembrano, J., Lavenu, A., Yañez, G., Riquelme, R., Garcia, M., Gonzalez, G., Herail, G., (2007). Neotectonics. In: Gibbons, W., Moreno, T. (Eds.), The Geology of Chile. *London Geological Society Press*, London, p. 414.

Christensen, N. I., & Mooney, W. D. (1995). Seismic velocity structure and composition of the continental crust: A global view. *Journal of Geophysical Research: Solid Earth (1978–2012)*, *100*(B6), 9761-9788.

Clift, P., & Vannucchi, P. (2004). Controls on tectonic accretion versus erosion in subduction zones: Implications for the origin and recycling of the continental crust. *Reviews of Geophysics*, *42*(2). *doi:10.1029/2003RG000127*

Clouard, V., Campos, J., Lemoine, A., Perez, A., & Kausel, E. (2007). Outer rise stress changes related to the subduction of the Juan Fernandez Ridge, central Chile. *Journal of Geophysical Research: Solid Earth*, *112*(B5). doi:10.1029/2005JB003999.

Cominguez, A. H., & Ramos, V. A. (1991). La estructura profunda entre Precordillera y Sierras Pampeanas de la Argentina : Evidencia de la sismica de reflexion profunda. *Revista Geologica de Chile*, *18*, 3-14

Comte, D., & Suárez, G., (1994). An inverted double seismic zone in Chile: Evidence of phase transformation in the subducted slab. *Science, 263*, 5144, 212-215. doi*:*10.1126/science.263.5144.212.

Comte, D., Dorbath, L., Pardo, M., Monfret, T., Haessler, H. , Rivera, L., Frogneux, M., Glass, B., & Meneses, C. (1999), A double-layered seismic zone in Arica, northern Chile. *Geophysical Research Letters, 26*, 1965-1968. doi:10.1029/1999GL900447

Comte, D., Haessler, H., Dorbath, L., Pardo, M., Monfret, T., Lavenu, A., Pontoise, B., & Hello, Y. (2002). Seismicity and stress distribution in the Copiapo, northern Chile subduction zone using combined on- and off-shore seismic observations. *Physics of the Earth and Planetary Interiors*, *132*(1), 197-217.

Connolly, J. A. D. (2005). Computation of phase equilibria by linear programming: a tool for geodynamic modeling and its application to subduction zone decarbonation. *Earth and Planetary Science Letters*, *236*(1), 524-541.

Contardo, X. J., & Cembrano, J. M. (2007). The Close Connection Between the Subduction Processes, the Morphology of the Continental Margin and the Marine Basins on the accretionary segment of the Chilean Margin. In *AGU Spring Meeting Abstracts* (Vol. 1, p. 07).

Contreras-Reyes, E., Grevemeyer, I., Flueh, E. R., Scherwath, M.,& Heesemann, M., (2007). Alteration of the subducting oceanic lithosphere at the southern central Chile trench-outer rise. *Geochemistry, Geophysics, Geosystems, 8*, Q07003. doi:10.1029/2007GC001632

Contreras-Reyes, E., Grevemeyer, I., Flueh, E. R., & Reichert, C., (2008). Upper lithospheric structure of the subduction zone offshore southern Arauco Peninsula, Chile at ~38°S. *Journal of Geophysical Research, 113*, B07303. doi:10.1029/2007JB005569

Contreras-Reyes, E., & Osses, A. (2010). Lithospheric flexure modelling seaward of the Chile trench: implications for oceanic plate weakening in the Trench Outer Rise region. *Geophysical Journal International*, *182*(1), 97-112. doi:10.1111/j.1365-246X.2010.04629.x

Contreras-Reyes, E., Flueh, E. R., & Grevemeyer, I. (2010). Tectonic control on sediment accretion and subduction off south central Chile: Implications for coseismic rupture processes of the 1960 and 2010 megathrust earthquakes. *Tectonics*, *29*(6). doi:10.1029/2010TC002734.

Contreras-Reyes, E., & Carrizo, D. (2011). Control of high oceanic features and subduction channel on earthquake ruptures along the Chile–Peru subduction zone. *Physics of the Earth and Planetary Interiors*, *186*, 49–58

Cordani, U. G., & Sato, K. (1999). Crustal evolution of the South American Platform, based on Nd isotopic systematics on granitoid rocks. *Episodes-Newsmagazine of the International Union of Geological Sciences*, *22*(3), 167-173.

Corona, G., (2007). Estructura Litosférica del Sistema Andes Sierras Pampeanas en la Banda 30°S–31°S a Partir de Datos de Gravedad y Sísmicos [Undergraduate final work thesis]: San Juan, Argentina, Facultad de Ciencias (in Spanish)

Cristallini, E. O., & Ramos, V. A. (2000). Thick-skinned and thin-skinned thrusting in the La Ramada fold and thrust belt: Crustal evolution of the High Andes of San Juan, Argentina (32 SL). *Tectonophysics*, *317*(3), 205-235.

Cundall, P. A., & Board, M. (1988). A microcomputer program for modeling large strain plasticity problems, Numerical Methods in Geomechanics G. *Swoboda, Rotterdam, Netherlands*. *6*, 2101–2108.

Currie, C., Wang, K., Hyndman, R., & He, J., (2004). The thermal effects of steady-state slab-driven mantle flow above a subducting plate: the Cascadia subduction zone and backarc. *Earth and Planetary Science Letters, 223,* 35–48.

Dahlquist, J.A., Pankhurst, R.J., Rapela, C.W., Galindo, C., Alasino P., Fanning, C.M., Saavedra, J. & Baldo, E. (2008). New SHRIMP U–Pb data from the Famatina Complex: constraining Early–Mid Ordovician Famatinian magmatism in the Sierras Pampeanas, Argentina. *Geologica Acta, 6*, 319-333

DeCelles, P. G. (2004). Late Jurassic to Eocene evolution of the Cordilleran thrust belt and foreland basin system, western USA. *American Journal of Science*, *304*(2), 105-168.

DeCelles, P. G., Ducea, M. N., Kapp, P., & Zandt, G. (2009). Cyclicity in Cordilleran orogenic systems. *Nature Geoscience*, *2*(4), 251-257.

Delouis, B., & Legrand, D., (2007). Mw 7.8 Tarapaca intermediate-depth earthquake of 13 June 2005 (northern Chile): Fault plane identification and slip distribution by waveform inversion. *Geophysical Research Letters, 34*, L01304, doi: 10.1029/2006GL028193

Delouis, B., Nocquet, J. M., & Vallée, M. (2010). Slip distribution of the February 27, 2010 Mw= 8.8 Maule earthquake, central Chile, from static and high-rate GPS, InSAR, and broadband teleseismic data. *Geophysical Research Letters*, *37*(17). doi:10.1029/2010GL043899.

DeMets, C., Gordon, R. G., Argus, D. F., & Stein, S. (1990). Current plate motions. *Geophysical Journal International*, *101*(2), 425-478.

Deshayes, P. (2008). Tomographie en vitesse et en atténuation de la zone de subduction au Chili central-ouest de l'Argentine (29° S-34° S) à partir de données sismologiques locales: apport à l'étude de la composition minéralogique (Doctoral dissertation, Université de Nice Sophia-Antipolis) (in French)

Doin, M. P., Fleitout, L., & Christensen, U. (1997). Mantle convection and stability of depleted and undepleted continental lithosphere. *Journal of Geophysical Research*, *102*(B2), 2771-2787.

Dorbath, C., Gerbault, M., Carlier, G., & Guiraud, M. (2008). Double seismic zone of the Nazca plate in northern Chile: High-resolution velocity structure, petrological implications, and thermomechanical modeling. *Geochemistry, Geophysics, Geosystems*, *9*(7). doi:10.1029/2008GC002020

Engdahl, E. R., & Scholz, C. H. (1977). A double Benioff zone beneath the central Aleutians: An unbending of the lithosphere. *Geophysical Research Letters, 4,* 473-476. doi:10.1029/GL004i010p00473

Engdahl E. R., van der Hilst R. D. & Berrocal J. (1995). Imaging of subducted lithosphere beneath South America. *Geophysical Research Letters, 22,* 16, 2317-2320. doi:10.1029/95GL02013

Engdahl, E. R., van der Hilst, R., & Buland, R. (1998). Global teleseismic earthquake relocation with improved travel times and procedures for depth determination. *Bulletin of the Seismological Society of America*, *88*(3), 722-743.

Espurt, N., Funiciello, F., Martinod, J., Guillaume, B., Regard, V., Faccenna, C., & Brusset, S. (2008). Flat subduction dynamics and deformation of the South American plate: Insights from analog modeling. *Tectonics*, *27*(3). doi:10.1029/2007TC002175

Faccenda, M., Burlini, L., Gerya, T. V., & Mainprice, D. (2008). Fault-induced seismic anisotropy by hydration in subducting oceanic plates. *Nature*, *455*(7216), 1097-1100.

Faccenda, M., Gerya, T. V., & Burlini, L., (2009). Deep slab hydration induced by bending-related variations in tectonic pressure. *Nature Geoscience, 2,* 790-793. doi:10.1038/ngeo656

Faccenda, M. & N. S. Mancktelow (2010). Fluid flow during unbending: Implications for slab hydration, intermediate-depth earthquakes and deep fluid subduction. *Tectonophysics, 494*, 149-154, doi:10.1016/j.tecto.2010.08.002.

Faccenda, M., Gerya, T. V., Mancktelow, N. S., & Moresi, L. (2012). Fluid flow during slab unbending and dehydration: Implications for intermediate-depth seismicity, slab weakening and deep water recycling. *Geochemistry, Geophysics, Geosystems*, *13*(1). doi:10.1029/2011GC003860.

Farías, M., R. Charrier, S. Carretier, J. Martinod, A. Fock, D. Campbell, J. Cáceres, & D. Comte (2008). Late Miocene high and rapid surface uplift and its erosional response in the Andes of central Chile (33°–35°S). *Tectonics*, 27, TC1005, doi:10.1029/2006TC002046.

Farías, M., Comte, D., Charrier, R., Martinod, J., Tassara, A., & Fock, A. (2010). Crustal-scale structural architecture of the Central Chile Andes based on 3D seismic tomography, seismicity, and surface geology: Implications for mountain building in subduction zones. *Tectonics*, *29*. doi:10.1029/2009TC002480

Flueh, E. R., Vidal, N., Ranero, C. R., Hojka, A., Von Huene, R., Bialas, J., & Zelt, C. (1998). Seismic investigation of the continental margin off-and onshore Valparaiso, Chile. *Tectonophysics*, *288*(1), 251-263.

Fromm, R., Alvarado, P., Beck, S. L., & Zandt, G., (2006). The April 9, 2001 Juan Fernandez Ridge (Mw 6.7) tensional outer-rise earthquake and its aftershock sequence. *Journal of Seismology, 10*(2), 163-170. doi:10.1007/s10950-006-9013-3

Fromm, R., Zandt, G., & Beck, S. L. (2004). Crustal thickness beneath the Andes and Sierras Pampeanas at 30 S inferred from Pn apparent phase velocities. *Geophysical Research Letters*, *31*(6). doi:10.1029/2003GL019231

Fry, A., N. Kusznir, M. Dabrowski, A. Rietbrock, & I. Podladtchikov (2009), Modelling stress accumulation and dissipation and the causes of intermediate-depth seismicity in subduction zones, *Geophysical Research Abstracts*, 11, EGU2009-8382

Fuentes, F. (2004). Petrología y metamorfismo de muy bajo grado de unidades volcánicas Oligoceno Miocenas en la ladera occidental de los Andes de Chile central (33°S). Ph.D. thesis, 407 pp. Univ. de Chile, Santiago (in Spanish)

Fujita, K., & Kanamori, H., (1981). Double seismic zones and stresses of intermediate depth earthquakes. *Geophysical Journal of Royal Astronomy Society*, *66*(1), 131-156. doi:10.1111/j.1365-246X.1981.tb05950.x

Fukao, Y., Obayashi, M., & Nakakuki, T. (2009). Stagnant slab: a review. *Annual Review of Earth and Planetary Sciences, 37*, 19-46. doi:10.1146/annurev.36.031207.124224

Fumagalli, P., & Poli, S. (2005). Experimentally determined phase relations in hydrous peridotites to 6· 5 GPa and their consequences on the dynamics of subduction zones. *Journal of Petrology*, *46*(3), 555-578. doi:10.1093/petrology/egh088

Fumagalli, P., Stixrude, L., Poli, S., & Snyder, D. (2001). The 10Å phase: a high-pressure expandable sheet silicate stable during subduction of hydrated lithosphere. *Earth and Planetary Science Letters*, *186*(2), 125-141.

Gans, C. R., Beck, S. L., Zandt, G., Gilbert, H., Alvarado, P., Anderson, M., & Linkimer, L. (2011). Continental and oceanic crustal structure of the Pampean flat slab region, western Argentina, using receiver function analysis: new high-resolution results. *Geophysical Journal International*, *186*(1), 45-58.

Gardi, A., Lemoine, A., Madariaga, R., & Campos, J. (2006). Modeling of stress transfer in the Coquimbo region of central Chile. *Journal of Geophysical Research: Solid Earth (1978–2012)*, *111*(B4). doi:10.1029/2004JB003440

Gerbault, M. (1999). Modélisation numérique de la naissance des déformations localisées: exemple du flambage lithosphérique (Doctoral dissertation) (in French)

Gerbault, M., Cembrano, J., Mpodozis, C., Farias, M., & Pardo, M. (2009). Continental margin deformation along the Andean subduction zone: Thermo-mechanical models. *Physics of the Earth and Planetary Interiors*, *177*(3), 180-205.

Gerya, T. V., & Meilick, F. I. (2011). Geodynamic regimes of subduction under an active margin: effects of rheological weakening by fluids and melts. *Journal of Metamorphic Geology*, *29*(1), 7-31.

Giambiagi, L. B., & Ramos, V. A. (2002). Structural evolution of the Andes in a transitional zone between flat and normal subduction (33.30°–33.45° S), Argentina and Chile. *Journal of South American Earth Sciences*, *15*(1), 101-116.

Giambiagi, L. B., Ramos, V. A., Godoy, E., Alvarez, P. P., & Orts, S. (2003). Cenozoic deformation and tectonic style of the Andes, between 33 and 34 south latitude. *Tectonics*, *22*(4), 1041.

Gilbert, H., Beck, S., & Zandt, G. (2006). Lithospheric and upper mantle structure of central Chile and Argentina. *Geophysical Journal International, 165*, 383–398. doi:10.1111/j.1365-246X.2006.02867.x.

Grevemeyer, I., Diaz-Naveas, J. L., Ranero, C. R., & Villinger, H. W. (2003). Heat flow over the descending Nazca plate in central Chile, 32 S to 41 S: Observations from ODP Leg 202 and the occurrence of natural gas hydrates. *Earth and Planetary Science Letters*, *213*(3), 285-298. doi.org/10.1016/S0012-821X(03)00303-0

Grevemeyer, I., Kaul, N., Diaz-Naveas, J. L., Villinger, H. W., Ranero, C. R., & Reichert, C. (2005). Heat flow and bending-related faulting at subduction trenches: case studies offshore of Nicaragua and Central Chile. *Earth and Planetary Science Letters*, *236*(1), 238-248. Doi:10.1016/j.epsl.2005.04.048

Grevemeyer, I., Kaul, N., & Diaz-Naveas, J. L. (2006). Geothermal evidence for fluid flow through the gas hydrate stability field off Central Chile—transient flow related to large subduction zone earthquakes?. *Geophysical Journal International*, *166*(1), 461-468.

Gripp, A. E., & Gordon, R. G. (2002). Young tracks of hotspots and current plate velocities. *Geophysical Journal International*, *150*(2), 321-361.

Groß, K., & Micksch, U. (2008). The reflection seismic survey of project TIPTEQ—the inventory of the Chilean subduction zone at 38.2° S. *Geophysical Journal International*, *172*(2), 565-571.

Gutscher, M. A. (2002). Andean subduction styles and their effect on thermal structure and interplate coupling. *Journal of South American Earth Sciences*, *15*(1), 3-10.

Gutscher, M. A., Spakman, W., Bijwaard, H., & Engdahl, E. R. (2000). Geodynamics of flat subduction: Seismicity and tomographic constraints from the Andean margin. *Tectonics*, *19*(5), 814-833.

Haberland, C., Rietbrock, A., Lange, D., Bataille, K., & Dahm, T. (2009). Structure of the seismogenic zone of the southcentral Chilean margin revealed by local earthquake traveltime tomography. *Journal of Geophysical Research: Solid Earth (1978–2012)*, *114*(B1). doi:10.1029/2008JB5802

Hacker, B. R. (1996). Eclogite formation and the rheology, buoyancy, seismicity, and H2O content of oceanic crust. *Geophysical Monograph Series*, *96*, 337-346.

Hacker, B. R., G. A. Abers, & S. M. Peacock (2003a). Subduction factory 1. Theoretical mineralogy, densities, seismic wave speeds, and H2O contents. *Journal Geophysical Research, 108*(B1), 2029. doi:10.1029/2001JB001127

Hacker, B. R., S. M. Peacock, G. A. Abers, & S. D. Holloway (2003). Subduction factory 2. Are intermediate-depth earthquakes in subducting slabs linked to metamorphic dehydration reactions, *Journal Geophysical Research, 108*(B1), 2030. doi:10.1029/2001JB001129

Hacker, B. R., & Abers, G. A. (2004). Subduction Factory 3: An Excel worksheet and macro for calculating the densities, seismic wave speeds, and H2O contents of minerals and rocks at pressure and temperature. *Geochemistry, Geophysics, Geosystems*, *5*(1). doi:10.1029/2003GC000614

Hacker, B. R., & Abers, G. A. (2012). Subduction Factory 5: Unusually low Poisson's ratios in subduction zones from elastic anisotropy of peridotite. *Journal of Geophysical Research: Solid Earth*, *117*(B6). doi:10.1029/2012JB009187

Hamza, V. & Munoz, M. (1996). Heat flow map of South America. *Geothermics*, *25*(48), 599-656

Hasegawa, A., N. Umino & A. Takagi (1978). Double planed deep seismic zone and upper mantle structure in the northeastern Japan arc, *Geophysical Journal of Royal Astronomy Society, 54*, 281–296. doi:10.1111/j.1365-246X.1978.tb04260.x

Haslinger, F., & Kissling, E. (2001). Investigating effects of 3-D ray tracing methods in local earthquake tomography. *Physics of the Earth and Planetary Interiors*, *123*(2), 103-114.

Havskov, J., Ottemöller, L., 2001. SEISAN earthquake analysis software, Version 7.2, University of Bergen, Norway, pp. 256

Heit, B., Yuan, X., Bianchi, M., Sodoudi, F., & Kind, R. (2008). Crustal thickness estimation beneath the southern central Andes at 30 S and 36 S from S wave receiver function analysis. *Geophysical Journal International*, *174*(1), 249-254.

Helffrich, G. (1996). Subducted lithospheric slab velocity structure: Observations and mineralogical inferences. *Geophysical Monograph-American Geophysical Union*, *96*, 215-222.

Helffrich, G., & Abers, G. A., (1997). Slab slow-velocity layer in the eastern Aleutian subduction zone. *Geophysical Journal International, 130*(3), 640-648. doi:10.1111/j.1365-246X.1997.tb01858.x

Heuret, A., & Lallemand, S. (2005). Plate motions, slab dynamics and back-arc deformation. *Physics of the Earth and Planetary Interiors*, *149*(1), 31-51.

Heuret, A., F. Funiciello, C. Faccenna, & S. Lallemand (2007), Plate kinematics, slab shape and back-arc stress: A comparison between laboratory models and current subduction zones, *Earth and Planetary Science Letters, 256*, 473-483. doi.org/10.1016/j.epsl.2007.02.004

Hori, S., Inoue, H., Fukao, Y., & Ukawa, M. (1985). Seismic detection of the untransformed 'basaltic'oceanic crust subducting into the mantle. *Geophysical Journal of the Royal Astronomical Society*, *83*(1), 169-197. doi: 10.1111/j.1365-246X.1985.tb05162.x

Husen, S., Kissling, E., & Flueh, E. R. (2000). Local earthquake tomography of shallow subduction in north Chile: A combined onshore and offshore study. *Journal of Geophysical Research: Solid Earth*, *105*(B12), 28183-28198

Isacks, B., & M. Barazangi (1977). Geometry of Benioff zones: Lateral segmentation and downward bending of the subducted lithosphere, in Island arcs, deep sea trenches and back-arc basins, Talwani M. and Pitman III. *American Geophysical Union Mon.*, 99-114.

Jackson, J. A., Austrheim, H., McKenzie, D., & Priestley, K. (2004). Metastability, mechanical strength, and the support of mountain belts. *Geology*, *32*(7), 625-628.

Jacobsen, S. D., Jiang, F., Mao, Z., Duffy, T. S., Smyth, J. R., Holl, C. M., & Frost, D. J. (2008). Effects of hydration on the elastic properties of olivine. *Geophysical Research Letters*, *35*(14).

James, D. E., & Snoke, J. A. (1994). Structure and tectonics in the region of flat subduction beneath central Peru: Crust and uppermost mantle. *Journal of Geophysical Research: Solid Earth*, *99*(B4), 6899-6912.

Jiao, W., Silver, P. G., Fei, Y., & Prewitt, C. T., (2000). Do intermediate- and deep-foc earthquakes occur on pre-existing weak zones? An examination of the Tonga subduction zone. *Journal Geophysical Research, 105*(B12), 28, 125-28, 138. doi:10.1029/2000JB900314

Jordan, T. E., B. Isacks, R. Allmendinger, J. Brewer, V. Ramos & C. Ando (1983). Andean tectonics related to geometry of the subducted Nazca Plate. *Geological Society of America Bulletin, 94*, 341-361. doi:10.1130/0016-7606(1983)94<341:ATRTGO>2.0.CO;2

Jordan, T. E., & R. W. Allmendinger (1986). The Sierras Pampeanas of Argentina: A modern analogue of Rocky Mountain foreland deformation. *American Journal of Science, 286*(10), 737–764, doi:10.2475/ajs.286.10.737.

Jordan, T. E., & Alonso, R. N. (1987). Cenozoic stratigraphy and basin tectonics of the Andes Mountains, 20-28 South latitude. *AAPG Bulletin*, *71*(1), 49-64.

Jung, H., Green, II H. W., & Dobrzinetskaya, L. F., (2004). Intermediate-depth earthquake faulting by dehydration embrittment with negative volume change. *Nature, 428*, 545-549. doi:10.1038/nature02412

Jung, H., Fei, Y., Silver, P. G., & Green, H. W. II, (2009). Frictional sliding in serpentine at very high pressure. *Earth and Planetary Science Letters, 277*(1-2), 273-279. doi:10.1016/j.epsl.2008.10.019

Kao, H. & W. P. Chen (1994). The double seismic zone in Kuril-Kamchatka: the tale of two overlapping single zones. *Journal of Geophysical Research, 99*, 6913-6930.

Kao, H. & R. J. Rau (1999). Detailed structures of the subducted Philippine Sea plate beneath northeast Taiwan: A new type of double seismic zone. *Journal of Geophysical Research, 104*, 1015–1033. doi:10.1029/1998JB900010

Karato, S. I., & Jung, H. (1998). Water, partial melting and the origin of the seismic low velocity and high attenuation zone in the upper mantle. *Earth and Planetary Science Letters*, *157*(3-4), 193-207.

Karato, S., (2003). Mapping water content in the upper mantle. In: J. Eiler and G. Abers (Editors), The subduction factory. *Geophysical Monograph Series, 138*, 135-152

Kawakatsu, H. & T. Seno (1983). Triple Seismic Zone and the Regional Variation of seismicity along the Northern Honshu arc. *Journal of Geophysical Research, 88*, 4215-4230.

Kay, S., V. Maksaev, R. Moscoso, C. Mpodozis, & C. Nasi (1987). Probing the evolving Andean lithosphere: mid-late Tertiary magmatism in Chile (29°-30.30°S) over the modern zone of subhorizontal subduction. *Journal Geophysical Research, 32*, 6173-6189.

Kay, S. M., Mpodozis, C., Ramos, V. A., & Munizaga, F. (1991). Magma source variations for mid–late Tertiary magmatic rocks associated with a shallowing subduction zone and a thickening crust in the central Andes (28 to 33 S). *Geological Society of America Special Papers*, *265*, 113-138.

Kay, R. W., & Kay, M. S. (1993). Delamination and delamination magmatism. *Tectonophysics*, *219*(1), 177-189.

Kay, S. M., & Abbruzzi, J. M. (1996). Magmatic evidence for Neogene lithospheric evolution of the central Andean "flat-slab" between 30°S and 32°S. *Tectonophysics*, *259*(1), 15-28.

Kay, S. M., Orrell, S., & Abbruzzi, J. M. (1996). Zircon and whole rock Nd-Pb isotopic evidence for a Grenville age and a Laurentian origin for the basement of the Precordillera in Argentina. *The Journal of Geology*, 637-648.

Kay, S. M., & Gordillo, C. E. (1994). Pocho volcanic rocks and the melting of depleted continental lithosphere above a shallowly dipping subduction zone in the Central Andes. *Contributions to Mineralogy and Petrology*, *117*(1), 25-44.

Kay, S.M. & Mpodozis, C. (2002). Magmatism as a probe to the Neogene shallowing of the Nazca plate beneath the modern Chilean flat- slab. *Journal of South American Earth Sciences*, *15*, 39-57.

Kay, S. M., Godoy, E., & Kurtz, A. (2005). Episodic arc migration, crustal thickening, subduction erosion, and magmatism in the south-central Andes. *Geological Society of America Bulletin*, *117*(1-2), 67-88.

Kelemen, P. B., & G. Hirth (2007). A periodic shear-heating mechanism for intermediate-depth earthquakes in the mantle. *Nature*, *446*, 787–790, doi:10.1038/nature05717

Kendrick, E., Bevis, M., Smalley Jr, R., Brooks, B., Vargas, R. B., Laurıa, E., & Fortes, L. P. S. (2003). The Nazca–South America Euler vector and its rate of change. *Journal of South American Earth Sciences*, *16*(2), 125-131. doi:10.1016/S0895-9811(03)00028-2

Kennett, B. L. N., & Engdahl, E. R. (1991). Traveltimes for global earthquake location and phase identification. *Geophysical Journal International*, *105*(2), 429-465.

Kennett, B. L. N., Engdahl, E. R., & Buland, R. (1995). Constraints on seismic velocities in the Earth from traveltimes. *Geophysical Journal International*, *122*(1), 108-124. doi:10.1111/j.1365-246X.1995.tb03540

Keppie, J. D., & Ramos, V. A. (1999). Odyssey ofterranes in the lapetus and Rheic oceans during the Paleozoic. *Laurentia-Gondwana connections before Pangea*, (336), 267-276.

King G.C.P., Stein R.S., & Lin J. (1994). Static stress changes and the triggering of Kirby, S.H., 1985. Rock mechanics observations pertinent to the rheology of the continental lithosphere and the localization of strain along shear zones. *Tectonophysics 18*, 1–27.

Kirby, S., Engdahl, R. E., & Denlinger, R. (1996). Intermediate-depth intraslab earthquakes and arc volcanism as physical expressions of crustal and uppermost mantle metamorphism in subducting slabs. *Geophysical Monograph Series*, *96*, 195-214. doi:10.1029/GM096p0195

Kissling E. & Haslinger S. (2001). Model parametrization in seismic tomography: a choice of consequence for the solution quality. *Physics of the Earth Planetary Interior, 123*, 89-101

Kissling, E., Ellsworth, W. L., Eberhart-Phillips, D., & Kradolfer, U. (1994). Initial reference models in local earthquake tomography. *Journal of Geophysical Research: Solid Earth*, *99*(B10), 19635-19646. doi:10.1029/93JB03138

Klein, F. W. (2000). User's Guide to HYPOINVERSE-2000 a Fortran Program to Solve for Earthquake Locations and Magnitudes, *USGS Open File Report*. Draft 5/19.

Klotz, J., Khazaradze, G., Angermann, D., Reigber, C., Perdomo, R., & Cifuentes, O. (2001). Earthquake cycle dominates contemporary crustal deformation in Central and Southern Andes. *Earth and Planetary Science Letters*, *193*(3), 437-446.

Kopp, H., Flueh, E. R., Papenberg, C., & Klaeschen, D. (2004). Seismic investigations of the O'Higgins Seamount Group and Juan Fernández Ridge: Aseismic ridge emplacement and lithosphere hydration. *Tectonics*, *23*(2). doi:10.1029/2003TC001590

Kuge, K., Kase, Y., Urata, Y., Campos, & J., Perez, A., (2010). Rupture characteristics of the 2005 Tarapaca, northern Chile, intermediate-depth earthquake : Evidence for heterogeneous fluid distribution across the subducting oceanic plate ?. *Journal of Geophysical Research*, *115*(B9), B11399. doi:10.1029/2010JB007999

Lallemand, S., Heuret, A., Faccenna, C., & Funiciello, F. (2008). Subduction dynamics as revealed by trench migration. *Tectonics*, *27*(3). doi:10.1029/2007TC002212

Lamb, S. (2006). Shear stresses on megathrusts: Implications for mountain building behind subduction zones. *Journal of Geophysical Research: Solid Earth (1978–2012)*, *111*(B7). doi:10.1029/2005JB003916

Lange D., Cembrano J., Rietbrok A., Haberland C., Dahm T., & Bataille K. (2008), First seismic record for intra-arc strike-slip tectonics along the Liquine-Ofqui fault zone at the obliquely convergent plate margin of the southern Andes. *Tectonophysics 455*(1–4), 14–24.

Latorre, D., Virieux, J., Monfret, T., Monteiller, V., Vanorio, T., Got, J. L., & Lyon-Caen, H. (2004). A new seismic tomography of Aigion area (Gulf of Corinth, Greece) from the 1991 data set. *Geophysical Journal International*, *159*(3), 1013-1031. doi:10.1111/j.1365-246X.2004.02412.x

Lay, T., & Wallace, T. C. (1995). *Modern global seismology* (Vol. 58). Academic press. p.357-396.

Lay, T., Ammon, C. J., Kanamori, H., Koper, K. D., Sufri, O., & Hutko, A. R. (2010). Teleseismic inversion for rupture process of the 27 February 2010 Chile (Mw 8.8) earthquake. *Geophysical Research Letters*, *37*(13). doi:10.1029/2010GL043379

Lemoine, A., Madariaga, R., & Campos, J. (2002). Slab-pull and slab-push earthquakes in the Mexican, Chilean and Peruvian subduction zones. *Physics of the Earth and Planetary Interiors*, *132*(1), 157-175.

Lenardic, A., & Moresi, L. N. (1999). Some thoughts on the stability of cratonic lithosphere: Effects of buoyancy and viscosity. *Journal of Geophysical Research*, *104*(B6), 12747-12.

Lenardic, A., Guillou-Frottier, L., Mareschal, J. C., Jaupart, C., Moresi, L. N., & Kaula, W. M. (2000). What the mantle sees: the effects of continents on mantle heat flow. *Geophysical Monograph Series*, *121*, 95-112.

Li, C., van der Hilst, R. D., Engdahl, E. R., & Burdick, S. (2008). A new global model for P wave speed variations in Earth's mantle. *Geochemistry, Geophysics, Geosystems*, *9*(5). doi:10.1029/2007GC001806

Lienert, B. R., & Havskov, J., (1995). Hypocenter 3.2: A computer program for locating earthquakes locally, regionally and globally. *Seismological Research Letters, 66*, 5, 26-36. doi:10.1785/gssrl.66.5.26

López-Escobar, L. (1984). Petrology and chemistry of volcanic rocks of the Southern Andes. In *Andean Magmatism* (pp. 47-71). Birkhäuser Boston.

Lowrie, A., & Hey, R. (1981). Geological and geophysical variations along the western margin of Chile near latitude 33 to 36 S and their relation to Nazca Plate subduction. *Nazca Plate; crustal formation and Andean convergence. Geological Society of America, Memoir*, *154*, 741-754.

MacDougall, J. G., Fischer, K. M., & Anderson, M. L. (2012). Seismic anisotropy above and below the subducting Nazca lithosphere in southern South America. *Journal of Geophysical Research: Solid Earth (1978–2012)*, *117*(B12). doi:10.1029/2012JB009538

Manea, V. C., Pérez-Gussinyé, M., & Manea, M. (2012). Chilean flat slab subduction controlled by overriding plate thickness and trench rollback. *Geology*, *40*(1), 35-38.

Marot, M., Monfret, T., Pardo, M., Ranalli, G., & Nolet, G. (2012). An intermediate-depth tensional earthquake (Mw 5.7) and its aftershocks within the Nazca slab, central Chile: A reactivated outer rise fault?. *Earth and Planetary Science Letters*, *327*, 9-16. doi: 10.1016/j.epsl.2012.02.003

Marquardt, C., Lavenu, A., Ortlieb, L., Godoy, E., & Comte, D. (2004). Coastal neotectonics in Southern Central Andes: uplift and deformation of marine terraces in Northern Chile (27 S). *Tectonophysics*, *394*(3), 193-219.

Martinod, J., Funiciello, F., Faccenna, C., Labanieh, S., & Regard, V. (2005). Dynamical effects of subducting ridges: insights from 3-D laboratory models. *Geophysical Journal International*, *163*(3), 1137-1150. doi:10.1111/j.1365246X.2005.02797.x

Martinod, J., Husson, L., Roperch, P., Guillaume, B., & Espurt, N. (2010). Horizontal subduction zones, convergence velocity and the building of the Andes. *Earth and Planetary Science Letters*, *299*(3), 299-309. doi:10.1016/j.epsl.2010.09.010

McGuire, J.J. & D. A. Wiens (1995). A double seismic zone in New Britain and the morphology of the Solomon plate at intermediate-depths. *Geophysical Research Letters, 22*, 1965-1968. doi:10.1029/95GL01806

Metois, M., Socquet, A., & Vigny, C. (2012). Interseismic coupling, segmentation and mechanical behavior of the central Chile subduction zone. *Journal of Geophysical Research: Solid Earth (1978–2012), 117*(B3). doi:10.1029/2011JB008736

Miranda S. (2001). Gravity crustal model for an Andean section at 32°S considering upper mantle lateral density variation. Brazilian Journal of Geophysics, 18(2)

Mishra, O. P., & Zhao, D., (2004). Seismic evidence for dehydration embrittlement of the subducting Pacific slab. *Geophysical Research Letters, 31*, L09610. doi:10.1029/2004GL019489

Monteiller V., Got J.-L., Virieux J. & P.G. Okubo, (2005). An efficient algorithm for double-difference tomography and location in heterogeneous media, with an application to Kilauea volcano, Hawaii, *Journal Geophysical Research, 110*, B12306. doi:10.1029/2004BJ003466

Montelli, R., G. Nolet, F. A. Dahlen, G. Maters, E. R. Engdahl & S. H. Hung (2004), Finite-frequency tomography reveals a variety of plumes in the mantle, *Science, 303*, 338-343. doi:10.1126/science.1092485

Mookherjee, M., & G. C. Capitani (2011). Trench parallel anisotropy and large delay times: Elasticity and anisotropy of antigorite at high pressures. *Geophysical Research Letters, 38*, L09315. doi:10.1029/2011GL047160

Müller, R.D., W. R. Roest, J.-Y. Royer, L. M. Grahagan & J. G. Sclater (1997). Digital isochrones of the world's sea floor, *Journal Geophysical Research, 102*, 3211-3214.

Muñoz, M. (2005). No flat Wadati–Benioff Zone in the central and southern central Andes. *Tectonophysics, 395*(1), 41-65.

Murdie, R. E., & Russo, R. M. (1999). Seismic anisotropy in the region of the Chile margin triple junction. *Journal of South American Earth Sciences*, *12*(3), 261-270. doi:10.1016/S0895-9811(99)00018-8

Nakajima, J., & Hasegawa, A.,(2006). Anomalous low-velocity zone and linear alignment of seismicity along it in the subducted Pacific slab beneath Kanto, Japan: Reactivation of subducted fracture zone?. *Geophysical Research Letters, 33*. L16309. doi:10.1029/2006GL026773

Nakajima, J., Tsuji, Y., Hasegawa, A., (2009a). Seismic evidence for thermally-controlled dehydration reaction in the subducting oceanic crust. *Geophysical Research Letters, 36*, L03303. doi:10.1029/2008GL036865

Nakajima, J., Tsuji, Y., Hasegawa, A., Kita, S., Okada, T., & Matsuzawa, T., (2009b). Tomographic imaging of hydrated crust and mantle in the subducting Pacific slab beneath Hokkaido, Japan: Evidence for hydration embrittlement as a cause of intraslab earthquakes. *Gondwana Research, 16*, 470-481

Nakajima, J., Hasegawa, A., & Kita, S., (2011). Seismic evidence for reactivation of a buried hydrated fault in the Pacific slab by the 2011 Mw9.0 Tohoku earthquake. *Geophysical Research Letters, 38*, L00G06. doi:10.1029/2011GL048432

O'Neill, C., Muller, R.D., & Steinberger, B., (2005). On the uncertainties in hot spot reconstructions and the significance of moving hotspot reference frames. *Geochemistry, Geophysics, Geosystems, 6*(4). doi:10.1029/2004GC000784

Orozco L. A., Favetto A., Pomposiello C., Rossello E., Booker J. (2013). Crustal deformation of the Andean foreland at 31° 30′S (Argentina) constrained by magnetotelluric survey. *Tectonophysics, 582*, 126–139. doi:10.1145/355993.356000

Paige, C. C., & Saunders, M. A. (1982). LSQR: An algorithm for sparse linear equations and sparse least squares. *ACM Transactions on Mathematical Software (TOMS), 8*(1), 43-71.

Pardo, M., Comte, D., & Monfret, T. (2002). Seismotectonic and stress distribution in the central Chile subduction zone. *Journal of South American Earth Sciences*, *15*(1), 11-22. doi:10.1016/S0895-9811(02)00003-2

Pardo, M., Monfret, T., Vera, E., Yáñez, G., & Eisenberg, A. (2004). Flat-slab to steep subduction transition zone in central Chile-western Argentina: body waves tomography and state of stress. In *AGU Fall Meeting Abstracts* (Vol. 1, p. 0164). abstract #S51B-0164

Peacock, S. M., & Wang, K., (1999). Seismic consequences of warm versus cool subduction metamorphism: examples from southwest and northeast Japan. *Science, 286*, 5441, 937-939. doi:10.1126/science.286.5441.937

Peacock, S. M. (2001). Are the lower planes of double seismic zones caused by serpentine dehydration in subducting oceanic mantle?. *Geology*, *29*(4), 299-302. doi:10.1130/0091-7613(2001)029<0299:ATLPOD>2.0.CO;2

Perarnau, M., Alvarado, P., & Saez, M. (2010). Estimación de la estructura cortical de velocidades sísmicas en el suroeste de la sierra de Pie de Palo, provincia de San Juan. *Revista de la Asociación Geológica Argentina*, *67*(4), 473-480.

Pérez-Gussinyé, M., Lowry, A. R., Phipps Morgan, J., & Tassara, A. (2008). Effective elastic thickness variations along the Andean margin and their relationship to subduction geometry. *Geochemistry, Geophysics, Geosystems*, *9*(2). doi:10.1029/2007GC001786

Pesicek, J. D., Engdahl, E. R., Thurber, C. H., DeShon, H. R., & Lange, D. (2012). Mantle subducting slab structure in the region of the 2010 M8. 8 Maule earthquake (30–40° S), Chile. *Geophysical Journal International*, *191*(1), 317-324.

Peyrat, S., Campos, J., de Chabalier, J. B., Perez, A., Bonvalot, A., Bouin, M.-P., Legrand, D., Nercessian, A., Charade, O., Patau, G., Clevede, E., Kausel, E., Bernard, P., & Vilotte, J.-P., (2006). Tarapacá intermediate-depth earthquake (Mw 7.7, 2005, northern Chile): A slab-pull event with horizontal fault plane constrained from seismologic and geodetic observations. *Geophysical Research Letters, 33*, L22308. doi:10.1029/2006GL027710

Peyrat, S., & Favreau, P., (2010). Kinematic and spontaneous rupture models of the 2005 Tarapacá intermediate depth earthquake. *Geophysical Journal International, 181*, 1,369-381. doi:10.1111/j.1365-246X.2009.04493.x

Pilger, R. H., & Handschumacher, D. W. (1981). The fixed-hotspot hypothesis and origin of the Easter—Sala y Gomez—Nazca trace. *Geological Society of America Bulletin*, *92*(7), 437-446. doi:10.1130/0016-7606(1981)92<437:TFHAOO>2.0.CO;2

Pilger, R.H. Jr. (1981), Plate reconstructions, aseismic ridges, and low angle subduction beneath the Andes. *Geological Society of American Bulletin, 92*, 448-456. doi: 10.1130/0016-7606

Podvin P. & Lecompte I. (1991). Finite difference computation of traveltimes in very contrasted velocity models: a massively parallel approach and its associated tools. *Geophysical Journal International*, *105*(1), 271-284.

Poliakov A. & Podladchikov Y. (1992). Diapirism and topography. *Geophysical Journal International*, 105(1), 271-284.

Porter, R., Gilbert, H., Zandt, G., Beck, S., Warren, L., Calkins, J., Alvarado, P., & Anderson, M. (2012). Shear wave velocities in the Pampean flat-slab region from Rayleigh wave tomography: Implications for slab and upper mantle hydration. *Journal of Geophysical Research: Solid Earth (1978–2012)*, *117*(B11). doi:10.1029/2012JB009350

Prevot, R., J.-L. Chatelain, S. W. Roecker and J.-R. Grasso (1994). A shallow double seismic zone beneath the central New Hebrides (Vanuatu): Evidence for fragmentation and accretion of the descending plate, *Geophysical Research Letters*, *21*, 2159-2162.

Ramachandran, K., & Hyndman, R. D. (2012). The fate of fluids released from subducting slab in northern Cascadia. *Solid Earth*, *3*, 121-129.

Ramos, V. A., Jordan, T. E., Allmendinger, R. W., Mpodozis, C., Kay, S. M., Cortés, J. M., & Palma, M. (1986). Paleozoic terranes of the central Argentine-Chilean Andes. *Tectonics*, *5*(6), 855-880. doi:10.1029/TC5i006p855

Ramos V.A. (1988a). Tectonics of the Late Proterozoic – Early Paleozoic: a collisional history of Southern South America. *Episodes, 11*(3), 168–174.

Ramos, V. A. (1988b). The tectonics of the Central Andes; 30°S to 33°S latitude. *Geological Society of America Special Papers*, *218*, 31-54.

Ramos, V.A., (1999). Plate tectonic setting of the Andean Cordillera. *Episodes 22*(3), 183–190.

Ramos, V. A., & Aleman, A. (2000). Tectonic evolution of the Andes. *Tectonic Evolution of South America*, *31*.

Ramos, V. A., Cristallini, E. O., & Pérez, D. J. (2002). The Pampean flat-slab of the Central Andes. *Journal of South American Earth Sciences*, *15*(1), 59-78. doi:10.1016/S0895-9811(02)00006-8

Ramos, V. A. (2004). Cuyania, an exotic block to Gondwana: review of a historical success and the present problems. *Gondwana Research*, *7*(4), 1009-1026.

Ramos V. A. (2009) Anatomy and global context of the Andes: Main geologic features and the Andean Orogenic cycle, in Kay S. M., Ramos V. A., and Dickinson W. R., eds, Backbone of the Americas: shallow subduction, plateau uplift, and ridge and terrane collision. *Society of America Memoir 204*, p. 31-65 doi:10.1130/2009

Ramos, V. A. (2010). The tectonic regime along the Andes: Present-day and Mesozoic regimes. *Geological Journal*, *45*(1), 2-25.

Ranalli, G., (1995). Rheology of the Earth, second ed. Chapman & Hall, p. 413.

Ranero, C. R., Morgan, J. P., McIntosh, K., & Reichert, C., (2003). Bending-related faulting and mantle serpentinization at the Middle America trench. *Nature, 425*, 367-373. doi:10.1038/nature01961

Ranero, C.R., & Sallares, V.,(2004). Geophysical evidence for hydration of the crust and mantle of the Nazca plate during bending at the north Chile trench. *Geology*, *32*(7), 549–552. doi:10.1130/G20379.1

Ranero, C. R., Villasenor, A., Morgan, J. P., Weinrebe, W., (2005). Relationship between bend-faulting at trenches and intermediate-depth seismicity. *Geochemistry Geophysics Geosystems, 6*, 12, Q12002, doi:10.1029/2005GC000997

Ratchkovsky. N.A., J. Pujol & N. N. Biswas (1997). Stress pattern in the double seismic zone beneath Cook Inlet, south-central Alaska. *Tectonophysics, 281*, 163-171. doi.org/10.1016/S0040-1951(97)00042-5

Regnier M., Chatelain, J.L., Smalley, R., Jr., Chiu, J.M., Isacks, B., & Araujo, M., (1992), Seismotectonics of Sierra Pie de Palo, a basement block uplift in the Andean foreland of Argentina. *Bulletin of the Seismological Society of America, 82*, p. 2549–2571.

Regnier, M., Chiu, J.M., Smalley, R., Jr., Isacks, B.L., & Araujo, M., (1994). Crustal thickness variation in the Andean foreland, Argentina, from converted waves. *Bulletin of the Seismological Society of America, 84*,1097–1111.

Rietbrock, A. & F. Waldhauser (2004). A narrowly double-seismic zone in the subducted Nazca plate, *Geophysical Research Letters, 31*, L10608. doi:10.1029/2004GL019610

Reynard, B., J. Nakajima, & H. Kawakatsu (2010). Earthquakes and plastic deformation of anhydrous slab mantle in double Wadati-Benioff zones. *Geophysical Research Letters, 37*, L24309. doi:10.1029/2010GL045494

Reynard, B. (2013). Serpentine in active subduction zones. *Lithos*, 178, 171-185. doi.org/10.1016/j.lithos.2012.10.012

Rivera, L. & A. Cisternas (1991). Stress tensor and fault plane solutions for a population of earthquakes. *Bulletin of Seismological Society of America, 80*, 600–614.

Robinson, R. (1986). Seismicity, structure, and tectonics of the Wellington region, New Zealand. *Geophysical Journal International, 87*, 379-409. doi:10.1111/j.1365-246X.1986.tb06629.x

Roecker, S. W. (1982). Velocity structure of the Pamir-Hindu Kush Region: Possible evidence of subducted crust. *Journal of Geophysical Research: Solid Earth (1978–2012)*, *87*(B2), 945-959. doi:10.1029/JB87iB02p00945

Roeder, D. (1988). Andean-age structure of Eastern Cordillera (Province of La Paz, Bolivia). *Tectonics*, *7*(1), 23-39.

Russo, R., VanDecar, J. C., Comte, D., Mocanu, V. I., Gallego, A., & Murdie, R. E. (2010). Subduction of the Chile Ridge: Upper mantle structure and flow. *GSA Today*, *20*(9), 4-10.

Russo, R. M. (2010). Subduction of the Chile Rise: Upper mantle structure and flow. *GSA Today*, *20*, 9, doi:10.1130/GSATG61A.1

Sacks, I. S. (1983). The subduction of young lithosphere. *Journal of Geophysical Research, 88*(B4), 3355–3366. doi:10.1029/JB088iB04p03355

Salazar, P. (2005), *Analisis del campo de esfuerzos en la zonade subduccion bajo Chile Central (30°-34°S)*, MSc. Thesis. University of Chile, Santiago, Chile, p. 196 (in Spanish).

Sallarès, V., & Ranero, C. R. (2005). Structure and tectonics of the erosional convergent margin off Antofagasta, north Chile (23°-30°S). *Journal of Geophysical Research: Solid Earth (1978–2012)*, *110*(B6). doi:10.1029/2004JB003418

Scalabrino B. (2009). *Déformation d'un continent au-dessus d'une dorsale océanique active en subduction*, Thèse, Université Montpellier 2 Sciences et Techniques du Languedoc (03/11/2009) , tel-00557618, version 1 (in French)

Scalabrino, B., Lagabrielle, Y., de la Rupelle, A., Malavieille, J., Polvé, M., Espinoza, F., Morata D. & Suarez, M. (2009). Subduction of an active spreading ridge beneath southern South America: A review of the Cenozoic geological records from the Andean foreland, central Patagonia (46–47 S). In *Subduction Zone Geodynamics* (pp. 227-246). Springer Berlin Heidelberg.

Schurr, B., Rietbrock, A., Asch, G., Kind, R., & Oncken, O. (2006). Evidence for lithospheric detachment in the central Andes from local earthquake tomography. *Tectonophysics*, *415*(1), 203-223.

Schwartz, J. J., & Gromet, L. P. (2004). Provenance of a late Proterozoic–early Cambrian basin, Sierras de Córdoba, Argentina. *Precambrian Research*, *129*(1), 1-21.

Seno, T. & B. Pongsawat (1981). A triple-planed structure of seismicity and earthquake mechanisms at the subduction zone of Miyagi Prefecture, northern Honshu, Japan. *Earth and Planetary Science Letters, 55*, 25-36. doi.org/10.1016/0012-821X(81)90083-2

Seno, T., & Yamanaka, Y., (1996). Double seismic zones, compressional deep trench-outer rise events, and superplumes, in Subduction Top to Bottom. *Geophysical Monograpth Series*, 96, edited by G. E. Bebout et al., AGU, Washington, D.C, pp. 347-355.

Seno, T., D. Zhao, Y. Kobayashi & M. Nakamura (2001). Dehydration of serpentinized slab mantle: Seismic evidence from southwest Japan. *Earth Planets Space, 53*, 861-871.

Shiobara, H., H. Sugioka, K. Mochizuki, S. Oki, T. Kanazawa, Y. Fukao and K. Suyehiro (2010). Double seismic zone in the North Mariana region revealed by llong-term ocean bottom array observation, *Geophysical Journal International, 183.* doi:10.111/j.1365-246X.2010.04799.x

Smalley, R.F., Jr., & Isacks, B.L., (1987). A high resolution local network study of the Nazca plate Wadati Benioff zone under western Argentina. *Journal of Geophysical Research, 92,* no. B13, p. 13,903–13,912. doi:10.1029/JB092iB13p13903

Smalley, R., & Isacks, B. L. (1990). Seismotectonics of thin-and thick-skinned deformation in the Andean Foreland from local network data: Evidence for a seismogenic lower crust. *Journal of Geophysical Research: Solid Earth (1978–2012)*, *95*(B8), 12487-12498.

Smalley, R., Pujol, J., Regnier, M., Chiu, J. M., Chatelain, J. L., Isacks, B. L., Araujo M, & Puebla, N. (1993). Basement seismicity beneath the Andean Precordillera thin-skinned thrust belt and implications for crustal and lithospheric behavior. *Tectonics*, *12*(1), 63-76.

Snoke, J. A., Munsey, J. W., Teague, A. C., Bollinger, G. A., (1984). A program for focal mechanism determination by combined use of polarity and SV-P amplitude ration data. *Earthquake notes, 55*, p.15

Sobolev, A. V., & Chaussidon, M. (1996). H2O concentrations in primary melts from supra-subduction zones and mid-ocean ridges: Implications for H2O storage and recycling in the mantle. *Earth and Planetary Science Letters*, *137*(1), 45-55.

Somoza, R., & Ghidella, M.E., (2005). Convergencia en el margen occidental de America del sur durante el Cenozoico: Subduccion de Nazca. Farallon y Aluk. *Revista de la Asociacion Geologica Argentina* 60, 797–809.

Soustelle, V. (2010). Interaction entre déformation et percolation de magma ou de fluide dans le manteau à l'aplomb des zones de subduction (Doctoral dissertation, Universite de Montpellier 2) (in French)

Stein, C. A., & Stein, S. (1992). A model for the global variation in oceanic depth and heat flow with lithospheric age. *Nature*, *359*(6391), 123-129.

Stein, C. A., (2003). Heat flow and flexure at subduction zones. *Geophysical Research Letters, 30*, 23, SDE 4-1. doi:10.1029/2003GL018478

Stuessy T. F., Foland K. A., Sutter J. F., Sanders R. W. & Silva M. (1984). Botanical and Geological Significance of Potassium-Argon Dates from the Juan Fernández Islands. *Science, 225*, 4657, 49-51. *doi:* 10.1126/science.225.4657.49

Swift, S., & Carr, M., (1974). The segmented nature of the Chilean seismic zone. *Physics of the Earth and Planetary Interiors, 9*(3), 183-191. doi:10.1013/0031-9201(74)90135-6

Syracuse, E. M., & Abers, G. A. (2006). Global compilation of variations in slab depth beneath arc volcanoes and implications. *Geochemistry, Geophysics, Geosystems, 7*(5). doi:10.1029/2005GC001045

Takei, Y. (2002). Effect of pore geometry on Vp/Vs: From equilibrium geometry to crack. *Journal of Geophysical Research: Solid Earth (1978–2012), 107*(B2), ECV-6. doi:10.1029/2001JB000522

Tassara, A. (2005). Interaction between the Nazca and South American plates and formation of the Altiplano–Puna plateau: Review of a flexural analysis along the Andean margin (15–34 S). *Tectonophysics, 399*(1), 39-57.

Tassara, A., & Echaurren, A. (2012). Anatomy of the Andean subduction zone: three-dimensional density model upgraded and compared against global-scale models. *Geophysical Journal International, 189*(1), 161-168. doi:10.1111/j.1365-246X.2012.05397.x

Tassara, A., Götze, H. J., Schmidt, S., & Hackney, R. (2006). Three-dimensional density model of the Nazca plate and the Andean continental margin. *Journal of Geophysical Research: Solid Earth, 111*(B9). doi:10.1029/2005JB003976.

Tebbens S. F., Cande S. C. (1997) Southeast Pacific tectonic evolution from early Oligocene to Present , *Journal Geophysical Research, 102*, 12061-12084.

Turcotte, D. L., & Schubert, G. (1982). Geodynamics: Applications of continuum mechanics to geological problems. *New York*.

Twiss, R. J., & Moore, E. M., (1992). *Normal faults*, in: Structural Geology, Chap.5, Publisher: Freeman, H. W., first edition, p.74-95

Uyeda, S. (1978). The new view of the earth: moving continents and moving oceans. WH Freeman.

Uyeda S., Watanabe T., & Volponi F. (1978). Report of heat flow measurements in the San Juan and Mendoza, Argentina. *Bulletin of Earthquakes Research Instr., Tokyo, 53,* 165-172

van Hunen, J., van den Berg, A. P., & Vlaar, N. J. (2001). Latent heat effects of the major mantle phase transitions on low-angle subduction. *Earth and Planetary Science Letters, 190*(3), 125-135.

van Hunen, J., van den Berg, A. P., & Vlaar, N. J. (2002). On the role of subducting oceanic plateaus in the development of shallow flat subduction. *Tectonophysics, 352*(3), 317-333.

van Hunen, J., van den Berg, A.P., & Vlaar, N.J., (2004). Various mechanisms to induce present-day shallow flat subduction and implications for the younger Earth: a numerical parameter study. *Physics of the Earth & Planetary Interiors, 146*, 179–194.

van Hunen, J., & Allen, M. B. (2011). Continental collision and slab break-off: A comparison of 3-D numerical models with observations. *Earth and Planetary Science Letters, 302*(1), 27-37.

von Huene, R., Corvalán, J., Flueh, E. R., Hinz, K., Korstgard, J., Ranero, C. R., & Weinrebe, W. (1997). Tectonic control of the subducting Juan Fernández Ridge on the Andean margin near Valparaiso, Chile. *Tectonics, 16*(3), 474-488.

Wagner, L. S., Anderson, M. L., Jackson, J. M., Beck, S. L., & Zandt, G. (2008). Seismic evidence for orthopyroxene enrichment in the continental lithosphere. *Geology, 36*(12), 935-938.

Wagner, L. S., Beck, S., & Zandt, G. (2005). Upper mantle structure in the south central Chilean subduction zone (30 to 36 S). *Journal of Geophysical Research, 110*(B1), B01308. doi:10.1029/2004JB003238

Wagner, L. S., Beck, S., Zandt, G., & Ducea, M. N. (2006). Depleted lithosphere, cold, trapped asthenosphere, and frozen melt puddles above the flat slab in central Chile and Argentina. *Earth and Planetary Science Letters, 245*(1), 289-301. doi:10.1016/j.epsl.2006.02.014

Waldhauser, F., & Ellsworth, W. L., (2000). A double-difference earthquake location algorithm: Method and application to the Northern Hayward Fault, California. *Bulletin of Seismological Society America, 90*, 6, 1,353-1,368. doi:10.1785/0120000006

Wang, K. & G. C. Rogers (1994). An explanation for the double seismic layers north of the Mendocino triple junction. *Geophysical Research Letters, 21*, 121-124.

Wang, J., & Zhao, D. (2012). P-wave anisotropic tomography of the Nankai subduction zone in Southwest Japan. *Geochemistry, Geophysics, Geosystems, 13*(5). doi:10.1029/2012GC004081

Wang, K. (2002). Unbending combined with dehydration embrittlement as a cause for double and triple seismic zones. *Geophysical research letters*, *29*(18), 1889. doi:10.1029/2002GL015441

Warren, L.M., Hughes, A. N., & Silver, P., (2007). Earthquake mechanics and deformation in the Tonga-Kermadec subduction zone from fault plane orientations of intermediate- and deep-focus earthquakes. *Journal Geophysical Research, 112*, B05314. doi:10.1029/2006JB004677

Warren, L. M., Langstaff, M. A., & Silver, P. G., (2008). Fault-plane orientations of intermediate-depth earthquakes in the Middle America trench. *Journal Geophysical Research, 113*, B01304. doi:10.1029/2007JB005028

Wells, D. L.,& Coppersmith, K. J., (1994). New empirical relationships among magnitude, rupture length, rupture width, rupture area, and surface displacement. *Bulletin of Seismology Society of America, 84*(4), 974-1,002.

Wessel, P., & Smith, W. H. (1998). New, improved version of Generic Mapping Tools released. *Eos, Transactions American Geophysical Union*, *79*(47), 579-579.

White, R. S., McKenzie, D., & O'Nions, R. K. (1992). Oceanic crustal thickness from seismic measurements and rare earth element inversions. *Journal of Geophysical Research: Solid Earth (1978–2012)*, *97*(B13), 19683-19715.

Wiens, D. A., Gilbert, H. J., Hicks, B., Wysession, M. E., & Shore, P. J., (1997). Aftershock sequences of moderate-sized intermediate and deep earthquakes in the Tonga Subduction Zone. *Geophysical Research Letters, 24*(16), 2059–2062. doi:10.1029/97GL01957

Woodward J. M., Nichols D., Zdraveva O., Whitfield P., & Johns T. (2008). A decade of tomography. *Geophysics, 73*. doi:10.1190/1.2969907

Worzewski, T., Jegen, M., Kopp, H., Brasse, H., Castillo, W. T., (2010). Magnetotelluric image of the fluid cycle in the Costa Rican subduction zone. *Nature Geosciences, 4*, 108-111. doi:10.1038/NGEO1041

Yamasaki, T. & T. Seno (2003). Double Seismic Zone and Dehydration Embrittlement of the Subducting Slab. *Journal Geophysical Research, 108.* doi:10.1029/2002JB001918

Yáñez, G., & Cembrano, J. (2000). Tectonic models for ridge collision at a continental plate boundary: The case of Juan Fernández ridge and Chile rise, Preliminary Results. In *Congreso Geológico Chileno* (No. 9, pp. 649-654).

Yáñez, G., Cembrano, J., Pardo, M., Ranero, C., & Selles, D. (2002). The Challenger–Juan Fernández–Maipo major tectonic transition of the Nazca–Andean subduction system at 33–34 S: geodynamic evidence and implications. *Journal of South American Earth Sciences*, *15*(1), 23-38. doi:10.1016/S0895-9811(02)00004-4

Yáñez, G., Ranero, G.R., von Huene, R. & Diaz, J. (2001). Magnetic anomaly interpretation across a segment of the southern Central Andes (32-34°S): Implications on the role of the Juan Fernández ridge in the tectonic evolution of the margin during the Upper Tertiary. *Journal of Geophysical Research*, *106*, 6325-6345. doi:10.1029/2000JB900337.

Zhao, D. (2007). Seismic images under 60 hotspots: search for mantle plumes. *Gondwana Research, 12*, 335-355. doi.org/10.1016/j.gr.2007.03.001

# **Appendix A:** Chapter 2 – *Part One* – Seismic Tomography

## Ray density, checkerboard and spike sensitivity tests

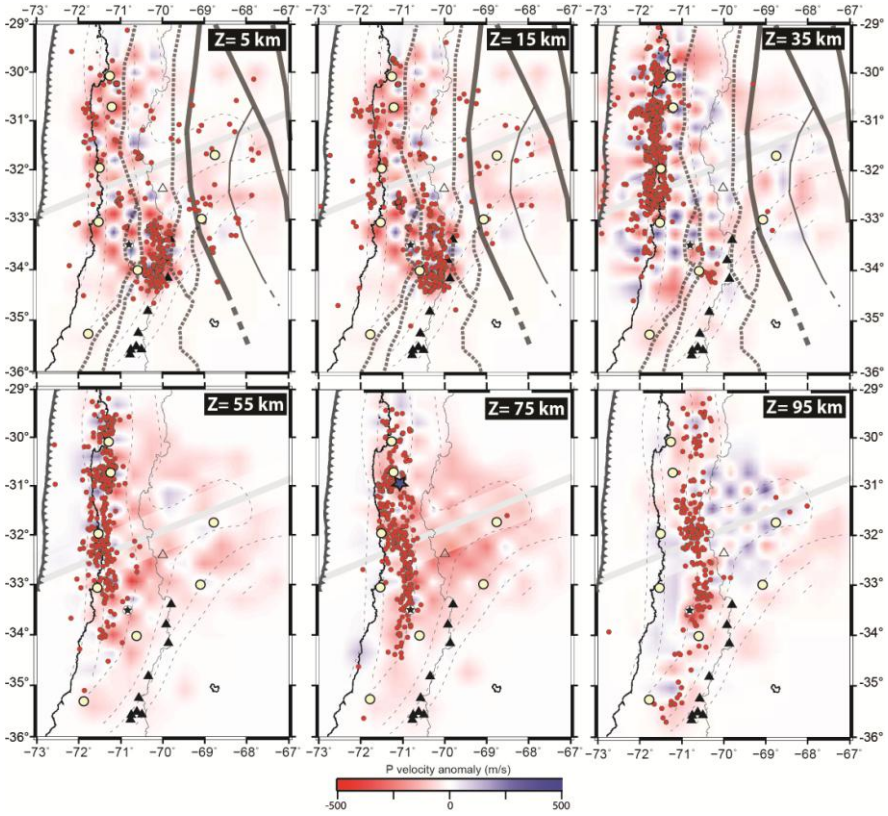


**Fig. A.1**: *Checkerboard test results in plan view, of our final model for P- (upper panel) and S-waves (lower panel), at 20 km depth intervals. The initial velocity perturbation is 500 and 300 m/s, respectively, shown for the 5 km depth slice in Fig. 2.1.11. The shape and amplitude of the anomaly is best recovered in the center of the region nearest to the coast, where seismicity is highest, down to 35 km depth. The backarc region however, is poorly resolved.*

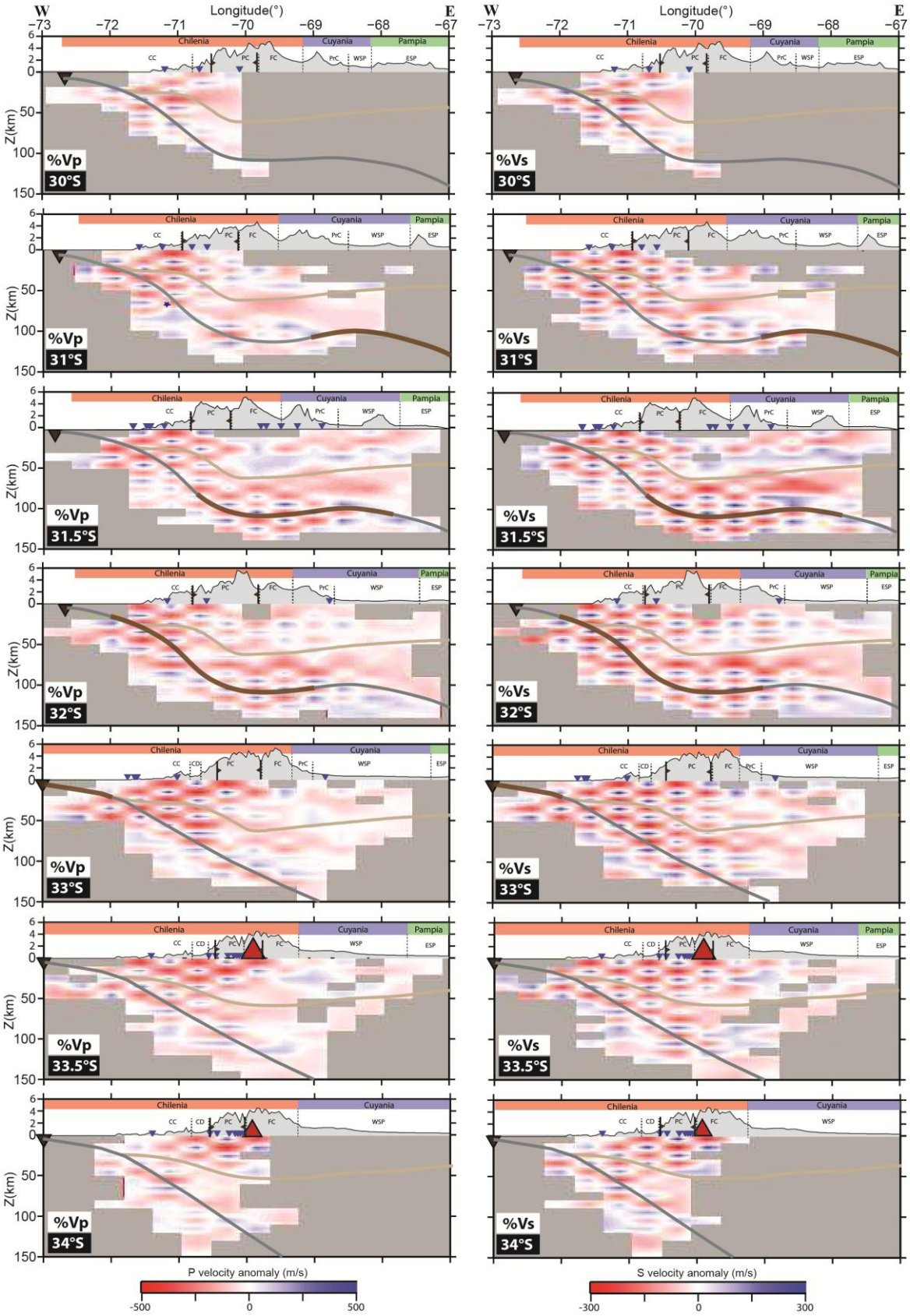


**Fig. A.2**: *Checkerboard test results in E-W cross-section view, of our final model for P- (left panel) and S-waves (right panel), at 1°S and 0.5°S latitude intervals. Figure legend is the same as Fig. A.1. The oceanic lithosphere near its surface, and the overriding crust and mantle resolve well the seismic perturbation amplitudes and geometry, with only exception the backarc region.*

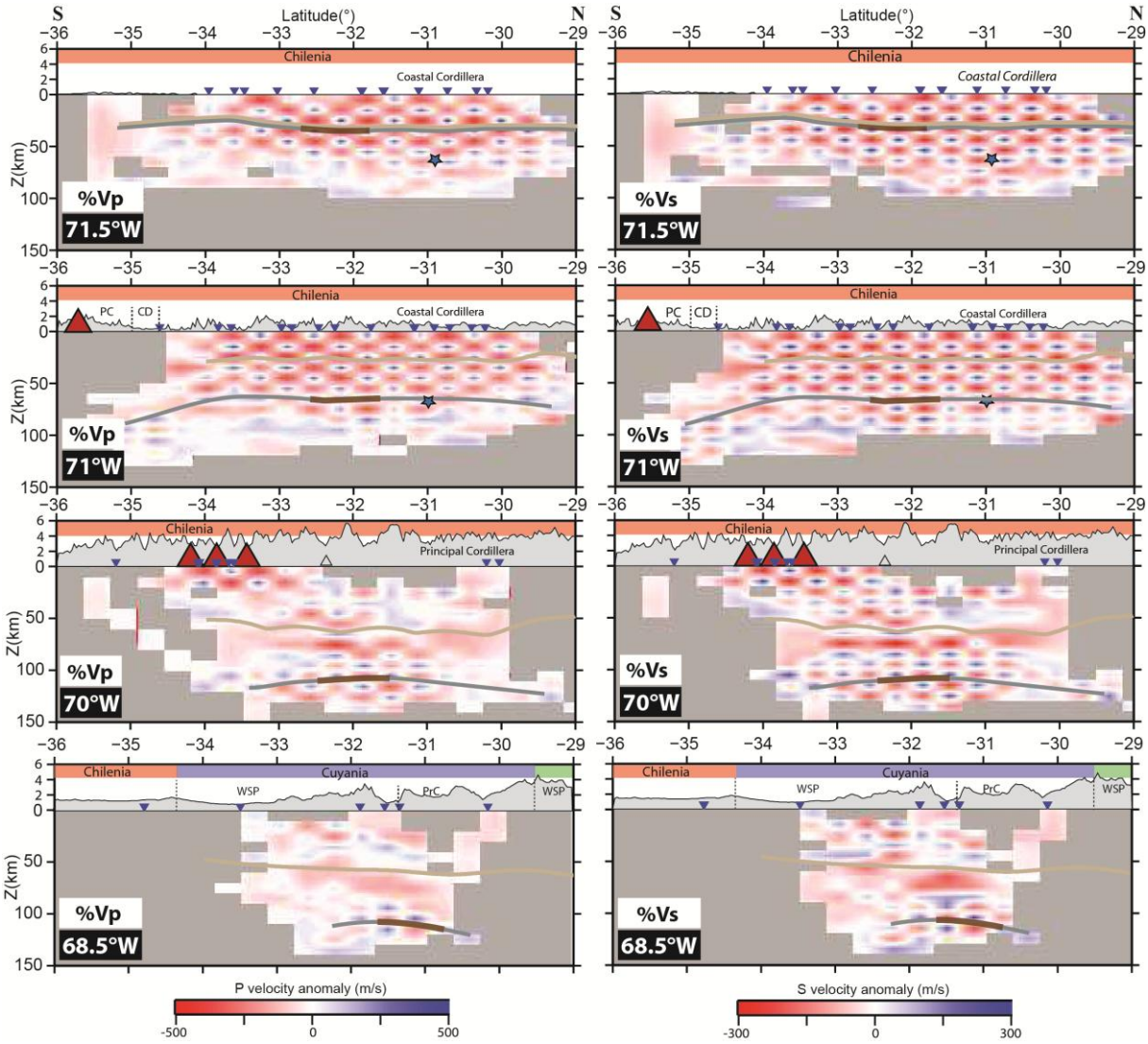


**Fig. A.3**: *Checkerboard test results in N-S vertical cross-section, at 1°W and 0.5°W longitude intervals. West of 71°S, the amplitudes and geometries of the initial velocity perturbation are well recovered.*

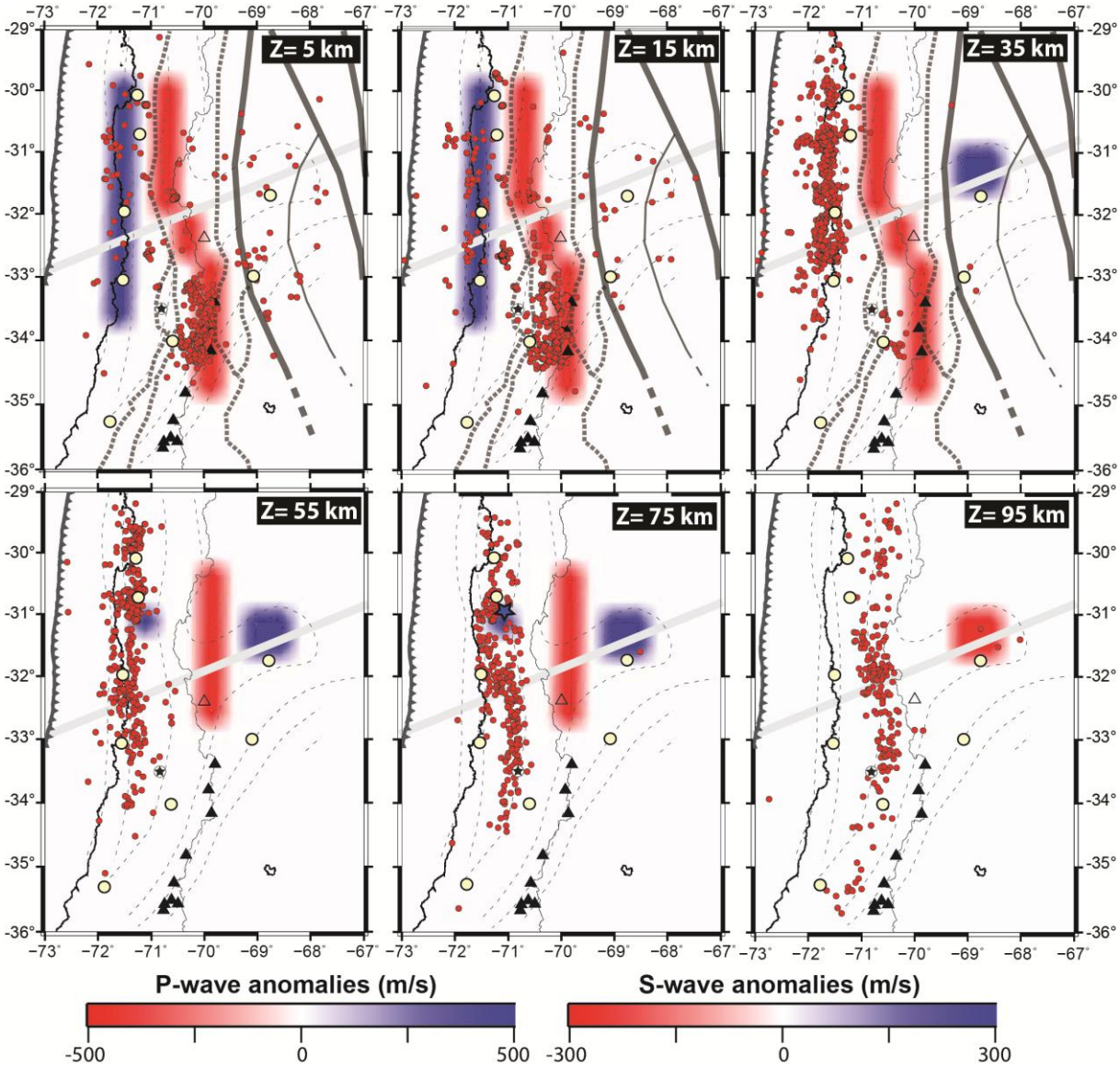


**Fig. A.5**: *« Spike » test of the initial P- and S-wave velocity perturbations at specific locations, show in plan view. Figure legend as in Fig. A.1.*

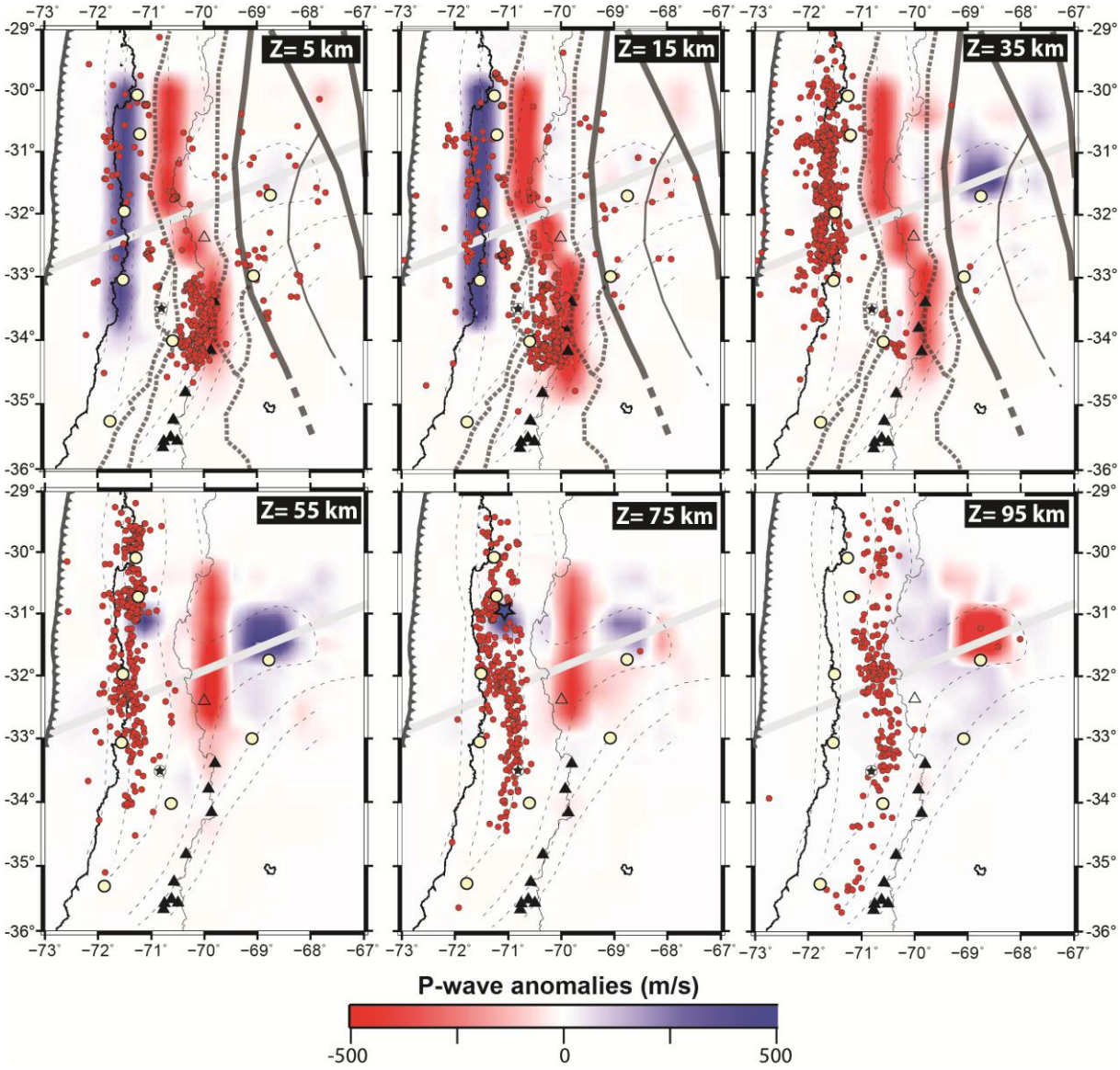


**Fig. A.6**: *« Spike » test of the final P-wave velocity perturbations at specific locations, show in plan view. Figure legend as in Fig. A.1.*

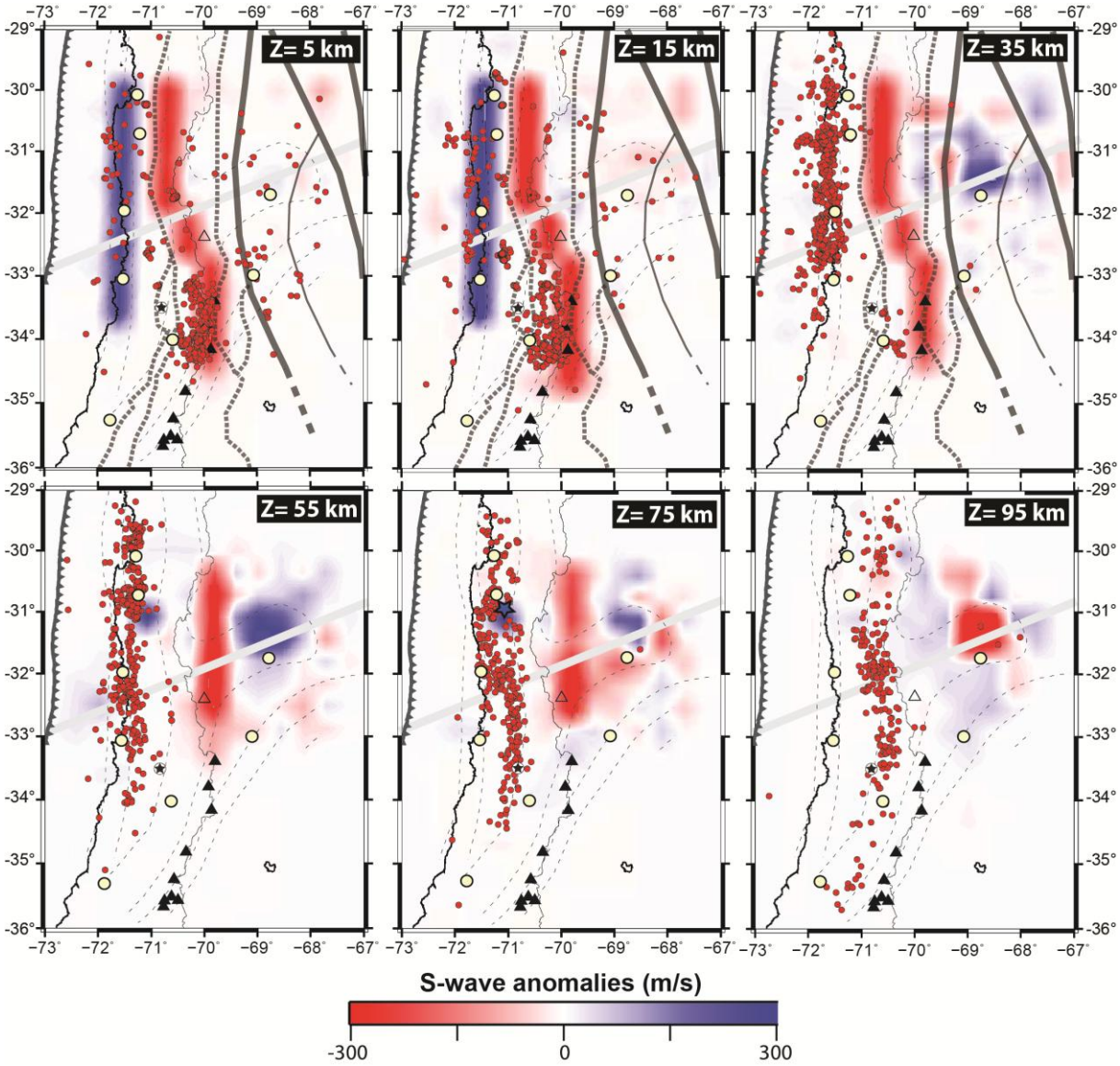


**Fig. A.7**: *« Spike » test of the final S-wave velocity perturbations at specific locations, show in plan view. Figure legend as in Fig. A.1.*

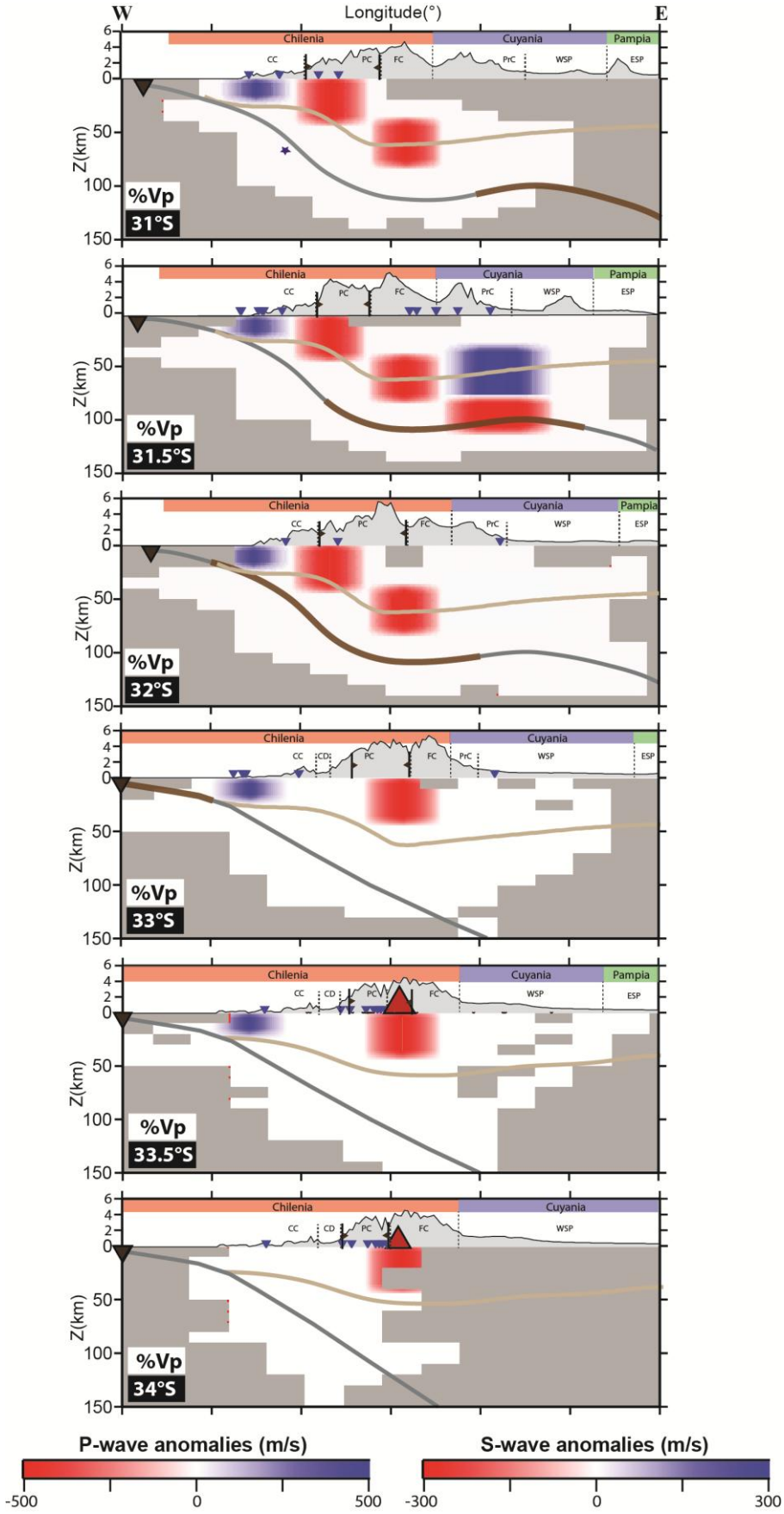


**Fig. A.8:** *« Spike » test of the initial P- and S-wave velocity perturbations at specific locations, shown along E-W vertical cross-sections. Figure legend as in Fig. A.1.*

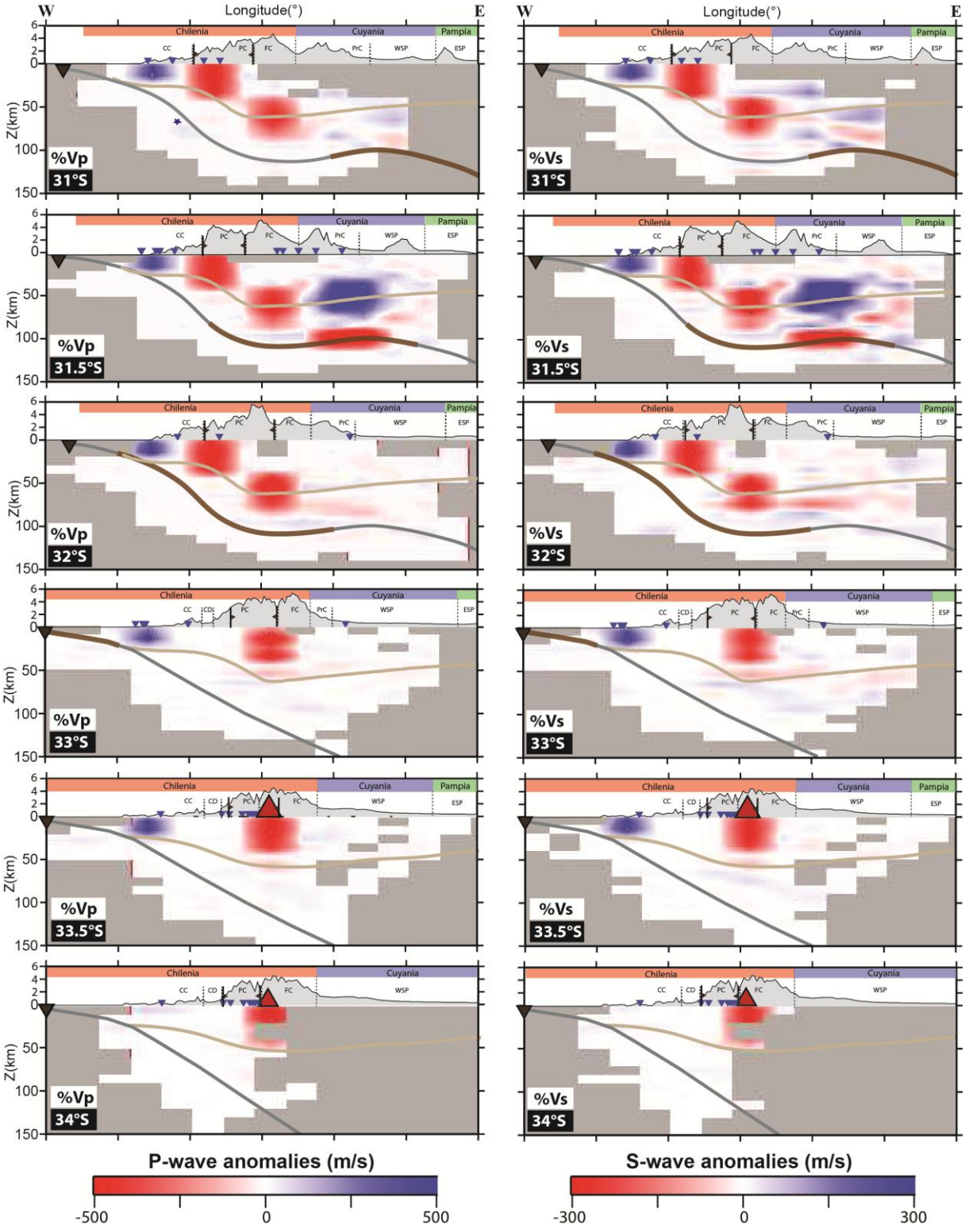


**Fig. A.9:** *« Spike » test of the final P- and S-wave velocity perturbations at specific latitudes, shown along E-W vertical cross-sections. Figure legend as in Fig. A.1.*

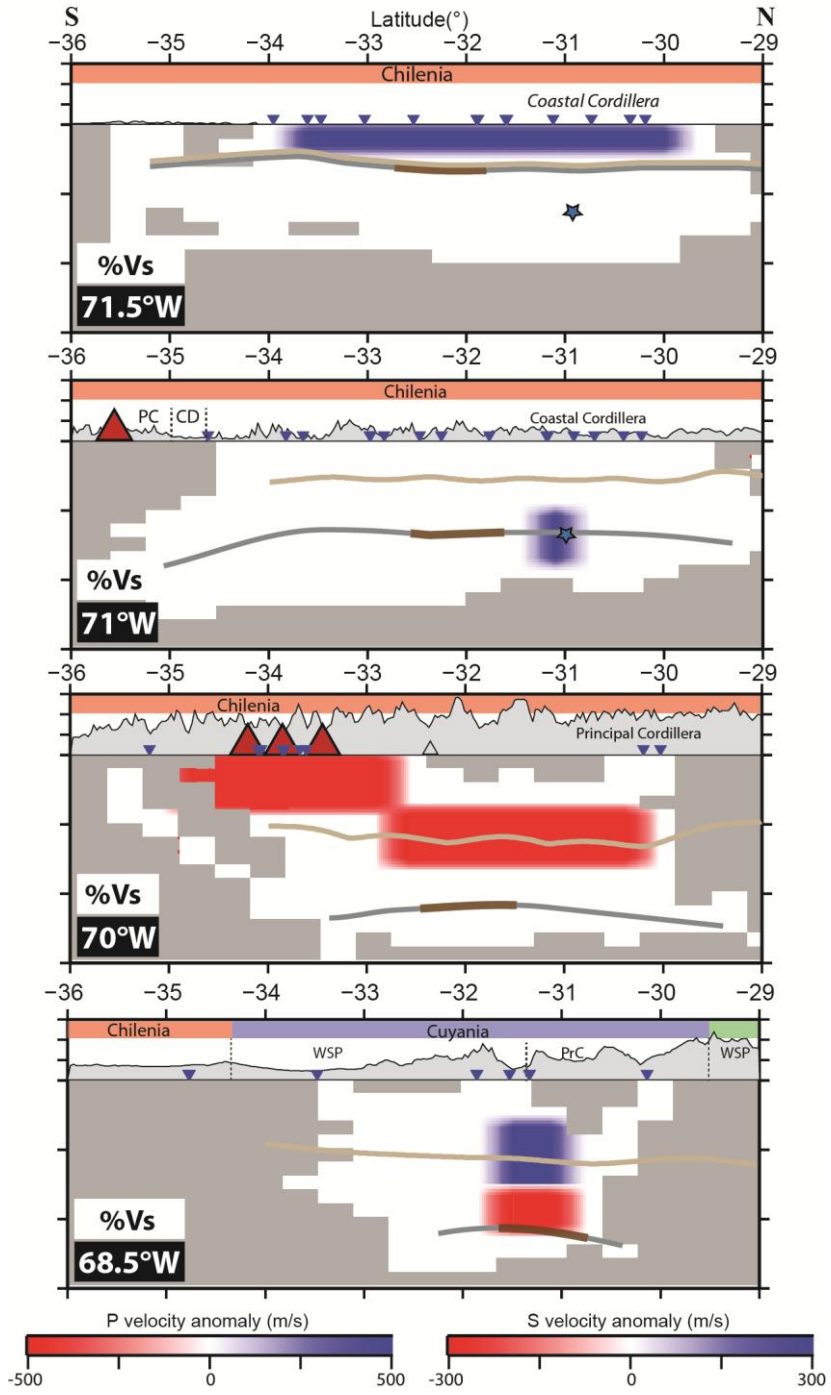


**Fig. A.10:** *« Spike » test of the initial P- and S-wave velocity perturbations at specific locations, show in N-S cross-section view. Figure legend as in Fig. A.1.*

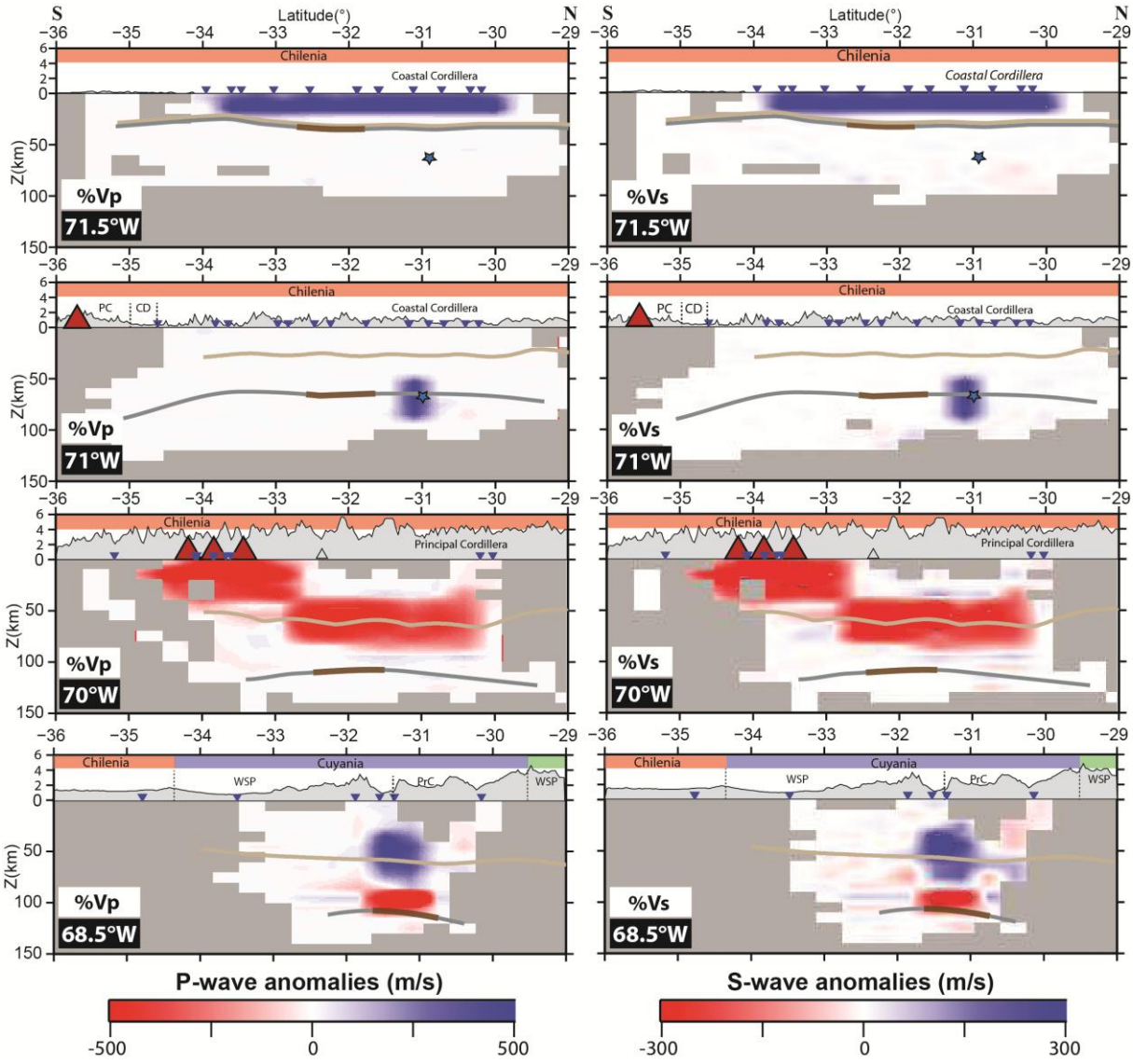


**Fig. A.11:** *« Spike » test of the final P- and S-wave velocity perturbations at specific locations, show along N-S vertical cross-sections. Figure legend as in Fig. A.1.*

# **Appendix B:** Chapter 2 – *Part Three* Petrological Modeling

## Individual mineral distributions in the continental and oceanic crusts, and, correlations with the seismic velocity field

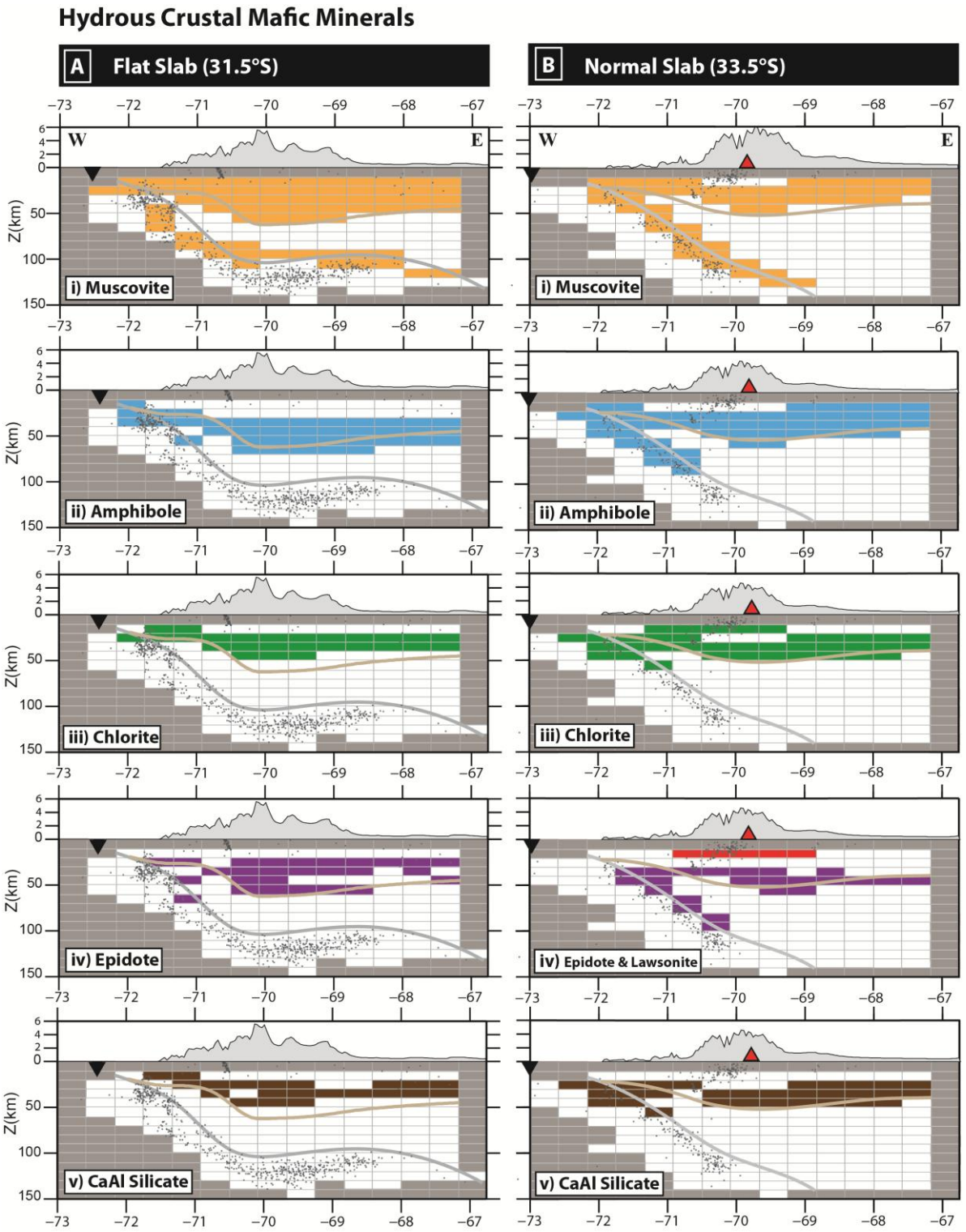


**Fig. B.1**: *Hydrous mafic mineral distribution for the continental and oceanic crusts, based on MORB-type rocks, regardless of the number of rock solutions per cell.*

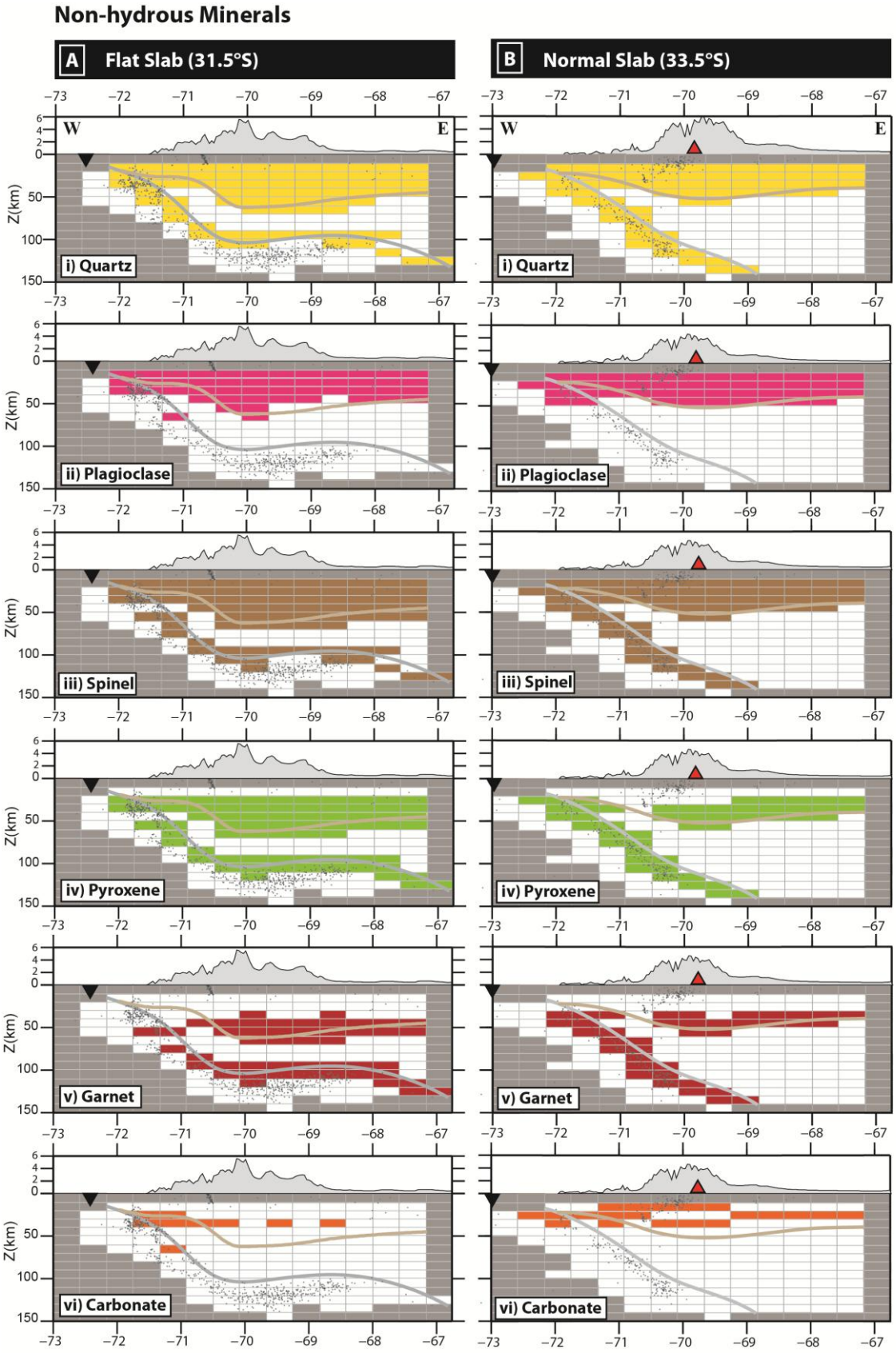


**Fig. B.2**: *Anhydrous mafic mineral distribution for the continental and oceanic crusts, based on MORB-type rocks, regardless of the number of rock solutions per cell.*

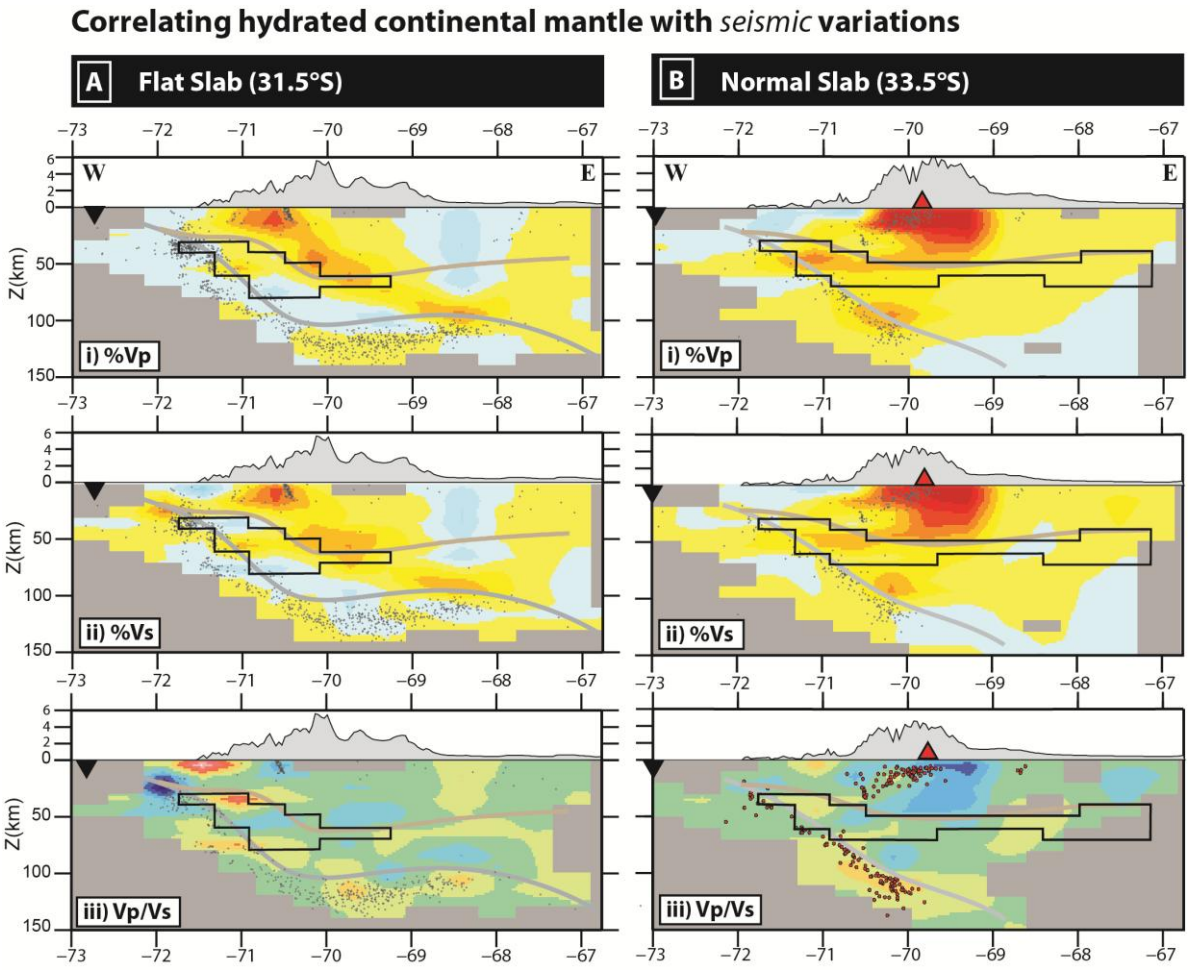


**Fig. B.3**: *Correlating the seismic velocity variations (i) %Vp, (ii) %Vs and (iii) Vp/Vs, with continental mantle serpentinization, described in Fig. 2.3.4 (upper panel) for the (A) flat and (B) normal subduction zones. The relationship between these two parameters is not obvious, indicating that either the degree of mantle hydration is insufficient, and/or, another more dominant factor influences the variations in seismic velocities.*

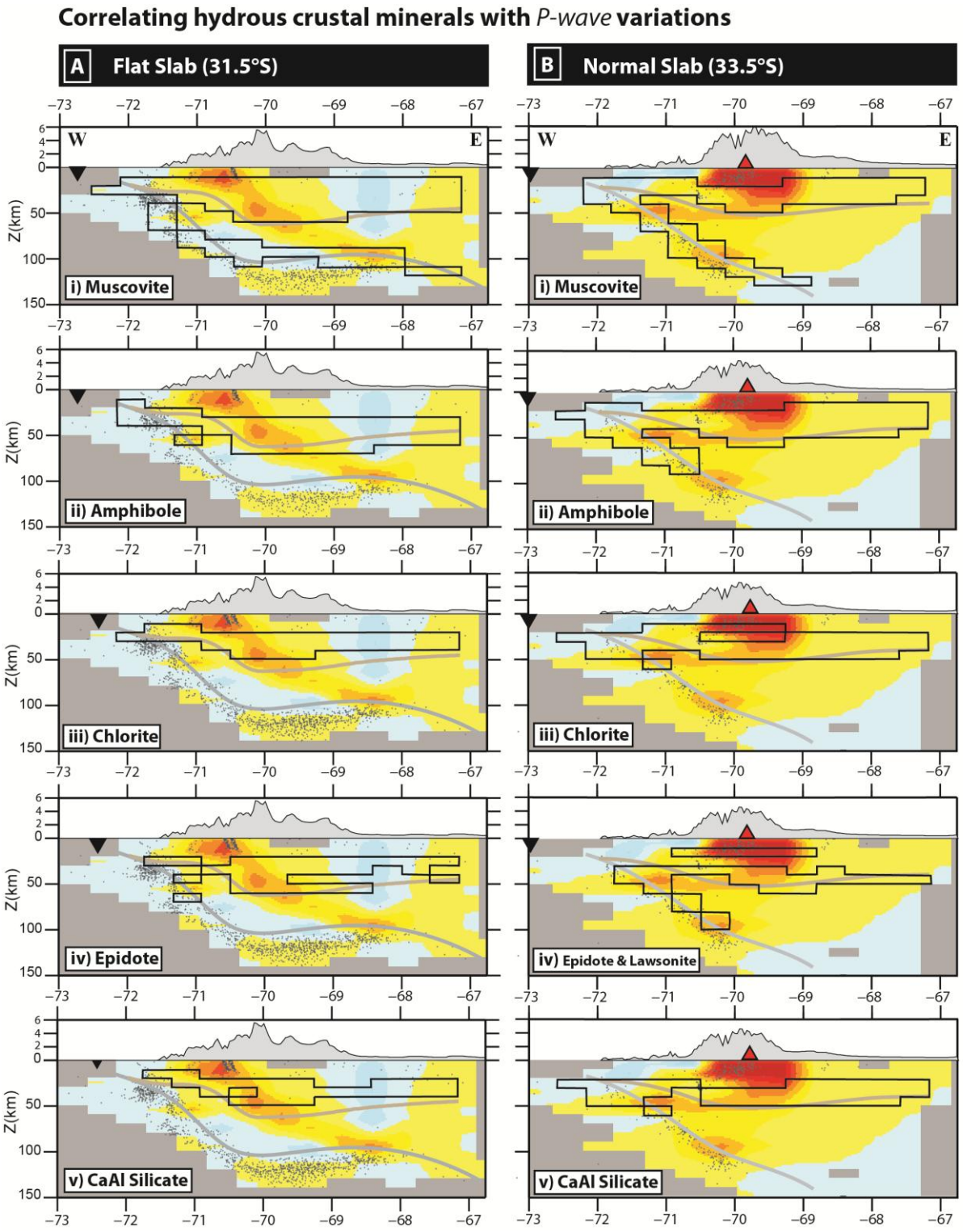


**Fig. B.4**: *Correlating the P-wave seismic velocity variations with the distribution of hydrous crustal minerals described in Fig. B.1 for the (A) flat and (B) normal subduction zones.*

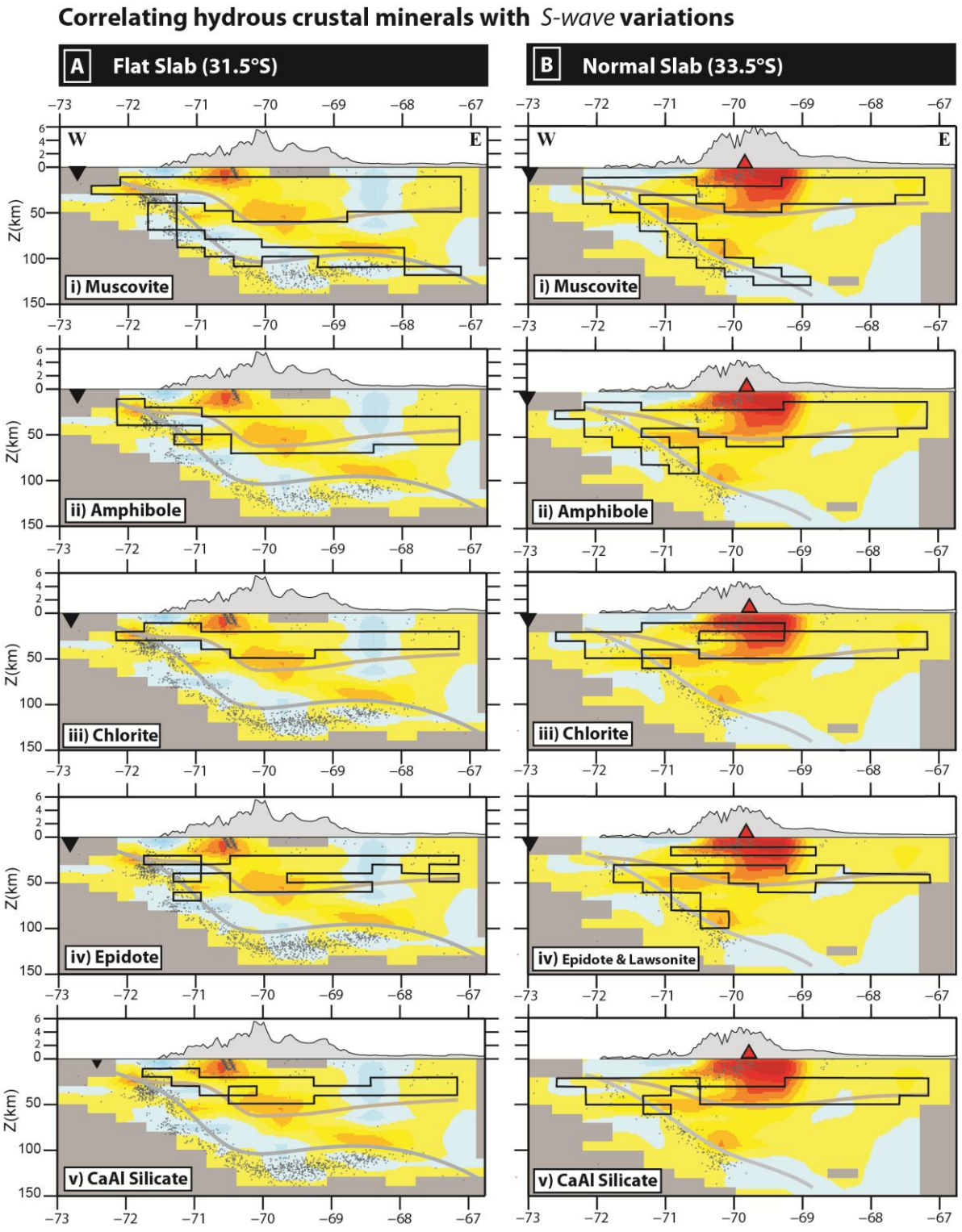


**Fig. B.5**: *Correlating the S-wave seismic velocity variations with the distribution of hydrous crustal minerals described in Fig. B.1 for the (A) flat and (B) normal subduction zones. Amphibole, chlorite, epidote and CaAl silicate (either lawsonite or prehnite) might be correlated with reductions in Vs, whereas a trend is not so obvious for Vp (Fig. B.4).*

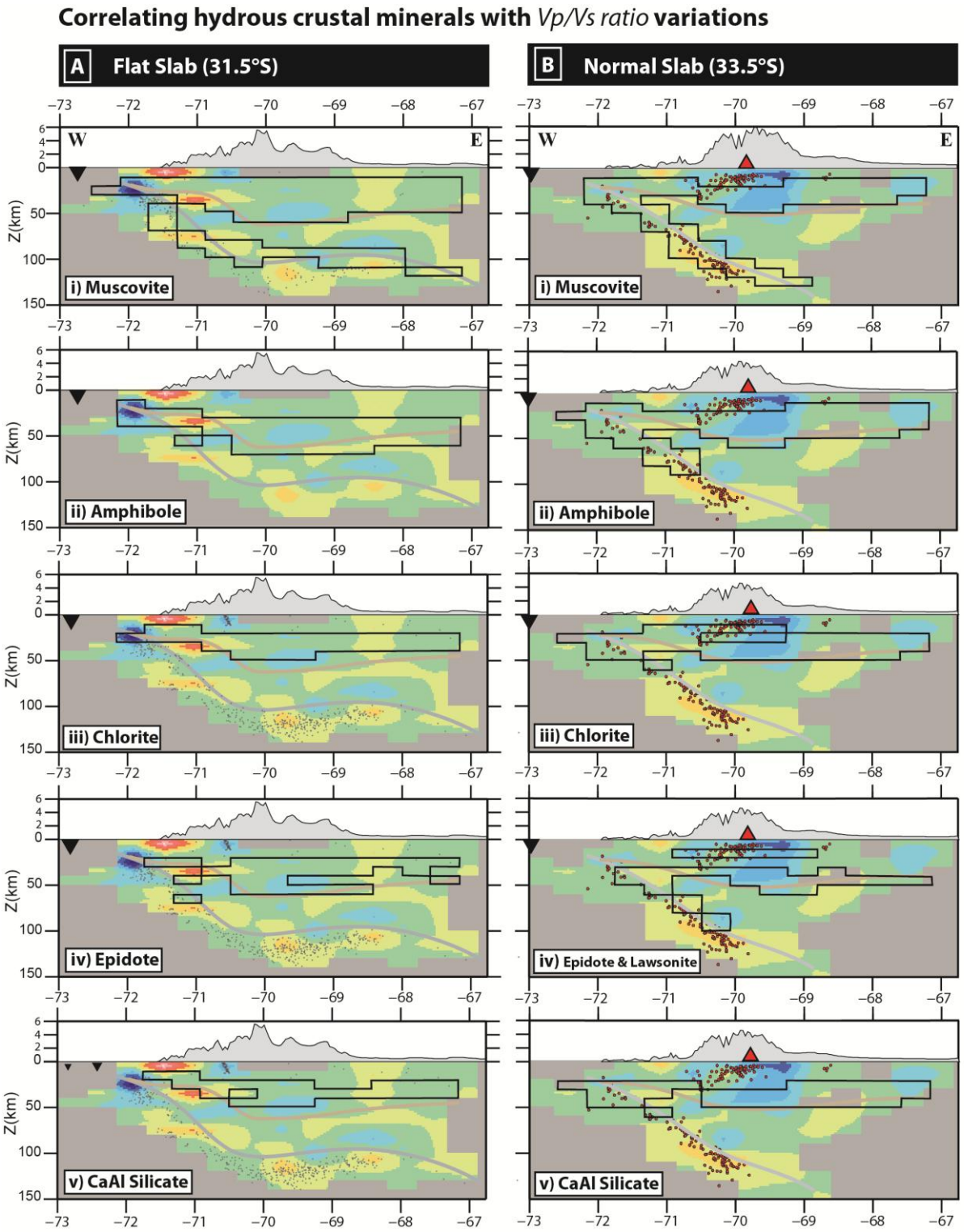


**Fig. B.6**: *Correlating the Vp/Vs ratio with the distribution of hydrous crustal minerals described in Fig. B.1 for the (A) flat and (B) normal subduction zones. A correlation is not clear.*

**Table A.1**: *Mafic MORB-type rock composition from Hacker and Abers (2004) used in our petrological modeling for the continental and oceanic crusts.*

| Mafic MORB-type Rock Compositions (vol%) | | | | | | | | | | | | | | | | | | | | | | | | |
|---|---|---|---|---|---|---|---|---|---|---|---|---|---|---|---|---|---|---|---|---|---|---|---|---|
| | **A** | **B1** | **B2** | **C** | **D** | **E** | **F** | **G** | **H1** | **H2** | **H3** | **H4** | **I1** | **I2** | **J1** | **J2** | **J3** | **J4** | **K1** | **K2** | **K3** | **K4** | **K5** | **K6** | **K7** |
| **qz** | | | | | 8.0 | 13.0 | 5.0 | 5.0 | 2.0 | 2.0 | 5.4 | 1.0 | | | 2.0 | 2.0 | 5.0 | 10.0 | 7.0 | 3.0 | 6.0 | 2.5 | 6.0 | | |
| **coe** | | | | | | | | | | | | | | | | | | | | | | | | 6.0 | 3.0 |
| **hAb** | | | | | | | | | | | | | 21.0 | | | | | | | | | | | | |
| **lAb** | 16.5 | 9.6 | 13.8 | | 19.0 | 20.0 | 21.0 | 22.0 | 20.0 | 11.0 | 10.5 | 18.0 | | 20.0 | 8.0 | | 18.0 | | | | | | | | |
| **an** | 38.5 | 38.4 | 41.3 | | | | | | | 6.0 | | 18.0 | 21.0 | 15.0 | | | | | | | | | | | |
| **alm** | | | | | | | | | | 11.0 | 7.4 | | | 5.0 | | | | | 17.0 | 17.0 | 18.1 | 8.0 | 18.0 | 18.0 | 19.0 |
| **gr** | | | | | | | | | | 8.0 | 2.6 | | | 13.0 | | | | | 7.0 | 15.0 | 8.0 | 7.5 | 13.0 | 13.0 | 14.0 |
| **py** | | | | | | | | | | 3.0 | 1.2 | | | 10.0 | | | | | 8.0 | 7.0 | 8.0 | 3.7 | 11.0 | 11.0 | 12.0 |
| **fo** | 1.0 | 7.5 | 7.5 | 13.2 | | | | | | | | | | | | | | | | | | | | | |
| **fa** | | 2.5 | 2.5 | 1.8 | | | | | | | | | | | | | | | | | | | | | |
| **en** | | 4.5 | | | | | | | | | | | 9.0 | 9.0 | | | | | | | 4.0 | | | | 1.0 |
| **fs** | | 5.5 | | | | | | | | | | | 9.0 | 9.0 | | | | | 1.0 | | 2.0 | | 4.0 | 4.0 | 3.0 |
| **di** | 32.3 | 25.6 | 28.0 | 77.4 | | | | | | | | | 5.0 | 5.0 | | | | | 11.0 | 15.0 | 19.5 | 7.5 | 24.0 | 24.0 | 21.0 |
| **hed** | 10.8 | 6.4 | 7.0 | 7.7 | | | | | | | | | 9.0 | 11.0 | | | | | 2.0 | 3.0 | 5.4 | 1.4 | 2.0 | 2.0 | 5.0 |
| **jd** | | | | | | | | | | | | | | 2.0 | | 8.0 | | 13.0 | 13.0 | 12.0 | 17.0 | 10.0 | 18.0 | 18.0 | 18.0 |
| **gl** | | | | | | | | | | | 6.9 | | | | 11.0 | 11.0 | 4.0 | 4.0 | 1.0 | | | 5.5 | | | |
| **fgl** | | | | | | | | | | 17.0 | 6.1 | | | | 6.0 | 6.0 | 4.0 | 4.0 | 5.0 | 10.0 | | 8.0 | | | |
| **tr** | | | | | | | 8.0 | 12.0 | 9.0 | 18.0 | 5.2 | 13.0 | 2.0 | | 12.0 | 14.0 | 15.0 | 15.0 | 10.0 | 4.0 | | 9.1 | | | |
| **fact** | | | | | | | 14.0 | 5.0 | 16.0 | 5.0 | 3.1 | 25.0 | 7.0 | | 17.0 | 17.0 | 5.0 | 5.0 | 1.0 | 2.0 | | 9.5 | | | |
| **ts** | | | | | | | | | 15.0 | 14.0 | | 12.0 | 9.0 | | | | | | 3.0 | | | | | | |
| **parg** | | | | | | | | | 10.0 | | | 12.0 | 7.0 | | | | | | | 8.0 | | 3.8 | | | |
| **phl** | | | | | | | | | | | 1.5 | | | | | | | | | | | | | | |
| **mu** | | | | | 2.0 | 2.0 | 2.0 | 2.0 | 2.0 | | 15.1 | | | | 2.0 | 2.0 | 2.0 | 2.0 | 2.0 | 2.0 | 2.0 | 2.0 | 2.0 | 2.0 | 2.0 |
| **clin** | | | | | 18.0 | 16.0 | 11.0 | 11.0 | 2.0 | | 4.3 | | | | 6.0 | 5.0 | 8.0 | 8.0 | | | | 2.7 | | | |

| | | | | | | | | | | | | | | | | | | | | | | | | | |
|---|---|---|---|---|---|---|---|---|---|---|---|---|---|---|---|---|---|---|---|---|---|---|---|---|---|
| **daph** | | | | | 10.0 | 8.0 | 6.0 | 8.0 | 3.0 | | 2.5 | | | | 3.0 | 4.0 | 8.0 | 8.0 | | | | 2.0 | | | |
| **zo** | | | | | | | | | | 4.0 | | | | | | | | | 10.0 | | 8.0 | | | | |
| **cz** | | | | | | | | | | | | | | | | | 5.0 | 5.0 | | | | | | | |
| **ep** | | | | | | | 8.0 | 32.0 | 18.0 | | 20.1 | | | | | | 23.0 | 23.0 | | | | | | | |
| **law** | | | | | | | 4.0 | | | | | | | | 30.0 | 28.0 | | | | | | 14.0 | | | |
| **pre** | | | | | | 14.0 | | | | | | | | | | | | | | | | | | | |
| **pump** | | | | | | 13.0 | 18.0 | | | | | | | | | | | | | | | | | | |
| **lmt** | | | | | 25.0 | | | | | | | | | | | | | | | | | | | | |
| **sp** | | | | | 2.0 | 3.0 | 3.0 | 3.0 | 3.0 | 1.0 | 1.7 | | | | 3.0 | 3.0 | 3.0 | 3.0 | 2.0 | 2.0 | 2.0 | 2.8 | 2.0 | 2.0 | 2.0 |
| **mt** | 1.0 | | | | 4.0 | 6.0 | | | | | 1.8 | 1.0 | 1.0 | 1.0 | | | | | | | | | | | |
| **cc** | | | | | 12.0 | 5.0 | | | | | 4.4 | | | | | | | | | | | | | | |
| | **Total vol% H2O** | | | | | | | | | | | | | | | | | | | | | | | | |
| | 0 | 0 | 0 | 0 | 55 | 53 | 71 | 70 | 75 | 58 | 64.9 | 62 | 25 | 0 | 87 | 87 | 74 | 74 | 32 | 26 | 10 | 56.6 | 2 | 2 | 2 |
| | **Composition (Weight %)** | | | | | | | | | | | | | | | | | | | | | | | | |
| **SiO2** | 51.5 | 49.6 | 50.1 | 52.8 | 43.1 | 46.0 | 48.5 | 48.1 | 49.0 | 50.9 | 46.1 | 51.7 | 51.8 | 50.5 | 48.1 | 47.7 | 49.5 | 49.8 | 50.8 | 48.4 | 50.3 | 48.0 | 50.4 | 50.4 | 48.5 |
| **Al2O3** | 17.3 | 15.9 | 17.8 | 0.0 | 16.0 | 17.9 | 17.7 | 17.1 | 17.0 | 16.7 | 18.7 | 15.3 | 15.3 | 16.4 | 17.9 | 17.6 | 16.5 | 16.3 | 17.4 | 16.5 | 16.7 | 17.2 | 16.2 | 16.2 | 16.8 |
| **FeO** | 4.0 | 6.6 | 3.8 | 3.5 | 8.8 | 9.6 | 9.4 | 10.6 | 10.1 | 10.8 | 11.8 | 10.2 | 11.0 | 11.2 | 9.3 | 9.8 | 10.3 | 10.3 | 10.1 | 11.4 | 10.5 | 10.3 | 10.6 | 10.6 | 11.3 |
| **MgO** | 6.6 | 10.9 | 9.5 | 22.0 | 7.1 | 7.2 | 7.6 | 7.8 | 8.0 | 7.7 | 5.2 | 7.3 | 7.7 | 7.5 | 7.7 | 7.8 | 8.1 | 8.1 | 8.1 | 8.0 | 8.2 | 8.1 | 8.3 | 8.3 | 8.5 |
| **CaO** | 18.5 | 15.8 | 17.1 | 21.8 | 9.7 | 9.7 | 9.6 | 9.7 | 10.7 | 10.2 | 9.2 | 11.6 | 10.8 | 11.7 | 9.0 | 8.9 | 9.2 | 9.2 | 10.3 | 12.0 | 11.2 | 10.4 | 11.5 | 11.5 | 11.8 |
| **Na2O** | 1.9 | 1.1 | 1.6 | 0.0 | 2.2 | 2.4 | 2.5 | 2.6 | 2.7 | 2.5 | 2.2 | 2.6 | 2.7 | 2.7 | 2.2 | 2.5 | 2.7 | 2.6 | 2.4 | 2.8 | 2.6 | 2.7 | 2.8 | 2.8 | 2.8 |
| **K2O** | 0.0 | 0.0 | 0.0 | 0.0 | 0.2 | 0.2 | 0.2 | 0.2 | 0.2 | 0.0 | 2.0 | 0.0 | 0.0 | 0.0 | 0.2 | 0.2 | 0.2 | 0.2 | 0.2 | 0.2 | 0.2 | 0.2 | 0.2 | 0.2 | 0.2 |
| **H2O** | 0.0 | 0.0 | 0.0 | 0.0 | 7.3 | 4.5 | 4.4 | 3.3 | 2.0 | 1.2 | 2.4 | 1.3 | 0.5 | 0.0 | 5.6 | 5.4 | 3.1 | 3.1 | 0.7 | 0.6 | 0.3 | 3.0 | 0.1 | 0.1 | 0.1 |
| **CO2** | 0.0 | 0.0 | 0.0 | 0.0 | 5.3 | 2.2 | 0.0 | 0.0 | 0.0 | 0.0 | 1.9 | 0.0 | 0.0 | 0.0 | 0.0 | 0.0 | 0.0 | 0.0 | 0.0 | 0.0 | 0.0 | 0.0 | 0.0 | 0.0 | 0.0 |

**Table A.1 Cont'd**: *Mafic MORB-type rock composition from Hacker and Abers (2004) used in our petrological modeling for the continental and oceanic crusts.*

**Table A.2**: *Hydrated mantle peridotite rock composition from Hacker and Abers (2004) used in our petrological modeling for the continental and oceanic mantle.*

| Hydrated Ultramafic Mantle-type Rock Compositions (vol%) | | | | | | | | | | | | | | | | | | |
|---|---|---|---|---|---|---|---|---|---|---|---|---|---|---|---|---|---|---|
| | **Lhz D** | **Lhz F** | **Lhz G** | **Lhz P** | **Lhz Q** | **Lhz S** | **Lhz T** | **Lhz U** | **Lhz V** | **Hz I** | **Hz J** | **Hz A** | **Hz B** | **Hz C** | **Hz D** | **Hz E** | **Atg A** | **Atg C** | **Atg D** |
| **lAb** | | 1.6 | 1.6 | | | | | | | | | | | | | | | | |
| **an** | | 9.8 | 9.8 | | | | | | | | | | | | | | | | |
| **alm** | | | | | | | | | | | | | | | | | | | |
| **gr** | | | | | | | | | | | | | | | | | | | |
| **py** | | | | | | | | | | | | | | | | | | | |
| **fo** | 46.7 | 54.1 | 53.1 | 34.1 | 20.9 | 31.9 | | | | | 65.5 | 67.9 | 66.6 | | | 45.1 | 53.1 | | |
| **fa** | 5.2 | 6.0 | 5.9 | 3.8 | 2.3 | 3.5 | | | | | 7.3 | 7.5 | 7.4 | | | 5.0 | 5.9 | | |
| **en** | 3.3 | 4.9 | 4.9 | | | 10.5 | | 29.5 | | | 14.7 | | | 38.6 | | | | | 60.6 |
| **fs** | 0.4 | 0.5 | 0.5 | | | 1.2 | | 3.3 | | | 1.6 | | | 4.3 | | | | | 6.7 |
| **di** | 1.7 | 1.7 | 1.7 | 6.8 | 14.5 | 15.8 | 13.4 | 13.3 | 12.9 | | | | | | | | | | |
| **sp** | 3.6 | 0.8 | 1.3 | | | | | | | | | | | | | | | | |
| **mt** | 3.6 | 0.8 | 1.3 | | | | | | | | | | | | | | | | |
| **hed** | 0.2 | 0.2 | 0.2 | 0.8 | 1.6 | 1.8 | 1.5 | 1.5 | 1.4 | | | | | | | | | | |
| **tr** | 12.4 | 6.9 | 6.9 | 6.9 | | | | | | | | | | | | | | | |
| **fact** | 1.8 | 1.0 | 1.0 | 1.0 | | | | | | | | | | | | | | | |
| **parg** | 21.2 | 11.8 | 11.8 | 11.9 | | | | | | | | | | | | | | | |
| **anth** | | | | | | | | | | | | | 15.2 | | | | | | |
| **ta** | | | | | | | | | | | | 13.9 | | | | | 41.0 | | |
| **clin** | | | | 31.2 | 28.4 | 31.8 | 26.2 | 27.6 | 25.3 | 7.0 | 9.9 | 9.6 | 9.7 | 9.0 | 7.5 | 8.7 | | | |
| **daph** | | | | 3.5 | 3.2 | 3.5 | 2.9 | 3.1 | 2.8 | 0.8 | 1.1 | 1.1 | 1.1 | 1.0 | 0.8 | 1.0 | | | |
| **atg** | | | | | 29.2 | | 45.3 | 0.0 | 50.7 | 78.8 | | | | | 70.3 | 40.2 | | 100.0 | |

| | | | | | | | | | | | | | | | | | | | |
|---|---|---|---|---|---|---|---|---|---|---|---|---|---|---|---|---|---|---|---|
| **br** | | | | | | | | | 6.9 | 13.4 | | | | | | | | | |
| **phA** | | | | | | | 10.7 | 21.8 | | | | | | 47.0 | 21.4 | | | | 32.7 |
| | **Total vol% H2O** | | | | | | | | | | | | | | | | | | |
| | 35.4 | 19.7 | 19.7 | 54.5 | 60.8 | 35.3 | 85.1 | 52.5 | 85.7 | 100 | 11 | 24.6 | 26 | 57 | 100 | 49.9 | 41 | 100 | 32.7 |
| | **Composition (Weight %)** | | | | | | | | | | | | | | | | | | |
| **SiO2** | 42.0 | 44.1 | 43.6 | 40.6 | 41.6 | 42.3 | 40.6 | 42.7 | 39.6 | 38.0 | 43.1 | 43.4 | 43.4 | 40.7 | 39.9 | 41.9 | 50.4 | 45.0 | 47.9 |
| **Al2O3** | 6.5 | 6.6 | 7.0 | 8.4 | 5.7 | 6.4 | 5.2 | 5.5 | 5.0 | 1.4 | 2.0 | 1.9 | 1.9 | 1.8 | 1.5 | 1.7 | 0.0 | 0.0 | 0.0 |
| **FeO** | 7.9 | 5.7 | 6.1 | 5.0 | 3.7 | 5.4 | 1.9 | 3.8 | 1.8 | 0.4 | 6.6 | 5.9 | 5.8 | 2.8 | 0.4 | 4.0 | 4.2 | 0.0 | 3.7 |
| **MgO** | 36.6 | 37.5 | 37.0 | 36.2 | 37.4 | 37.0 | 37.9 | 37.8 | 38.0 | 45.4 | 47.0 | 46.8 | 47.2 | 47.9 | 45.9 | 46.1 | 43.5 | 42.7 | 44.5 |
| **CaO** | 5.2 | 5.1 | 5.1 | 4.6 | 4.1 | 4.5 | 3.8 | 3.8 | 3.7 | 0.0 | 0.0 | 0.0 | 0.0 | 0.0 | 0.0 | 0.0 | 0.0 | 0.0 | 0.0 |
| **Na2O** | 0.8 | 0.6 | 0.6 | 0.4 | 0.0 | 0.0 | 0.0 | 0.0 | 0.0 | 0.0 | 0.0 | 0.0 | 0.0 | 0.0 | 0.0 | 0.0 | 0.0 | 0.0 | 0.0 |
| **K2O** | 0.0 | 0.0 | 0.0 | 0.0 | 0.0 | 0.0 | 0.0 | 0.0 | 0.0 | 0.0 | 0.0 | 0.0 | 0.0 | 0.0 | 0.0 | 0.0 | 0.0 | 0.0 | 0.0 |
| **H2O** | 0.8 | 0.4 | 0.4 | 4.8 | 7.6 | 4.5 | 10.5 | 6.5 | 11.9 | 14.8 | 1.4 | 2.0 | 1.7 | 6.8 | 12.2 | 6.2 | 2.0 | 12.3 | 3.9 |
| **CO2** | 0.0 | 0.0 | 0.0 | 0.0 | 0.0 | 0.0 | 0.0 | 0.0 | 0.0 | 0.0 | 0.0 | 0.0 | 0.0 | 0.0 | 0.0 | 0.0 | 0.0 | 0.0 | 0.0 |

**Table A.2 Cont'd**: *Hydrated mantle peridotite rock composition from Hacker and Abers (2004) used in our petrological modeling for the continental and oceanic mantle.*

**Table A.3**: *Anhydrous mantle peridotite rock composition from Hacker and Abers (2004) used in our petrological modeling for the continental and oceanic mantle.*

| Non-Hydrated Ultramafic Mantle-type Rock Compositions (vol%) | | | | | | | | | | | | | | | | | | | |
|---|---|---|---|---|---|---|---|---|---|---|---|---|---|---|---|---|---|---|---|
| | **Lhz 1** | **Lhz 2** | **Lhz A** | **Lhz B** | **Lhz H** | **Lhz L** | **Lhz M** | **Lhz N** | **Lhz O** | **Lhz W** | **Dunite** | **Wehrlite** | **Oliv. Clinopyr.** | **Hz 1** | **Hz 2** | **Hz F** | **Hz G** | **Hz H** | **Hz K** | **Atg E** |
| **lAb** | | | | | 1.6 | 1.6 | | | | | | 3.3 | | | | | | | | |
| **an** | | | | | 10.1 | 10.0 | | | | | | 9.8 | | | | | | | | |
| **alm** | | | | | | | | 3.2 | 4.1 | 5.2 | | | | | 0.7 | 0.6 | | | 1.5 | |
| **gr** | | | | | | | | 1.4 | 1.7 | 2.2 | | | | | 0.5 | 0.2 | | | 0.6 | |
| **py** | | | | | | | | 8.9 | 11.2 | 14.3 | | | | | 5.4 | 1.6 | | | 4.0 | |
| **fo** | 45.4 | 67.0 | 48.0 | 44.3 | 52.5 | 53.9 | 45.8 | 51.0 | 51.2 | 51.4 | 90.0 | 31.5 | 13.2 | 72.5 | 61.7 | 72.0 | 71.0 | 69.9 | 72.3 | 44.5 |
| **fa** | 5.1 | 7.0 | | 4.9 | 5.8 | 6.0 | 5.1 | 5.7 | 5.7 | 5.7 | 10.0 | 3.5 | 1.8 | 7.5 | 5.4 | 8.0 | 7.9 | 7.8 | 8.0 | 4.9 |
| **en** | 22.5 | 19.2 | 24.8 | 22.3 | 15.3 | 15.2 | 22.3 | 9.0 | 5.6 | 1.1 | | 4.0 | | 18.2 | 16.8 | 15.8 | 18.2 | 18.2 | 12.2 | 45.5 |
| **fs** | 2.5 | 1.8 | | 2.5 | 1.7 | 1.7 | 2.5 | 1.0 | 0.6 | 0.1 | | 1.0 | | 1.8 | 1.6 | 1.8 | 2.0 | 2.0 | 1.4 | 5.1 |
| **di** | 20.0 | 2.9 | 19.7 | 17.7 | 10.4 | 10.4 | 17.7 | 17.8 | 17.9 | 18.0 | | 37.6 | 77.4 | | 6.7 | | | | | |
| **hed** | | 0.1 | | 2.0 | 1.2 | 1.2 | 2.0 | 2.0 | 2.0 | 2.0 | | 9.4 | 7.7 | | | | | | | |
| **jd** | | | | | | | | | | | | | | | 1.2 | | | | | |
| **sp** | 4.5 | 1.0 | 7.5 | 3.2 | 0.8 | | 2.4 | | | | | | | | | | 0.4 | 1.1 | | |
| **mt** | | 1.0 | | 3.2 | 0.8 | | 2.4 | | | | | | | | | | 0.4 | 1.1 | | |
| **Composition (Weight %)** | | | | | | | | | | | | | | | | | | | | |
| **SiO2** | 47 | 44.64 | 46.28 | 45.63 | 45.81 | 46 | 46.28 | 45.85 | 45.26 | 44.45 | 41.38 | 49.20 | 52.80 | 45 | 46.02 | 44.39 | 44.47 | 43.94 | 43.74 | 50.00 |
| **Al2O3** | 3 | 0.72 | 5.37 | 2.26 | 4.56 | 4 | 1.69 | 3.23 | 4.05 | 5.16 | 0.00 | 4.21 | 0.00 | 0 | 1.92 | 0.58 | 0.31 | 0.77 | 1.46 | 0.00 |
| **FeO** | 5 | 6.9 | 0.0 | 8.3 | 6.1 | 5 | 7.7 | 6.5 | 6.7 | 6.9 | 7.1 | 5.7 | 3.5 | 6 | 5.0 | 6.9 | 7.1 | 7.6 | 7.0 | 6.2 |
| **MgO** | 40 | 46.9 | 43.3 | 38.5 | 38.3 | 39 | 39.2 | 38.8 | 38.3 | 37.5 | 51.6 | 26.7 | 22.0 | 49 | 45.0 | 48.1 | 48.1 | 47.6 | 47.5 | 43.8 |
| **CaO** | 5 | 0.8 | 5.1 | 5.0 | 5.0 | 5 | 5.0 | 5.6 | 5.7 | 5.9 | 0.0 | 13.8 | 21.8 | 0 | 1.9 | 0.1 | 0.0 | 0.0 | 0.2 | 0.0 |
| **Na2O** | 0 | 0.0 | 0.0 | 0.0 | 0.2 | 0 | 0.0 | 0.0 | 0.0 | 0.0 | 0.0 | 0.4 | 0.0 | 0 | 0.2 | 0.0 | 0.0 | 0.0 | 0.0 | 0.0 |
| **K2O** | 0 | 0.0 | 0.0 | 0.0 | 0.0 | 0 | 0.0 | 0.0 | 0.0 | 0.0 | 0.0 | 0.0 | 0.0 | 0 | 0.0 | 0.0 | 0.0 | 0.0 | 0.0 | 0.0 |
| **H2O** | 0 | 0.0 | 0.0 | 0.0 | 0.0 | 0 | 0.0 | 0.0 | 0.0 | 0.0 | 0.0 | 0.0 | 0.0 | 0 | 0.0 | 0.0 | 0.0 | 0.0 | 0.0 | 0.0 |
| **CO2** | 0 | 0.0 | 0.0 | 0.0 | 0.0 | 0 | 0.0 | 0.0 | 0.0 | 0.0 | 0.0 | 0.0 | 0.0 | 0 | 0.0 | 0.0 | 0.0 | 0.0 | 0.0 | 0.0 |

**Table A.4**: *Mafic MORB-type rocks names referred to in Table A.1 and Fig. 2.3.1.*

| Mafic MORB-type Rocks | |
|---|---|
| **A** | Diabase |
| **B1** | Gabbronorite |
| **B2** | Olivine Gabbro |
| **C** | Olivine Clinopyroxene |
| **D** | Zeolite facies |
| **E** | Prehnite-Pumpellyite facies |
| **F** | Pumpellyite-Actinolite facies |
| **G** | Greenschist facies |
| **H1** | Epidote-Amphibolite facies |
| **H2** | Garnet-Amphibolite facies |
| **H3** | Epidote-Garnet Amphibolite facies |
| **H4** | Amphibolite facies |
| **I1** | Granulite facies |
| **I2** | Garnet-Granulite facies |
| **J1** | Lawsonite-Blueschist facies |
| **J2** | Jadeite-Lawsonite Blueschist facies |
| **J3** | Epidote Blueschist |
| **J4** | Jadeite-Epidote Blueschist |
| **K1** | Zoisite-Amphibole Eclogite |
| **K2** | Amphibole Eclogite |
| **K3** | Zoisite Eclogite |
| **K4** | Lawsonite-Amphibole Eclogite |
| **K5** | Eclogite |
| **K6** | Coesite Eclogite |
| **K7** | Diamond Eclogite |

**Table A.5**: *Mineral names, annotations, chemical formulae and group, referred to in Tables A.1 and A.2.*

| | | | |
|---|---|---|---|
| **qz** | quartz | SiO2 | tectosilicate |
| **coe** | coesite | SiO2 | tectosilicate |
| **hAb** | high albite | NaAlSi3O8 | high-T plagioclase |
| **lAb** | low albite | NaAlSi3O8 | low-T plagioclase |
| **an** | anorthite | CaAl2Si2O8 | plagioclase |
| **alm** | almandine | Fe3Al2Si3O12 | Fe garnet |
| **gr** | grossular | Ca3Al2Si3O12 | Ca garnet |
| **py** | pyrope | Mg3Al2Si3O12 | Mg garnet |
| **fo** | forsterite | Mg2SiO4 | Mg olivine |
| **fa** | fayalite | Fe2SiO4 | Fe olivine |
| **en** | enstatite | Mg2Si2O6 | Mg orthopyroxene |
| **fs** | ferrosilite | Fe2Si2O6 | Fe orthopyroxene |
| **di** | diopside | CaMgSi2O6 | Mg clinopyroxene |
| **hed** | hedenbergite | CaFeSi2O6 | Fe clinopyroxene |
| **jd** | jadeite | NaAlSi2O6 | NaAl clinopyroxene |
| **gl** | glaucophane | Na2Mg3Al2Si8O22(OH)2 | NaMg amphibole |
| **fgl** | ferroglaucophane | Na2Fe3Al2Si8O22(OH)2 | NaFe amphibole |
| **tr** | tremolite | Ca2Mg5Si8O22(OH)2 | CaMg amphibole |
| **fact** | ferroactinolite | Ca2Fe5Si8O22(OH)2 | CaFe amphibole |
| **ts** | tschermakite | Ca2Mg3Al4Si6O22(OH)2 | MgAl amphibole |
| **parg** | pargasite | NaCa2Mg4Al3Si6O22(OH)2 | NaCaMgAl amphibole |
| **hb** | hornblende | Ca2(Mg.Fe)4(Al.Fe)Si7AlO22(OH)2 | generic amphibole |
| **anth** | anthophyllite | Mg7Si8O22(OH)2 | Mg orthoamphibole |
| **phl** | phlogopite | KMg3AlSi3O10(OH)2 | Mg biotite |
| **mu** | muscovite | KAl3Si3O10(OH)2 | low-Si K white mica |
| **cel** | celadonite | KMgAlSi4O10(OH)2 | high-Si K white mica |
| **ta** | talc | Mg3Si4O10(OH)2 | phyllosilicate |
| **clin** | clinochlore | Mg5Al2Si3O10(OH)8 | Mg chlorite |
| **daph** | daphnite | Fe5Al2Si3O10(OH)8 | Fe chlorite |
| **atg** | antigorite | Ca2Al3Si3O12(OH) | high-T serpentine |
| **zo** | zoisite | Ca2Al3Si3O12(OH) | high-P epidote group |
| **cz** | clinozoisite | Ca2Al3Si3O12(OH) | low-P epidote group |
| **ep** | epidote | Ca2FeAl2Si3O12(OH) | Fe epidote |
| **law** | lawsonite | CaAl2Si2O7(OH)2•H2O | high-P CaAl silicate |
| **pre** | prehnite | Ca2Al2Si3O10(OH)2 | low-P CaAl silicate |
| **pump** | pumpellyite | Ca4MgAl5Si6O21(OH)7 | low-T CaAl silicate |
| **lmt** | laumontite | CaAl2Si4O12•4H2O | low-T zeolite |
| **br** | brucite | Mg(OH2) | hydroxide |
| **phA** | phase A | Mg7Si2O8(OH)6 | high-P sheet silicate |
| **sp** | spinel | MgAl2O4 | MgAl spinel |
| **mt** | magnetite | FeFe2O4 | FeFe spinel |
| **cc** | calcite | CaCO3 | carbonate |

# **Appendix C:** Chapter 3 – Results and Interpretations

## Seismic Tomography

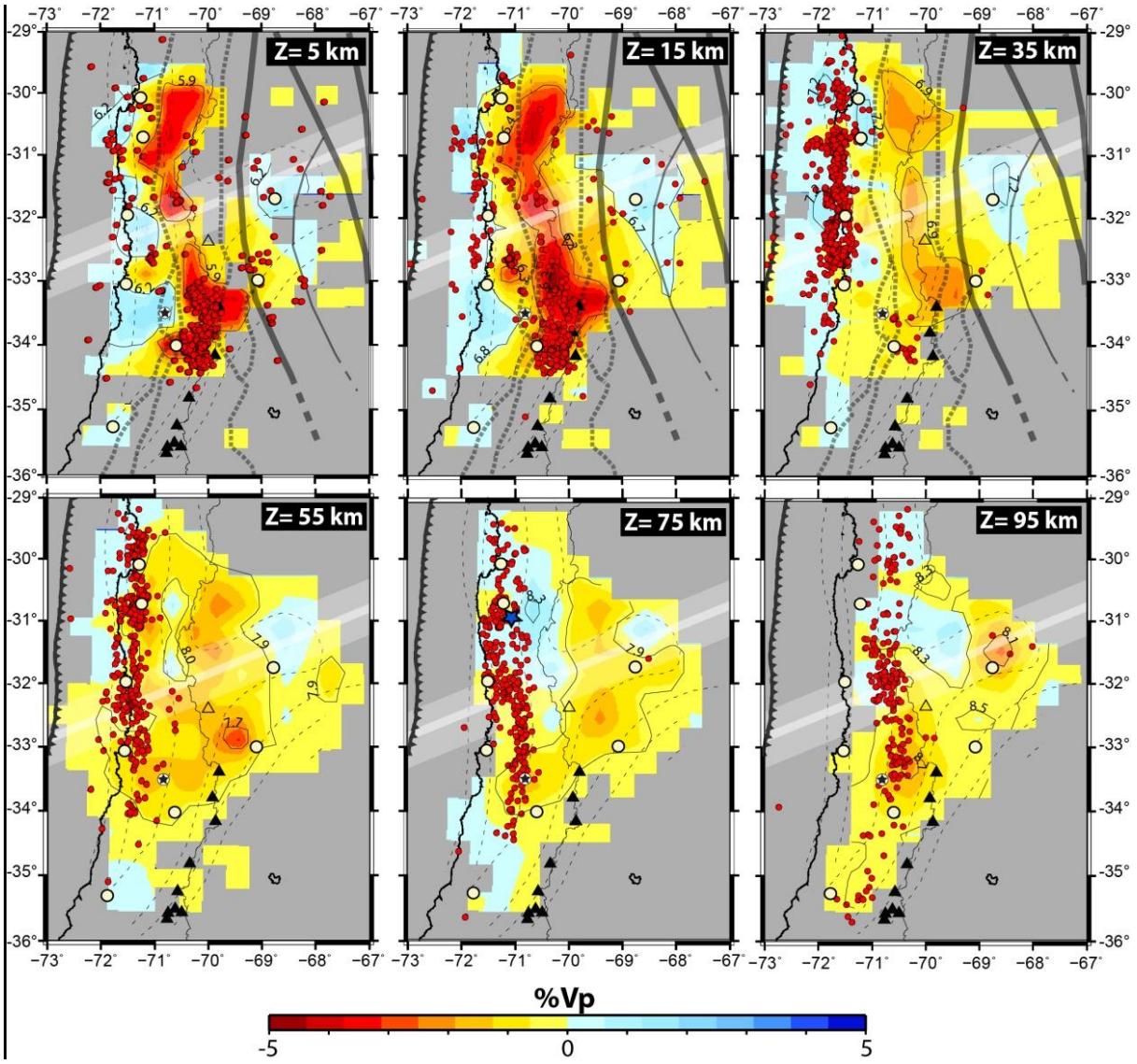


**Fig. C.1***: Horizontal cross-sections of the P-wave perturbations, relative to our background model, at depth intervals of 20 km. Contour lines are the absolute P-wave velocities. Red dots are the seismicity at these depth slices. Blue star is the hypocenter of the Punitaqui earthquake (exactly 70 km depth). Coastline, trench and political border between Chile and Argentina are shown by black sinuous lines. White circles locate the major cities and the capital city Santiago with a star. Thin dotted lines are the slab contour lines from Anderson et al. (2007). Black triangles show the positions of the active volcanoes. Small empty triangle at the center indicates the location of the Aconcagua highest peak of the region (6500 m).*

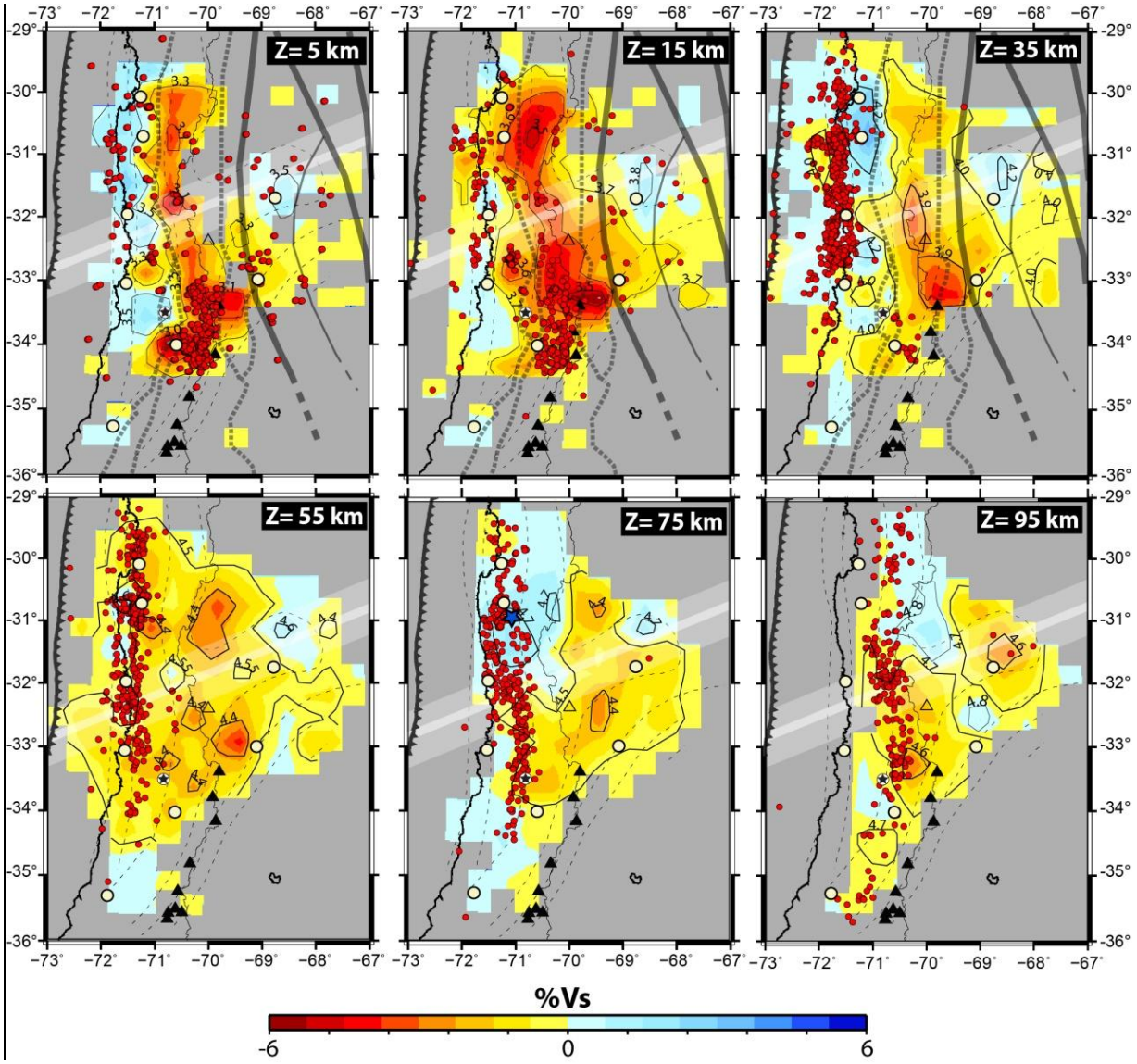


**Fig. C. 2** *: Horizontal cross-section at 20 km depth intervals showing the S-wave velocity perturbation, with respect to our background model. Legend is the same as for Fig. C.1.*

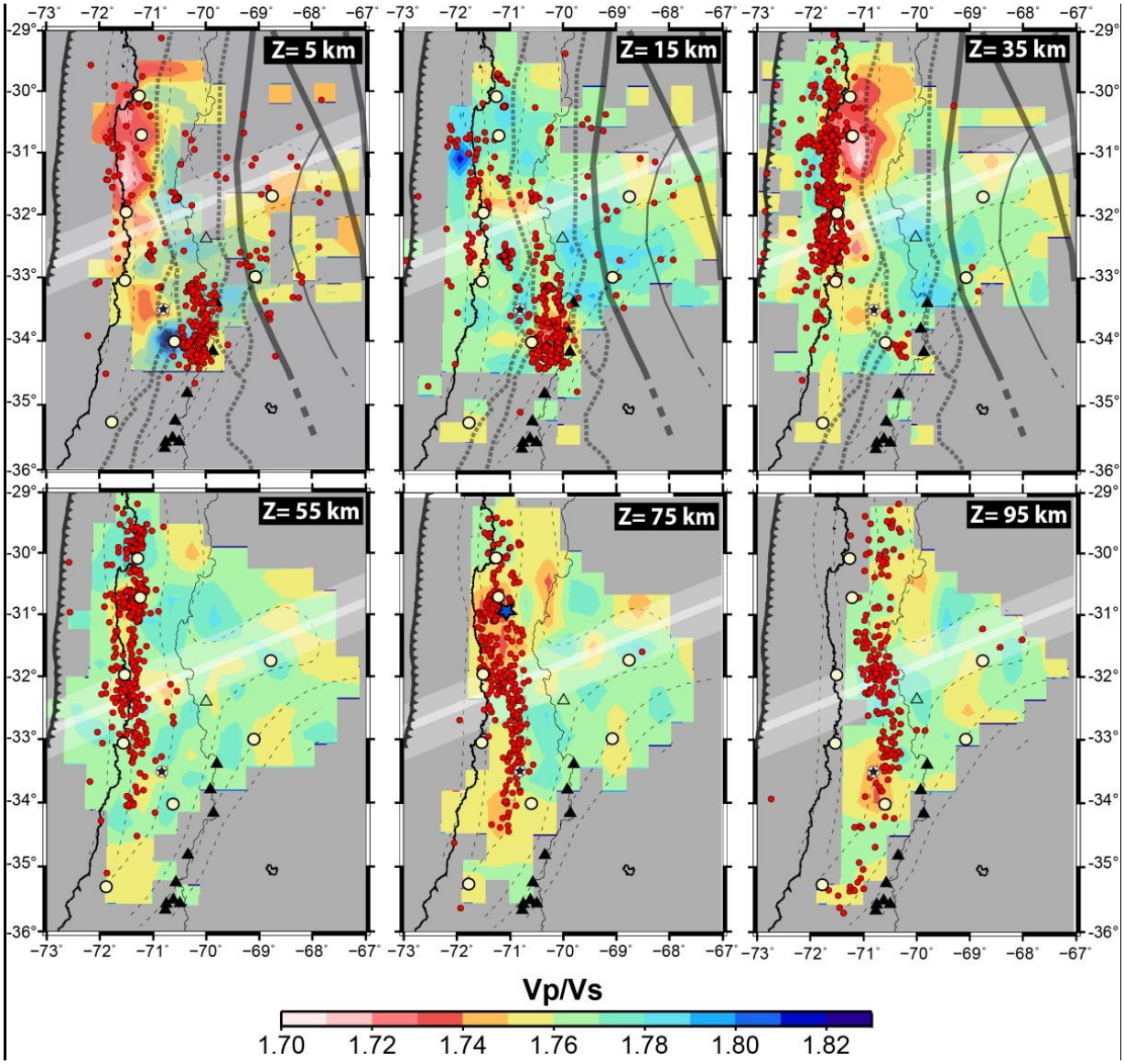


**Fig. C.3***: Horizontal cross-section at 20 km depth intervals of the Vp/Vs ratios. Legend is the same as for previous figures.*

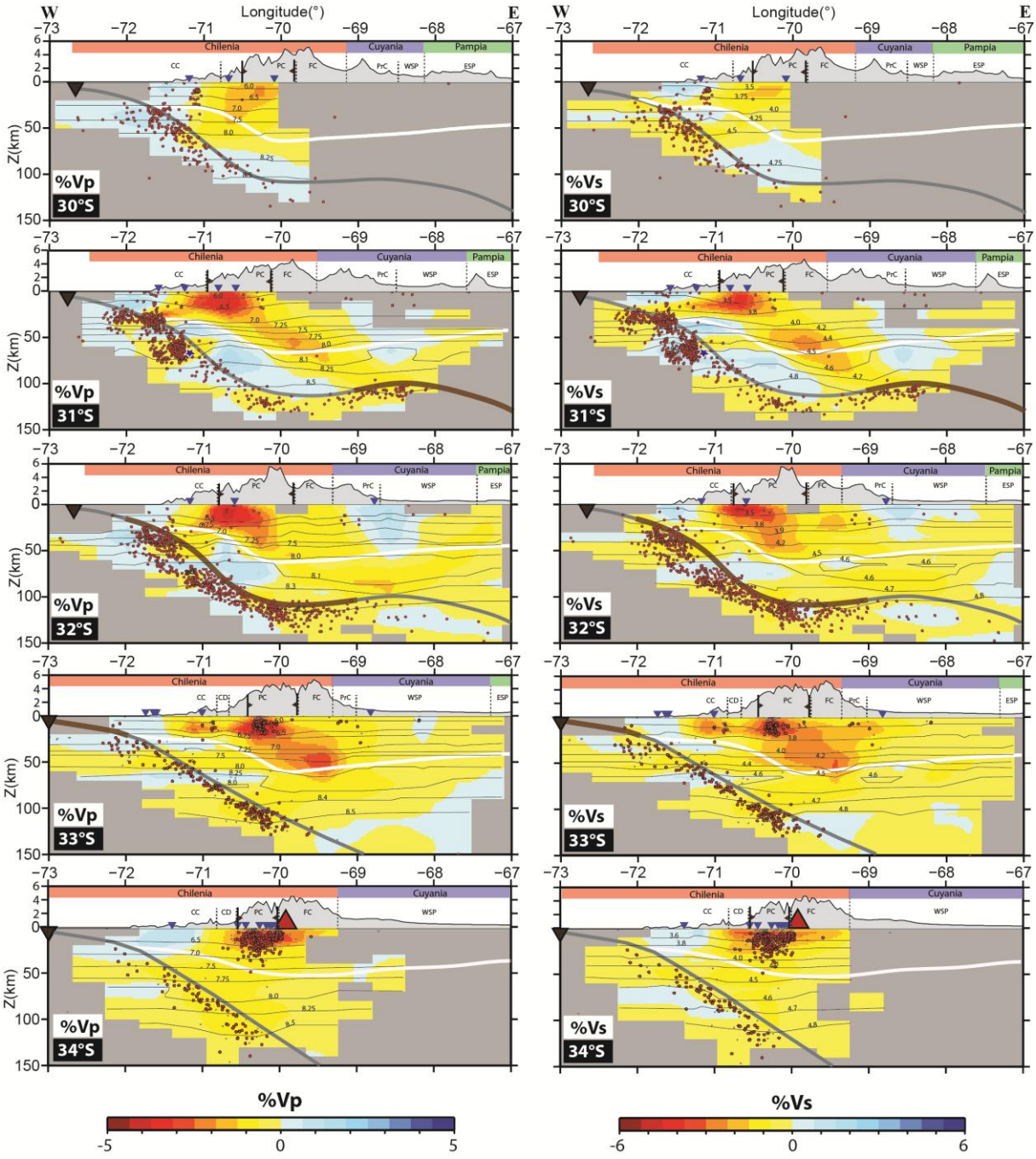


**Fig. C.4**: *E-W vertical profiles along the region, from north to south, at 0.5° and 1°S intervals, showing the P- and S-wave velocity perturbation, relative to our background model. Superimposed are contour lines that represent the absolute values, respectively. The seismicity is shown in black/red dots, and represents the entire catalog, and not just those chosen for the tomography inversion. The slab surface (thick grey line) is inferred from the slab seismic distribution, and the suspected location of the subducted Juan Fernandez ridge material (brown line segment). Topography, location of active volcanoes (red triangle), geological provinces and terranes and seismic station location (inverted blue triangles) are shown in the upper quadrant of each profile.*

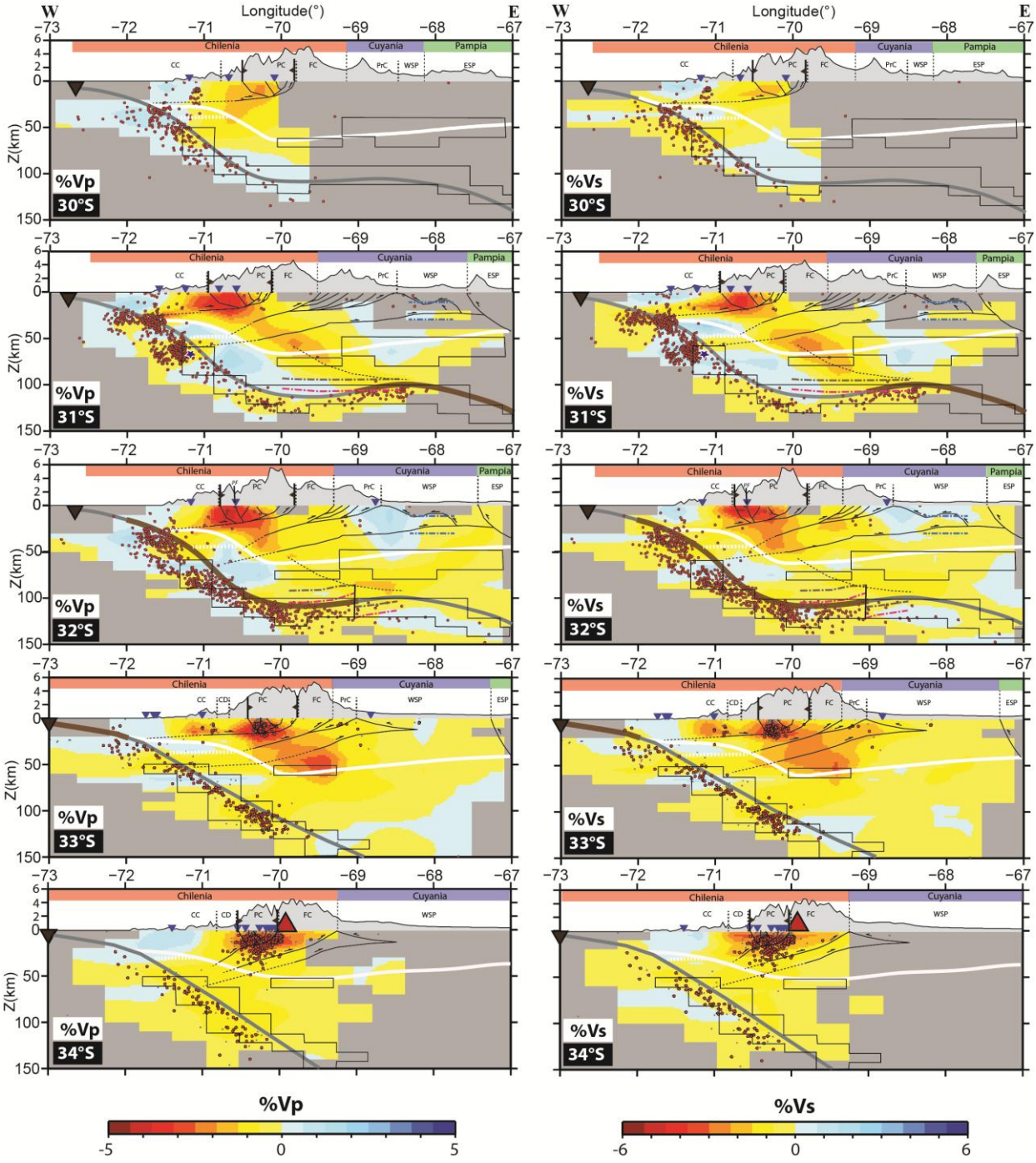


**Fig. C.5***: E-W vertical profiles along the region, from north to south, at 0.5° and 1°S intervals, showing the P- and S-wave velocity perturbation, relative to our background model. Boxes represent the fields where eclogite can be present. Curved solid and dotted lines in the continental crust (defined by the Moho in white or brown thick line) indicate the approximate geometry at depth of inferred major detachment faults (from Ramos et al. 2002 and Farias et al. 2010), and our speculation of their westward extension into the mantle wedge or slab interface, which remains purely hypothetical, and based on our seismic tomography results and other independent studies (see text).Seismic interfaces are shown by grey (slab interface and crustal discontinuities) and pink (oceanic Moho) dotted lines, by Gans et al. (2011).Legend is the same as previous figure.*

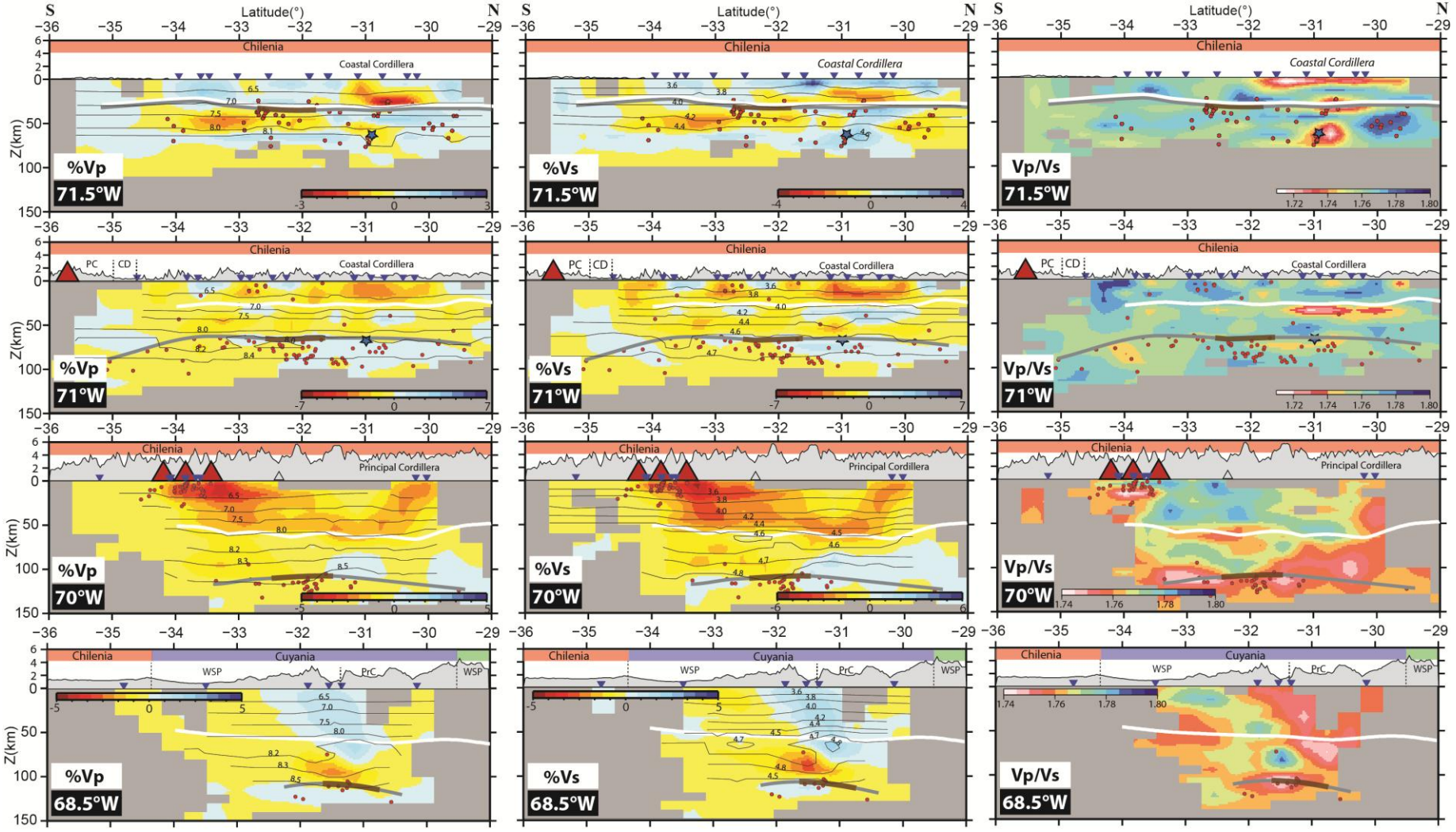


**Fig. C. 6** *: N-S vertical profiles at different longitudes, transecting (from top to bottom) the forearc, mantle wedge nose, continental mantle and Cuyania regions, for P-wave and S-wave perturbations and Vp/Vs ratios. Legend is the same as for previous figures.*